MONTANUNIVERSITÄT LEOBEN

Dissertation

The role of grain boundaries and segregation effects in molybdenum and its alloys

Katharina Leitner

Department of Physical Metallurgy and Materials Testing
in cooperation with Plansee SE

Leoben, February 2017

Copyright © 2017 by Katharina Leitner. All rights reserved.

Department of Physical Metallurgy and Materials Testing
Montanuniversität Leoben
Franz-Josef-Straße 18
8700 Leoben, Austria

Affidavit

I declare in lieu and oath, that I wrote this thesis and performed the associated research myself, using only literature cited in this volume.

Leoben, 20.02.2017 Katharina Leitner

Danksagung

Als Erstes möchte ich mich sehr herzlich bei Prof. Helmut Clemens bedanken, der mir es ermöglichte, ein so hoch interessantes Thema an seinem Lehrstuhl zu erarbeiten. Durch seine guten Ideen bei diversen Diskussionen und durch seinen unermüdlichen Einsatz Publikationen in nur einer Nacht zu verbessern gelang es mir eine hochwertige wissenschaftliche Arbeit zu erstellen.
Lieber Helmut, vielen herzlichen Dank für deinen unermüdlichen Einsatz für mich.

Ein großes Dankeschön gilt auch Dr. Sophie Primig, die während ihrer Zeit bei uns am Lehrstuhl meine Dissertation betreute. Sie verließ uns leider nach Australien, nahm sich aber weiterhin die Zeit meine Dissertation vom anderen Ende der Welt aus zu unterstützen.
Liebe Sophie, danke für die vielen wunderbaren Stunden mit dir und für die tatkräftige Unterstützung meines Auslandsaufenthaltes in Australien. Diese Forschungsreise hat nicht nur mein Leben sondern auch noch viel mehr dein Leben auf eine wunderbare Weiße verändert.

Einen ganz besonderen Dank möchte ich der Firma Plansee SE aussprechen, die mir ein höchst interessantes Thema als Dissertation anvertraute und meine gesamte Arbeit finanzierte.
Lieber Wolfram, herzlichen Dank für das Vertrauen in mich und mein Können. Es waren nicht nur wunderbare wissenschaftliche Diskussionsstunden sondern auch einzigartige menschliche Begegnungen, die ich in der gemeinsamen Zeit erfahren durfte.
Lieber Alex, danke für die super Betreuung meiner Dissertation. Durch unsere Telefongespräche konnte ich ständig mein Wissen über Refraktärmetalle erweitern. Ich hoffe, ich konnte auch dir einen kleinen Einblick in die atomare Welt des Molybdäns eröffnen.
Bedanken möchte ich mich auch bei Dr. Karl Huber, Dr. Michael Schober und Dr. Jürgen Schatte, die mich tatkräftig unterstützt haben. Durch eure technischen und industriellen Hintergedanken hat meine Dissertation maßgeblich an Qualität gewonnen.

Großer Dank gebührt auch Herrn Prof. Roland Stickler, der mir mit seinem unendlichen Wissen immer zur Seite stand.
Lieber Herr Professor, vielen Dank, dass Sie in ihrem hohen Alter immer wieder die weite Reise nach Leoben auf sich genommen haben um mit uns gemeinsam über Molybdän zu diskutieren. Durch ihr fachkundiges Wissen und insbesondere ihre Kenntnisse über bereits vergessene Literatur konnte ich vieles über die Historie von Refraktärmetallen lernen.

Ein besonderer Dank gilt auch dem gesamten Moly-Task-Force-Team. Danke Christopher, David, Roland, und Maximilian für die lustigen gemeinsamen Molybdän-Stunden.

Ich möchte mich auch sehr herzlich bei meiner neuen Gruppenleiterin Verena Maier-Kiener bedanken, die mir in den letzten Monaten bei jeglichen organisatorischen Fragen zur Seite gestanden ist.
Liebe Verena, ich glaube wir sind nun alle schwer begeistert von der Nandoindentation. Ich wünsche dir als Gruppenleiterin alles Gute für die Zukunft.

Bedanken möchte ich mich auch bei meinen Büro- und Arbeitskollegen am Institut, die mich in jeder Lebenslage unterstützten (und aushielten). Danke Turki, Chrisi, Stephi, David, Phil, Hofi, Irmi, Andreas und Gerhard für die vielen lustigen gemeinsamen Stunden.

Ein besonderer Dank gilt auch meinem studentischen Mitarbeiter Jadranko und meinem Diplomanden Dominik, die beide unermüdlich gegen die Widerspenstigkeit des Molybdäns kämpften. Vielen herzlichen Dank für euren Einsatz und für eure Begeisterung bei der Arbeit, ihr wart mir immer eine große Hilfe.

Ich möchte mich auch bei sämtlichen Mitarbeiten des Departments für Metallkunde und Werkstoffprüfung bedanken, die mir auf unterschiedlichste Art und Weise bei der Erstellung meiner Dissertation geholfen haben. Besonders hervorheben möchte ich unser Sekretariat, das uns unermüdlich jegliche organisatorische Arbeit abnimmt, damit wir uns auf unsere wissenschaftliche Arbeit konzentrieren können.

Ein Dankeschön geht auch an Stefan Wurster, René de Kloe und Alexander Leitner, die mich in diversen Publikationen tatkräftig mit ihrem Fachwissen unterstütz haben.

A special thank goes to Australia to the group of Prof. Juley Cairney and Prof. Simon P. Ringer where I had the opportunity to get a deeper insight in the preparation of atom probe samples and crystallographic analyses. Thanks to Andrew, Anna, Katja, Tong, Adriana and especially Peter who warmly welcomed me at the ACMM in Sydney. I had a really great time with you in the office as well as at after work social events.

Auch allen meinen Freunden und Studienkollegen möchte ich Danke für die wunderschöne gemeinsame Zeit in Leoben sagen.

Zu guter letzte möchte ich mich zutiefst bei meiner gesamten Familie bedanken.
Liebe Mama, lieber Papa, danke, dass ihr immer an mich glaubt und mir in jeder Lebenslange eine Stütze seid. Ich hoffe ich kann euch in meinem Leben das zurückgeben, was ich von euch an Liebe, Vertrauen und Fürsorge erfahren durfte.
Liebe Anna und lieber Stefan, ihr seid einfach die besten Geschwister, die man sich vorstellen kann. Danke, dass wir immer so wunderbar zusammenhalten.
Bedanken möchte ich mich auch bei Phillip, Kathrin, den Eltern und Geschwistern von Thomas für die vielen schönen gemeinsamen familiären Stunden.
Als Letztes möchte ich mich aber bei meinen Ehemann und besten Freund Thomas bedanken. Danke, dass du immer für mich da bist und mich in jeder Lebenslage unterstützt. Ohne dich wäre meine Arbeit nicht so perfekt, und ohne dich wäre ich nicht der Mensch, der ich heute bin. Vielen Dank für diese einzigartige gemeinsame Zeit und für diese wunderbare Seilschaft, die wir bilden.

Abstract

Molybdenum is a refractory metal and widely used in the lighting-, electronic-, coating-, and high temperature industry. The combination of a high electrical and thermal conductivity, together with a low coefficient of thermal expansion and a high strength at elevated temperature, makes molybdenum perfectly suited for high performance products. However, a brittle-to-ductile transition at temperatures close to room temperature as well as an increased embrittlement of the recrystallized state complicate the production and the use as a structural material. In molybdenum and its alloys it is believed that grain boundary segregation plays a significant role regarding the ductility and strength. Therefore, combining mechanical properties with the grain boundary chemistry on the nanometer scale is a promising approach to understand the embrittlement of molybdenum.

In this PhD thesis high-resolution characterization techniques such as the three-dimensional atom probe were applied to investigate the grain boundary chemistry of powder-metallurgically processed technically pure molybdenum and its alloys. In order to study the solute decorations effectively a new atom probe sample preparation method with correlative transmission Kikuchi diffraction was developed. With this technique it was possible to characterize several high-angle grain boundaries of pure molybdenum and its alloys in order to combine crystallographic with chemical information of analyzed grain boundaries. The results of atom probe investigations on technically pure molybdenum reveal that oxygen, nitrogen and phosphorus are typical grain boundary segregation elements. These solutes are known to have a detrimental effect on the grain boundary strength and may provoke intergranular fracture.

Mechanical tests support these assumptions, as they show that delamination cracks indeed mainly follow high-angle grain boundaries, which seem to be particularly weakened by the before-mentioned segregation elements. The present results further indicate that grain boundary segregation of carbon and boron has a beneficial effect in technically pure molybdenum, as these elements promote transgranular fracture and can lead to grain boundary strengthening. Additionally, concentration of detrimental segregation elements at grain boundaries can be reduced by decreasing the grain size or by reducing the overall content of these solutes.

The present work clearly identifies the effect of typical grain boundary segregation elements on the strength and fracture behavior of technically pure molybdenum. This newly gained knowledge will help to develop strategies to further enhance the material's mechanical properties, especially in respect to its brittleness, and paves the way for a targeted grain boundary engineering.

Kurzfassung

Molybdän zählt zu den Refraktärmetallen und findet breite Anwendung in der Licht-, Elektronik-, Beschichtungs-, und Hochtemperaturindustrie. Die Kombination aus hoher elektrischer und thermischer Leitfähigkeit, vereint mit einem geringen Wärmeausdehnungskoeffizienten und einer guten Warmfestigkeit zeichnen Molybdän als Hochleistungswerkstoff aus.

Nichtsdestotrotz erschweren ein Spröd-Duktil-Übergang nahe Raumtemperatur und die interkristalline Sprödigkeit im rekristallisierten Zustand die Produktion und Anwendbarkeit. Speziell Korngrenzenverunreinigungen beeinflussen die Festigkeit und Duktilität von Molybdän und seiner Legierungen maßgeblich. Um ein Verständnis für den Einfluss von Verunreinigungen auf diese Sprödigkeit zu erlangen ist es notwendig mechanische Eigenschaften mit atomarer Analytik der Korngrenzenchemie zu verbinden.

In der vorliegenden Dissertation werden hochauflösende Charakterisierungsmethoden, wie die drei-dimensionale Atomsondentomographie, angewandt um die Korngrenzenchemie von pulvermetallurgisch hergestelltem technisch reinem Molybdän und dessen Legierungen zu untersuchen. Um solche Segregationen effektiv analysieren zu können, wurde im Rahmen dieser Arbeit eine neue korrelative Präparationsmethodik mit Hilfe von *„Transmission Kikuchi Diffraction“* entwickelt. Mit dieser Technik war es möglich, eine große Anzahl von Großwinkel-Korngrenzen zu untersuchen um kristallographische und chemische Informationen der Korngrenze zu korrelieren.

Die Ergebnisse zeigen, dass Phosphor, Stickstoff und Sauerstoff typische Segregationen an den Korngrenzen von technisch reinem Molybdän sind. Diese Verunreinigungen sind dafür bekannt einen negativen Einfluss auf die Korngrenzenfestigkeit zu haben und die Neigung zu interkristallinen Bruch und Sprödigkeit zu erhöhen. Mechanische Tests bestätigen diese Annahmen, da Delaminationsrisse in der Tat überwiegend entlang von Großwinkel-Korngrenzen verlaufen, die durch die genannten Segregationen zusätzlich geschwächt sind. Die vorliegenden Ergebnisse zeigen des Weiteren, dass sich Korngrenzensegregationen von Kohlenstoff und Bor positiv auf technisch reines Molybdän auswirken, da sie transkristallinen Bruch fördern und zu einer Korngrenzenverfestigung führen können. Zusätzlich kann die Konzentration der schädlichen Segregationselemente an den Korngrenzen durch Verringern der Korngröße sowie auch durch die Verringerung des Gesamtgehalts an Fremdatomen im Material reduziert werden.

In der vorliegenden Arbeit wurden typische Korngrenzensegregationselemente in Molybdän und dessen Legierungen analysiert und deren Einfluss auf Festigkeit und Bruchverhalten identifiziert. Dieses neu gewonnene Wissen trägt dazu bei, Strategien zur weiteren Verbesserung der mechanischen Eigenschaften von Molybdän zu entwickeln und ebnet den Weg für eine gezielte Einstellung von Korngrenzenchemie durch die Dotierung mit Fremdatomen.

Part I

Part II

Appendix A, B and C

Abbreviations

AES	Auger electron spectroscopy
APT	atom probe tomography
bcc	body-centered cubic
DBTT	ductile-to-brittle-transition temperature
EBSD	electron back-scatter diffraction
EDX	energy dispersive X-ray analysis
EELS	electron-energy loss spectroscopy
fcc	face-centered cubic
FIB	focused ion beam
HV	high voltage
IPF	inverse pole figure
MHC	molybdenum-hafnium-carbon alloy
Mo	molybdenum
ND	normal direction
PM	powder metallurgical
RD	rolling direction
ROI	region of interest
RT	room temperature
SEM	scanning electron microscope
SIMS	secondary ion mass spectroscopy
TD	transverse direction
t-EBSD	transmission-EBSD
TEM	transmission electron microscopy
TKD	transmission Kikuchi diffraction
TZM	titanium-zircon-molybdenum alloy

1 Motivation

Molybdenum (Mo) and many of its alloys exhibit a melting point of around 2620°C, a good electrical as well as thermal conductivity, and a low coefficient of thermal expansion, which enable their application e.g. in the lighting-, electronic-, coating-, and high temperature industry. Heat sinks for high performance electronics and sputter targets for coating technology are typical Mo products, which are mainly processed over the powder metallurgical (PM) production route.

However, Mo is known to suffer from pronounced brittleness around room temperature (RT), that limits the field of application and complicates the production process. Recrystallization heat treatments further deteriorate the applicability as they lead to an even more brittle material behavior. In general, the brittleness is linked to the grain boundaries, as it is known that these are the weakest structural constituents of Mo. It is argued that, on the one hand, Mo exhibits intrinsically weak grain boundaries and, on the other hand, impurity segregation at grain boundaries may provoke further embrittlement. Hence, one important field of research is the comprehensive investigation of the local grain boundary chemistry in order to understand the fracture behavior.

Therefore, in this thesis a systematic analysis of grain boundary segregation in technically pure Mo and its alloys was conducted to gain more knowledge about the influence of the overall impurity concentration on the amount and type of solute decorations at grain boundaries and the consequences on the brittleness. It has to be emphasized that in this work an industrially processed pure Mo is characterized in terms of its grain boundary segregation, which is in contrast to numerous studies from literature focusing on model alloys. This knowledge can help to further improve the mechanical properties of brittle materials by targeted decoration of grain boundaries.

In order to perform such high-resolution analyses, advanced characterization techniques are required. Thus, the atom probe, with its ability to detect individual atoms, was used to get insights into the grain boundary composition on the atomic scale. Furthermore, a new preparation method was especially developed for these investigations, which reduced the manipulation time and the contamination of the specimens. This new technique was used to prepare atom probe samples of several grain boundaries from a PM produced pure Mo and Mo alloys, which allowed a comprehensive investigation of their grain boundary segregation behavior.

For technically pure Mo the as-deformed and the recrystallized condition were studied to correlate the grain boundary segregation to the material state and the grain boundary character. Furthermore, the role of specific elements on ductility and strength was evaluated by correlating the grain boundary decorations with the fracture behavior of Mo model alloys.

This thesis should help to get a better understanding of the segregation phenomena in industrially processed Mo materials and to open a pathway into potential segregation design methods to improve the ductility, strength and toughness of Mo.

2 State-of-the-art

Molybdenum is a refractory metal with a melting point of 2620°C and a body-centered cubic (bcc) crystal structure. Additionally, a high bonding energy with a strong covalence ratio and a high stacking fault energy is characteristic for Mo [1,2]. Further outstanding properties are its good electrical and thermal conductivity combined with a low thermal expansion coefficient and a high strength at elevated temperatures. Mo exhibits a good corrosion resistance against liquid alkali metals and a decent performance in high neutron flux environments. Nevertheless, above 600°C, a protective atmosphere or vacuum are necessary to avoid the formation of the volatile MoO_3 oxide. The physical and mechanical properties are summarized in Table 1. Due to the previously mentioned advantages, Mo is used in the high temperature, electronic, lighting and coating industries. For example, crucibles for single crystal growth, stirrers for glass melts, supports in power electronic devices and sputter targets, are typical products made out of Mo and its alloys. However, Mo has the disadvantage of a ductile-to-brittle-transition-temperature (DBTT) around RT, hence showing poor ductility at RT under certain conditions. [1,3–5].

Table 1: Physical properties of Mo at RT [1].

Properties of molybdenum

Atomic number	42	Lattice constant	0.3147 nm
Atomic mass	95.94 g/mol	Linear thermal expansion coefficient	$5.2 \cdot 10^{-6}$ m/(m K)
Melting point	2620°C	Thermal conductivity	140 W/(m K)
Density	10.28 g/cm³	Specific heat	0.254 J/(g K)
Crystal structure	bcc	Elastic modulus	320 GPa

The majority of Mo products are produced via the PM production route, which is based on the pressing and sintering of powder followed by different sequences of deformation processes including intermediate and/or final heat treatments leading to recovery and/or a recrystallization. A two-step reduction of MoO_3 powder under hydrogen atmosphere is required to obtain pure molybdenum powder. After uniaxial or cold-isostatic pressing of the powder, a conventional sintering process above 1800°C is carried out. In order to reach the required dimension, to close residual micro-pores and to generate the desired microstructure of the semi-finished products, a thermo-mechanical-process at elevated temperatures is performed. Due to the high brittleness of as-sintered Mo, a hot-deformation above 1000°C is necessary for the first step of forming. Nevertheless, with increasing degree of deformation, the ductility increases and lower temperatures can be used during the next deformation steps. Semi-finished Mo products with a degree of deformation around 70-90% exhibit a distinct subgrain structure, which allows RT deformation. After a certain number of deformation steps

a stress-relieve annealing is conducted. Finally, heat treatments are performed, which lead via recovery to a stress-relieved and in certain cases also to a partly or total recrystallized microstructure. Depending on the degree of deformation and the amount of final cold working recrystallization takes place between 900°C and 1400°C. It is well known that recrystallization of Mo is mainly influenced by recovery processes due to its high stacking fault energy [1,4–8]. Nowadays, PM processed pure metals exhibit low contents of impurities and a fine grained, uniform microstructure. Mo is a single bcc phase metal and does not show solid state phase transformations, and thus, the mechanical properties of technical pure Mo can only be adjusted by varying the thermomechanical treatments to control the microstructure [8].

2.1 Fracture behavior of molybdenum

In general, Mo shows brittle fracture at RT in its as-deformed and recrystallized state. The as-deformed condition is characterized by cleavage fracture whereas, the recrystallized state exhibits intergranular fracture. Beside the microstructure, the loading conditions and the temperature are some of the main parameters influencing the fracture behavior of Mo materials.

Furthermore, Mo and its alloys exhibit a pronounced ductile-to-brittle-transition, which is typical for bcc structured metals and is influenced by a number of material and loading parameters, such as grain size, grain shape, grain boundary character, amount of dislocations, alloying content, stress state and strain rate. The DBTT of Mo, which is typically close to RT, limits its applicability as high-performance material and makes its processing challenging. Even more, recrystallization leads to an increase of the DBTT and to intergranular fracture, which is disadvantageous for its production and application [1–3,5,9–11].

Additionally, the elongated grain shape of the deformed microstructure of Mo causes severe delamination - a decohesion (splitting) of grain boundaries - in the transition and upper shelf regions during mechanical tests, like the Charpy impact test, which also complicates the manufacturing procedure. In the past it was believed, that linear arrangements of flattened former micro-pores increase the susceptibility to delamination [12–14]. In contrast, Cockeram [9,15–18] has shown that elongated, pancake-shaped grains result in delamination and an anisotropic fracture toughness. In Fig. 1 the failure mode of such microstructures is illustrated: Fig. 1a represents a schematic drawing of a V-notched sample, as it is typically used in Charpy impact tests. A magnified inverse pole figure (IPF) map of as-deformed Mo is shown as an overlay to visualize the orientation of the crack in respect to the elongated grains. When the sample is loaded, a crack starts to propagate from the root of the notch through the sample (the designated crack growth direction is marked by dotted blue arrows in Fig. 1b and c). Due to the elongated grains, delamination occurs along the grain boundaries, perpendicular to the designated crack growth direction (red arrows in Fig. 1b and c). As a

consequence, ligaments are left behind, where plane stress conditions prevail (shaded in gray). This change from dominating plane strain to plane stress conditions due to delamination leads to a more ductile failure of the ligaments, which is known as thin-sheet toughening or delamination toughening. Finally, plastically deformed ligaments can be observed between delamination cracks after the fracture of the sample, as depicted in Fig. 1d. Depending on the specimen orientation in respect to the grain elongation direction this toughing contributes to a different extent. This effect is not only observed in Mo but also in other bcc structures, as for example in API-X80 steel [19–21], in ultrafine grained ferritic steels [22–24]or in ultrafine-grained fully perlite [25].

After recrystallization, the more globular grain shape leads to the disappearance of the delamination effect. However, this annealing promotes intergranular fracture and an increase of the DBTT. Thus, the as-deformed material state is more ductile than the recrystallized state, which, however, can still not be completely explained. Therefore, design processes are necessary to improve the lifetime of such high-performance materials by understanding and controlling their fracture mechanisms [26].

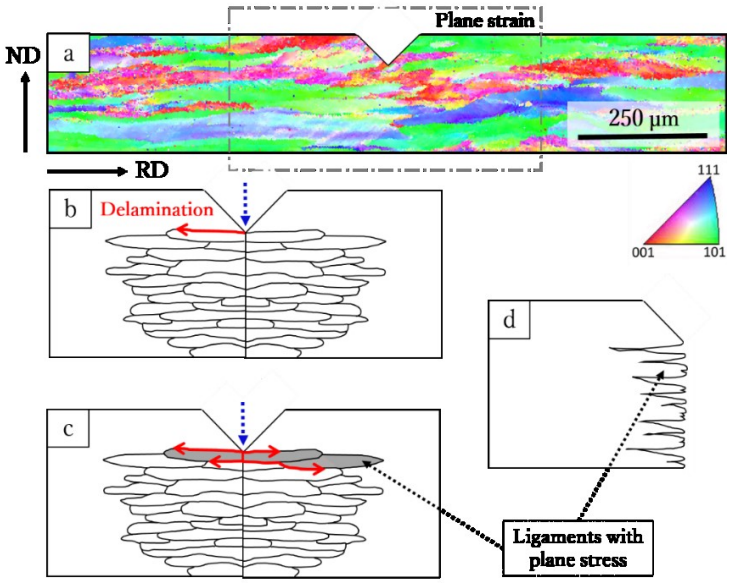

Fig. 1: Illustration of the delamination toughening typical for as-deformed Mo: (a) Schematic drawing of a V-notched sample with an overlaid IPF map of as-deformed Mo. The inset shows the IPF coloring perpendicular to the surface of the sample (transverse direction); (b) and (c) Crack propagation during loading (the designated crack growth direction is marked by dotted blue arrows, the delamination is marked by red arrows). As a consequence of delamination, ligaments are left behind, where plane stress conditions prevail (shaded in gray); (d) Side view on the fractured sample, indicating the ligaments responsible for delamination toughening.

2.2 Intergranular embrittlement of molybdenum

The intergranular embrittlement of the recrystallized material state is a main disadvantage for the applicability of Mo products. Until today, the low grain boundary cohesion and the difference in mechanical properties to the as-deformed or only recovered structure is still not fully understood. Nevertheless, grain size as well as impurity atoms play a significant role regarding ductility and strength [3]. From the literature it is known that intrinsic as well as extrinsic effects influence the embrittlement as described in the following subchapters.

2.2.1 Intrinsic brittleness of molybdenum

One explanation for the brittleness of Mo is its intrinsically low grain boundary strength [2,11,27–29]. Watanabe et al. [28,30,31] studied the influence of the grain boundary type (grain boundary character distribution) on the fracture behavior of Mo. They observed a low resistance of random high-angle grain boundaries against crack propagation. These random grain boundaries show no symmetrical structure because of almost no coincidence of atomic positions in both adjoining grains. Therefore, it is argued that a high amount of random high-angle grain boundaries results in a fully intergranular fracture, as illustrated in Fig. 2a.

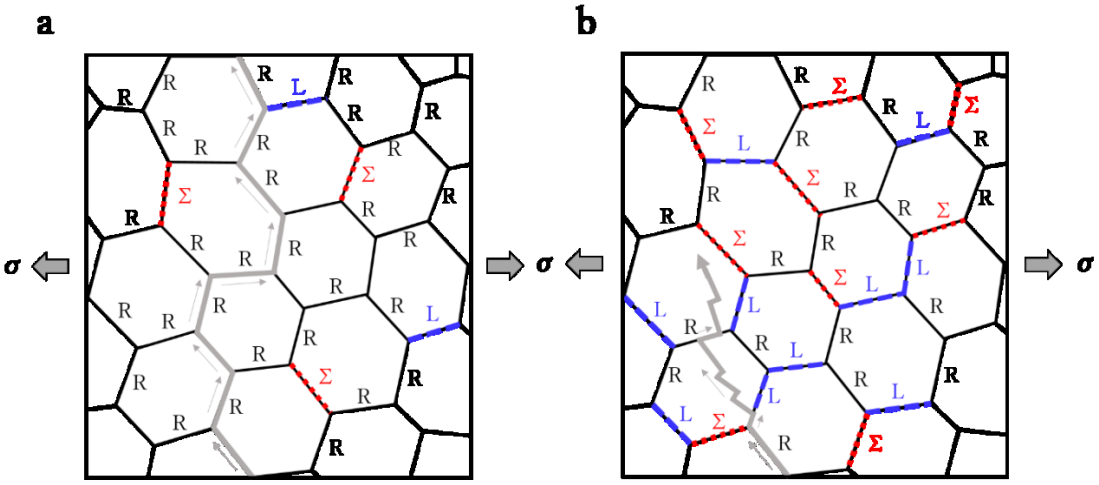

Fig. 2: Schematic illustration of the grain boundary type-dependent fracture behavior in polycrystalline metals; (a) A high amount of random high-angle grain boundaries (R, black) leads to intergranular fracture. (b) An increase of low-sigma boundaries (Σ, red) and low-angle grain boundaries (L, blue) results in a higher percentage of transgranular fracture. [Redrawn from [28,32].

In contrast, a high amount of low-angle and so-called low-sigma grain boundaries lead to an increased percentage of transgranular fracture. Low sigma grain boundaries are symmetric high-angle grain boundaries described by the coincidence-site lattice model [33]. They are characterized by a low sigma value (e.g. Σ3), whereas random high-angle grain boundaries exhibit a high sigma value because almost no atomic positions of the adjoining grains coincide. For example, the low-energy (111) and (112) Σ3 coincidence boundaries in Mo exhibit a high fracture stress and promote transgranular fracture [2]. From that it is apparent that a large number of low energy boundaries is necessary for a high resistance against crack

propagation (see Fig. 2b). Therefore, the grain boundary character, describing the orientation relationship between two adjacent crystals, and the orientation of the grain boundary plane, significantly influence the grain boundary strength and further the fracture behavior of pure Mo. Hence, by promoting specific grain boundary types, it is possible to control the toughness and fracture mode. Also in other systems, like in Al–Li and Fe–Pd alloys, the optimization of the microstructure improves the materials properties and expands the field of application [28], which is known as grain boundary engineering. Nevertheless, it was also found that grain size and shape, texture, dislocation density, and temperature play a major role for the understanding of fracture mechanics in refractory metals [34].

2.2.2 Grain boundary segregation embrittlement of molybdenum

In addition to intrinsic embrittlement processes, it is known that extrinsic effects, like solute decorations of grain boundaries, may contribute significantly to the strength and ductility. The quality of modern PM produced technically pure Mo is high, but still small amounts of impurities in the parts per millions range can be found. In Table 2 a typical chemical composition of the main impurities in an industrial PM processed Mo plate with 14.5 mm thickness is presented. The amount of impurity atoms is remarkably low with the highest contents being tungsten, carbon and oxygen.

Table 2: Chemical composition of main impurities in an industrial PM processed Mo plate. The chemical analysis was provided by Plansee SE [35–37].

Element	W[a]	C[b]	O[c]	N[c]	Fe[a]	P[a]	Si[d]	K[a]	Ba[a]	Cr[a]	Cu[a]
Content [µg/g]	126	19	11	< 5	6	<10	<5	<5	<2	3	3

a... Inductively coupled plasma-atomic emission spectrometry, b...Combustion analyses, c...Carrier-gas analyses, d...Graphite tube-atomic adsorption spectrometry

Tungsten, which has a high solubility in Mo, is a typical accompanying trace element already present in the raw material [1]. Other elements, which have a low solubility in the bulk, as for example oxygen and nitrogen, tend to segregate to the grain boundaries and influence their energy and strength [38]. Thereby, either grain boundary weakening or grain boundary strengthening occurs depending on the type and amount of the segregation present at the interface [39]. Recently, the term segregation engineering was introduced to describe such manipulations of grain boundaries with solute decorations [40].

2.2.2.1 Equilibrium segregation

To decrease the energy of the alloying system, foreign atoms with a low bulk solubility and a high misfit in the matrix segregate to distorted sites (crystalline defects) like grain boundaries, which is called equilibrium segregation. Nevertheless, to achieve such decorations the temperature has to be high enough to ensure diffusion. Equilibrium segregation typically leads to thin layers on grain boundaries with a width/thickness smaller than in the range of a few nanometers. The segregation tendency is inversely proportional to the solubility of the element in the bulk. Additionally, the concentration of the segregating element on the grain boundary increases with its volume concentration and decreases with increasing temperature. Therefore, a high overall concentration of the solute, a temperature high enough to assure diffusion and a slow cooling rate are necessary to generate high equilibrium enrichments at the grain boundary. Several models have been defined to describe such a segregation process. The Langmuir-McLean model follows the classical thermodynamics and explains the constitution of a monolayer by foreign atoms [26,41]. Additionally, Sea and Hondros [42] considered multilayer segregation and the Fowler-Guttmann model [43,44] focuses on the interaction between segregation atoms. However, in industrially alloys there is typically not only one segregation element present but usually several types of solutes (multicomponent-systems), whereof a large variety of elements segregate to the grain boundaries. Hence, co-segregation and site-competition effects influence the segregation behavior, which has been explained by Guttmann and McLean [45]. Furthermore, non-equilibrium segregation exists, where an interaction between solute atoms and thermal vacancies occurs. This existence of such solute-vacancy complexes are required to obtain non-equilibrium segregation. During rapid cooling to low temperatures a supersaturation of vacancies can be provoked. To decrease the total energy of the system, the concentration of vacancies is reduced by annihilation at vacancy sinks, like grain boundaries. On their way to the grain boundaries they trap solute atoms in solute-vacancy complexes and thereby transport them to the grain boundaries. This type of segregation results in a wider spread of segregating elements around the grain boundaries and is mainly present in quenched materials with an excess of vacancies. For more details the reader is referred to [46].

In general, a pronounced effect of the lattice type is expected when the solute is an interstitial atom. The size of interstitial lattice sites in face-centered cubic (fcc) is larger than in bcc structures, which facilitates segregation in bcc materials. In contrast, for substitutional solute atoms no effect of the lattice type is expected. Nevertheless, regardless of the segregation type, the segregation amount varies from boundary to boundary. In the past, it has been shown that the segregation amount correlates with the misorientation of the grain boundary and further with the grain boundary energy [47]. To perform such studies a perfect bi-crystal with a well-controlled misorientation is necessary [26]. Fraczkiewicz et al. [48] determined a dependency with misorientation for bismuth segregation in a copper <100> tilt bi-crystal. For small angles the amount of enrichments increases with increasing rotation angle. However, for

high-angle grain boundaries the amount of segregation varies depending on the grain boundary energy. Low energies indicate a low enrichment factor at the grain boundaries.
Generally, segregation of carbon, oxygen, nitrogen, boron, phosphorus, and sulfur were found at the grain boundaries in Mo materials by either atom probe tomography (APT) or Auger electron spectroscopy (AES) and seem to play an important role for ductility and strength. Mo products are typically not exposed to rapid cooling during the production route (see section 2, "State-of-the-art"), and, therefore, mainly equilibrium segregation is expected to occur. The effects of the mentioned solute decorations of Mo grain boundaries are discussed in the following.

2.2.2.2 Oxygen segregation

In the study of Kumar et al. [7], which was one of the first comprehensive experiments with AES, the intergranular embrittlement of Mo was investigated. With the characterization of binary Mo-O and ternary Mo-O-C single crystals, oxygen segregation was correlated with intergranular fracture. Already in 1977, oxygen was detected at grain boundaries of pure Mo with the atom probe [49,50], but also recent APT studies confirm the presence of oxygen segregation [35,51]. Also other characterization techniques reveal oxygen enrichments at grain boundaries, nevertheless, in PM produced Mo a high amount of oxygen is especially contained in micro-pores [37,52]. Kimura [10] assumed that recrystallized Mo always exhibits intergranular fracture, independent of the amount of oxygen enrichments at the grain boundaries. Nevertheless, a high amount of oxygen segregation would further enhance this fracture behavior. Recently, ab-initio calculations confirm the promoting effect of oxygen for intergranular fracture [53] and recommend the suppression of oxygen segregation to grain boundaries by other strengthening solute decorations. In conclusion, oxygen is known to have a weakening effect on the grain boundaries of Mo.

2.2.2.3 Carbon segregation

The beneficial effect of carbon on the grain boundary strength in Mo has been studied by many authors, especially in the recrystallized material state [10,54–62]. Three-point-bending experiments by Kadokura et al. [63] show that the carbon content (up to 10 mass ppm) influences the occurrence of transgranular fracture. The maximum strength increased and the DBTT decreased with increasing carbon content. It is assumed that carbon segregates to the grain boundaries and acts there as a grain boundary strengthener. Ab-initio calculations confirm that carbon is a beneficial element at grain boundaries of Mo, which increases both, ductility and strength [64,65]. Nevertheless, a lower segregation tendency for carbon than for oxygen was reported by Drachinskiy et al. [59]. This correlates with the investigations made by Kumar and Eyre [7], where a high amount of carbon was necessary to ensure a beneficial strengthening effect. Furthermore, they assume that solute decoration of grain boundaries

with carbon suppresses the detrimental oxygen segregation, causing an indirect strengthening effect. Also Krajnikov et al. [57] suggested that carbon strengthens the grain boundaries by reducing oxygen segregation. Although, Milner et al. [66] admitted an improved strength by reducing the oxygen content with carbon additions. Other authors report a direct strengthening effect of carbon on the intrinsically weak grain boundaries of Mo [54,58]. Figure 3 illustrates the indirect and direct strengthening mechanisms of carbon in Mo. It is known that oxygen segregation deteriorates weak grain boundaries and promotes intergranular fracture. Additions of carbon lead to carbon decorations at the grain boundaries, which can cause a transgranular fracture mode. This is either due to a direct strengthening of the grain boundary by the positive effect of carbon segregation as seen in Fig. 3b or an indirect improving of the ductility by suppressing oxygen segregation from the grain boundary by carbon decorations (visible in Fig. 3c).

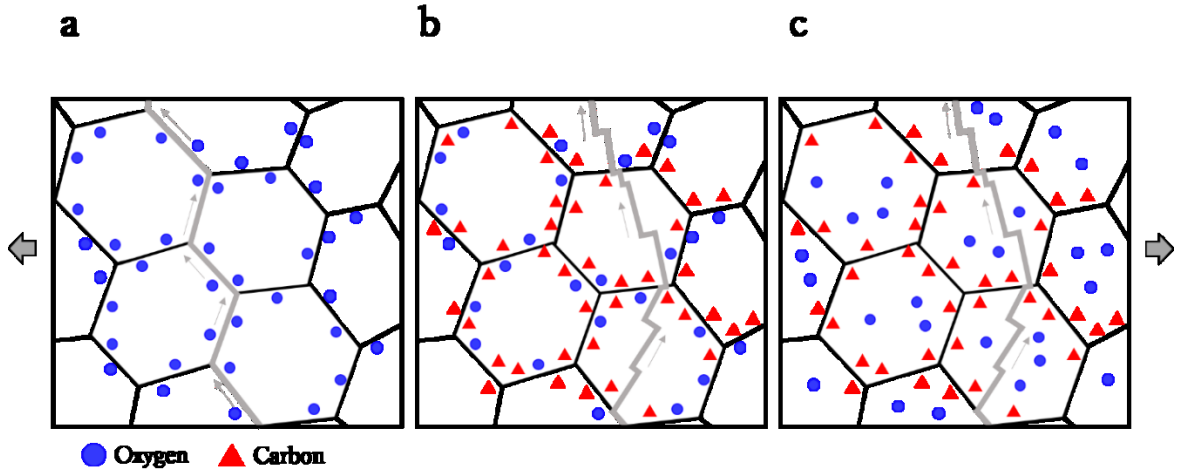

Fig. 3: Strengthening mechanisms of carbon in Mo: (a) Mo with oxygen segregation (blue circle) which promotes intergranular fracture through intrinsically weak grain boundaries; (b) Additions of carbon (red triangle) cause a direct strengthening effect of the grain boundaries by solute decorations of carbon. (c) Additions of carbon cause an indirect strengthening effect by removing detrimental oxygen atoms from the grain boundary.

2.2.2.4 Other segregating solutes

Besides carbon and oxygen, also nitrogen, phosphorus, sulfur, and boron segregation were detected at Mo grain boundaries in several studies [35,51,52,67]. Concerning the nitrogen enrichments, a decreases of the cohesion at the grain boundary was observed [53,68], however, recent ab-initio calculations do not confirm a weakening effect [69]. It seems that nitrogen decorations have an insignificant influence on the intergranular embrittlement of Mo. Additionally, phosphorus segregation was analyzed in PM produced Mo [35,52]. Calculations reported that phosphorus changes from the substitutional site in the bulk to an interstitial site at the grain boundary [69]. Joshi and Stein [70] correlated the brittle fracture behavior of Mo with the presence of phosphorus segregation at the grain boundaries, which decreases the grain boundary cohesion. Also in tungsten, solute decorations of phosphorus

were analyzed by AES, however, the authors excluded a direct effect on the ductility and strength. They assumed that grain shape, size and distribution, as well as dislocation density and temperature play a major role regarding intergranular fracture of tungsten [34]. The element boron is mentioned as grain boundary strengthener in Mo. Already, Lutz et al. [62] observed that boron has a positive effect on the ductility and strength of unworked sintered Mo. Morito [55] described carbon and boron as elements, which improve the grain boundary cohesion. Atom probe investigation of Mo weldments with zirconium, aluminum, carbon, and boron additions indicate that these elements segregate to grain boundaries and lead to a depletion of oxygen and possibly of nitrogen. Even more, a fracture mode change from inter- to transgranular mode was observed [51,67]. Recent ab-initio calculation confirm the positive influence of boron and suggest that it is a promising grain boundary strengthener in Mo [69].
It seems that especially interstitial elements influence the grain boundary strength of Mo either in a positive or a negative way. Therefore, targeted grain boundary contamination is a microstructural design method to improve the material properties of Mo. By grain boundary segregation engineering the intrinsically weak grain boundaries can be strengthened by either carbon or boron solute decorations.
However, for PM produced Mo products it has to be considered, that the occurrence of micro-pores, which are former sinter pores, influence the segregation behavior. Deformation processes, like rolling, condense these micro-voids and cause nanometer sized regions, containing several types of impurities [37].

2.3 Grain boundary segregation characterization

In order to understand the influence of grain boundary segregation on the mechanical properties, the grain boundary chemistry has to be studied at the atomic scale. The information of the type and concertation of solute decorations is essential to solve materials engineering challenges, as for example intergranular embrittlement. Therefore, characterization techniques with the possibility of a direct analyzation of the interface, an atomic resolution in at least one dimension, a high sensitivity for the present elements and the possibility of quantitative evaluations are required [71,72].
For this reason, two types of characterization methods for the direct study of grain boundary segregation exist: the surface analysis techniques as well as the microscopic and tomographic techniques [73], which are explained in the following.

2.3.1 Surface analysis techniques

Two examples for surface analysis techniques are Auger electron spectroscopy (AES) and secondary ion mass spectroscopy (SIMS). In the past, AES was the main method to analyze fracture surfaces, especially for the investigation of the intergranular embrittlement of Mo [7,56,57,74]. A closer description of the experimental set-ups and the measurement method is given elsewhere [38,75–77]. The challenge of determining the grain boundary segregation elements by AES is, to get access to unmodified grain boundaries of the material for the analysis. Therefore, this method is well suitable for materials which exhibit intergranular fracture, as the fracture surface of a broken specimen reveals prior grain boundaries. Since under normal atmosphere the fresh fracture surface gets immediately covered with environmental oxygen and/or carbon, the experiments have to be performed under high vacuum conditions in the order of 10^{-8}Pa. Additionally, the fracture process can expose former micro-pores with impurities (especially in PM produced metals), which influence the measurement of the grain boundary chemistry. Due to the lateral resolution of 10-20 nm and a sensitivity down to 1 atomic layer, AES is suitable for the detection of concentrations lower than 0.1 to 1 at.%, depending on the type of the element. However, it has to be considered that the elements hydrogen and helium cannot be detected [71,78]. Furthermore, there is a tendency to overestimate the segregation content because samples break along the most brittle grain boundaries, which often exhibit the highest concentration of decoration atoms. Nevertheless, AES is a powerful tool to study material systems with solute decorations of at least one atomic layer. However, the investigation of intergranular embrittlement of pure Mo is challenging. The amount of impurities in technically pure Mo is so low, that a detection of solute decorations is not possible even with modern AES instruments [37]. Additionally, for the most interesting species, oxygen and carbon, contamination effects in the vacuum chamber can never be fully excluded.

Another surface sensitive technique with a high depth resolution (down to 2 nm) is SIMS. For a description of the technique the reader is referred to [38]. SIMS is known to have a lower lateral resolution (20-50 nm) than AES, since the ion beam cannot be focused as well as the electron beam. In contrast to AES, the detection of hydrogen is possible and the method has a higher sensitivity (up to ppb range). Similar to AES, intergranular fracture of a sample in ultra-high vacuum is needed for the characterization of grain boundary segregation. The main disadvantage of SIMS, however, is the complicated interpretation of the spectra and the necessity of standards for quantification [71,78]. Therefore, SIMS has not become a popular surface analyzation technique for the investigation of the embrittlement of bcc metals.

2.3.2 Microscopic and tomographic techniques

Analytic electron microscopy and atom probe tomography (APT) are the most commonly used microscopic techniques to study the grain boundary chemistry of metals. These two methods provide information of the type and position of solutes at interfaces on the atomic scale, without fracturing the sample. Transmission electron microscopy (TEM) is a powerful instrument to combine high-resolution imaging with highly localized analytical tools, such as energy dispersive X-ray analysis (EDX) or electron-energy loss spectroscopy (EELS) [38,78]. Thus, a full characterization of grain boundaries with segregation can be achieved. With the help of modern focused-ion-beam (FIB) instruments a site-specific specimen preparation becomes possible and interfaces or even triple junctions can be located in a TEM sample (a foil usually thinner than 100 nm). Thereby, layers of segregation as well as small precipitates and inclusions can be investigated at the grain boundaries. For the analysis of elements with a high atomic number ($Z > 11$) EDX is the favorable method whereas EELS is powerful for the light elements. A detection sensitivity of 0.1-1 at.% can be achieved by EELS depending on the experimental factors as well as element types [79]. Nevertheless, the sample preparation may be difficult and especially time consuming, depending on the material type and state [38]. Additionally, the contamination by hydrocarbon deposition, the damage of the specimen due to the high-energy incident electron-beam and the influence of the specimen thickness and orientation complicate the measurements [79]. Furthermore, the data evaluation and interpretation is difficult and sometimes correlative simulations are necessary. In order to study solute enrichments in pure Mo, analytical electron microscopy has some considerable disadvantages: Mo exhibits a high atomic number and, therefore, TEM samples have to be extremely thin to make sufficient transmission for an accurate investigation possible. Due to the brittleness of Mo the specimen preparation is difficult and time consuming. Additionally, the amount of segregation in technically pure Mo is so low that EDX and EELS come close to their detection limits.

APT overcomes these problems and is therefore a powerful tool to characterize segregation in pure Mo and Mo alloys. Field evaporation of individual atoms from the apex of a needle-shaped specimen makes a three-dimensional analyzation of interfaces on the atomic scale possible. Furthermore, the atom probe allows the detection of all elements in the periodic system, which makes it one of the strongest analytical characterization techniques available. A spatial resolution down to 0.3 nm laterally and 0.2 nm in depth, combined with a sensitivity of around 10-20 ppm can be achieved by this method. With APT, chemical compositions, phase transformations, segregation, decomposition, precipitation formations, and even crystallography can be studied [38,80–83]. The physical principle of APT is schematically illustrated in Fig 4. A high voltage (HV) between 2-20kV is applied on a needle-shaped specimen, which is cooled down to cryogenic temperature, to create a high electric field on the apex of the tip. The strength of the electric field is proportional to the applied voltage and inversely proportional to the radius and curvature of the tip. Due to additional pulses by

voltage or laser, electrons can be stripped from the atoms on the surface by a tunneling process and the resulting positive ions are accelerated away towards the counter electrode onto a position-sensitive detector, which is called field evaporation. Especially the availability of laser pulsing makes APT applicable for worse- and non-conducting materials. With the position-sensitive detector the X and Y position can be detected, whereas, the Z direction is calculated over the evaporation sequence. The chemical information of each detected ion is measured by time-of-flight mass spectroscopy. The reconstruction of the measured volume is built up atom-by-atom by projecting of the detected X and Y-positions of the ions onto the surface of a virtual specimen. Due to trajectory effects of the evaporated ions a point-projection model is commonly used for the reconstruction of the APT data, with the field factor and image compression factor as the main parameters. With the identification of the mass spectra a complete three-dimensional reconstruction can be obtained [81,84].
However, local magnification effects, peak overlaps, multiple hit detection, and preferential evaporation have to be consider for the data evaluation and interpretation. The main disadvantage of the technique is the small analyzed sample volume during one measurement (~50x50x250 nm^3) and a detection efficiency between 37% and 80%, depending on the instrument [81]. APT is well suited for studying grain boundaries of Mo, although a high electric field is necessary to ensure field evaporation. The high electric field generates a high stress under the surface of the tip, which makes the analysis of weak grain boundaries difficult. Thus, a high fracture rate and a small success rate has to be accepted. Besides these experimental problems, APT allows the most comprehensive analysis of grain boundaries in Mo of all methods mentioned above.

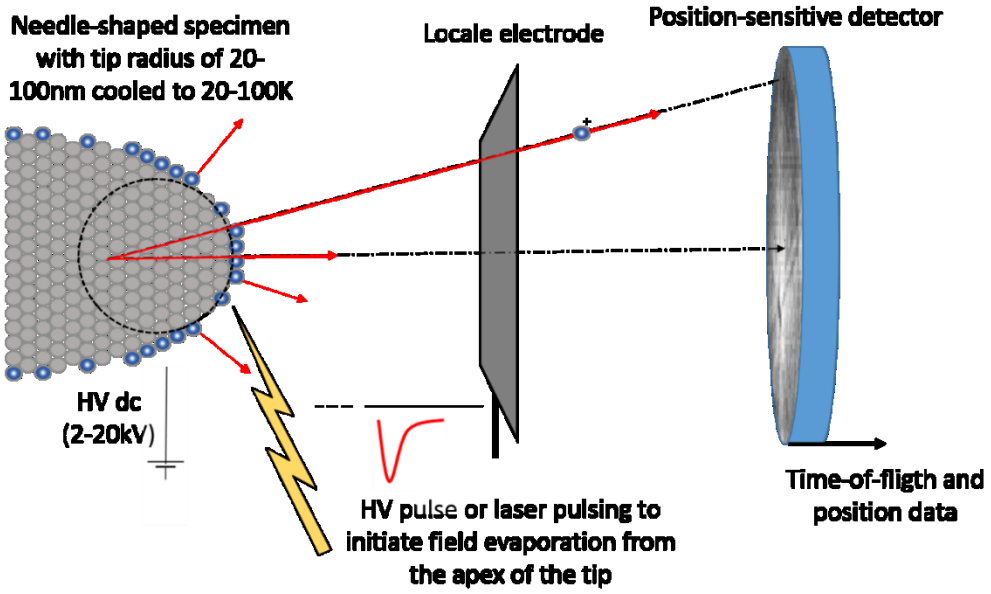

Fig. 4: The physical principle of APT redrawn from [81].

Nevertheless, a specific sample preparation is required to obtain successful APT results. For a standard bulk composition analysis the electro-polishing method is suitable [80]. However, if a specific region of interest (ROI), as for example an interface, has to be studied, a site-specific preparation is necessary. In general, the first 200 nm of a tip are measured and, therefore, the ROI has to be located in the first 100-150 nm of the APT sample for a successful investigation. In the past, grain boundaries were prepared by back-polishing of electrolytic samples with correlative TEM [81,83,85,86]. However, this process is time-consuming, especially, for materials with large grain sizes. State-of-the-art FIB instruments simplify the preparation procedure as the ion beam can be used to position a grain boundary in the apex of the tip [87–89]. The implementation of the lift-out technique by Miller et al. [90,91] further expanded the field of application of APT. Felfer et al. [92,93] intensively studied the optimization of the APT specimen preparation, and developed a sample holder which can be used in FIB, TEM and APT to simplify the preparation process. M. Herbig et al. [94] revised this grid holder to make it compatible for all instrument types used for TEM and APT with exact control of the sample orientation. Additionally, Felfer et al. [92] optimized the milling and deposition parameters to increase the percentage of successful measurements in the atom probe. However, a correlative technique is necessary to prepare grain boundaries for APT, as the visibility in the scanning electron microscope (SEM) gets poor in the last preparation steps, which makes the tracking of the interface difficult. With support of the TEM the interface can be imaged and positioned in the top of the tip. If available, also transmission detectors in the FIB are easy to use for the preparation. However, if a standard TEM is needed, the preparation time takes longer and the sample gets additionally contaminated in the environment during change between instruments and due to the electron beam in the TEM. In general, the carbon contamination in scanning and transmission microscopes has to be considered for the interpretation of the APT results [67]. Mo samples containing a grain boundary were already successfully prepared by a FIB/TEM combination [35,37]. Therefore, a new combined preparation method was developed in this PhD thesis. A closer description and the main advantages are summarized in the next chapter.

To conclude, some aspects have to be taken into account before a characterization method is selected for the analysis of grain boundary segregation:

1) Which type of segregation will be studied?
   Equilibrium segregation are generally monolayers, whereas non-equilibrium segregation are spread over several nm up to µm. AES and SIMS are better to characterize non-equilibrium segregation, whereas the atom probe is perfect for the study of equilibrium segregation. In PM produced Mo materials no rapid cooling processes are conducted during the production route. Therefore, mainly equilibrium segregation will appear at the grain boundaries.
2) Which elements are expected at the interface?
   The atom probe is the only instrument which can detect all elements of the periodic system. AES can be used when no carbon, oxygen and hydrogen enrichments are the main interest. Especially in Mo, the main solutes are light species like oxygen, nitrogen, carbon and, boron which cannot be detected by EELS.
3) Is a comprehensive study necessary due to inhomogeneity in the material?
   PM processed pure metals, like Mo, exhibit inhomogeneity in form of micro-voids and nano-sized segregation regions, however, no typical segregation zones as known from ingot-product are present. Nevertheless, in the atom probe the analyzed sample volumes are so small that at least two measurements are necessary to obtain reliable results. AES analyses would reveal more statistically relevant results, however, the other mentioned drawbacks have to be considered.
4) What kind of specimen preparation is needed for a successful analysis?
   Samples for SIMS and AES can be easily prepared. However, TEM and APT samples need a more time consuming preparation process. Depending on the material and the region of interest, the preparation can be challenging and a FIB assisted process will be required.

3 Summary of publications

In the following chapters the main results and findings of the PhD thesis are explained and discussed by summarizing the listed publications. The workflow of this thesis is defined by four development stages as illustrated in Fig. 5. Firstly, the APT sample preparation method was improved as basis to obtain a comprehensive grain boundary segregation study of technically pure Mo and the model alloy Mo-Hf. In the next steps, the present solute decorations are correlated to the occurring fracture behavior of the as-deformed and recrystallized material states as well as to the chemical composition. In the end, beneficial and detrimental solute decorations are highlighted and guidelines for an improved ductility and strength are given.

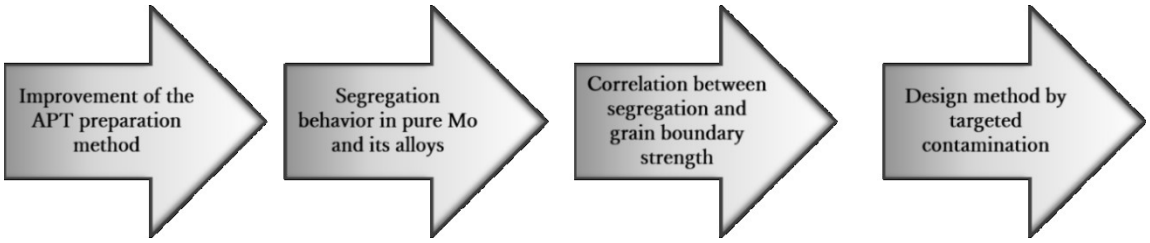

Fig. 5: The workflow of this PhD thesis.

3.1 Publication list

Publication A:
A novel approach for site-specific atom probe specimen preparation by focused ion beam and transmission electron backscatter diffraction.
K. Babinsky, R. De Kloe, H. Clemens, S. Primig. Ultramicroscopy. 144 (2014) 9–18.

Publication B:
Correlating atom probe crystallographic measurements with transmission Kikuchi diffraction data.
A. J. Breen, K. Babinsky, A. C. Day, K. Eder, C. J. Oakman, P. W. Trimby, S. Primig, J. M. Cairney, and S. P. Ringer. Microsc. Microanal. (2017) in press.

Publication C:
Grain boundary study of technically pure molybdenum by combining APT and TKD
K. Babinsky, W. Knabl, A. Lorich, R. De Kloe, H. Clemens, S. Primig. Ultramicroscopy. 159 (2015) 445–451.

Publication D:
Towards grain boundary segregation engineering of technically pure molybdenum
K. Leitner (née Babinsky), P. Felfer , J. Cairney, W. Knabl, A. Lorich, H. Clemens, S. Primig. Submitted to SCI-journal [under review]

Publication E:
Materials by design: engineering grain boundary chemistry in molybdenum
K. Leitner, D. Scheiber, S. Primig, H. Clemens, E. Povoden-Karadeniz, L. Romaner. [in preparation for SCI-journal]

Publication F:
Fracture behavior and delamination toughening of molybdenum in Charpy impact tests.
K. Babinsky, S. Primig, W. Knabl, A. Lorich, R. Stickler, H. Clemens. JOM. 68 (2016) 2854–2863.

Remarks:

In the appended papers, all experiments, the data analyses and the compositions of the publications were performed by myself, Katharina Leitner, with the following exceptions:

Publication A	The optimization of the TKD parameters was done by R. De Kloe.
Publication B	The experiments of the nano-sized aluminum alloy was performed by K. Eder and the corresponding TKD maps established by P. Trimby. The calculations and the main part of the writing was conducted by A. Breen. A. Day optimized the calculation parameters.
Publication D	A part of the FIB and APT work was conducted at the Australian Centre for Microscopy & Microanalysis (ACMM) at the University of Sydney together with P. Felfer and J. Cairney. P. Felfer improved the visualization of the APT data.
Publication E	The ab-initio calculation part was conducted by D. Scheiber and L. Romaner. E. Povoden-Karadeniz contributed calphad calculations.
Publication F	The Charpy impact tests were performed by W. Kopper at the Department of Physical Metallurgy and Materials Testing, Montanuniversität Leoben

Further publications:

Atom probe study of grain boundary segregation in technically pure molybdenum.
K. Babinsky, J. Weidow, W. Knabl, A. Lorich, H. Leitner, S. Primig. Materials Characterization. 87 (2014) 95–103.

Boron grain boundary segregation in a heat treatable steel.
C. Haslberger, C. Turk, K. Babinsky, D. Caliskanoglu, H. Clemens, S. Primig. BHM Berg- und Hüttenmännische Monatshefte. 160 (2015) 204–208.

Grain boundary segregations in technically pure molybdenum.
K. Babinsky, S. Primig, W. Knabl, A. Lorich, T. Weingärtner, J. Weidow, et al.. Proceeding in: 18. Planseeseminar, Plansee SE, Austria, 2013: pp. RM111/1–15.

Neue Ansätze zur Zielpräparation von Atomsondenspitzen mittels Focused Ion Beam und Durchstrahlungs-EBSD
K. Babinsky, P. Haslberger, Ch. Turk, H. Clemens, S. Primig. Proceeding der 14. Internationalen Metallographie-Tagung, Sonderbände der Praktischen Metallographie. 46 (2014) 361-366.

3.2 Transmission Kikuchi diffraction assisted atom probe sample preparation of grain boundaries

In order to conduct a successful atom probe analysis an adequate and state-of-the art specimen preparation is required, as described in section 2.3.2, "Microscopic and tomographic techniques". The ROI, e.g. a grain boundary, has to be positioned in the first 100-150 nm of the needle-shaped atom probe sample. Therefore, the standard electro-polishing method is not usable for the preparation of grain boundaries, especially for materials with large grain sizes, as it is unlikely that a grain boundary will be located by chance in the small analyzed volume. However, with modern FIB systems, a site-specific preparation ensures that even small features like thin films, precipitates, or segregation at dislocations and grain boundaries are contained in the APT sample [95,96]. For that, either the lift-out technique or a re-sharpening by FIB of electrolytically polished tips can be used to position grain boundaries in the apex of an APT sample [90–93]. Nevertheless, a correlative tool is necessary to overcome the poor visibility in the FIB/SEM in the last preparation steps of annular milling. So far, TEM analyses support the tracking of grain boundaries in the last preparation steps to position the ROI in the apex of the tip and to improve the reconstruction. However, a time-consuming repeated sample exchange between TEM and FIB is unavoidable. Even more, if the grain boundary character is studied, diffraction patterns have to be recorded, which leads to additional contamination of the APT sample [35,51,67]. For segregation studies the key aim is to combine grain boundary chemistry data with crystallographic information to improve the understanding of grain boundary properties. This can be achieved, for example by nano-beam diffraction in the TEM [94,97], by analyzing the crystallography with APT [98,99] or by electron back-scatter diffraction (EBSD) investigations [100,101], which are all complex and time-consuming processes.

Therefore, this study **(Publication A and C)** proposes transmission Kikuchi diffraction (TKD), also named transmission-EBSD (t-EBSD), as new correlative tool for the APT specimen preparation. This method simplifies the preparation process of grain boundaries and facilitates the determination of crystallographic information in a simple and fast way. TKD is based on EBSD, but instead of the back-scattered electrons, the transmitted electrons are recorded by a standard EBSD detector. Therefore, samples have to be thin and appropriate for electron transmission, which is fulfilled by APT specimens close to the apex. TKD provides a higher resolution than normal EBSD and was primary used to study nanocrystalline materials with a fine microstructure [102–105]. In this work, TKD is applied to support the last preparation steps in the FIB/SEM of an APT sample containing a grain boundary. Figure 6 illustrates the schematic set-up for TKD analyses in a FIB/SEM dual beam microscope. No time-consuming exchange of instruments between ion milling and TKD analysis is necessary, as everything is provided in one microscope. In Fig. 7 an example of the preparation of a grain boundary with correlative TKD is presented.

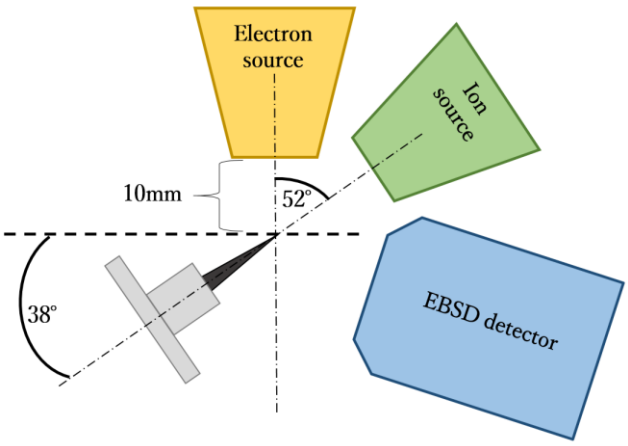

Fig. 6: Schematic set-up for a TKD mapping in an FIB/SEM dual beam microscope equipped with an EBSD detector, redrawn from [106].

When the grain boundary is not visible anymore in the FIB/SEM, the tracking of the grain boundary is supported by TKD. A step by step ion milling and TKD mapping procedure is necessary to locate the ROI in the apex of the tip. With this procedure the grain boundary can be positioned at the ideal location for a successful APT study. Furthermore, the crystallographic information obtained by TKD provides knowledge about the grain boundary character. This method can be applied either on pre-electropolished tips, or on lift-out samples. Figure 8 illustrated the TKD-assisted preparation of lifted-out samples. Therefore, EBSD is used to pre-select specific orientations and TKD to finally position a grain boundary in the apex of the tip.

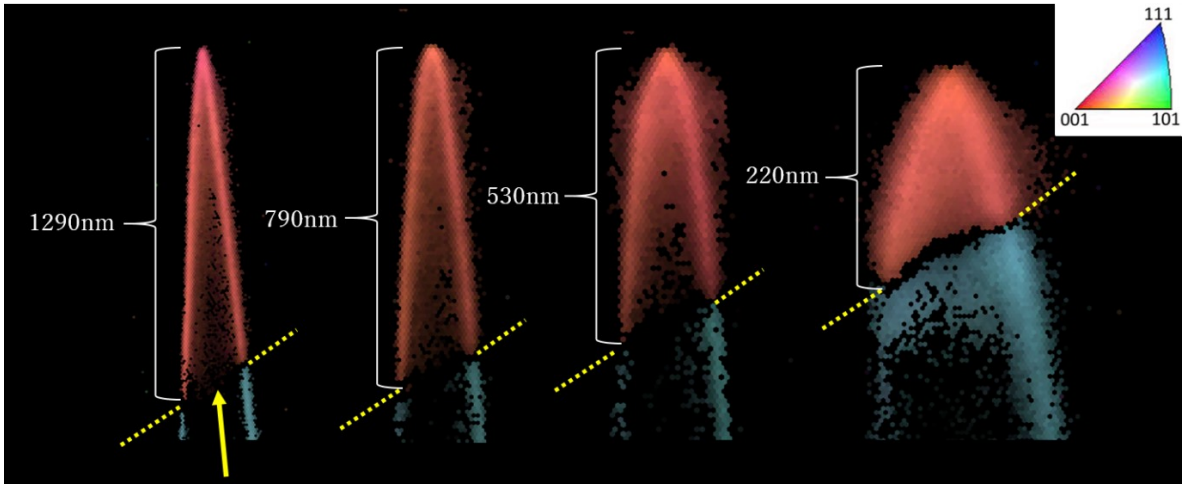

Fig. 7: Representation of the TKD-assisted APT sample preparation process, redrawn from [106]. TKD mappings support the final ion milling procedure to track the grain boundary and to obtain crystallographic information. The inset shows the IPF coloring which indicates the crystal direction perpendicular to the surface of the tip (side view).

For a closer description of the technique and the used parameters the reader is referred to **Publication A**. Today, TKD is widely applied as correlative method to support the APT preparation process and to obtain crystallographic information. Besides subgrain and grain boundaries, also small phases and different precipitates are successfully prepared with correlative TKD and studied in the atom probe [105,107–113].

In **Publication B** the crystallographic information of a grain boundary obtained by TKD is compared to structural analyses of the APT reconstruction. Already in the past, studies were performed to get crystallographic information of a measured grain boundary by only using the lattice information from the atom probe data set [114,115]. However, the obtained results had never been verified by another independent technique to confirm the accuracy. In **Publication B,** misorientation measurements (rotation angle and axis) received from TKD and crystallographic analyses from APT of the same specimen containing a grain boundary were directly compared (materials: technically pure Mo and nano-crystalline Al–0.5Ag). The crystallographic information obtained by APT is discussed with special focus on the effects of the used instrument settings and the reconstruction calibration methods [84,116,117].

In Table 3 the TKD and APT results of the rotation angle and axis of the analyzed grain boundary of technically pure Mo are listed. Here different reconstruction parameters (APT1 to 3) were used to verify the influence of the calibration on the crystallographic measurements.

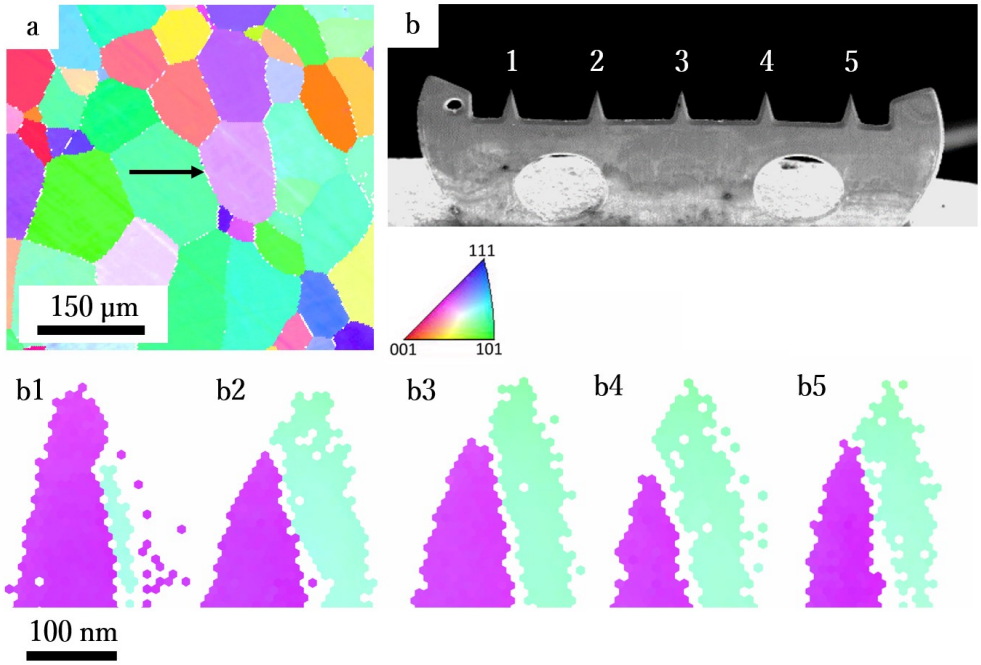

Fig. 8: Representation of the TKD-assisted APT sample preparation of a lift-out: (a) EBSD map for the selection of the grain boundary (see black arrow); (b) A Mo grid used as a post with five positions; (b1-b5) Correlative TKD maps of the five APT samples on the molybdenum grid. The grain boundary is positioned within the first 100nm of each sample with a misorientation of 38°.

From Table 3 it is obvious that the maximum deviation of the determined rotation angle from TKD and APT is 2°. Inaccuracies in the reconstruction (calibration parameters), as well as calculation errors from the misorientation measurement influence the error of the APT results. For further information the reader is referred to **Publication B**.

Table 3: Crystallographic measurements (rotation angle and axis) of a grain boundary of technically pure Mo determined by TKD and APT, redrawn from **Publication B**.

Method	Rotation angle [Degree]	Rotation axis [h k l]
TKD	**32.0**	**[0.196 0.640 0.743]**
APT1	34.0	[0.148 0.627 0.765]
APT2	32.7	[0.186 0.679 0.710]
APT3	32.8	[0.050 0.652 0.757]

3.3 Grain boundary segregation in technically pure molybdenum

In order to understand and to find strategies to decrease the intergranular embrittlement of Mo, many studies have been performed so far (see section 2, "State-of-the-art") [51,55,66,118–120]. Single crystals, as well as model alloys were produced and investigated in terms of grain boundary character and solute decoration. However, so far no segregation study was performed on industrially processed technically pure Mo, which is actually used in many products. Therefore, in the framework of the present thesis two technically pure Mo plates, different in their chemical composition (see Table 4), were investigated in their as-deformed and recrystallized state **(Publication C and D)**. These two material conditions were chosen due to their significant difference in their mechanical and fracture behavior.

Table 4: Chemical composition of main impurities of Mo plate 1 and 2. The chemical analysis was provided by Plansee SE [35–37].

Element	C[b]	O[c]	N[a]	Fe[a]	P[a]	Si[a]	K[a]	Ba[a]	W[a]
Plate 1	11	19	< 1.3	3.7	2.4	1.1	4	1.0	120
Plate 2	11	31	< 0.4	3.2	1.2	1.3	19	2.2	140

a...Glow discharge mass spectroscopy, b...Combustion analyses, c...Carrier-gas analyses

As the amounts of impurities in the industrially processed Mo are remarkably low, the atom probe is perfectly suited to characterize the solute decorations at the grain boundaries. In order to compensate for small sample volumes analyzed in APT, a large variety of high-angle grain boundaries were studied. Furthermore, with the correlative method of TKD a comprehensive crystallographic and chemical characterization of individual grain boundaries was possible.

Typical grain boundary segregation elements of an industrially processed technically pure Mo plates are phosphorus, nitrogen, oxygen, and carbon. However, solute decorations of carbon were only detected in the recrystallized condition at low-sigma grain boundaries, which are specific symmetrical high-angle grain boundaries described by the coincidence-site lattice model [33]. Individual segregation amounts described by one-dimensional concentration profiles and interfacial excess values are provided by **Publications C and D**. All of the detected elements, except carbon, promote the intergranular embrittlement of Mo. In contrast to that, carbon is known to have a beneficial effect on the grain boundary energy and strength. However, the number of low-sigma grain boundaries and the excess of carbon segregation could be too low to generate a significant strengthening of the material. In Fig. 9, the TKD mapping and the APT reconstruction with a one-dimensional concentration profile of an analyzed low-sigma grain boundary (Σ3 with 7° deviations according to Brandon´s criterion [121]) of recrystallized Mo is presented. Segregation enrichments of carbon, nitrogen, oxygen, and phosphorus are present at the grain boundary.

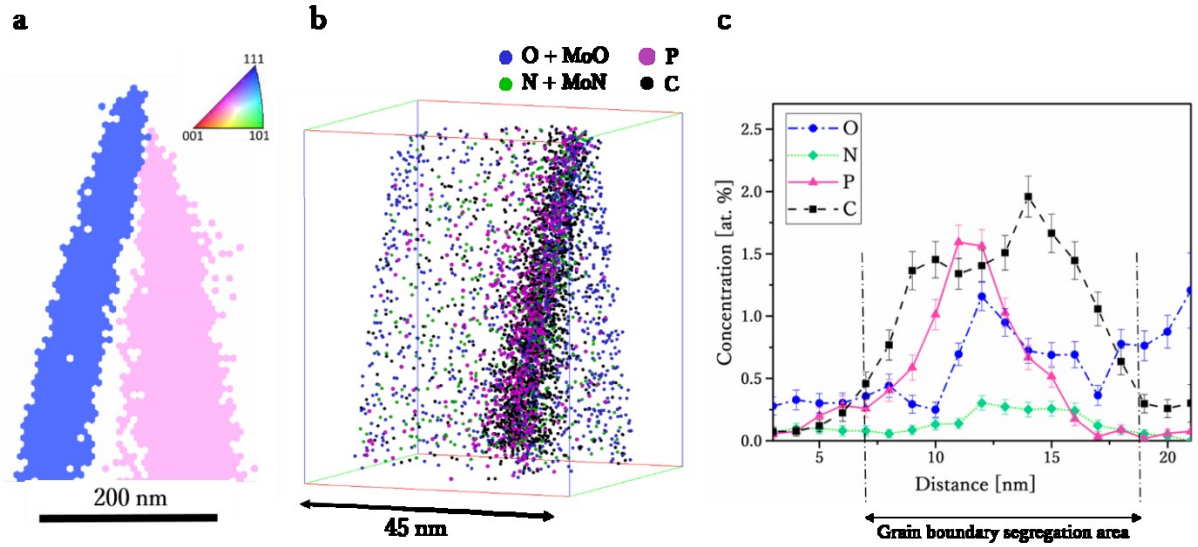

Fig. 9: (a) TKD mapping and (b) APT reconstruction (Mo atoms are blanked) with (c) a one-dimensional concentration profile through the low-sigma grain boundary of recrystallized Mo redrawn from **Publication D**.

By comparing the overall segregation amount of the analyzed high-angle grain boundaries of as-deformed and recrystallized Mo in Fig. 10a it is evident, that the recrystallized state in general exhibits more solute decoration at the grain boundary. Due to the lower amount of available grain boundary volume in the recrystallized state a higher enrichment factor of segregation is provoked. Therefore, it is assumed that the intergranular embrittlement of the recrystallized condition is a result of the higher content of detrimental decorations at the grain boundaries. A smaller grain size of the recrystallized condition could be advantageous, as segregation would be distributed over a larger grain boundary volume, which leads to lower enrichment factors. In the as-deformed state the amount of solute decorations increases with

the rotation angle of grain boundaries, which is especially observed for interstitial solute elements like oxygen and nitrogen (see Fig. 10b). Therefore, a high number of low-angle grain boundaries are beneficial regarding ductility and strength in the as-deformed state.

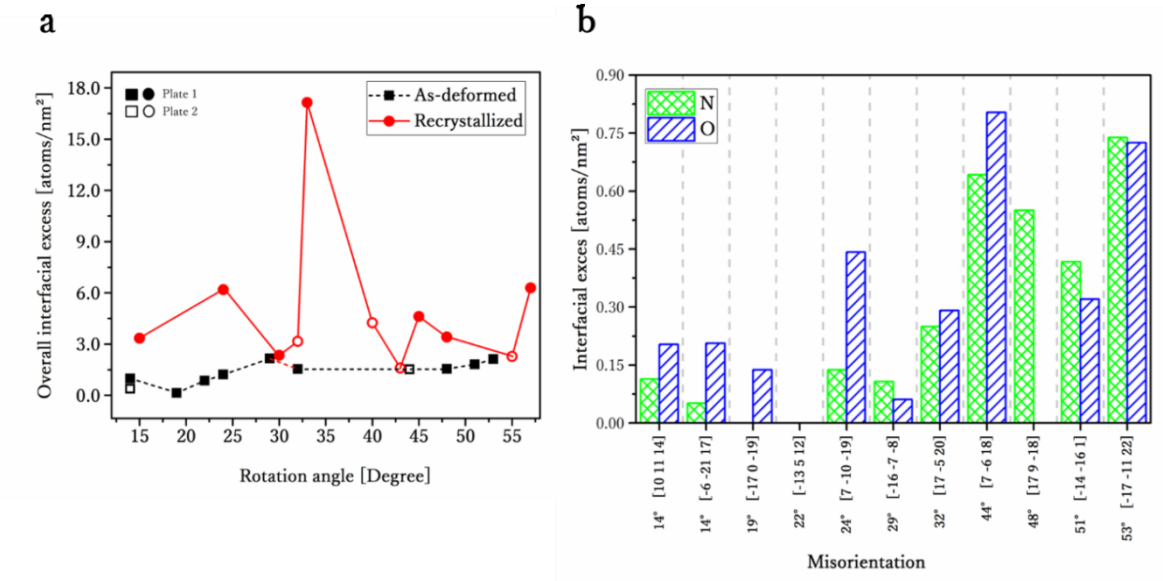

Fig. 10: (a) Overall interfacial excess in atoms/nm² of both states of Mo (as-deformed in black, recrystallized in red) plotted over the rotation angle of the measured grain boundaries. Plate 1 and 2 are marked by square and circles, respectively (redrawn from **Publication D**); (b) Interfacial excess in atoms/nm² of the interstitial elements oxygen and nitrogen at the analyzed grain boundaries in the as-deformed condition, plotted over the rotation angle (in degree) and the rotation axis (in hkl).

However, the overall content of impurities (with a low bulk solubility) influences the segregation content even more. Thus, a higher impurity content leads to a higher interfacial excess at the grain boundaries. For a closer description of this effect the reader is referred to **Publication C**. To conclude, a high amount of weakening elements leads to a high enrichment factor at the intrinsically weak grain boundaries of Mo and promotes a further decrease of the already low grain boundary strength. To improve the material properties and to reduce the intergranular embrittlement, a small grain size with a high amount of low-sigma grain boundaries, a low amount of high-angle grain boundaries and a low content of detrimental elements like oxygen are suggested. Nevertheless, a targeted contamination by strengthening elements like carbon and boron could help to improve the ductility of Mo.

3.4 Grain boundary strengthening by segregation engineering

From literature it is known that targeted contamination of grain boundaries with certain elements can help to improve the ductility and strength of brittle materials [40]. In PM produced technically pure Mo a high amount of oxygen is present at the grain boundaries (see section 3.3, "Grain boundary segregation in technically pure molybdenum") which promotes intergranular embrittlement. In order to reduce the content of detrimental segregation at grain boundaries, targeted contamination can be used to replace those elements at the grain boundary. Especially, carbon and boron strengthen the grain boundary and may suppress oxygen enrichments. Such strengthening of the grain boundary can even lead to a fracture mode change from inter- to transgranular.

To verify the beneficial effect of grain boundary segregation engineering on Mo materials, Mo-Hf alloys with increasing hafnium content (0.18-3.33 at.%) were characterized with respect to their grain boundary chemistry (**Publication E**). These alloys were also used to study the solid solution hardening and softening effect of hafnium in Mo to get a better understanding of the strengthening mechanisms in the Mo based alloy MHC (molybdenum-hafnium-carbon alloy with the nominal composition of 1.2 m.% Hf (0.64 at.%) and 0.05-0.12 m.% C (0.4-0.96 at.%)) [122,123]. Tensile tests on these alloys indicated a fracture mode change from intergranular fracture for specimens with low hafnium content, to transgranular fracture for samples with a high hafnium content. This, however, was not an effect of a changed grain boundary type distribution, as the amount of low-sigma grain boundaries does not differ between these alloys. Hence, solute decorations at the grain boundaries may be the main cause for the change of the fracture behavior ("grain boundary segregation engineering"). In Table 5 the contents of hafnium and the main impurities is given for the five alloys studied (A1-A5). For a better comparison, also the chemical composition of technically pure Mo (A0) is included. It is evident that with increasing hafnium content the amount of trace elements like zirconium, titanium, tungsten, boron, and oxygen increases. It is known that tungsten is an accompanying element of molybdenum, whereas zirconium accompanies hafnium. The amount of oxygen increases with increasing hafnium content due to the formation of HfO_2 during the production process, with a maximum of the HfO_2 content in A5 (0.71vol. %). The carbon and nitrogen levels are almost constant throughout the different alloy systems. Further information about the microstructure and the mechanical properties of these alloys can be found in the publications of Pöhl et al., e.g. [122,123].

Several grain boundaries of the alloys A0-A5 were analyzed by APT to investigate the influence of the overall chemical composition on the elements present at the grain boundaries. In Fig. 11 SEM images of the fracture surfaces of A1 (Fig. 11a) and A5 (Fig. 11c) are shown together with illustrations of the composition of two corresponding grain boundaries obtained from APT, (Fig. 11b) and (Fig. 11d).

Table 5: Content of hafnium (in at.%) and the main impurities (in µg/g) of five Mo-Hf alloys (A1-A5) and pure Mo (A0), redrawn from **Publication E**.

Element	Hf[a]	Zr[a]	Ti[a]	W[a]	C[b]	O[c]	N[c]	B[a]	P[d]
A0	0	1	2	120	11	19	<5	0.005	1.8
A1	0.18	26	56	161.5	13	35	<5	0.008	0.6
A2	0.67	137	223	180	15	330	<5	0.007	0.6
A3	1.09	243	371	174	14	560	<5	0.008	0.4
A4	2.17	479	654	153	25	910	<5	0.06	0.9
A5	3.32	771	1055	204	16	980	<5	0.08	0.6

a...Inductively coupled plasma-optical atom emission spectroscopy, b...Combustion analyses, c...Carrier gas hot extraction, d...Glow-discharge-mass-spectroscopy

It is noticeable that a high amount of oxygen and nitrogen segregation was found at grain boundaries of the intergranular fractured A1, whereas the transgranular fractured A5 indicates large enrichments of carbon and boron without any oxygen decorations.

Figure 12 gives an overview of the average interfacial excess of the detected segregation elements, to comparing the grain boundary chemistry of all studied alloys. It is obvious, that the increase of the overall hafnium content leads to additional boron and carbon segregation and to a significant reduction of oxygen at grain boundaries. Therefore, it seems that especially boron and carbon decorations strengthen the grain boundary, which has also been reported in literature [51,55,62,63,67]. Furthermore, these elements seem to suppress oxygen segregation to the grain boundaries and, thus, mitigate intergranular embrittlement by reducing the oxygen content at the grain boundaries. Nitrogen and phosphorus, which are typical solute decorations in pure Mo and are known to have detrimental effects on the grain boundary strength, are present in lower amounts at the grain boundaries of Mo-Hf alloys, especially at higher hafnium contents. Nevertheless, the overall chemical composition of phosphorus must be taken into account in respect to the segregation amount. Their lower content at the grain boundaries of A4 and A5 seems to additionally enhance the grain boundary strength.

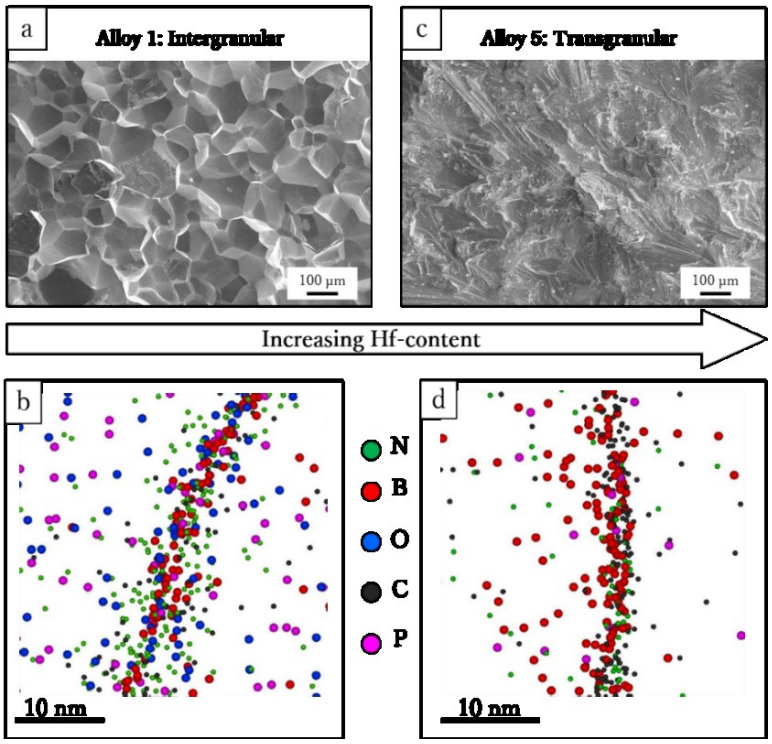

Fig. 11: (a) Fracture surface of A1 after tensile test; (b) Grain boundary chemistry of A1 obtained by APT; (c) Fracture surface of A5 after tensile test; (d) Grain boundary chemistry of A5 obtained by APT. Mo atoms are blanked. The illustrations are assembled and redrawn from Publication E.

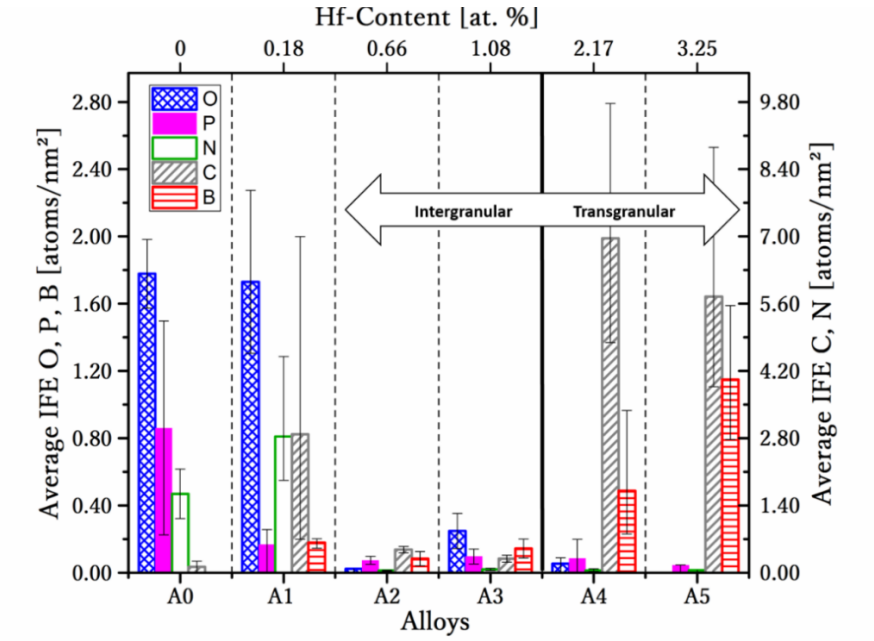

Fig. 12: The average interfacial excess values in atoms/nm² of oxygen, phosphorus, boron, nitrogen, and carbon are presented in dependence of the alloy systems redrawn from **Publication E.** Oxygen, phosphorus and boron are scaled on the left axis, whereas carbon and nitrogen are shown on the right axis. The error bar indicates the maximum and minimum excess detected. Between alloy A3 and A4 the fracture mode change was observed.

In summary, three effects by increased hafnium content in the Mo-Hf alloys could be responsible for higher grain boundary strength as illustrated in Fig. 12:

- Carbon and boron, which are introduced during the production route with increasing hafnium content, enhance the grain boundary strength by their segregation to grain boundaries.
- Increased segregation of carbon and boron to grain boundaries suppresses the enrichment of detrimental elements, such as oxygen, nitrogen and phosphorus (see Figs. 13b and c).
- Oxygen decorations are suppressed due to the increased formation of HfO_2 with increasing hafnium content and due to carbon and boron segregation (see Fig. 13c).

Therefore, hafnium does not have a direct beneficial impact on the fracture behavior of Mo alloys, but the introduced trace elements carbon and boron improve the material properties. Additionally, hafnium acts as a getter for oxygen by forming HfO_2.

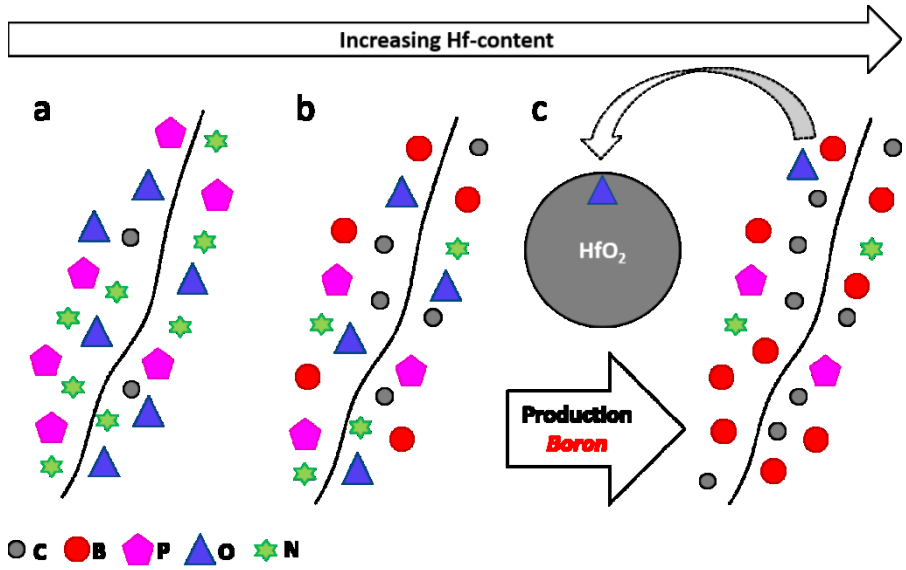

Fig. 13: Schematic illustration of the main grain boundary strengthening effects in Mo-Hf alloys to provoke transgranular fracture: (a) Typical grain boundary segregation in technically pure Mo; (b) Targeted contamination of the grain boundaries by carbon and boron which are introduced during production with increasing hafnium content; (c) Strengthening effect of Mo-Hf alloys by carbon and boron segregations. Additionally, oxygen is gettered by HfO_2 and removed from the grain boundaries.

The experimental results were additionally compared to *ab initio* calculations, which can be found in **Publication E.** Calculated and measured interfacial excess values of a low-sigma grain boundary are compared and discussed ($\Sigma 11$ with 51.5° rotation angle and [1 20 19] rotation axis with 2.5° deviation according the Brandon´s criterion). For further details the reader is referred to **Publication E.** In conclusion, APT and *ab initio* results indicate similar solute decoration amounts at the low-sigma grain boundary and, therefore, the previously discussed strengthening processes can be confirmed by the calculations.

The present results demonstrate that grain boundary segregation engineering is a helpful tool to improve the material properties. However, it has to be mentioned that in these alloys a fracture mode change was provoked, but no increase in fracture elongation was observed. Nevertheless, future work can be based on this newly gained knowledge in order to further improve material properties and to expand investigations onto other promising alloys systems.

3.5 Charpy impact tests with correlative electron back-scatter diffraction study

Charpy impact tests were performed and correlated with high resolution EBSD characterizations to combine APT analyses of grain boundary segregation in technically pure Mo with mechanical properties from experiments **(Publication F).** The Charpy impact test is a simple technological test and a common method for material characterization in industry. Since many structural materials are exposed to impact loadings, the Charpy impact test is a useful experiment to gain more knowledge of the material properties at high deformation speeds and low test temperatures at multi-axial stress states. Additionally, the DBTTs of bcc structured materials can be easily studied. Mo exhibits a pronounced DBTT close to RT. It is also known that deformed Mo suffers from delamination in the transition and upper shelf region, whereas the recrystallized material state shows an increase of the DBTT and intergranular embrittlement (see chapter 2.1, "Fracture behavior of molybdenum"). It is already known that grain size, grain shape, grain boundary character, alloying content, stress state, and strain rate influence the DBTT. Furthermore, also the testing conditions, such as loading speed, support distance as well as sample geometry and size influence the DBTT. In Fig. 14 the effect of alloying on the DBTT is presented by comparing the Charpy absorbed energies in the transition region of stress-relieved technically pure Mo and the Mo alloy TZM (nominal composition of 0.5 m.% (0.97 at.%) Ti, 0.08 m.% (0.08 at.%) Zr and 0.01 – 0.04 m.% (0.08-0.32 at.%) C. By alloying titanium and zirconium an increase of the transition temperature region can be provoked. It is also evident that the behavior in Charpy impact tests depends strongly on the specimen orientation. In general, samples in L-T orientation, where the global crack follows the designated crack growth direction, show an upper shelf of around 50 J (a description of the extraction direction is given in **Publication F**). In contrast, macroscopic delamination causes a deviation of the designated crack growth direction in L-S oriented samples, which leads a reduction of the local crack driving force and to a creation of a larger surface area. Both effects result in a higher upper shelf energy for L-S specimens, compared to L-T.

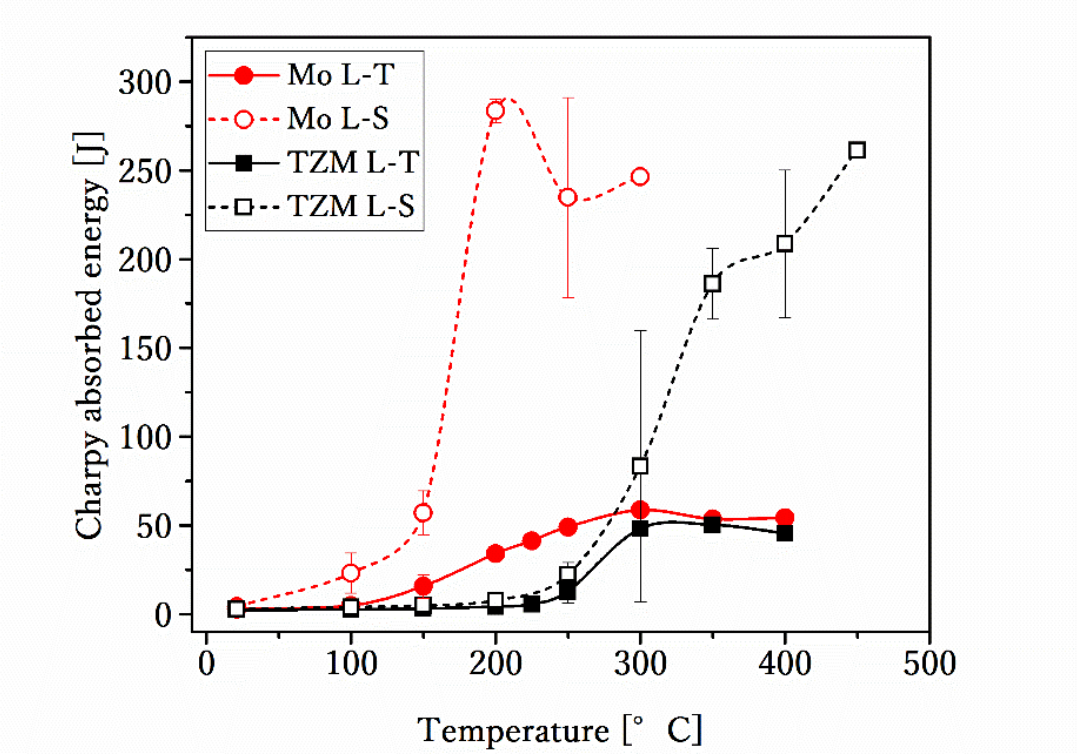

Fig. 14: Charpy impact test curves for Mo and TZM in their stress-relieved state in L-T and L-S orientation.

The same effect of macroscopic delamination can be studied for T-S oriented samples (**see Publication F**). T-L specimens exhibit the same fracture mechanisms as L-T samples. Microscopic delamination results in a thin-sheet toughening effect in these two sample orientations (L-T and T-L), which is explained in chapter 2.1, "Fracture behavior of molybdenum". More details can be found in **Publication F**. Furthermore, with the high resolution of EBSD it was possible to study the delamination cracks of the tested Mo and TZM samples; with an example of such cracks in an L-S sample of TZM shown in Fig. 15. It is evident that these delamination cracks follow grain boundaries with high misorientation. The same crack growth behavior can be studied in technically pure Mo (**see Publication F**). From APT investigations it is already known that grain boundaries in the as-deformed and recrystallized state of pure Mo contain a high amount of detrimental segregation, which decrease the strength of the intrinsically weak grain boundaries. Delamination cracks seem to follow the path with the lowest crack growth resistance in the material, which are the grain boundaries with high misorientation in the case of Mo. Samples of Mo are more or less prone to delamination, depending on the orientation of the crack in respect to the grain elongation direction.

Nevertheless, for a comprehensive correlative study of grain boundary chemistry and strength the nanoscale characterization technique of APT should be compared to mechanical tests on the same length scale. Therefore, micro-bending tests seem to be more adequate than Charpy impact test. A direct correlation of strength and chemistry of the same boundary would be possible.

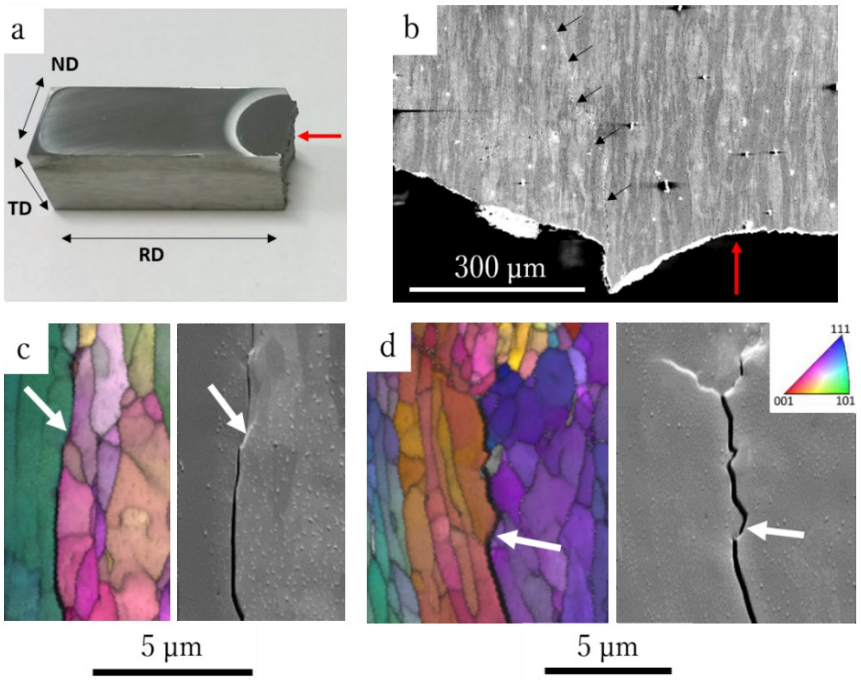

Fig. 15: EBSD-characterization of delamination cracks in an L-S sample of TZM tested at RT: (a) Fractured sample with the electro-polished area for the EBSD analyzation; (b) SEM-image of a crack, which grows perpendicular to the designated crack growth direction (delamination crack); (c-d) IPF mappings of crack tips of delamination with image quality overlay. The corresponding SEM images are shown on the right side. The inset in the upper right corner shows the IPF coloring which indicates the crystal direction perpendicular to the (c) transverse direction (TD) and (d) normal direction (ND). The white arrows mark the delamination cracks.

4 Summary and outlook

Studies in literature indicate that the brittle fracture behavior of Mo can be mainly attributed to its weak grain boundaries. However, it is still not fully clear if the low grain boundary strength of Mo originates primarily from its intrinsic brittleness or if it is dominated by the weakening effect of grain boundary segregation.

In order to clarify the influence of segregation phenomena the grain boundary chemistry of several Mo materials was characterized in the present PhD thesis by atom probe tomography and correlated to their mechanical properties. Thereby, industrially produced technically pure Mo plates, as well as Mo-based model alloys with targeted contaminations were comprehensively studied.

The main results can be summarized as follows:

- A new preparation method by correlative TKD was developed to improve and facilitate the preparation process and to obtain crystallographic information of the grain boundary.
- A comprehensive study of the grain boundary segregation in industrial produced technically pure Mo plates was conducted. At high-angle grain boundaries mainly oxygen, nitrogen, phosphorus, and carbon enrichments were detected. Pronounced carbon segregation was only observed at low-sigma grain boundaries in the recrystallized condition. The overall chemical composition as well as the grain size influences the content of solute decorations at the grain boundaries. A smaller grain size and a lower overall impurity content leads to reduced solute decorations at the grain boundaries.
- Boron and carbon has been identified as strengthening elements in Mo-Hf based model alloys. In these alloys, the formation of HfO_2 and the segregation of boron and carbon may result in a suppression of oxygen at the grain boundaries, which in turn reduces the embrittlement.
- EBSD investigations have shown that delamination mainly occurs at high-angle grain boundaries, which are contaminated by detrimental elements like nitrogen, oxygen and phosphorus.

The results of this study reveal that the intergranular fracture of Mo is promoted by grain boundary segregations of oxygen, nitrogen and phosphorus. In order to improve the grain boundary strength and reduce the embrittlement, the following guidelines for the design of optimized Mo and their alloys can be given:

In general, a lower overall concentration of impurities leads to less segregation of foreign atoms at the grain boundaries, which is important for the reduction of detrimental segregation elements like nitrogen, phosphorus and oxygen. Additionally, a smaller grain size, especially in the recrystallized condition, would be advantageous, as this increases the present grain boundary volume and, therefore, reduces the absolute concentration of detrimental

segregation atoms at the grain boundaries. A high concentration of low-sigma grain boundaries could further improve the mechanical properties of Mo because beneficial carbon segregation were detected at these grain boundaries. In general, boron and carbon should be added in small amounts, as they strengthen the grain boundary, decrease the DBTT and promote transgranular fracture.

In order to directly investigate the effect of the grain boundary type and the influence of grain boundary segregation, future studies should focus on combining high resolution analytical techniques with highly localized mechanical testing of individual grain boundaries. Additionally, a study of the segregation processes throughout the whole production and processing route of molybdenum - including the sintered, the as-deformed, the partly-recrystallized and the fully recrystallized state - would further help to improve the understanding of segregation phenomena and their impact on resulting material properties.

5 References

[1] W. Martienssen, H. Warlimont, Springer Handbook of Condensed Matter and Materials Data, Springer, Berlin, Heidelberg, New York, 2005.

[2] S. Tsurekawa, T. Tanaka, H. Yoshinaga, Grain boundary structure, energy and strength in molybdenum, Materials Science and Engineering: A. 176 (1994) 341–348.

[3] A.J. Bryhan, Joining of Molybdenum Base Metals and Factors Which lnfluence Ductility, WRC Bulletin. 312 (1986) 21.

[4] Plansee, Molybdän, https://www.plansee.com/de/werkstoffe/molybdaen.html, January 2017

[5] E. Pink, R. Eck, Refractory metals and their alloys, in: R.W. Cahn, P. Haasen, E.J. Kramer, K.H. Matucha (Eds.), Materials Science and Technology, VCH, Weinheim, New York, Basel, Cambridge, Tokyo, 2006: pp. 591–638.

[6] E. Pink, Rekristallisationsdiagramme von Molybdän und Wolfram, Planseeberichte Für Pulvermetallurgie. 13 (1965) 100–104.

[7] A. Kumar, B.L. Eyre, Grain Boundary Segregation and Intergranular Fracture in Molybdenum, Proceedings of the Royal Society A: Mathematical, Physical and Engineering Sciences. 370 (1980) 431–458.

[8] S. Primig, Recovery and Recrystallization Behavior of Technically Pure Molybdenum, Dissertation, Montanuniversität Leoben, 2012.

[9] B.V. Cockeram, E.K. Ohriner, T.S. Byun, M.K. Miller, L.L. Snead, Weldable ductile molybdenum alloy development, Journal of Nuclear Materials. 382 (2008) 229–241.

[10] H. Kimura, Overview, Intergranular Fracture in BCC metals, Transactions of the Japan Institute of Metals. 29 (1988) 521–539.

[11] J.B. Brosse, R. Fillet, M. Biscondi, Intrinsic intergranular brittleness of molybdenum, Scripta Metallurgica. 15 (1981) 619–623.

[12] R. Stickler, H. Hödl, Charakterisierung des Delaminationsverhalten von Mo-Blechen. Messungen an 5mm und 2mm Blechen im Anlieferungszustand., Plansee Report 96DEL3a. (1996) 4.

[13] C. Stickler, Charakterisierung des Delaminationsverhalten von Mo-Ronden mittels Biegeversuch, Plansee Report 97DEL2a. (1997) 6.

[14] R. Stickler, H. Hödl, Charaketrisierung des Delaminationsverhalten von Mo-Blechen. Vorversuche zur Entwicklung einer Prüfmethode., Plansee Report 96DEL2a. (1996) 12.

[15] B. V. Cockeram, The role of stress state on the fracture toughness and toughening mechanisms of wrought molybdenum and molybdenum alloys, Materials Science and Engineering A. 528 (2010) 288–308.

[16] B. V. Cockeram, The fracture toughness and toughening mechanisms of wrought low carbon arc cast, oxide dispersion strengthened, and molybdenum-0.5 pct titanium-0.1 pct zirconium molybdenum plate stock, Metallurgical and Materials Transactions A. 36 (2005) 1777–1791.

[17] B. V. Cockeram, The mechanical properties and fracture mechanisms of wrought low carbon arc cast (LCAC), molybdenum-0.5pct titanium-0.1pct zirconium (TZM), and oxide dispersion strengthened (ODS) molybdenum flat products, Materials Science and Engineering A. 418 (2006) 120–136.

[18] B. V. Cockeram, Measuring the fracture toughness of molybdenum-0.5 pct titanium-0.1 pct zirconium and oxide dispersion-strengthened molybdenum alloys using standard and subsized bend specimens, Metallurgical and Materials Transactions A. 33 (2002) 3685–3707.

[19] M.S. Joo, D.-W. Suh, J.H. Bae, H.K.D.H. Bhadeshia, Role of delamination and crystallography on anisotropy of Charpy toughness in API-X80 steel, Materials Science and Engineering: A. 546 (2012) 314–322.

[20] M.S. Joo, D. Suh, J. Bae, H.K.D.H. Bhadeshia, Toughness Anisotropy in X70 and X80 Linepipe steels, Materials Science and Technology. 30 (2014) 439–446.

[21] M.S. Joo, D.W. Suh, J.H. Bae, N. Sanchez Mouriño, R. Petrov, L. a I. Kestens, et al., Experiments to separate the effect of texture on anisotropy of pipeline steel, Materials Science and Engineering A. 556 (2012) 601–606.

[22] Y. Kimura, T. Inoue, F. Yin, K. Tsuzaki, Inverse Temperature Dependence of Toughness in an Ultrafine Grain-Structure Steel, Science. 320 (2008) 1057–1060.

[23] R. Song, D. Ponge, D. Raabe, Mechanical properties of an ultrafine grained C-Mn steel processed by warm deformation and annealing, Acta Materialia. 53 (2005) 4881–4892.

[24] R. Song, D. Ponge, D. Raabe, J.G. Speer, D.K. Matlock, Overview of processing, microstructure and mechanical properties of ultrafine grained bcc steels, Materials Science and Engineering A. 441 (2006) 1–17.

[25] A. Hohenwarter, A. Taylor, R. Stock, R. Pippan, Effect of large shear deformations on the fracture behavior of a fully pearlitic steel, in: Metallurgical and Materials Transactions A: Physical Metallurgy and Materials Science, 2011: pp. 1609–1618.

[26] A. Fraczkiewicz, K. Wolski, Intergranular Segregation and Crystalline Material Fracture, in: L. Priester (Ed.), Grain Boundaries and Crystalline Plasticity, John Wiley & Sons, Inc, Hoboken, NJ, USA, 2011: pp. 281–321.

[27] S. Tsurekawa, S. Kokubun, T. Watanabe, Effect of grain boundary microstructures of brittle fracture in polycrystalline molybdenum, Materials Science Forum. 304-306 (1999) 687–692.

[28] T. Watanabe, S. Tsurekawa, The control of brittleness and development of desirable mechanical properties in polycrystalline systems by grain boundary engineering, Acta Materialia. 47 (1999) 4171–4185.

[29] L.C. Lim, T. Watanabe, Fracture toughness and brittle-ductile transition controlled by grain boundary character distribution (GBCD) in polycrystals, Acta Metallurgica et Materialia. 38 (1990) 2507–2516.

[30] T. Watanabe, Grain boundary engineering: historical perspective and future prospects, Journal of Materials Science. 46 (2011) 4095–4115.

[31] T. Watanabe, S. Tsurekawa, Toughening of brittle materials by grain boundary engineering, Materials Science and Engineering: A. 387-389 (2004) 447–455.

[32] T. Watanabe, An approach to grain boundary design of strong and ductile polycrystals, Res Mechanica. 11 (1984) 47–84.

[33] P. Lejcek, Grain Boundaries: Description, Structure and Thermodynamics, in: R. Hull, C. Jagadish, R.M. Osgood, J.J. Parisi, Z. Wang, H. Warlimont (Eds.), Grain Boundary Segregation in Metals, Springer Berlin Heidelberg, Berlin Heidelberg, 2010: pp. 5–22.

[34] B. Gludovatz, S. Wurster, T. Weingärtner, a. Hoffmann, R. Pippan, Influence of impurities on the fracture behaviour of tungsten, Philosophical Magazine. 91 (2011) 3006–3020.

[35] K. Babinsky, J. Weidow, W. Knabl, A. Lorich, H. Leitner, S. Primig, Atom probe study of grain boundary segregation in technically pure molybdenum, Materials Characterization. 87 (2014) 95–103.

[36] K. Babinsky, W. Knabl, A. Lorich, R. De Kloe, H. Clemens, S. Primig, Grain boundary study of technically pure molybdenum by combining APT and TKD, Ultramicroscopy. 159 (2015) 445–451.

[37] K. Babinsky, S. Primig, W. Knabl, A. Lorich, T. Weingärtner, J. Weidow, et al., Grain boundary segregations in technically pure molybdenum, in: 18. Planseeseminar, Plansee SE, 2013: pp. RM111/1–15.

[38] P. Lejcek, Grain Boundary Segregation in Metals, Springer Berlin Heidelberg, Berlin, Heidelberg, 2010.

[39] D. Raabe, S. Sandlöbes, J. Millán, D. Ponge, H. Assadi, M. Herbig, et al., Segregation engineering enables nanoscale martensite to austenite phase transformation at grain boundaries: A pathway to ductile martensite, Acta Materialia. 61 (2013) 6132–6152.

[40] D. Raabe, M. Herbig, S. Sandlöbes, Y. Li, D. Tytko, M. Kuzmina, et al., Grain boundary segregation engineering in metallic alloys: A pathway to the design of interfaces, Current Opinion in Solid State and Materials Science. 18 (2014) 253–261.

[41] D. McLean, Grain Boundaries in Metals, Clarendon Press, University of Michigan, 1957.

[42] M.P. Seah, E.D. Hondros, Grain Boundary Segregation, Proceedings of the Royal Society A: Mathematical, Physical and Engineering Sciences. 335 (1973) 191–212.

[43] R.H. Fowler, E.A. Guggenheim, Statistical thermodynamics: a version of statistical mechanics for students of physics and chemistry, The University Press, Cambridge, 1939.

[44] M. Guttmann, Equilibrium segregation in a ternary solution: A model for temper embrittlement, Surface Science. 53 (1975) 213–227.

[45] M. Guttmann, D. McLean, Grain boundary segregation in multicomponent systems, in: W.C. Johnson, J.M. Blakely (Eds.), Interfacial Segregation, ASM, Metals Park, 1979: pp. 261–348.

[46] X. Tingdong, C. Buyuan, Kinetics of non-equilibrium grain-boundary segregation, Progress in Materials Science. 49 (2004) 109–208.

[47] T. Watanabe, T. Murakami, S. Karashima, Misorientation dependence of grain boundary segregation, Scripta Metallurgica. 12 (1978) 361–365.

[48] a. Fraczkiewicz, M. Biscondi, Intergranular Segregation of Bismuth in Copper Bicrystals, Le Journal de Physique Colloques. 46 (1985) C4–497–C4–503.

[49] A.R. Waugh, M.J. Southon, Surface analysis and grain-boundary segregation measurements using atom-probe techniques, Surface Science. 89 (1979) 718–724.

[50] A.R. Waugh, M.J. Southon, Surface studies with an imaging atom-probe, Surface Science. 68 (1977) 79–85.

[51] M.K. Miller, E.A. Kenik, M.S. Mousa, K.F. Russell, A.J. Bryhan, Improvement in the ductility of molybdenum alloys due to grain boundary segregation, Scripta Materialia. 46 (2002) 299–303.

[52] S.M. Tuominen, S.P. Clough, Grain boundary segregation of sulfur and nitrogen in sintered molybdenum, Metallurgical Transactions A. 10 (1979) 127–129.

[53] R. Janisch, C. Elsässer, Segregated light elements at grain boundaries in niobium and molybdenum, Physical Review B. 67 (2003) 224101.

[54] S. Suzuki, H. Matsui, H. Kimura, The effect of heat treatment on the grain boundary fracture of recrystallized molybdenum, Materials Science and Engineering. 47 (1981) 209–216.

[55] F. Morito, Intergranular Fracture Surface Analysis of Molybdenum ", Surface and Interface Analysis. 15 (1990) 427–432.

[56] A. Krajnikov, F. Morito, V. Slyunyaev, Impurity-induced embrittlement of heat-affected zone in welded Mo-based alloys, International Journal of Refractory & Hard Materials. 15 (1997) 325–339.

[57] A. Krajnikov, A. Drachinskiy, V. Slyunyaev, Grain boundary segregation in recrystallized molybdenum alloys and its effect on brittle intergranular fracture, International Journal of Refractory Metals and Hard Materials. 11 (1992) 175–180.

[58] K. Tsuya, N. Aritomi, On the effects of vacuum annealing and carburizing on the ductility of coarse-grained molybdenum, Journal of the Less Common Metals. 15 (1968) 245–257.

[59] A.S. Drachinskiy, A. V. Kraynikov, V.N. Slyunyaev, Interrelation of Impurity Enrichment of Grain Boundaries and the Cold-Shortness Point During Annealing of Molybdenum, Phys. Met. Metallogr. 66 (1988) 111–119.

[60] Y. Hiraoka, Significant effect of carbon content in the low-temperature fracture behavior of molybdenum, Materials Transactions, JIM. 31 (1990) 861–864.

[61] W. Kopecky, A.I. Paschkowsky, Der Einfluss von Kohlenstoff und Zusätzen von Elementen der Eisengruppe auf die mechanischen Eigenschaften von Molybdän und Wolframeinkristallen.pdf, Planseeberichte Für Pulvermetallurgie. 19 (1971) 7–17.

[62] H. Lutz, F. Benesovsky, R. Kieffer, Versuche zur Desoxidation von Sintermolybdän mit Kohlenstoff, Bor und Silizium, Journal of the Less Common Metals. 16 (1968) 249–264.

[63] T. Kadokura, Y. Hiraoka, Y. Yamamoto, K. Okamoto, Change of Mechanical Property and Fracture Mode of Molybdenum by Carbon Addition, Materials Transactions. 51 (2010) 1296–1301.

[64] A. Tahir, R. Janisch, A. Hartmaier, Ab initio calculation of traction separation laws for a grain boundary in molybdenum with segregated C impurites, Modelling and Simulation in Materials Science and Engineering. 21 (2013) 075005.

[65] R. Janisch, T. Ochs, A. Merkle, C. Elsässer, Structure and stability of grain boundaries in molybdenum with segregated carbon impurities, in: MRS Proceedings, 1999.

[66] A. Milner, T.R. Bergstrom, Ductility of sintered unworked molybdenum-carbon alloys, Journal of the Less Common Metals. 12 (1967) 253–257.

[67] M.K. Miller, A.J. Bryhan, Effect of Zr, B and C additions on the ductility of molybdenum, Materials Science and Engineering A. 327 (2002) 80–83.

[68] Y. Hiraoka, B. Edwards, B. Eyre, Effects of Nitrogen on Grain Boundary Fracture in Molybdenum, Materials Science Forum. 126-128 (1993) 153–156.

[69] D. Scheiber, R. Pippan, P. Puschnig, A. Ruban, L. Romaner, Ab-initio search for cohesion-enhancing solute elements at grain boundaries in molybdenum and tungsten, International Journal of Refractory Metals and Hard Materials. 60 (2016) 75–81.

[70] A. Joshi, D.F. Stein, Intergranular brittleness studies in tungsten using Auger spectroscopy, Metallurgical Transactions. 1 (1970) 2543–2546.

[71] P. Lejcek, Approaches to Study Grain Boundary Segregation, in: R. Hull, C. Jagadish, R.M. Osgood, J.J. Parisi, Z. Wang, H. Warlimont (Eds.), Grain Boundary Segregation in Metals, Springer Berlin Heidelberg, Berlin Heidelberg, 2010: pp. 39–63.

[72] E.D. Hondros, Grain boundary segregation assessment of investigative techniques, in: G.A. Chadwick, D.A. Smith (Eds.), Grain Boundary Structure and Properties, Academic, London, 1976: pp. 265–298.

[73] E.D. Hondros, M.P. Seah, S. Hofmann, P. Lejcek, Physical Metallurgy, 4th ed., Elsevier Science B. V., North-Holland, Amsterdam, 1996.

[74] T.N. Nowicki, M. Biscondi, Oxygen segregation in 32 [001] molybdenum tilt grain boundaries II. enthalpies of segregation determination from AES and grain boundary grooves measurements, Le Journal de Physique Colloques. 49 (1988) C5–409–C5–416.

[75] A.R. Chourasia, D.R. Chopra, Auger Electron Spectroscopy, in: Handbook of Instrumental Technqiues for Analytical Chemistry, Texas, 1971: pp. 791–808.

[76] P. Auger, Sur l'effet photoélectrique composé, J. Phys. Radium. 6 (1925) 205–208.

[77] K.D. Childs, B.A. Carlson, L.A. La Vanier, J.F. Moulder, D.F. Paul, W.F. Stickle, et al., Handbook of Auger Electron Spectroscopy, 3rd editio, Physical Electronics, Inc., Minnesota, 1995.

[78] V.J. Keast, D.B. Williams, Grain boundary chemistry, Current Opinion in Solid State and Materials Science. 5 (2001) 23–30.

[79] R. Brydson, Electron Energy Loss Spectroscopy, Microscopy, Tayler & Francis, London and New York, 2001.

[80] M.K. Miller, A. Cerezo, M.G. Hetherington, G.D.W. Smith, Atom probe field ion microscopy, Clarendon Press, Oxford, 1996.

[81] B. Gault, M. Moody, J. Cairney, S. Ringer, Atom probe microscopy, Springer, 2012.

[82] B. Gault, M.P. Moody, J.M. Cairney, S.P. Ringer, Atom probe crystallography, Materials Today. 15 (2012) 378–386.

[83] D. Larson, T. Prosa, T. Kelly, Local Electrode Atom Probe Tomography - A user's guide, 2013.

[84] B. Gault, M.P. Moody, F. De Geuser, G. Tsafnat, A. La Fontaine, L.T. Stephenson, et al., Advances in the calibration of atom probe tomographic reconstruction, Journal of Applied Physics. 105 (2009).

[85] M. Thuvander, H.-O. Andrén, APFIM studies of grain and phase boundaries: a review, Materials Characterization. 44 (2000) 87–100.

[86] A. Henjered, H. Nordén, A controlled specimen preparation technique for interface studies with atom-probe field-ion microscopy, Journal of Physics E: Scientific Instruments. 16 (1983).

[87] D.J. Larson, D.T. Foord, a. K. Petford-Long, H. Liew, M.G. Blamire, A. Cerezo, et al., Field-ion specimen preparation using focused ion-beam milling, Ultramicroscopy. 79 (1999) 287–293.

[88] D.. Larson, D.. Foord, A.. Petford-Long, T.. Anthony, I.. Rozdilsky, A. Cerezo, et al., Focused ion-beam milling for field-ion specimen preparation:, Ultramicroscopy. 75 (1998) 147–159.

[89] M. Miller, K. Russell, Review of atom probe FIB-based specimen preparation methods, Microscopy and Microanalysis. 13 (2007) 428–436.

[90] M.K. Miller, K.F. Russell, G.B. Thompson, Strategies for fabricating atom probe specimens with a dual beam FIB., Ultramicroscopy. 102 (2005) 287–298.

[91] M.K. Miller, K.F. Russell, Atom probe specimen preparation with a dual beam SEM/FIB miller., Ultramicroscopy. 107 (2007) 761–766.

[92] P.J. Felfer, T. Alam, S.P. Ringer, J.M. Cairney, A reproducible method for damage-free site-specific preparation of atom probe tips from interfaces, Microscopy Research and Technique. 75 (2012) 484–491.

[93] P. Felfer, S.P. Ringer, J.M. Cairney, Shaping the lens of the atom probe: fabrication of site specific, oriented specimens and application to grain boundary analysis., Ultramicroscopy. 111 (2011) 435–439.

[94] M. Herbig, P. Choi, D. Raabe, Combining structural and chemical information at the nanometer scale by correlative transmission electron microscopy and atom probe tomography, Ultramicroscopy. 153 (2015) 32–39.

[95] F. Pérez-Willard, D. Wolde-Giorgis, T. Al-Kassab, G. a López, E.J. Mittemeijer, R. Kirchheim, et al., Focused ion beam preparation of atom probe specimens containing a single crystallographically well-defined grain boundary., Micron. 39 (2008) 45–52.

[96] W. McKenzie, E. Marquis, P. Munroe, Focused ion beam sample preparation for atom probe tomography, Microscopy: Science, Technology, Applications and Education. (2010) 1800–1810.

[97] M. Herbig, D. Raabe, Y.J. Li, P. Choi, S. Zaefferer, S. Goto, Atomic-scale quantification of grain boundary segregation in nanocrystalline material, Physical Review Letters. 112 (2013) 1–5.

[98] L. Yao, M.P. Moody, J.M. Cairney, D. Haley, a V Ceguerra, C. Zhu, et al., Crystallographic structural analysis in atom probe microscopy via 3D Hough transformation., Ultramicroscopy. 111 (2011) 458–63.

[99] G. Sha, L. Yao, X. Liao, S.P. Ringer, Z. Chao Duan, T.G. Langdon, Segregation of solute elements at grain boundaries in an ultrafine grained Al-Zn-Mg-Cu alloy., Ultramicroscopy. 111 (2011) 500–5.

[100] S. Mandal, K.G. Pradeep, S. Zaefferer, D. Raabe, A novel approach to measure grain boundary segregation in bulk polycrystalline materials in dependence of the boundaries' five rotational degrees of freedom, Scripta Materialia. 81 (2014) 16–19.

[101] M. Herbig, M. Kuzmina, C. Haase, R.K.W. Marceau, I. Gutierrez-Urrutia, D. Haley, et al., Grain boundary segregation in Fe–Mn–C twinning-induced plasticity steels studied by correlative electron backscatter diffraction and atom probe tomography, Acta Materialia. 83 (2015) 37–47.

[102] R.R. Keller, R.H. Geiss, Transmission EBSD from 10 nm domains in a scanning electron microscope, Journal of Microscopy. 245 (2012) 245–251.

[103] P.W. Trimby, Orientation mapping of nanostructured materials using transmission Kikuchi diffraction in the scanning electron microscope., Ultramicroscopy. 120 (2012) 16–24.

[104] S. Suzuki, Features of transmission EBSD and its application, The Journal of The Minerals, Metals & Materials Society. 65 (2013) 1254–1263.

[105] G.C. Sneddon, P.W. Trimby, J.M. Cairney, Transmission Kikuchi diffraction in a scanning electron microscope: A review, Materials Science and Engineering R: Reports. 110 (2016) 1–12.

[106] K. Babinsky, R. De Kloe, H. Clemens, S. Primig, A novel approach for site-specific atom probe specimen preparation by focused ion beam and transmission electron backscatter diffraction, Ultramicroscopy. 144 (2014) 9–18.

[107] S.M. Reddy, A. Van Riessen, D.W. Saxey, T.E. Johnson, D. a Rickard, D. Fougerouse, et al., Mechanisms of deformation-induced trace element migration in zircon resolved by atom probe and correlative microscopy, Geochimica et Cosmochimica Acta. 195 (2016) 158–170.

[108] Y. Chen, K.P. Rice, T.J. Prosa, Site-specific sample preparation using correlative microscopy : APT and tEBSD, MicroscopyandAnalysis. 30 (2016) 4–7.

[109] P. Haslberger, C. Turk, K. Babinsky, D. Caliskanoglu, H. Clemens, S. Primig, Boron Grain Boundary Segregation in a Heat Treatable Steel, BHM Berg- Und Hüttenmännische Monatshefte. 160 (2015) 204–208.

[110] D. Lang, C. Pöhl, D. Holec, J. Schatte, E. Povoden-Karadeniz, W. Knabl, et al., On the chemistry of the carbides in a molybdenum base Mo-Hf-C alloy produced by powder metallurgy, Journal of Alloys and Compounds. 654 (2016) 445–454.

[111] T. Klein, M. Schachermayer, F. Mendez-Martin, T. Schöberl, B. Rashkova, H. Clemens, et al., Carbon distribution in multi-phase γ-TiAl based alloys and its influence on mechanical properties and phase formation, Acta Materialia. 94 (2015) 205–213.

[112] F. Danoix, X. Sauvage, D. Huin, L. Germain, M. Gouné, A direct evidence of solute interactions with a moving ferrite/austenite interface in a model Fe-C-Mn alloy, Scripta Materialia. 121 (2016) 61–65.

[113] K.P. Rice, Y. Chen, T.J. Prosa, D.J. Larson, Implementing Transmission Electron Backscatter Diffraction for Atom Probe Tomography, Microscopy and Microanalysis. 22 (2016) 583–588.

[114] L. Yao, S.P. Ringer, J.M. Cairney, M.K. Miller, The anatomy of grain boundaries: Their structure and atomic-level solute distribution, Scripta Materialia. 69 (2013) 622–625.

[115] V.J. Araullo-Peters, B. Gault, S.L. Shrestha, L. Yao, M.P. Moody, S.P. Ringer, et al., Atom probe crystallography: Atomic-scale 3-D orientation mapping, Scripta Materialia. 66 (2012) 907–910.

[116] B. Gault, D. Haley, F. de Geuser, M.P. Moody, E. a Marquis, D.J. Larson, et al., Advances in the reconstruction of atom probe tomography data., Ultramicroscopy. 111 (2011) 448–57.

[117] B. Gault, F. de Geuser, L.T. Stephenson, M.P. Moody, B.C. Muddle, S.P. Ringer, Estimation of the Reconstruction Parameters for Atom Probe Tomography, Microscopy and Microanalysis. 14 (2008) 296–305.

[118] M.K. Miller, H. Kurishita, APFIM Characterization of Grain Boundary Segregation in Titanium Carbide-Doped Molybdenum, Le Journal de Physique IV. 6 (2008) 1–6.

[119] K.S. Lee, S. Morozumi, Effects of Alloying Elements on the Workability and Ductility of Interstitial-Free Molybdenum, Transactions of the Japan Institute of Metals. 25 (1984) 401–410.

[120] Y. Hiraoka, S. Yoshimura, Low temperature fracture strength and ductility of carburized Mo-Ti alloys, International Journal of Refractory Metals and Hard Materials. 13 (1995) 205–210.

[121] D.G. Brandon, The structure of high-angle grain boundaries, Acta Metallurgica. 14 (1966) 1479–1484.

[122] C. Pöhl, J. Schatte, H. Leitner, Solid solution hardening of molybdenum–hafnium alloys: Experiments and Modeling, Materials Science and Engineering: A. 559 (2013) 643–650.

te, H. Leitner, Solid solution softening of polycrystalline molybdenum–hafnium alloys,
d Compounds. 576 (2013) 250–256.

6 Publication A

A novel approach for site-specific atom probe specimen preparation by focused ion beam and transmission electron backscatter diffraction

K. Babinsky [1*], R. De Kloe [2], H. Clemens [1], S. Primig [1]

1 Department of Physical Metallurgy and Materials Testing, Montanuniversität Leoben, Austria

2 AMETEK B. V., EDAX business unit, The Netherlands

Abstract:

Atom probe tomography (APT) is a suitable technique for chemical analyses with almost atomic resolution. However, the time-consuming site-specific specimen preparation can be improved. Recently, transmission electron backscatter diffraction (t-EBSD) has been established for high resolution crystallographic analyses of thin foils. In this paper we present the first successful application of a combined focused ion beam (FIB)/t-EBSD preparation of site-specific APT specimens using the example of grain boundary segregation in technically pure molybdenum.

It will be shown that the preparation of a grain boundary can be substantially accelerated by t-EBSD analyses in-between the annular milling FIB procedure in the same microscope. With this combined method, a grain boundary can easily be recognized and positioned in the first 220 nm of an APT sample much faster than e.g. with complementary investigations in a transmission electron microscope. Even more, the high resolution technique of t-EBSD gives the opportunity to get crystallographic information of the mapped area and, therefore, an analysis of the grain boundary character to support the interpretation of the APT data files. To optimize this newly developed technique for the application on needle-shaped APT specimens, a parameter study on enhanced background correction, acceleration voltage, and tilt angle was carried out. An acceleration voltage of 30 kV at specimen surface tilt angles between -45° and -35° from horizontal plane leads to the best results. Even for molybdenum the observation of crystal orientation data up to about 200 nm specimen thickness is possible.

6.1 Introduction

Atom probe tomography (APT) is a highly sensitive tool to detect individual atoms within a needle-shaped specimen [1–3]. Therefore, it is used to study multiphase materials, interfaces in multilayer films, segregation at dislocations or grain boundaries as well as precipitates with almost atomic resolution [4]. Due to the small amounts of impurities, APT is a very suitable method to study grain boundary segregation in technically pure metals [5,6]. However, a limitation of APT is for example the complex specimen preparation [4]. Conventional APT specimen preparation techniques by electro-polishing limit the field of application for grain boundary segregation studies due to the small volume probed by APT.

Nowadays, it is possible to produce specimens out of site-specific regions of interest employing focused ion beam (FIB) systems [7,8]. With this technique, the site-specific specimen preparation of features as grain boundaries is possible for further APT analyses [4].

One of the first site-specific methods to study grain boundaries in the atom probe was applied by Miller et al. [9]. A small wedge or lamella containing a single grain boundary is lifted out of a bulk material with a micromanipulator and is attached to a post material by welding with e.g. platinum [10–12]. Another preparation method is the use of electro-polished APT specimens with re-sharpening them with a FIB in the region of interest [6,13]. Due to the fact that the visibility in the FIB/scanning electron microscope (SEM) for radii lower than ~ 500 nm is poor, additional studies in the transmission electron microscope (TEM) have been applied to analyze the location of a grain boundary [6,10,14]. However, a time-consuming repeated exchange between TEM and FIB/SEM is necessary for this technique [6]. Furthermore, to get information about the characteristics of the grain boundary, diffraction patterns have to be recorded. These processes contaminate the specimen and influence the APT analyses [15]. Sha et al. [16] instead used the major zone lines and crystallographic poles of two neighbor grains in a desorption map of an atom probe analysis to investigate the crystallographic structure of the grains. This technique was recently developed by Yao at al. [17]. However, this kind of investigation is complex and time-consuming.

Due to the obvious drawbacks of these methods, we propose a new characterization method for the site-specific preparation of grain boundaries in APT specimens based on transmission electron backscatter diffraction (t-EBSD) in this study. Our technique decisively simplifies the preparation process and gives detailed information about the crystallographic grain boundary properties.

The application of t-EBSD expands the field of conventional electron backscatter diffraction (EBSD) in the SEM. It is possible to quantitatively analyze the microstructure of materials based on crystallographic orientations with higher spatial resolution than standard EBSD by using a thin specimen in conventional EBSD systems [18]. In transmission mode, the orientation information contained in the diffraction patterns is derived from only the last 10-20 nm of material at the lower surface before the electrons exit the sample, which enables the

higher spatial resolution [18]. Keller et al. [19] firstly proposed to position a thin TEM foil above a commercial EBSD camera to acquire Kikuchi patterns by collecting transmitted forward scattered electrons to improve the spatial resolution of conventional EBSD. This technique is easily applicable because a standard EBSD detector and a commercial software is used.

Keller et al. [19] initially termed the method "transmission-EBSD" (t-EBSD) in 2012, but Trimby [20] and Suzuki [18] who did parameter studies proposed the term "transmission Kikuchi diffraction" (TKD). Another acronym was recommended by Brodusch et al. [21]. He defined the method as "transmission electron forward scatter diffraction" (t-EFSD) due to the fact that the appearing process is physically related to electron forward scattering. In this study, we decided to use the more easily recognizable name "t-EBSD", as specified by Keller et al., although this definition is perhaps not exactly correct.

So far, t-EBSD has only been used to analyze ultrafine-grained materials [22–24] and nanosized particles [25]. These authors used thin foils for all studies. In our work, we apply for the first time t-EBSD on needle-shaped APT specimens with a tip radius of about 100 nm for site-specific APT specimen preparation. Thus, in this investigation we present the first successful application of a combined FIB/ t-EBSD preparation process for APT site-specific specimens and a t-EBSD parameter study on APT tips to optimize the new technique.

6.2 Material and methods

For this study technically pure molybdenum was used to investigate grain boundary segregation which is not well understood in this material. The same material has been studied by TEM and APT in a previous study [6] which can be used as reference. An industrially processed hot-rolled sheet of molybdenum in the as-deformed and recrystallized stage was investigated. The production procedure of this sheet (termed sheet "1" in [6]) as well as the chemical composition is described in detail in [6]. In the present study, the recrystallized stage (grain size ~ 48 µm parallel to the rolling direction) was selected for the demonstration of the APT specimen preparation process by FIB/t-EBSD. The parameter study was carried out with both, the recrystallized and as-deformed stage (with a recovered subgrain structure) of the same technically pure molybdenum sheet.

Prior to the preparation process in the FIB combined with t-EBSD, APT specimens were produced by the standard electro-polishing method. Small rods (10 × 0.3 × 0.3 mm3) were cut out of the sheet with their largest dimension parallel to the normal direction. The electrolyte for polishing of the APT specimen was 12.5 vol. % H_2SO_4 in ethanol in a gold ring (microloop) as counter electrode. A detailed description of the electro-polishing process is given in [26].

All preparation work was done in a FEI Versa 3D DualBeam (FIB/SEM) workstation equipped with an EDAX Hikari XP EBSD system, therefore, no exchange between different

microscopes was necessary. The EDAX OIM Data Collection 7 software was used for the measurements and the EDAX OIM Analysis 7 for the evaluation of the EBSD data files.
For a successful APT measurement, the region of interest has to be located in the first few hundreds of nanometers below the apex. Thus, annular milling in the FIB was performed to position the grain boundary close to the apex of the needle-shaped specimen. All preparation steps were carried out with an acceleration voltage (Acc. V.) of 30 kV. To keep the gallium implantation low, the last annular milling steps were performed at an Acc. V. of 5 kV. However, it is always difficult to deduce if the grain boundary is in the volume for radii lower than ~ 500 nm due to the poor visibility in the FIB/SEM [6]. Therefore, the last preparation steps were supported by t-EBSD analyses to clearly identify the position of the grain boundary in the specimen. The t-EBSD analyses during the preparation process were carried out at an Acc. V. of 20 kV with a spot size of 2.5. The step size was set to 10 nm and for the last scan prior to the APT measurement to 5 nm. A 4x4 binning of the EBSD camera (i.e. a resolution of 160 x 120) was used. The scan speed was between 30 and 60 frames per second. All FIB preparation and t-EBSD work was done at a tilt angle of 52° which is also the position of the ion column and a working distance of 10 mm which is the intersection point. Fig. 1 shows the schematic set-up at 0° (a) and 52° (b) stage tilt in the microscope chamber. The stage tilt of 52° belongs to a specimen surface tilt angle of -38° degree from horizontal plane. In all further descriptions only the specimen surface tilt from horizontal plane is mentioned. The actual set-up for the FIB and t-EBSD preparation process is illustrated in Fig. 1 c.
The standard EBSD software is set-up for a tilt angle of 70°, while at t-EBSD an angle of 142° (or-38°) has to be used. An APT tip of a tungsten single crystal with a [001] direction in the axial direction was used to test this set-up. An enhanced background correction (dynamic background subtraction and normalize intensity histogram) was used in the EDAX OIM Data Collection 7 software. Furthermore, the set-up parameters for the Hough transformation were optimized to improve the band detection. A binned pattern size of 120, a theta step size of 0.5, and a standard 9x9 mask were used with the classic+ Hough setting. For the triplet indexing algorithm, the band centers and an interplanar tolerance angle of 3 degrees were used in all measurements. As both the point of origin of the patterns and the detector position were at fixed working distance, the projection of the patterns in all measurements was comparable. In the analysis software, the minimum confidence index was set to 0.1 in order to discard mis-indexed points. To clearly identify the grain boundary in the APT specimen, image quality (IQ) maps overlaid with inverse pole figure (IPF) crystal direction maps were constructed after each annular milling step. Repeated exchanges between annular milling and t-EBSD analyses were necessary to position the grain boundary in the first 220 nm of the APT specimen.

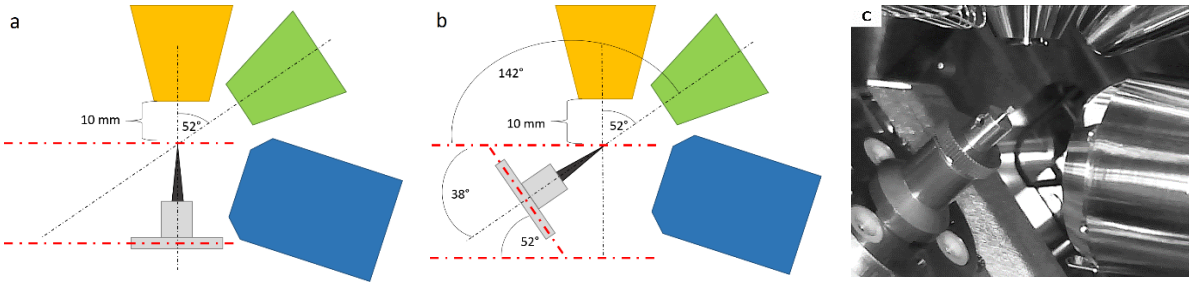

Fig. 1: (a) Schematic set-up in the microscope chamber at a stage tilt of 0°. The APT specimen is placed vertically, parallel to the optical axis of the electron column (yellow). The ion source (green) is located in an angle of 52° to the electron source. The beams have their intersection point at a working distance of 10 mm. The EBSD detector (blue) is located in the bottom right corner of the chamber. Due to the fact that the CCD camera is positioned at the back side of the microscope, the entire set-up is mirror-inverted if examined in the front view of the microscope. (b) The schematic set-up in the microscope chamber at a stage tilt of 52°. The specimen surface tilt angle is 142° from horizontal plane, therefore, the OIM data collection software is set to a -38° tilt angle. (c) The actual set-up in the chamber at a stage tilt angle of 52°.

The subsequent APT analysis of the FIB/t-EBSD prepared specimen was carried out with a LEAP 3000X HR from Cameca operated in laser mode. A laser energy of 0.6 nJ, a base temperature of 60 K and a pulse rate of 200 kHz were used. The target evaporation rate was set to 0.5 %. For the reconstruction of the analysis the IVAS 3.6.6 data software by Cameca was used.

Furthermore, to optimize the t-EBSD technique for APT specimens, a parameter study using similar EBSD settings was carried out. The influences of the specimen surface tilt angle (-50°, -45° and -35°), Acc. V. (20 kV and 30 kV) and types of enhanced background correction (dynamic background subtraction with normalize intensity histogram and additional background division as well as median smoothing) were studied. Additionally, the appearance of the band contrast reversal was examined. The annular milling process in the FIB is carried out at a fixed working distance of 10 mm. To analyze the parameters, Kikuchi patterns and IQ overlaid with IPF maps were used. The gray scale value in the IQ maps represents the average intensity of the bands of the Kikuchi patterns at each data point [18].

6.3 Results and discussion

6.3.1 FIB/t-EBSD combined APT specimen preparation process:

An electro-polished APT tip of recrystallized technically pure molybdenum was sharpened by FIB until a grain boundary was positioned ~1 µm below the apex and hardly visible anymore by SEM or FIB. At this point, the novel site-specific preparation procedure by t-EBSD and FIB started. After the set-up of the EBSD software, t-EBSD analyses were performed in-between the subsequent annular milling steps. These subsequent steps of the preparation process are shown in Fig. 2. The inset shows the IPF coloring which indicates the crystal direction perpendicular to the specimen surface. The Kikuchi pattern in Fig. 2 is a typical

example of the pattern quality for the preparation process of a molybdenum APT specimen. In the beginning, the grain boundary was 1290 nm below the apex of the APT specimen. Additional annular milling removed material from the top and thus the grain boundary came closer to the apex as visible in Fig. 2.

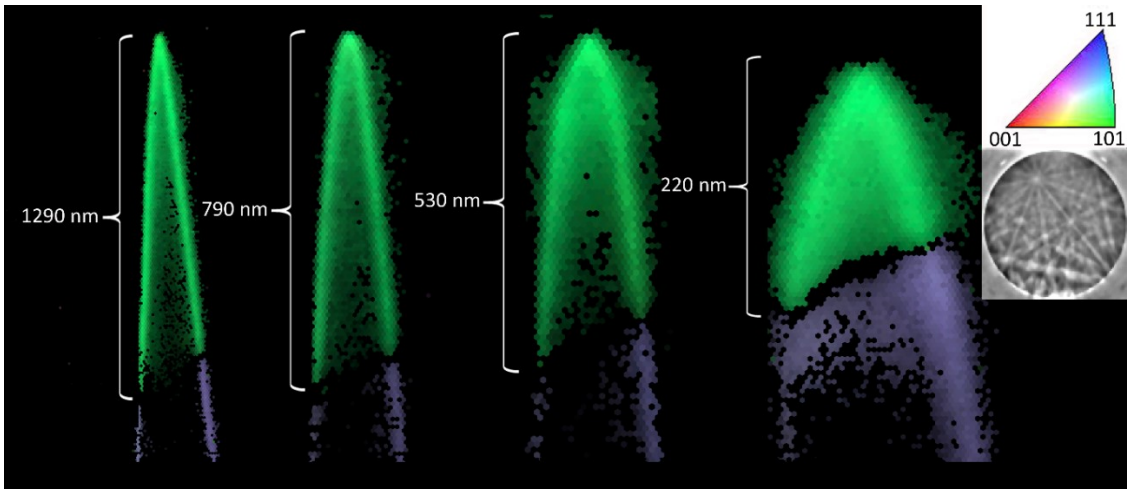

Fig. 2: The FIB/t-EBSD combined preparation process for an APT specimen with a grain boundary in the first 200 nm (IPF overlaid with IQ maps). Subsequent t-EBSD analyses in-between the annular milling procedure with the FIB are performed to give information about the location of the grain boundary (left to right). By removing material from the top of the tip the grain boundary comes closer to the apex. After the last preparation step the grain boundary is located in the first 220 nm of the APT specimen. The inset shows the IPF coloring which indicates the crystal direction perpendicular to the specimen surface facing away from the EBSD detector. The Kikuchi pattern is a typical example of the pattern quality for the preparation process of a molybdenum APT specimen.

After the last preparation step the grain boundary was located in the first 220 nm of the APT specimen. Using t-EBSD, a clear identification of the crystallography of the mapped area is possible and, therefore, an analysis of the grain boundary character. The IQ maps represent the characteristics of the crystal lattice of the specimen. In the regions close to grain boundaries, the crystal lattice is distorted [18]. Therefore, as visible in Fig. 2, close to the grain boundary some mis-indexing appears due to overlapping information from the two grains. These points have been discarded by the confidence index filter (confidence index of 0.1). The misorientation analysis indicates a grain boundary angle of 48°. Therefore, this boundary is a high-angle boundary. Note that the diffraction patterns come from the last ~20 nm of the sample, which may under/overestimate the location of the grain boundary in a 3D volume. Therefore, the final APT specimen was imaged from 4 sides (90° intervals) to estimate the grain boundary trace. The t-EBSD assisted FIB preparation process could be finished in a short period of time because the time-consuming exchange between TEM and FIB was not necessary due to the fact that the EBSD system is mounted on the same microscope. Furthermore, the tilt angle of the APT sample for the t-EBSD analyses and the annular milling procedure is identical. Additionally, the EBSD detector can remain inserted during the FIB work. All these advantages reduce the required preparation time. As

demonstrated in Fig. 2, a specimen surface tilt angle of -38° works perfectly for t-EBSD measurements.

The reconstruction of the subsequent successful APT measurement presented in Fig. 3 of the same specimen shows the grain boundary with segregants. Both analyses (t-EBSD and APT) contain a grain boundary ~220 nm away from the apex of the specimen. In the APT reconstruction the segregating elements, nitrogen (green) and phosphorus (pink) as well as molybdenum-oxide (blue) are shown in Fig. 3a.

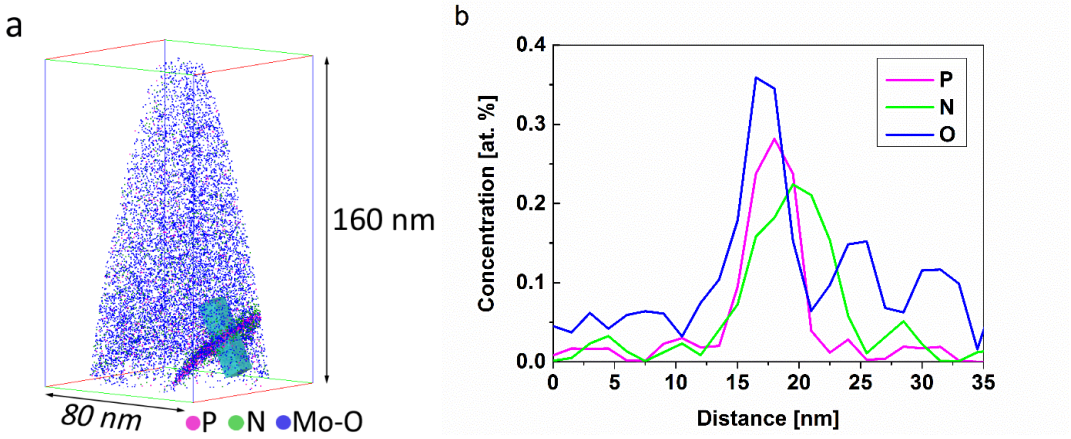

Fig. 3: (a) The reconstruction of the subsequent successful APT measurement of the FIB/t-EBSD prepared specimen. The inset shows the corresponding color code for the ions/molecules detected. The elements phosphorus (pink) and nitrogen (green) as well as the molybdenum-oxygen molecules (blue) are shown. All other elements are blanked. The region of interest for the one-dimensional concentration profile of the grain boundary is shown as a turquoise box. (b) The one-dimensional concentration profile of the region of interest marked in (a). This profile runs through the grain boundary. A higher concentration of phosphorus (pink), nitrogen (green) and oxygen (blue), which belongs to the molybdenum-oxygen molecules, is present at the grain boundary.

The one-dimensional concentration profile in Fig. 3b, which corresponds to the turquoise box in Fig. 3a, shows the concentration of nitrogen, phosphorus and molybdenum-oxide. Grain boundary segregation in the same material was already observed by the present authors [6]. In this study the same segregants were detected at the boundary.

The chemical bulk composition of the reconstructed APT specimen is presented in Table 1. The entire gallium content was implanted during the FIB preparation process. Hydrogen and oxygen are impurities in molybdenum, but may also come from the atom probe chamber. The oxygen present at the grain boundary was detected as molybdenum-oxygen molecule. Some carbon may stem from the t-EBSD measurements in the SEM [15]. In comparison, in our previous study [6] we found no carbon in the bulk composition of a specimen of sheet “1” (recrystallized stage). No t-EBSD analyses were performed in that study whereby the carbon content remained low. Tungsten is a typical impurity element in molybdenum and originates from the production process.

Table 1: Bulk composition of the measured volume (Fig. 3a) by APT of the FIB/t-EBSD prepared specimen.

Element	Content [at.%]
Mo	97.441
Ga	0.011
H	2.474
C	0.015
P	0.007
N	0.006
Ca	0.013
W	0.005
O	0.029

In this study t-EBSD was used for multiple reasons: First of all, FIB preparation and t-EBSD analyses can be done in the same microscope. Therefore, no time-consuming exchange is necessary. Additionally, any contamination through the ambient atmosphere during this exchange is prevented. Just one specimen holder is necessary. Therefore, specimen fracture or damage during re-mounting of the sample is prevented. The high resolution up to 10 nm of t-EBSD gives the opportunity to clearly identify a grain boundary or any other region of interest in the apex of an APT specimen. Crystallographic information as for example the character of grain boundaries can be easily analyzed to support the interpretation of the APT data files. Generally, t-EBSD improves the site-specific APT specimen preparation process by FIB considerably.

6.3.2 Parameter study

In previous investigations t-EBSD parameter studies for thin foils out of aluminum, aluminum alloys, steel, nickel, and niobium alloys have already been carried out [18,20,21] but cone-shaped specimens such as APT tips have not been examined so far. Therefore, the background correction procedure, the Acc. V., the tilt angle, as well as the specimen thickness were investigated in this study to optimize the set-up for further analyses using APT specimens.

In general, Kikuchi patterns are generated by transmitted forward scattered electrons which are diffracted by the lattice planes [21]. Thin foils have an almost flat surface, consequently, the background correction works similar to standard EBSD. However, APT specimens have a needle-shaped form with variable surface orientation and, thus, a static background correction is not applicable anymore. To get a good quality pattern for correct indexing, enhanced background corrections have to be selected in the data collection software. In Fig. 4 two patterns, obtained from an APT specimen in the as-deformed stage, are shown with different

enhanced background corrections. Fig. 4a represents the selection of dynamic background subtraction and normalize intensity histogram. A good pattern quality is observed and the band indexing works well. The additional selection of background division and median smoothing further improves the pattern quality and, therefore, the indexing over the whole APT tip as visible in Fig. 4b. In general, the selected enhanced background correction balances the effects of noise, poor pattern quality and differences in detector illumination due to the conical shape of the APT tips.

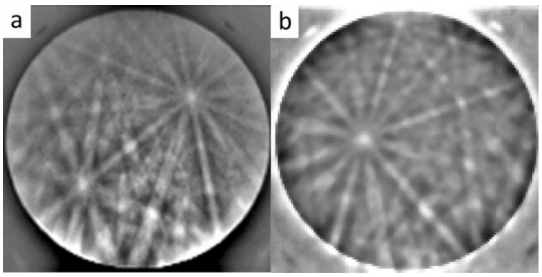

Fig. 4: Kikuchi pattern obtained from an APT specimen (as-deformed stage), (a) with enhanced background correction of dynamic background subtraction and normalize intensity histogram, (b) with additional selection of background division and median smoothing.

Furthermore, the Acc. V. of 30 kV and 20 kV for t-EBSD analyses of APT specimens were studied. Fig. 5 shows the IQ overlaid with IPF maps for an APT specimen in the as-deformed stage analyzed with 20 kV and 30 kV at a specimen surface tilt of -40°. In the apex of the needle four sub-grains are visible. Furthermore, 2.5 µm below the apex a high-angle boundary is present. The specimen was cut out of the as-deformed stage of the molybdenum sheet, therefore, many low-angle boundaries can be found in this condition. With both Acc. V. the indexing of the patterns works well according to the IQ [18]. Due to the high resolution of the t-EBSD technique also in the thinnest parts of several tenths of nanometers the formation of patterns is possible. With 30 kV also the thicker regions of the specimen can transmit electrons. As shown in Fig. 5, ~1 µm below the apex the specimen is too thick in the center to transmit electrons for an Acc. V. of 20 kV and, as consequence, no patterns are observed along the center of the specimen. At the same region Kikuchi patterns are formed by using an Acc. V. of 30 kV. In general, Fig. 5 indicates that the pattern quality is high at the edge of the needle-shaped specimens. In this region transmitted forward scattered electrons as well as backscattered electrons are assumed to be diffracted and collected by the EBSD detector. The edge is thinner than the center of the specimen due to its conical shape. The IQ overlaid with IPF maps of the specimen show clearly that an Acc. V. of 30 kV enables also an analysis of thicker parts of the conically shaped specimen. A closer analysis, as shown in Fig. 6, of the apex region of the APT specimen gives additional information about the influence of the Acc. V. at different tilt angles.

The images show the top 600 nm of an APT specimen containing four low-angle boundaries. The crystal lattice is distorted at the boundaries resulting in poor indexing of these regions [18]. The IQ overlaid with IPF maps at 30 kV have a better spatial resolution than at 20 kV. The IQ maps are brighter in case of 30 kV. This provides an important influence on the t-EBSD parameter selection for the final APT specimen preparation process.

Fig. 5: IQ overlaid with IPF maps of an APT specimen of the as-deformed stage analyzed with 20 kV and 30 kV at a specimen surface tilt of -40°. In the first 500 nm of the molybdenum tip, three low-angle boundaries are visible. At ~2.5 µm below the apex a high-angle boundary is present in the specimen. For the IPF coloring inset which indicates the crystal direction perpendicular to the specimen surface please refer to Fig. 2.

Suzuki [18] observed the same dependency for thin aluminum foils investigated by t-EBSD. The thicker the specimen the higher the Acc. V. should be. For a thickness of only several tenths of nanometers lower Acc. V. give better results. Trimby [20] confirms in his study that for thicker aluminum-alloy foils (a few hundreds of nanometers) an Acc. V. of 30 kV is suitable while for thinner regions an Acc. V. of 15 kV produce good patterns. In general, patterns collected at lower Acc. V.s are more sensitive to specimen thickness and display broader Kikuchi bands. In his investigations, the ideal sample thickness for a good t-EBSD measurement was in the range of 100 nm. He achieved a spatial resolution of 5-10 nm for nickel and around 10 nm for an aluminum alloy.

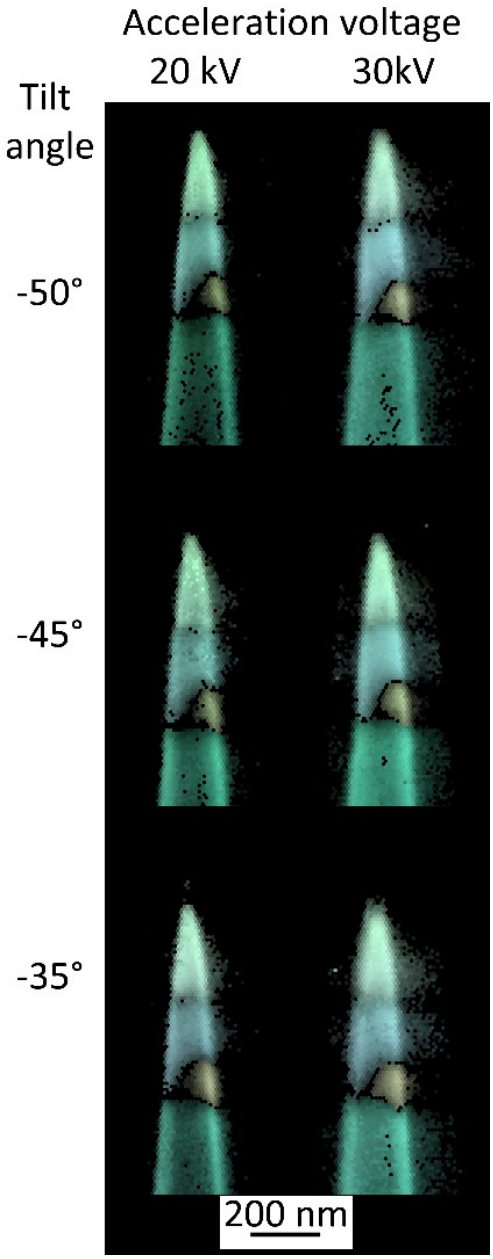

Fig. 6: Closer analysis of the t-EBSD measurements shown in Fig. 5. IQ overlaid with IPF maps of an APT specimen in the as-deformed stage analyzed with 20 kV and 30 kV at specimen surface tilt angle of -50°, -45°, and -35°. For the IPF coloring inset which indicates the crystal direction perpendicular to the specimen surface please refer to Fig. 2.

Influences of drift should be considered and may be reduced by performing fast scans or by letting the system stabilize prior to a scan. Furthermore, the contamination of carbon through the electron beam influences the subsequent APT measurements. Since the beginning of electron microscopy this kind of contamination has been a problem for all applications [15]. Due to the electron irradiation adsorbed organic molecules cross-link, which causes a contaminating film on the surface of the specimens [27–29].

Nowadays, the vacuum systems in TEM and SEM improved significantly, but the problem of contamination is not eliminated, particularly, for small scans with high resolution [29]. With decreasing electron energy the rate of contamination increases [27]. This causes a strong

influence of the carbon layer deposit by the electron beam on low voltage TEM and SEM analyses in high resolution mode. In case of APT specimens, the contamination may be a function of specimen thickness and location of the beam on the tip surface.

Furthermore, the specimen surface tilt angles of -50°, -45°, and -35° are investigated as shown in Fig. 6. All angles work well for transmission, but the best results were obtained at -35°. The brightest, and therefore best IQ maps were realized with 30 kV Acc. V. and a tilt angle of -35°. Generally, the best IQ maps were observed for -35° and for -45°. Thus, the FIB preparation is performed at -38° (stage tilt of 52° in the system) which is also a suitable tilt angle for t-EBSD measurements. This fact accelerates the preparation process because no tilting between FIB preparation and t-EBSD is necessary. The analyses shown in Figs. 5 and 6 represent clearly that Acc. V. and tilt angle as well as the specimen thickness play a significant role for the quality of t-EBSD measurements.

Also Suzukzi [18] and Brodusch et al. [21] examined the pattern quality in dependence of the tilt angle in case of thin foils. In the investigations of Suzuki [18], the spatial resolution of an thin aluminum film is higher at lower tilt angles (20° from the horizontal plane), but the indexing results are better at higher tilt angles (40° from the horizontal plane). Brodusch et al. [21] observed a good pattern quality between 20° and 40° tilt angle from the horizontal plane for a thin aluminum-silicon alloy film. Fig. 7 shows Kikuchi patterns at different tilt angles and regions (specimen thickness) of the specimen by using Acc. V. of 30 kV. As visible in Fig. 7 the pattern for all tilt angles in the upper, thin region of the tip (point 1 and 2) are sharp and clear. If the specimen surface tilt angle of the APT specimen is increased (from -35° to -50°) and the specimen gets closer to parallel to the screen plane of the EBSD detector, the pattern is shifted upwards as visible in Fig 7 (marked by black arrows). Due to the gnomonic projection [30] the bands in the upwards shifted patterns exhibit narrower widths as illustrated by the red lines in the patterns. With increasing thickness of the APT specimens for all tilt angles the contrast of the patterns decreases. In point 4 the patterns start to inverse their contrast based on scattering processes.

Suzuki [18] also observed a band contrast reversal in thicker parts of thin foils. In 1954, Alam et al. [31] noticed characteristic differences in conventional backscatter Kikuchi patterns by changing the angle of the incident electron beam. Winkelmann et al. [32] studied this phenomenon for backscattered electrons by comparing dynamic electron diffraction calculations with experimental data files of a silicon sample. He observed that the depth distribution of backscattered electrons plays a significant role in the band contrast reversal in standard EBSD configuration.

According to Winkelmann´s investigations a contrast reversal in a Kikuchi band appears when the incident angle of the electron beam is decreased. For example, electrons, which are diffracted in deeper regions observe localized inelastic scattering processes. Particularly, electrons near the center of the Kikuchi band experience increased scattering whereby a central intensity minimum and, thus, dark Kikuchi bands are created. On standard EBSD it is not visible under typical tilt angles as the electrons that have travelled deep enough to be affected will not escape anymore.

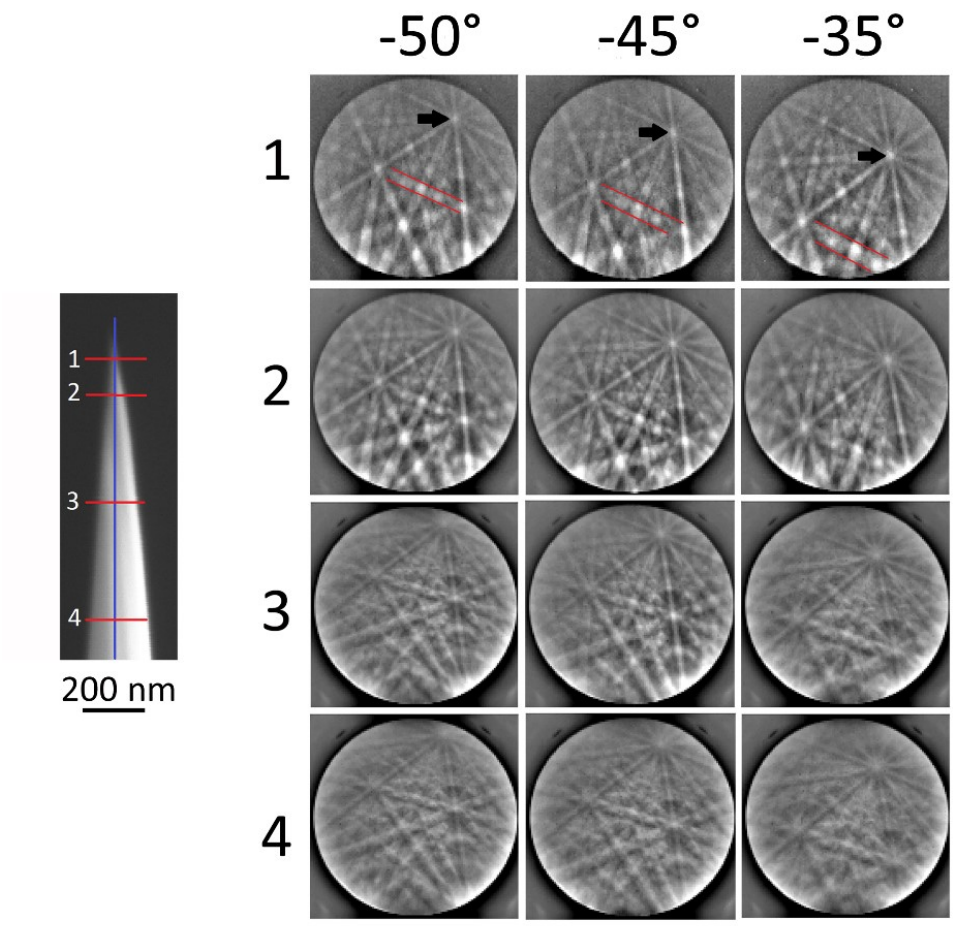

Fig. 7: Kikuchi patterns at different tilt angles and regions of an APT molybdenum specimen in the as-deformed stage (same specimen as in Figs. 5 and 6) by using an Acc. V. of 30 kV. Each intercept point of the red lines with the blue one (marked with numbers) in the left SEM image of the specimen belongs to a Kikuchi pattern with the corresponding number. If the specimen surface tilt angle of the APT specimen is increased (from -35° to -50°) and the specimen gets closer to parallel to the screen plane of the EBSD detector, the pattern is shifted upwards (marked by black arrows). Due to the gnomonic projection bands that project higher on the EBSD detector exhibit narrower widths as illustrated by the red lines in the patterns.

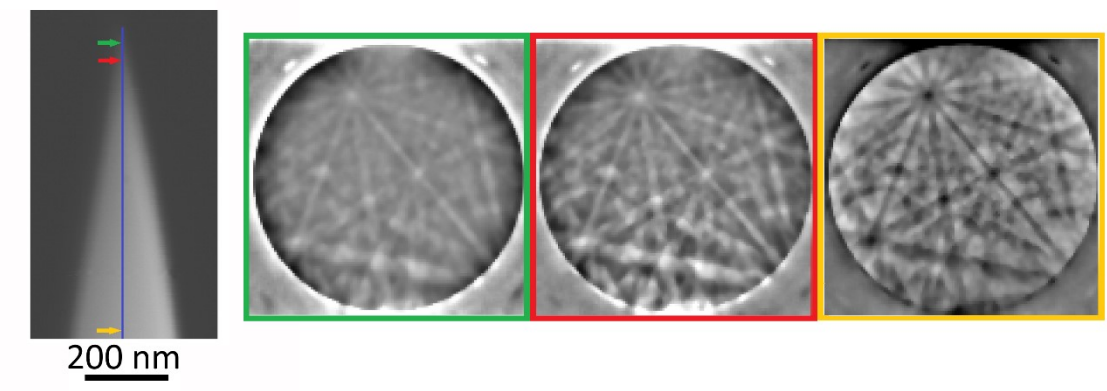

Fig. 8: Reversal of pattern contrast along the axis of an APT molybdenum specimen in the recrystallized stage observed at specimen surface tilt angle of -38° and an Acc. V. of 30 kV. Each intercept point of the colored arrows with the blue line in the left SEM image of the specimen belong to a Kikuchi pattern with the corresponding color. The three arrows indicate the points where the Kikuchi patterns were recorded. With increasing specimen radius the pattern quality improves. For lager radii, marked by the yellow arrow the pattern, contrast reverses due to the additional scattering processes.

The same processes occur during t-EBSD measurements. In thicker parts of the specimen the electrons are additionally scattered by atoms located along the travel direction. Especially electrons near to the center of the Kikuchi band experience increased scattering resulting in inverse, dark Kikuchi bands. Fig. 8 represents the reversal of pattern contrast along the axis of an APT specimen in the recrystallized stage.

The three arrows indicate the points where the Kikuchi patterns were recorded with an Acc. V. of 30 kV. At the apex of the APT specimen (green arrow), where the thickness is only several tenths of nanometers, the pattern contrast and sharpness is poor. With increasing specimen radius the pattern quality improves. Suzuki [18] observed that high Acc. V.s do not really work for very thin parts of TEM foils. At the measurement point with the red arrow the Kikuchi pattern is sharp and has a good contrast. For larger radii, marked by the yellow arrow in Fig. 8 the pattern contrast reverses due to the additional scattering processes. Crystallographically, the inverted patterns contain the same information as normal Kikuchi patterns.

In the standard EBSD software, however, bright peaks in the Hough transform are used for the indexing of the bands. Therefore, the inverted contrasts bands are not indexed correctly resulting in errors of a few degrees in crystal orientation [18]. Fig. 9 represents the problem for APT specimens with pattern contrast reversal in the center.

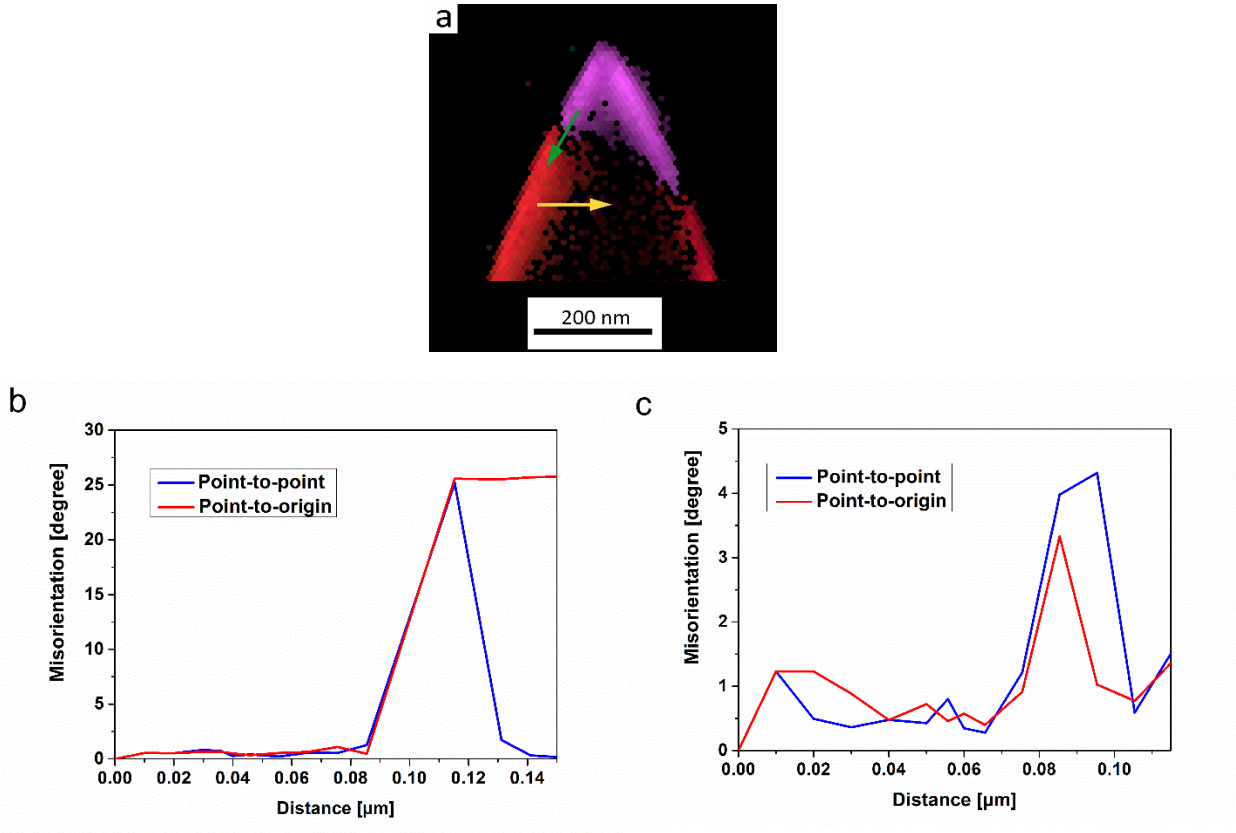

Fig. 9: The indexing problem for APT specimens with pattern contrast reversal in the center. (a) IQ overlaid with IPF map of an APT molybdenum specimen in the recrystallized stage analyzed with 30 kV at a specimen surface tilt angle of -50°. For the IPF coloring inset which indicates the crystal direction perpendicular to the specimen surface please refer to Fig. 2. The arrows indicate the measuring direction for the misorientation (b) between two grains (green arrow) and (c) inside one grain (yellow arrow). In thicker parts the patterns at the edges are correctly indexed, but in the center region, where inverse patterns appear, poor indexing results in a misorientation artifact of ~3° within one grain.

In thicker regions of the specimen the patterns at the edges are correctly indexed but in the center region where inverse patterns appear poor indexing results in a misorientation artifact within one grain. This should be considered for further analyses of the grain boundary character in the EBSD software. All orientation analyses should be carried out at the edges of a tip as visible in Fig. 9. Correct indexing leads to accurate results of the orientation difference between two grains. The angle of the grain boundary shown in Fig. 9 is ~24°, therefore, it represents a high-angle boundary.

Fig. 10 shows the Kikuchi pattern at radial position for a thickness of ~200 nm. At a radius of ~100 nm the molybdenum specimen is thin enough to avoid the contrast reversal. However, the conical shape of the specimen leads to blurred patterns at the edges. These blurred patterns further complicate indexing at the edges of the APT tip.

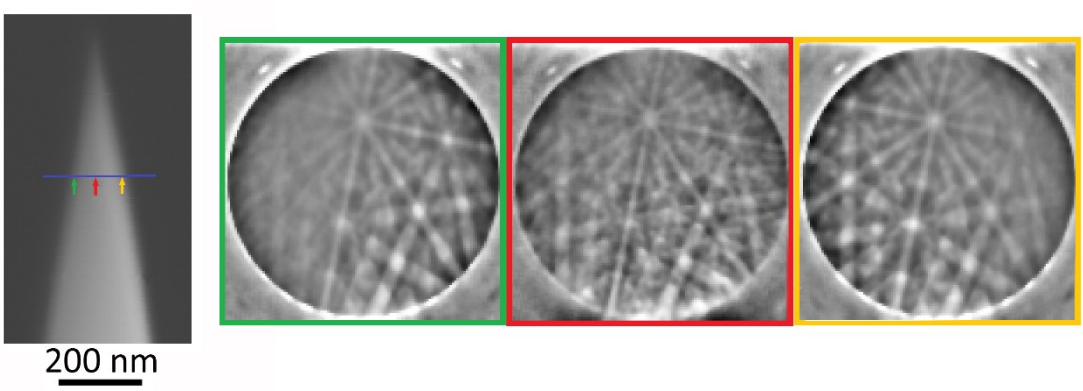

Fig. 10: Kikuchi pattern at radial position for a thickness of ~200 nm of an APT molybdenum specimen in the recrystallized stage at -38° and 30 kV. Each intercept point of the colored arrows with the blue line in the left SEM images of the specimen belong to a Kikuchi pattern with the corresponding color. The conical shape of the specimen leads to blurred patterns at the edges.

Concerning this parameter study all further t-EBSD analyses should be carried out at an Acc. V. of 30 kV at specimen surface tilt angles between -45° and -35° from horizontal plane (stage tilt of 45° and 55° in the system) which gives good patterns. Because FIB preparation is performed at specimen surface tilt of -38° (stage tilt of 52°) in the microscope, which also gives good t-EBSD patterns, this angle should be chosen for all further t-EBSD analyses.

6.4 Summary and Outlook

t-EBSD is a new powerful tool to improve the site-specific preparation of APT specimens by FIB with special regions of interest as, for example, grain boundaries. In this study the annular milling FIB procedure was supported by subsequent t-EBSD analyses for the clear identification of the location of a grain boundary in the APT tip of technically pure molybdenum. By applying annular milling and t-EBSD analyses the grain boundary could be easily positioned in the first 200 nm of the sample for a further APT measurement. Even more, crystallographic information of the mapped area and, therefore, an analysis of the grain boundary character were obtained by t-EBSD to support the interpretation of the APT data files. The t-EBSD parameter study of enhanced background correction, Acc. V., tilt angle and specimen thickness was carried out to optimize the new developed technique for further APT specimen preparation of region of interests.

Even if t-EBSD has only been applied to study ultrafine-grained materials as well as precipitates by using thin foils so far [22,23,25,33] this technique is a promising strong tool for investigations of APT specimens. The preparation process of grain boundaries or other regions of interest in the FIB for APT analysis can be substantially improved. Crystallographic information of the APT specimens can be determined quickly and easily instead of using time-consuming TEM analyses. The high resolution up to 5-10 nm gives the opportunity of a site-specific preparation and identification of grain boundaries as well as small phases, e.g.

residual austenite films [34] or precipitates [35]. Even for molybdenum, a metal with atomic number of 42, the observation of crystal orientation data up to about 200 nm specimen thickness with at Acc. of 30 kV is possible. Furthermore, high pressure torsion samples can be investigated by t-EBSD as a complementary technique prior to an APT measurement. The crystallographic information achieved by t-EBSD supports the reconstruction of the APT data files. Generally, this new technique gives good results, however, the minimization of carbon contamination is still a challenge. Further studies will be necessary to reduce this problem.

Acknowledgements

Thanks to Dr. Stefan Wurster from the Chair of Materials Physics of the Montanuniversität Leoben for his scientific and technical input as wells as for his support during running the t-EBSD analyses on APT specimens. Furthermore, the authors are grateful to Dr. Wolfram Knabl and Dr. Alexander Lorich from Plansee SE for providing the sample material for the analyses.

References

[1] M.K. Miller, R.G. Forbes, Atom probe tomography, Mater. Charact. 60 (2009) 461–469.

[2] M.K. Miller, The development of atom probe field-ion microscopy, Mater. Charact. 44 (2000) 11–27.

[3] M.K. Miller, T.F. Kelly, K. Rajan, S.P. Ringer, The future of atom probe tomography, Mater. Today. 15 (2012) 158–165.

[4] T.F. Kelly, M.K. Miller, Invited review article: Atom probe tomography, Rev. Sci. Instrum. 78 (2007) 031101–1–20.

[5] M. Miller, A. Bryhan, Effect of Zr, B and C additions on the ductility of molybdenum, Mater. Sci. Eng. A. 327 (2002) 80–83.

[6] K. Babinsky, J. Weidow, W. Knabl, A. Lorich, H. Leitner, S. Primig, Atom probe study of grain boundary segregation in technically pure molybdenum, Mater. Charact. 87 (2014) 95–103.

[7] A. Cerezo, P.H. Clifton, M.J. Galtrey, C.J. Humphreys, T.F. Kelly, D.J. Larson, et al., Atom probe tomography today, Mater. Today. 10 (2007) 36–42.

[8] P.R. Munroe, The application of focused ion beam microscopy in the material sciences, Mater. Charact. 60 (2009) 2–13.

[9] M.K. Miller, K.F. Russell, G.B. Thompson, Strategies for fabricating atom probe specimens with a dual beam FIB, Ultramicroscopy. 102 (2005) 287–298.

[10] P. Felfer, S.P. Ringer, J.M. Cairney, Shaping the lens of the atom probe: fabrication of site specific, oriented specimens and application to grain boundary analysis., Ultramicroscopy. 111 (2011) 435–439.

[11] F. Pérez-Willard, D. Wolde-Giorgis, T. Al-Kassab, G. a López, E.J. Mittemeijer, R. Kirchheim, et al., Focused ion beam preparation of atom probe specimens containing a single crystallographically well-defined grain boundary., Micron. 39 (2008) 45–52.

[12] J.M. Cairney, D.W. Saxey, D. McGrouther, S.P. Ringer, Site-specific specimen preparation for atom probe tomography of grain boundaries, Phys. B. 394 (2007) 267–269.

[13] J. Weidow, H.-O. Andrén, Grain and phase boundary segregation in WC–Co with small V, Cr or Mn additions, Acta Mater. 58 (2010) 3888–3894.

[14] J. Weidow, H.-O. Andrén, Grain and phase boundary segregation in WC–Co with TiC, ZrC, NbC or TaC additions, Int. J. Refract. Met. Hard Mater. 29 (2011) 38–43.

[15] M. Postek, An approach to the reduction of hydrocarbon contamination in the scanning electron microscope, Scanning. 18 (1996) 269–274.

[16] G. Sha, L. Yao, X. Liao, S.P. Ringer, Z. Chao Duan, T.G. Langdon, Segregation of solute elements at grain boundaries in an ultrafine grained Al-Zn-Mg-Cu alloy., Ultramicroscopy. 111 (2011) 500–5.

[17] L. Yao, M.P. Moody, J.M. Cairney, D. Haley, a V Ceguerra, C. Zhu, et al., Crystallographic structural analysis in atom probe microscopy via 3D Hough transformation., Ultramicroscopy. 111 (2011) 458–63.

[18] S. Suzuki, Features of transmission EBSD and its application, JOM. 65 (2013) 1254–1263.

[19] R.R. Keller, R.H. Geiss, Transmission EBSD from 10 nm domains in a scanning electron microscope, J. Microsc. 245 (2012) 245–251.

[20] P.W. Trimby, Orientation mapping of nanostructured materials using transmission Kikuchi diffraction in the scanning electron microscope., Ultramicroscopy. 120 (2012) 16–24.

[21] N. Brodusch, H. Demers, M. Trudeau, R. Gauvin, Acquisition parameters optimization of a transmission electron forward scatter diffraction system in a cold-field emission scanning electron microscope for nanomaterials Characterization., Scanning. 9999 (2013) 1–12.

[22] J.L. Sun, P.W. Trimby, X. Si, X.Z. Liao, N.R. Tao, J.T. Wang, Nano twins in ultrafine-grained Ti processed by dynamic plastic deformation, Scr. Mater. 68 (2013) 475–478.

[23] P.W. Trimby, Y. Cao, Z. Chen, S. Han, K.J. Hemker, J. Lian, et al., Characterizing deformed ultrafine-grained and nanocrystalline materials using transmission Kikuchi diffraction in a scanning electron microscope, Acta Mater. 62 (2014) 69–80.

[24] J. Kacher, P. Elizaga, S.D. House, K. Hattar, M. Nowell, I.M. Robertson, Thermal stability of Ni/NiO multilayers, Mater. Sci. Eng. A. 568 (2013) 49–60.

[25] N. Brodusch, H. Demers, R. Gauvin, Nanometres-resolution Kikuchi patterns from materials science specimens with transmission electron forward scatter diffraction in the scanning electron microscope., J. Microsc. 250 (2013) 1–14.

[26] M.K. Miller, A. Cerezo, M.G. Hetherington, G.D.W. Smith, Atom probe field ion microscopy, Clarendon Press, Oxford, 1996.

[27] P. Hirsch, M. Kässens, M. Püttmann, L. Reimer, Contamination in a scanning electron microscope and the influence of specimen cooling, Scanning. 16 (2008) 101–110.

[28] A.J.V. Griffiths, T. Walther, Quantification of carbon contamination under electron beam irradiation in a scanning transmission electron microscope and its suppression by plasma cleaning, J. Phys. Conf. Ser. 241 (2010) 012017.

[29] R.F. Egerton, P. Li, M. Malac, Radiation damage in the TEM and SEM., Micron. 35 (2004) 399–409.

[30] K.Z. Baba-Kishi, Measurement of crystal parameters on backscatter Kikuchi diffraction patterns, Scanning. 20 (2006) 117–127.

[31] M.N. Alam, M. Blackman, D.W. Pashley, High-angle Kikuchi patterns, Proc. R. Soc. A Math. Phys. Eng. Sci. 221 (1954) 224–242.

[32] A. Winkelmann, G. Nolze, Analysis of Kikuchi band contrast reversal in electron backscatter diffraction patterns of silicon., Ultramicroscopy. 110 (2010) 190–4.

[33] J.L. Sun, P.W. Trimby, F.K. Yan, X.Z. Liao, N.R. Tao, J.T. Wang, Grain size effect on deformation twinning propensity in ultrafine-grained hexagonal close-packed titanium, Scr. Mater. 69 (2013) 428–431.

[34] C. Lerchbacher, S. Zinner, H. Leitner, Atom probe study of the carbon distribution in a hardened martensitic hot-work tool steel X38CrMoV5-1, Micron. 43 (2012) 818–826.

[35] M. Nöhrer, S. Zamberger, S. Primig, H. Leitner, Atom probe study of vanadium interphase precipitates and randomly distributed vanadium precipitates in ferrite, Micron. 54 (2013) 57–64.

7 Publication B

Correlating atom probe crystallography measurements with transmission Kikuchi diffraction data

A.J. Breen[1], K. Babinsky[2], A.C. Day1, K. Eder[1], C.J. Oakman[1], P.W. Trimby[1], S. Primig[3], J.M. Cairney[1], S.P. Ringer[1,4]

1 Australian Centre for Microscopy and Microanalysis, and School of Aerospace, Mechanical and Mechatronic Engineering, The University of Sydney, NSW 2006, Australia

2 Department of Physical Metallurgy and Materials Testing, Montanuniversität Leoben, Franz-Josef Straße 18, 8700 Leoben, Austria

3 School of Materials Science and Engineering, The University of New South Wales, Sydney, NSW 2052, Australia

4 Australian Institute for Nanoscale Science and Technology, and School of Aerospace, Mechanical and Mechatronic Engineering, The University of Sydney, Australia 2006.

Abstract:

Correlative microscopy techniques offer a synergistic approach to many research problems. One such combination that has been studied in limited detail is the use of atom probe tomography (APT) and transmission Kikuchi diffraction (TKD) on the same tip specimen. From combining these two powerful microscopy techniques, the microstructure of important engineering alloys can be studied in greater detail. For the first time, the accuracy of crystallographic measurements made using APT will be independently verified using TKD. Experimental data from two atom probe tips, one a nanocrystalline Al-0.5Ag alloy specimen collected on a straight flight path atom probe and the other a high purity Mo specimen collected on a reflectron fitted instrument, will be compared. We find that the average minimum misorientation angle, calculated from calibrated atom probe reconstructions with two different pole combinations, deviate 0.7° and 1.4° respectively from the TKD results. The type of atom probe and experimental conditions appear to have some impact on this accuracy and the reconstruction and measurement procedures are likely to contribute further to degradation in angular resolution. The challenges and implications of this correlative approach will also be discussed.

7.1 Introduction

Atom probe tomography (APT) enables the position and chemical identity of millions of individual atoms to be reconstructed in 3D and has one of the highest analytical spatial resolutions of any microanalysis technique currently available [1]. It is therefore ideal for looking at the 3D nanostructure of materials such as studying the chemistry and topography of individual interfaces [2–4]. A small, needle shaped specimen with an end-tip radius of less than 100 nm is held at cryogenic temperatures and is exposed to a standing voltage and additional voltage or laser pulse to enable the evaporation of individual ions from the surface of the tip towards a position sensitive detector. The recorded time-of flight permits the mass-to-charge ratio of each ion to be calculated whereas the detected co-ordinates and the sequence of evaporation enable the original ion positions to be reconstructed in 3D through a back projection algorithm.

The spatial resolution is sometimes high enough so that individual lattice planes within crystalline materials can be detected. This has enabled the emergence of atom probe crystallography studies [5–7] which facilitates calibration of the reconstruction and advanced reconstruction approaches such as lattice rectification [8–10] as well as the opportunity to fully define the crystallographic nature of individual grain boundaries and compare this directly to interfacial chemistry [11,12]. It is possible to conduct chemico-textural orientation mapping at resolutions otherwise not available [13,14]. However, there remains significant limitations and challenges with this avenue of APT analysis. Currently it is difficult to do the required calculations on commercially available software and therefore usually requires the user to have some programming experience. Crystallographic information can often be difficult to detect depending on the type of material being analyzed and the experimental conditions being used. There has also never been any verification from an independent technique to assess the accuracy of the crystallographic measurements being made.

Transmission Kikuchi Diffraction (TKD) in the scanning electron microscope (SEM) [15,16] offers a fast and convenient means of collecting complementary crystallographic information on atom probe specimens. Also known as transmission electron back-scattered diffraction (t-EBSD), it offers significant improvements to lateral spatial resolution compared to conventional EBSD. The technique works by passing the primary electron beam through the sample and analyzing the transmitted diffracted electrons on a standard EBSD detector. The lateral spatial resolution depends on a combination of experimental parameters including sample thickness, step size, and beam spot size but is typically less than 10 nm [16] and small enough to observe changes in crystallographic texture in nanocrystalline materials. The angular resolution is similar to that of conventional EBSD and dependent on the parameters used for pattern indexing as well as the pixel resolution used for pattern binning and is typically ~0.5° using standard Hough-transform based indexing [17,18]. For the results

shown in this manuscript it was measured to be ~0.3° after solution refinement techniques were used in the commercial software.

The technique is conveniently suited to atom probe specimens for a number of reasons. Optimal sample thickness for TKD in the SEM primarily depends on beam energy and the material being analyzed but is typically in the range of 100 nm, similar to the thickness of the end of an atom probe tip. It is also common to use a dual beam SEM/Focused Ion Beam (FIB) for atom probe sample preparation and many of these instruments have an EBSD detector already installed so TKD can often be done without any additional transporting of the sample. The time it takes to do the additional TKD experiments depends on the step size, size of the specimen and pixel resolution used for pattern binning but multiple orientation maps of high quality are achievable within a single session on the microscope.

It is important to point out that TKD is currently a 2D technique - the orientation maps produced are representative of the bottom ~10 – 20 nm of the specimen relative to the detector depending on the material [19]. In one respect, this is a great advantage and what enables such clear texture to be observed in the first place at the nm scale. On the other hand, the information provided does not fully define the grain morphology in 3D nor the complete crystallographic nature of individual interfaces such as the boundary planes. However, when combined with APT, it becomes possible for very accurate and complete crystallographic analysis of individual grains in 3D.

Several authors have recently reported combining APT experiments with complementary crystallographic information from other techniques. TKD has been used to facilitate site specific FIB based sample preparation of individual interfaces in atom probe samples [19,20]. Recently, nanobeam diffraction (NBD) in the transmission electron microscope (TEM), was used for complementary crystallographic information on a cold-drawn pearlite atom probe tip [21]. Another study involving the in situ determination of the misorienation angle of a grain boundary using complementary field ion microscopy (FIM) was also reported by [22]. Here we extend these studies by directly comparing misorientation measurements between TKD and state-of-the-art APT crystallography measurements on the same specimen in order to gain insight into the angular resolution currently achievable for APT. Additionally, crystallographic measurements made on straight flight path atom probes are compared to those on reflectron fitted instruments. A reflection, while dramatically improving mass resolution of the technique, has also been suspected of degrading the spatial resolution and reconstruction accuracy due to complications in reconstructing the curved ion trajectories. The following study will investigate this theory. TKD offers a fast and convenient way to guide crystallographic measurements made directly on APT reconstructions.

7.2 Materials and methods

To initiate the study, a sample that was easy to prepare, had a high chance of running successfully in the atom probe, was likely to have clear crystallographic information from both APT and TKD and numerous grains within the first several nm of an atom probe tip was desired. A nanocrystalline Al-0.5Ag with Si impurities that was severely plastically deformed through high pressure torsion (HPT) satisfied these requirements and was chosen for the experiments on the straight flight-path instrument.

In contrast, the technically pure Mo was selected as a more challenging specimen for comparison purposes and was used for the reflectron-fitted atom probe experiments. A different specimen preparation method was required (because the grain size was much larger) and less crystallographic signal was present in the APT data. It allowed some insight into the robustness of the study being performed. For additional information on the technically pure Mo, including composition and processing conditions the reader is directed to [23,24].

7.2.1 Nanocrystalline Al-0.5Ag sample preparation and data acquisition

The needle shaped specimen of the nanocrystalline Al-0.5Ag with Si impurities was prepared using the standard 2-stage electropolishing technique with the universal electrolytes [1]. The grain size was small enough so that there was a high chance to capture multiple grain boundaries within a specimen prepared this way. The sample was then loaded into a Zeiss® Ultra® Plus equipped with an Oxford Instruments® Aztec® EBSD system (version 3.0) and Nordlys® Nano detector for TKD mapping. Prior to acquisition, the chamber and sample were plasma cleaned using an Evactron Plasma cleaner for approximately 1 minute using room air. The sample was then tilted by 20° to obtain a horizontal orientation. The step size of the maps was chosen to be 10 nm, with a pattern resolution of 168x128 pixels (8x8 binned from full resolution), and an acquisition speed of 67 points per second. The accelerating voltage was 30 kV and current was ~15 nA. TKD maps were taken over a range of projections (0°, 90°, 180° and 270°) by manually rotating the sample in the holder and analyzed using the Oxford Instruments® HKL® software.

The same sample was then loaded into a CAMECA® LEAP® 4000X Si atom probe, which has a straight flight path design. Data was collected at 40 K using voltage pulsing (20% pulse fraction, 2000 Hz, 0.5% evaporation rate). Data was reconstructed using the commercially available IVAS software. The mass spectrum and corresponding ranging can be found in the supplementary material. A reconstruction calibration protocol described by [25], was also performed to ensure spatial integrity of the tomogram as well accuracy in the subsequent crystallographic measurements. To mitigate changes in the image compression factor (ICF) and field factor (kf), which are known to occur throughout the experiment [26], crystallographic calibration was performed within a ~ 1 million atom slice in z, where crystallography was approximately constant. Any subsequent crystallographic measurements

were taken from this region. To determine the effect of crystallographic calibration on the accuracy of the misorientation measurements, a reconstruction that was not calibrated was also used for comparison. MATLAB® was then used to further analyze the crystallographic information in the detector hit maps and reconstruction from within the epos (extended pos) file that can be generated from IVAS®.

7.2.2 Technically pure Mo sample preparation and data acquisition

The technically pure Mo had a much larger grain size so samples were instead prepared using electropolishing as well as additional sharpening via a correlative TKD and focused ion beam (FIB) annular milling procedure, to ensure a grain boundary was positioned close to the apex of the specimen [19]. An FEI® Versa® 3D DualBeam® (FIB/SEM) workstation equipped with an EDAX® Hikari® XP EBSD system was used for this part of the study. The TKD mapping conditions were very similar to those used on the previous sample. An accelerating voltage of 30 kV and current of 11 nA were used. The diffraction pattern resolution was 160x120 pixels with 4x4 binning from full resolution enabling an acquisition speed of 40 frames/sec. A 10 nm step size was used. TKD maps for a series of projections (0°, 90°, 180° and 270°) were again taken. The EDAX® OIM® Analysis 7 software was then used for the analysis of the EBSD data files.

The sample was then loaded into a CAMECA® LEAP® 3000X HR atom probe, which has a reflectron design. A specimen temperature of 60 K, target evaporation rate of 1% and laser pulsing using a green laser (λ = 532 nm) with 0.6 nJ laser energy at 250 kHz pulse frequency were used during experimental acquisition. The conditions used were to help with specimen success rate but are not ideal for the observation of crystallographic information. The data collected was subsequently reconstructed using IVAS® and calibrated similarly with one notable difference being the use of a 40 mm virtual flight path length, rather than the physical 382 mm. This was found to be a better representation of the flight displacement along the z-direction from detector to specimen apex, and offered improved convergence of calibration metrics. It was difficult to get enough crystallographic information to determine misorientation between the two grains contained within the reconstruction from a single ~1 million atom z-slice, so instead, two different regions, each containing enough information about one of the grains, were calibrated instead. The calibration parameters were then averaged across the whole reconstruction before misorientation measurements were taken. A non-calibrated reconstruction was also used for comparison. The resultant epos file was again used for subsequent crystallographic analysis using MATLAB®. The mass spectrum and corresponding ranging can be found in the supplementary material.

7.3 Results

The results from TKD and atom probe crystallographic measurements are presented for each material and atom probe design. Mapping the grain orientation relative to the detector and measuring the associated misorientation between grains is highly automated for the TKD analysis using the commercially available EBSD software. However, making misorientation measurements in atom probe reconstructions remains a very manual process, which has only been discussed in limited detail previously, so some attention is given here to the procedure undertaken.

7.3.1 Straight flight path atom probe analyses vs. TKD misorientation measurements

Fig. 1a shows the calibrated tomographic reconstruction (ICF = 1.63, kf = 4, ε = 0.57, L = 90 mm) and associated crystallographic measurements of the nanocrystalline Al-0.5Ag with Si impurities. The Si impurities, as well as density fluctuations in the reconstruction, highlight the captured grain boundary. A ~1 million atom slice has been taken out of the center of the reconstruction that, when viewed along the z-projection, clearly shows zone line and poles (Fig. 1b). By comparing this to a stereographic projection of the crystal structure of Al, the Miller indices corresponding to each pole can be determined.

A plane orientation extraction algorithm (POE), as described previously [31], has been used to very precisely determine the normal to the sets of planes detected within these pole regions of the reconstruction (Figs. 1c-f). The algorithm works by producing a 1D spatial distribution map (SDM) along a range of different directions in 3D. A 1D SDM is a histogram of atomic distances along a particular directional component within a given region of interest (ROI). A fast Fourier transform (FFT) is then applied to each SDM and the signal intensity is plotted over the range of directions, expressed in polar angles. The highest signal corresponds to the normal to the sets of detected planes. A clear maximum could be observed for all families of planes. Finally, the SDMs corresponding to the maximums in each pole region are provided, the peak-to-peak distance of which should be close to the actual plane spacings in the analyzed sample.

This information can then be used to determine the orientation of each grain relative to the detector and further, the misorientation between each of the grains.

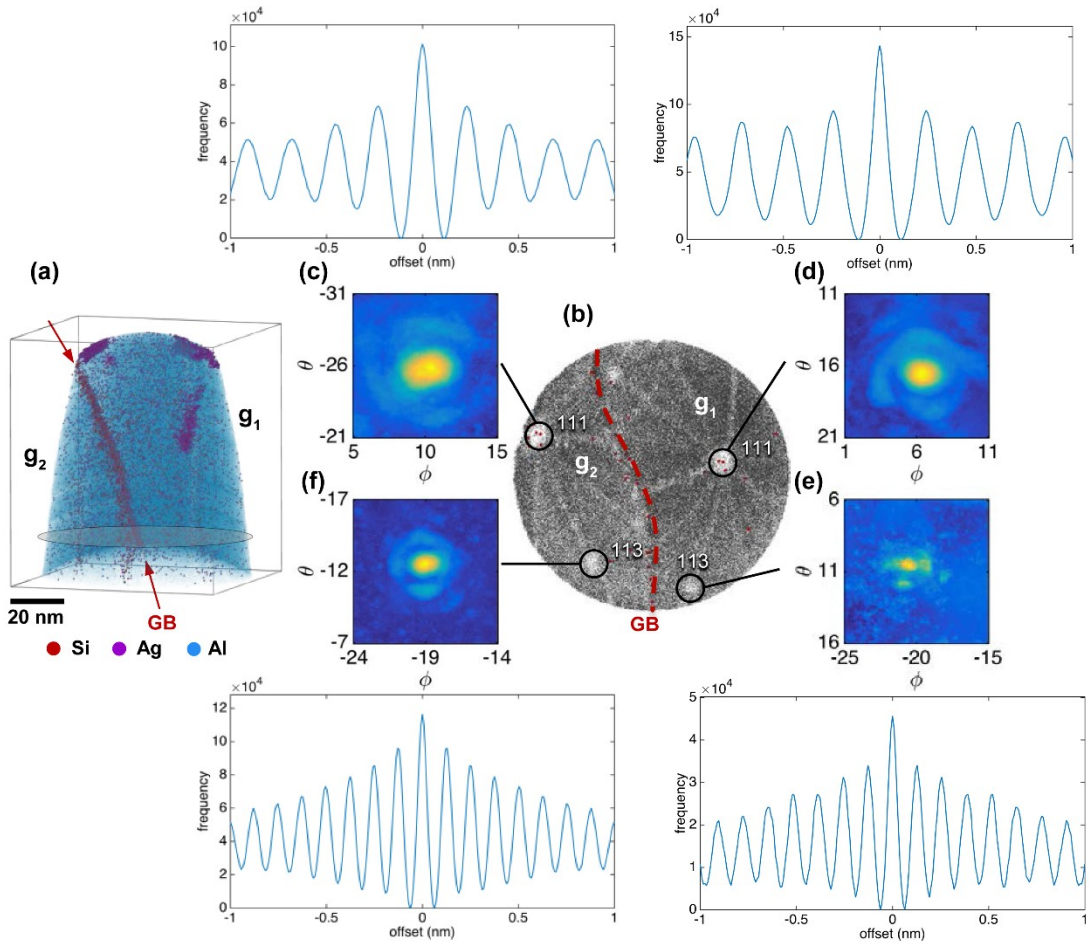

Fig. 1: (a) Nanocrystalline Al-0.5Ag atom probe reconstruction; (b) ~ 1 million atom slice from the region of interest marked in (a) showing grain boundary and indexed pole information in each grain, (c)-(f) the POE and SDM results from each indexed pole.

The polar angles can be converted to Cartesian unit vectors within the specimen frame using the following sets of equations:

$$\begin{aligned} x &= -\sin\theta \\ y &= \sin\phi\cos\theta \\ z &= \cos\phi\cos\theta \end{aligned} \tag{1}$$

It should be noted that the convention used here, and throughout the manuscript, is that previously defined by [6] which differs from the typical spherical co-ordinates definition.
The orientation matrix of each grain is defined using the following equation:

$$C_c = g \cdot C_s \tag{2}$$

Where C_c and C_s are the crystal frame and specimen frame respectively and g is the orientation matrix. g can be thought of as the rotation required to get the directions in C_s aligned with C_c. However, since there are slight errors in the measured orientation of directions in the C_s frame, due to inaccuracies in the tomographic reconstruction, C_s must be calibrated first. To do this, a new set of C_s directions were fitted to those measured within the reconstruction using two restraints:

1. The angles between the fitted directions are equal to the theoretical angles between those crystallographic directions.
2. The residual sum of squares (RSS) of the angles (ϕ) between the measured and fitted directions in the C_s frame was minimized.

$$RSS = \sum_{i=1}^{n} \varphi_i^2 \quad (3)$$

Where n is the number of directions identified within the atom probe reconstruction and used in the calculation, typically n=3 was used for the results in this manuscript. Such a calculation can be performed using the solver function in software such as Microsoft Excel® or MATLAB®. The misorientation, i.e. the transformation necessary to rotate from one crystal orientation to the next, can then be calculated as:

$$M_{12} = g_1 g_2^{-1} \quad (4)$$

To determine the minimum misorientation, or disorientation, between the grains, all orientation variants of one of the grains must be considered. These variants can be found in texture and crystallographic texts such as [27]. For a cubic system, 24 orientation variants exist. The minimum misorientation angle, i.e., the grain boundary angle, can be calculated from the following equation:

$$\theta = min \left| cos^{-1} \left\{ \frac{tr(M_{12}) - 1}{2} \right\} \right| \quad (5)$$

The misorientation axis is the real eigenvector of M12, a 3x1 column vector x, corresponding to the real eigenvalue λ :

$$M_{12}x = \lambda x \quad (6)$$

A worked example for calculating the disorientation between the grains in the nanocrystalline Al-0.5Ag atom probe reconstruction shown in Fig. 1 is provided in the supplementary material. For more information regarding the mathematics of texture analysis the reader is referred to [27].

To further correlate the TKD and APT results, 3D orientation mapping of the APT reconstruction was performed using MATLAB®. Due to the strong segregation of the Si impurities to the interface, filtering based on a nearest neighbour (NN) distribution of the Si atoms could be used to define the grain boundary surface. Si-Si 50NN ≤ 9 nm was found to work well (Fig. 2a,b). Additional filtering using a 3D point selection tool enabled removal of any remaining atoms not belonging to the interface. Atoms on either side of the boundary were then defined. A boundary hull of each grain was 3D rendered and coloured according to the vertical crystallographic direction relative to the detector using the inverse pole figure (IPF) notation (Fig. 2c).

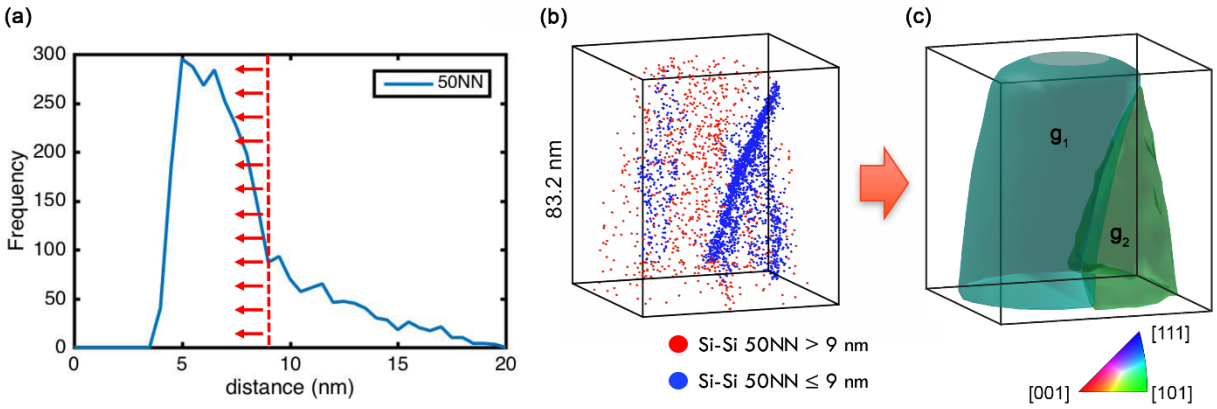

Fig. 2: (a) Si-Si 50NN histogram, (b) Si-Si 50 NN ≤ 9 nm is used to filter out atoms at interface and define boundary. (c) The interface and boundary atoms of reconstruction are used to define hulls of each grain colored according to the vertical crystallographic orientation.

A comparison of the TKD and APT orientation maps is shown in Fig. 3. TKD maps are shown at 4 different projections at ~90° intervals in Fig. 3a, the red box on the final map indicates the approximate region of the corresponding APT reconstruction. Grains in the TKD maps were colored according to the crystallographic direction in the vertical direction, i.e. the direction close to the vertical axis of the tip, so that the coloring would be similar to that observed in the APT orientation maps. The relative crystal orientation of each grain is also provided. The corresponding 3D orientation maps of the APT reconstruction are shown in Fig. 3b at 4 projections also at ~ 90° intervals, and a clear correlation between the crystallographic information for the two techniques can be obtained. Fig. 3c is a 1D concentration profile of the impurity species along the direction approximately normal to the grain boundary, which was measured from the APT reconstruction. It has been included to demonstrate how the chemical information contained within the APT data can be compared directly to the crystallographic information for precise chemical and structural analysis of grain boundaries in these materials.

A summary of the measurements from each technique is given in Table 1. From the TKD results, the average orientation of each grain was calculated using the HKL® software and the minimum misorientation between the two grains was measured. From the APT data, three separate measurements of the same grain boundary are given. The first one is for the calibrated reconstruction. The second is a measurement using the default or non-calibrated IVAS® reconstruction parameters and same pole selection. The third measurement is for the calibrated reconstruction using a different selection of poles. The average minimum misorientation angle/axis pair calculated from the calibrated reconstruction with different pole selections, is 40.7°/[0.045 0.198 0.979]. The misorientation angle and axis deviate 0.7° and 2.6° respectively from the TKD results.

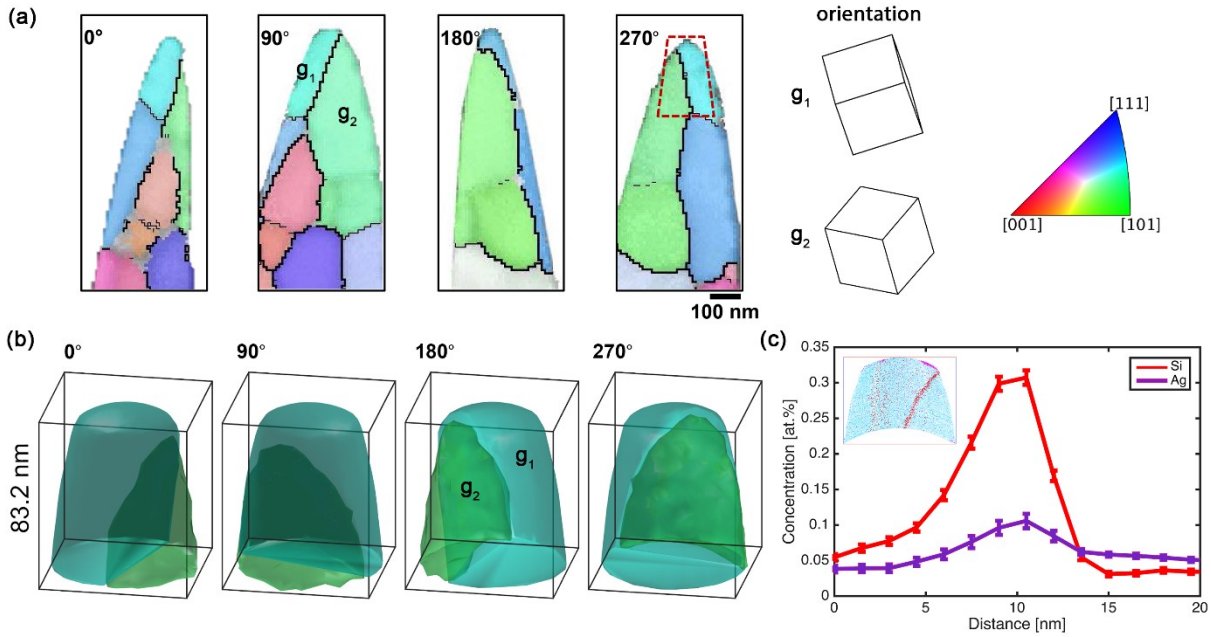

Fig. 3: (a) TKD maps of the Al-0.5Ag sample at 4 different projections; (b) 3D orientation maps of APT reconstruction; (c) 1D concentration profile perpendicular to grain boundary (shown in insert).

Table 1: Misorientation measurements of Al-0.5Ag: TKD vs. APT (straight flight path). Three different APT measurements of the same grain boundary are provided varying reconstruction parameters and pole selection.

	Calibration parameters				Poles g1			Poles g2				
	ICF	k_f	L (mm)	ε	1	2	3	1	2	3	Angle (°)	Axis [h k l]
TKD	-	-	-	-	-	-	-	-	-	-	**41.4**	**[0.003 0.197 0.980]**
APT 1	1.63	4	90	0.57	1	1	2	1	1	$\bar{2}$	39.9	[0.054 0.168 0.984]
					1	1	0	1	1	2		
					1	3	2	1	3	0*		
APT 2	1.65	3.3	90	0.50	1	1	2	1	1	$\bar{2}$	39.3	[0.028 0.277 0.960]
					1	1	0	1	1	2		
					1	3	2	1	3	0*		
APT 3	1.63	4	90	0.57	2	1	2	1	1	4	41.5	[0.035 0.228 0.973]
					1	1	$\bar{5}$	3	1	2		
					1	3	1*	5	3	$\bar{2}$*		

ICF, image compression factor.
Three different APT measurements of the same grain boundary are provided varying reconstruction parameters and pole selection.
*Direction calculated from cross-product of the other two.

7.3.2 Reflectron fitted atom probe analyses vs. TKD misorientation measurements

A similar crystallographic analysis procedure was then undertaken for the technically pure Mo specimen. Fig. 4a shows the calibrated atom probe reconstruction collected for the sample (ICF = 1.28, kf = 2.56, ε = 0.37, L = 40 mm). Strong segregation of the N and P impurity species can be seen at the grain boundary running down the center of the reconstruction. Once again, pole and zone line structure could be observed throughout the reconstruction although this was weaker than in the previous example (Figs. 4b,f). Density maps from ~ 1 million atom slices of two regions within the reconstruction have been used. It was still possible to index individual poles and clear periodicity of lattice planes was observed within these regions as indicated by the POE and SDMs (Figs. 4c-e,g-i). Using this information, the orientation of each grain, as well as the misorientation between them, could be calculated using the method described in the previous section. These measurements could then be compared directly to those from the TKD maps taken of the tip prior to the atom probe experiment.

Fig. 5 shows a comparison between the TKD and APT analyses of the same grain boundary region. Once again, the grains have been colored according to the crystallographic direction in the vertical direction as measured from both techniques. Fig. 5a shows 4 TKD maps of the specimen at projections spaced ~ 90° apart – the relative measured orientation of each grain is also provided. Fig. 5b shows the corresponding 3D orientation maps of the APT reconstruction, also at 4 projections spaced ~ 90° apart. The coloring from each technique is very similar, indicating close agreement in the crystallographic measurements and facilitates easy comparison between the two results. A 1D concentration profile of the impurity elements along the direction normal to the grain boundary is also provided to highlight again the ability to combine very precise atomic chemical and crystallographic information of individual grain boundaries with this analysis approach.

A summary of the minimum misorientation measurements is given in Table 2.

Similarly to before, the average orientation of each grain was calculated and a minimum misorientation was measured using these values. Three separate measurements of the same boundary in the atom probe data were conducted from the calibrated reconstruction, non-calibrated reconstruction and the calibrated reconstruction with a different selection of poles. The average minimum misorientation angle, calculated from the measurements taken on the calibrated reconstruction with different pole selections, is 33.4°/[0.099 0.640 0.761]. The misorientation angle and axis deviate 1.4° and 5.7° respectively from the TKD result.

Table 2: Crystallographic measurements of technically pure Mo: TKD vs. APT (reflectron). Three different APT measurements of the same grain boundary are provided varying reconstruction parameters and pole selection.

	Calibration parameters				Poles g1			Poles g2				
	ICF	k_f	L (mm)	ε	1	2	3	1	2	3	Angle (°)	Axis [h k l]
TKD	-	-	-	-	-	-	-	-	-	-	**32.0**	**[0.196 0.640 0.743]**
APT 1	1.28	2.56	40	0.37	0	1	1	$\bar{2}$	$\bar{1}$	$\bar{1}$	34.0	[0.148 0.627 0.765]
					1	1	2	1	1	1		
					1	2	1	3	2	$\bar{1}$*		
APT 2	1.65	3.3	382	0.37	0	1	1	$\bar{2}$	$\bar{1}$	$\bar{1}$	32.7	[0.186 0.679 0.710]
					1	1	2	1	1	1		
					1	2	1	3	2	$\bar{1}$*		
APT 3	1.28	2.56	40	0.37	0	1	1	$\bar{1}$	$\bar{1}$	1	32.8	[0.050 0.652 0.757]
					1	1	1	2	1	$\bar{1}$		
					1	2	$\bar{1}$*	3	2	1*		

ICF, image compression factor.
Three different APT measurements of the same grain boundary are provided varying reconstruction parameters and pole selection.
*Direction calculated from cross-product of the other two.

7.4 Discussion

7.4.1 Angular resolution

From the presented results, it was possible to gain insight into the angular resolution of orientation and misorientation measurements made directly from APT reconstructions through the use of complementary TKD results on the same tip specimen. Such information is useful because APT crystallography studies are starting to become popular as a means of combining atomic scale chemical and crystallographic measurements across individual grain boundaries yet there has been limited investigation into the accuracy of such measurements. It is important to point out that the angular resolution of TKD, while significantly high, still has a margin of error. A quick way to estimate this error is to perform a transection across a deformation free grain and view the pixel – pixel misorientation data. For the data presented, this was found to be on average approximately ± 0.3°. When measuring the misorientation between two separate grains, the margin of error is double this value or ± 0.6°. Higher angular resolutions would be possible with higher diffraction pattern resolutions but this would increase the time required to generate the TKD maps.

An accurate estimate of the true angular resolution using APT is difficult due to the time each individual measurement takes and the influence of so many variables including the reconstruction calibration and the protocols used to make the measurement itself and falls outside the scope of this manuscript. However, to gain some insight into the effect of reconstruction calibration and pole selection, three separate measurements were taken

changing these parameters on each sample. It was presumed that the carefully calibrated reconstructions would result in significantly more accurate misorientation measurements, but based on the measurements in Table 1 and Table 2, this could not be substantiated and is perhaps an indication of the robustness in making misorientation measurements from APT reconstructions. Never the less, some variance in the results, depending on parameter selection, was observed.

For the calibrated atom probe reconstructions, the maximum deviation of misorientation angle is 2°. However, when the measurements using different pole selection are averaged, this falls to 1.4° and suggests that the accuracy can be improved by averaging multiple measurements using a different selection of poles. The deviation in the misorientation axis is larger, i.e. on average ~4°. This was to be expected, since the nature of the misorientation axis calculation is even more sensitive to variation in the orientation of each grain – the same compounding error is also seen in calculations from EBSD and TKD data. It is also worth pointing out that this is particularly the case when low angle grain boundaries are being studied [28] but in the presented study only high angle grain boundaries were considered. These errors must be a significant consideration when observing changes in segregation behavior with misorientation across interfaces, because even small deviations from special crystallographic arrangements at grain boundaries can have a strong effect on segregation behavior [29,30]. The type of APT instrument (straight flight path vs. reflectron) appears to have some impact on angular resolution of misorientation measurements. It was assumed that measurements from a reflectron fitted instrument would be worse due to distortions in the reconstruction caused by the curved flight path of the ions and indeed, even after careful calibration and incorporating the 40 mm flight path, approximately twice the level of deviation in the misorientation angle/axis pair was observed.

Interestingly, the best result came from the non-calibrated reconstruction. More measurements would be needed to further confirm this observation and perhaps the calibration methods used for these reconstructions needs further development. Even so, misorientation measurements were still possible to within an accuracy of several degrees and there is significant scope for improvement. It is also worth noting that pole and zone line structure is often less clear on reflectron instruments – even though lattice planes may still be conserved within the resultant reconstructions. Crystallographic signal intensity mapping approaches [31] would be useful to enhance this information, particularly in situations where zone and pole line signal is too poor to index. The reason for the discrepancy is likely to be caused predominantly from inaccuracies in the reconstruction calibration and measurement itself. A likely source of error is caused from the imperfectly reconstructed atom probe data and the requirement to fit the Cs frame to this structure.

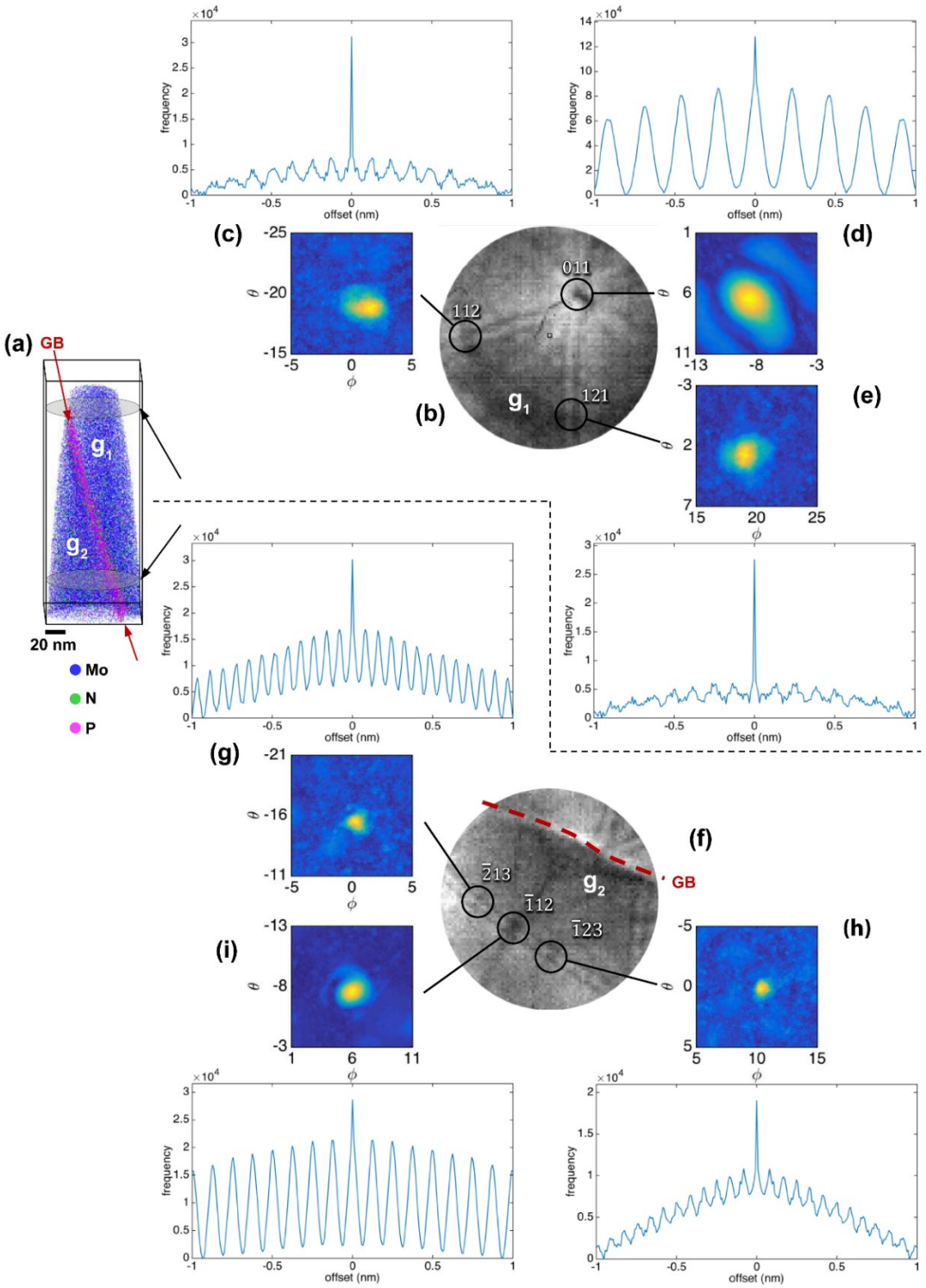

Fig. 4: (a) Technically pure Mo atom probe reconstruction; (b) and (f) density maps of top and bottom grains respectively with indexed pole structure; (c)-(e), (g)-(i) POEs and SDMs of indexed families of planes.

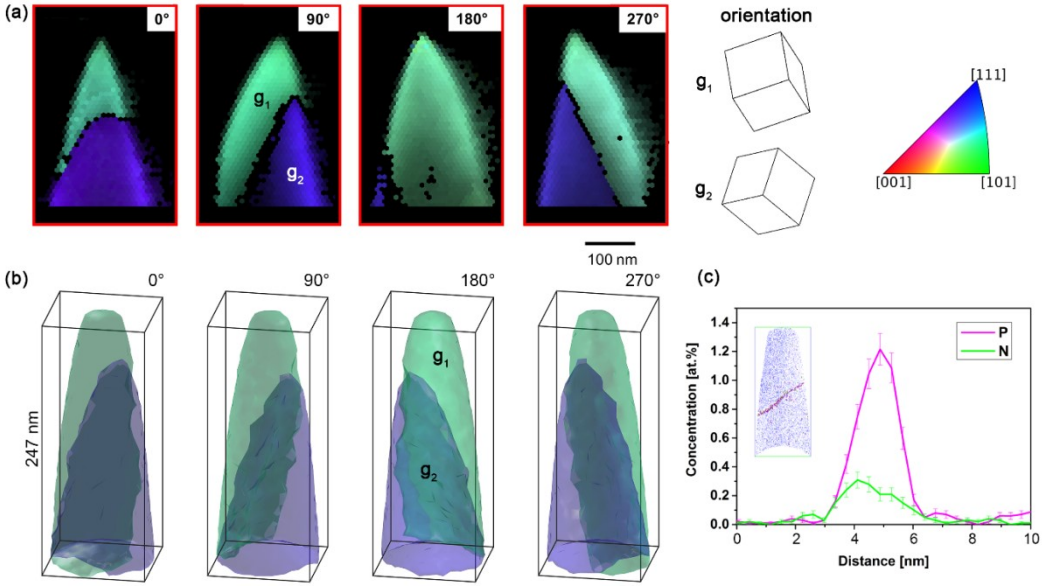

Fig. 5: (a) TKD maps of technically pure Mo sample at different projections; (b) 3D orientation maps of APT reconstruction; (c) 1D concentration profile in direction perpendicular to grain boundary (shown in insert).

It is worth noting that the image compression factor (ICF) and kf, which are used in the typical reconstruction protocol, change throughout the atom probe experiment [26] and may have added to measurement error. Some effort was made to mitigate this effect. For the nanocrystalline Al-0.5Ag dataset, it was possible to measure the orientation of each grain from a single calibrated slice within the reconstruction thereby avoiding any change in crystallography in depth. For the technically pure Mo, it was difficult to obtain sufficient crystallographic information of each grain within a single slice in depth. Consequently, an average ICF and kf from two slices, that contained sufficient crystallographic information about each grain, was calculated and applied to the entire reconstruction. The orientation of each grain was then measured at each slice. A dynamic reconstruction approach as proposed by [26], would have enabled the observed crystal structure in each grain to remain approximately constant in depth and hence would have probably improved the accuracy of the measurement further. However, this reconstruction calibration protocol takes much longer to implement for a small gain in accuracy.

Perhaps a more accurate approach for future work would be to measure the orientation directly from the pole and zone lines observed in the detector hit map, thereby alleviating any need to interrogate the tomographic reconstruction directly. Such an approach should achieve similar accuracy to that reported by [22] of ± 0.4° with the added benefit that the APT experiments could continue without the time consuming process of a FIM experiment which would require large changes to the vacuum within the analysis chamber. Further improvements could also be possible with improved reconstruction methods and measurement protocols such as improved indexing and interpretation of spacing between observed zone line and pole patterns as well as averaging multiple measurements based on a different selection of poles.

7.4.2 Correlating the TKD and APT orientation maps

Figure 2 outlines the process used to filter out the boundary using a NN analysis, which worked well due to the strong segregation of impurity species in both examples. In cases where this type of segregation is not observed, density fluctuations within the reconstruction could be used instead to highlight the boundaries using techniques such as the interface detection method proposed by [32].

Figure 3 and Fig. 5 are useful for directly comparing the crystallographic information each technique provides. In both samples, the calculated color of the grains, based on the IPF, was very similar between the two techniques indicating that crystallographic alignment was very close in the vertical direction. The 3D orientation maps from the atom probe reconstructions highlight the unique ability of APT to give additional information about grain morphology and completely describe the boundary to five degrees of freedom, including the boundary plane orientation if desired. It should be noted that the 3D APT orientation maps only show the global orientation average of each grain whereas the TKD orientation maps can show local changes in crystallography within the grains themselves due to strain or dislocations. However, all misorientation measurements in the presented study were based on average grain orientation. While local changes in crystallography can be observed in APT, this is generally only in the pole and zone line regions and it is difficult to determine whether this change is due to inaccuracies in the reconstruction or true changes in local crystallography.

Alignment between the TKD and APT results is an important consideration. It is interesting to note that the longer TKD maps in Fig. 3 demonstrate clearly that, depending on orientation, the grain structure can appear quite different since only 2D crystallographic information in the bottom 10-20 nm of the sample, relative to the detector, is being displayed. This potentially adds a level of complexity to working out corresponding grains between the two techniques, and may even render some grains invisible to TKD if they are buried within the center of the atom probe tip. However, this was not an issue for the examples shown since only a single boundary was captured in each APT reconstruction. Due to the angular field-of-view of APT being limited to ~ 30-40° because of the electrode and detector configuration, ions on the periphery of most tips are not detected and so what is reconstructed is a conical sub-volume of the original specimen. It is therefore difficult to precisely align the location of the APT reconstruction to the TKD map without multiple boundaries being captured in each. In cases where sufficient crystallographic information is present within the atom probe reconstructions to determine grain orientation, this information can be used to help match up individual grains, otherwise density fluctuations and atomic segregation to the interfaces can be a useful means for grain alignment. TKD could also potentially guide reconstructions of these materials if changes in grain morphology and boundary orientation are identified, however, this process would currently be challenging.

7.4.3 Efficiency and future outlooks

While APT crystallography is important for reasons outlined previously, it is also time consuming particularly for the non-expert with limited programming experience. In cases where only a misorientation value across a grain boundary is required, TKD may currently be the ideal choice to get these measurements since it is convenient, rapid and currently more accurate. However, APT crystallography will continue to be important for reconstruction calibration and full crystallographic quantification of nanocrystalline grains, including the boundary plane orientations. What is required is development very similar to that observed with EBSD technology whereby the process becomes much more automated. With improvements to the reconstruction algorithm, signal detection algorithms and modification of software to automatically index patterns, such as through utilization of the Hough transform, this could one day be a reality. TKD can be a very useful metric to guide this process.

7.5 Conclusion

The highly accurate crystallographic measurements that TKD provides can be useful for atom probe specimen preparation procedures as well as complementing the chemical, structural and morphological information that APT provides in 3D at the atomic level. Atom probe crystallography studies, whereby lattice information is directly observed from within the atom probe data, are particularly useful for reconstruction calibration and enabling chemico-textural orientation mapping in 3D at resolutions otherwise unavailable.

Here we have used TKD to independently verify atom probe crystallography measurements for the very first time. Two grain boundaries, one in a nanocrystalline Al-0.5Ag alloy and the other in technically pure Mo, have been studied using complementary TKD and APT. We found that for the two grain boundaries, measurements of the minimum misorientation angle from the calibrated atom probe reconstructions was at most only 2.0° different from the TKD measurements. The minimum misorientation angle, calculated from calibrated atom probe reconstructions with two different pole combinations, deviate 0.7° and 1.4° respectively from the TKD results. Also interesting to note was that the measurements from the straight flight path instrument had approximately half the deviation of the reflection instrument (2.4° and 5.7° on average respectively). The accuracy of the APT measurement appears to be dependent on inaccuracies in the reconstruction as well as calculation errors from the misorientation measurement itself.

The results have significant implications to the structural analysis of individual grain boundaries at the atomic level which plays a critical role in the understanding of structure-property relationships in polycrystalline materials. Regardless of the atom probe instrument used and the material being analyzed, it appears that crystallographic measurements to within several degrees of accuracy are currently possible, so long as enough crystallographic

information can be detected, and efforts are being made to improve crystallographic signal detection for non-ideal specimens [31,33]. With improved reconstruction and measurement protocols this accuracy could also be improved in the future. TKD will not entirely supersede APT for crystallographic measurements, since APT crystallography will always be useful for reconstruction calibration and measuring the 3D crystallographic orientation of grain boundary planes for instance. But it will be invaluable as a tool to guide these measurements as well as providing a convenient, accurate and more rapid means of directly correlative grain texture information of atom probe specimens.

Acknowledgements

The authors acknowledge the scientific and technical support of the AMMRF (ammrf.org.au) node at the Australian Centre for Microscopy and Microanalysis (ACMM) at the University of Sydney as well as at the Department of Physical Metallurgy and Materials Testing, Montanuniversität Leoben. The nanocrystalline Al was fabricated by Oliver Renk at the Erich Schmidt institute in Leoben. The technically pure Mo was supplied by Plansee SE, Austria. The authors are particularly grateful to Thomas Hartley for assistance with graphic design of figures and related presentations, Dr. Takanori Sato for experimental atom probe support and Mr. Nathan Wallace and Dr. Baptiste Gault for assistance with crystallographic analysis.

References

[1] M.K. Miller, A. Cerezo, M.G. Hetherington, G.D.W. Smith, Atom probe field ion microscopy, Clarendon Press, Oxford, 1996.

[2] B. Gault, M. Moody, J. Cairney, S. Ringer, Atom probe microscopy, Springer, 2012.

[3] D. Larson, T. Prosa, T. Kelly, Local Electrode Atom Probe Tomography - A user's guide, 2013.

[4] M.K. Miller, R.G. Forbes, The Local Electrode Atom Probe, in: Atom-Probe Tomography, Springer, 2014: pp. 229–258.

[5] B. Gault, M.P. Moody, J.M. Cairney, S.P. Ringer, Atom probe crystallography, Materials Today. 15 (2012) 378–386.

[6] M.P. Moody, B. Gault, L.T. Stephenson, D. Haley, S.P. Ringer, Qualification of the tomographic reconstruction in atom probe by advanced spatial distribution map techniques, Ultramicroscopy. 109 (2009) 815–824.

[7] F. Vurpillot, G. Da Costa, a. Menand, D. Blavette, Structural analyses in three-dimensional atom probe: a Fourier transform approach, Journal of Microscopy. 203 (2001) 295–302.

[8] A.J. Breen, M.P. Moody, A. V. Ceguerra, B. Gault, V.J. Araullo-Peters, S.P. Ringer, Restoring the lattice of Si-based atom probe reconstructions for enhanced information on dopant positioning, Ultramicroscopy. 159 (2015) 314–323.

[9] M.P. Moody, A. V Ceguerra, A.J. Breen, X.Y. Cui, B. Gault, L.T. Stephenson, R. K. W. Marceau, R. C. Powles, S. P. Ringer, Atomically resolved tomography to directly inform simulations for structure–property relationships, Nature Communications. 5 (2014) 5501.

[10] F. Vurpillot, L. Renaud, D. Blavette, A new step towards the lattice reconstruction in 3DAP, Ultramicroscopy. 95 (2003) 223–229.

[11] V.J. Araullo-Peters, B. Gault, S.L. Shrestha, L. Yao, M.P. Moody, S.P. Ringer, J. M. Cairney, Atom probe crystallography: Atomic-scale 3-D orientation mapping, Scripta Materialia. 66 (2012) 907–910. doi:10.1016/j.scriptamat.2012.02.022.

[12] L. Yao, M.P. Moody, J.M. Cairney, D. Haley, a V Ceguerra, C. Zhu,S. P. Ringer, Crystallographic structural analysis in atom probe microscopy via 3D Hough transformation., Ultramicroscopy. 111 (2011) 458–63.

[13] M.-R. He, S.K. Samudrala, G. Kim, P.J. Felfer, A.J. Breen, J.M. Cairney, D. S. Gianola, Linking stress-driven microstructural evolution in nanocrystalline aluminium with grain boundary doping of oxygen, Nature Communications. 7 (2016) 11225.

[14] H.W. Yen, S.W. Ooi, M. Eizadjou, A. Breen, C.Y. Huang, H.K.D.H. Bhadeshia, et al., Role of stress-assisted martensite in the design of strong ultrafine-grained duplex steels, Acta Materialia. 82 (2015) 100–114.

[15] R.R. Keller, R.H. Geiss, Transmission EBSD from 10 nm domains in a scanning electron microscope, Journal of Microscopy. 245 (2012) 245–251.

[16] P.W. Trimby, Orientation mapping of nanostructured materials using transmission Kikuchi diffraction in the scanning electron microscope., Ultramicroscopy. 120 (2012) 16–24.

[17] P.W. Trimby, Y. Cao, Z. Chen, S. Han, K.J. Hemker, J. Lian, X. Liao, P. Rottmann, S. Samudrala, J. Sun, J. T. Wang, J. Wheeler, J. M. Cairney, Characterizing deformed ultrafine-grained and nanocrystalline materials using transmission Kikuchi diffraction in a scanning electron microscope, Acta Materialia. 62 (2014) 69–80.

[18] S. Zaefferer, A critical review of orientation microscopy in SEM and TEM, Crystal Research and Technology. 46 (2011) 607–628.

[19] K. Babinsky, R. De Kloe, H. Clemens, S. Primig, A novel approach for site-specific atom probe specimen preparation by focused ion beam and transmission electron backscatter diffraction, Ultramicroscopy. 144 (2014) 9–18.

[20] K.P. Rice, Y. Chen, T.J. Prosa, D.J. Larson, Implementing Transmission Electron Backscatter Diffraction for Atom Probe Tomography, Microscopy and Microanalysis. 22 (2016) 583–588.

[21] M. Herbig, P. Choi, D. Raabe, Combining structural and chemical information at the nanometer scale by correlative transmission electron microscopy and atom probe tomography, Ultramicroscopy. 153 (2015) 32–39.

[22] J. Takahashi, K. Kawakami, Y. Kobayashi, In situ determination of misorientation angle of grain boundary by field ion microscopy analysis., Ultramicroscopy. 140 (2014) 20–5.

[23] K. Babinsky, J. Weidow, W. Knabl, A. Lorich, H. Leitner, S. Primig, Atom probe study of grain boundary segregation in technically pure molybdenum, Materials Characterization. 87 (2014) 95–103.

[24] S. Primig, H. Clemens, W. Knabl, a. Lorich, R. Stickler, Orientation dependent recovery and recrystallization behavior of hot-rolled molybdenum, International Journal of Refractory Metals and Hard Materials. 48 (2015) 179–186.

[25] B. Gault, M.P. Moody, F. De Geuser, G. Tsafnat, A. La Fontaine, L.T. Stephenson, et al., Advances in the calibration of atom probe tomographic reconstruction, Journal of Applied Physics. 105 (2009).

[26] B. Gault, S.T. Loi, V.J. Araullo-Peters, L.T. Stephenson, M.P. Moody, S.L. Shrestha, et al., Dynamic reconstruction for atom probe tomography, Ultramicroscopy. 111 (2011) 1619–1624.

[27] O. Engler, V. Randle, Introduction to texture analysis : macrotexture, microtexture and orientation mapping, Gordon & Breach, Amsterdam, The Netherlands, n.d.

[28] D.J. Prior, Problems in determining the misorientation axes, for small angular misorientations, using electron backscatter diffraction in the SEM, Journal of Microscopy. 195 (1999) 217–225.

[29] M. Herbig, D. Raabe, Y.J. Li, P. Choi, S. Zaefferer, S. Goto, Atomic-scale quantification of grain boundary segregation in nanocrystalline material, Physical Review Letters. 112 (2013) 1–5.

[30] G.S. Rohrer, Grain boundary energy anisotropy: A review, Journal of Materials Science. 46 (2011) 5881–5895.

[31] V.J. Araullo-Peters, A. Breen, A. V. Ceguerra, B. Gault, S.P. Ringer, J.M. Cairney, A new systematic framework for crystallographic analysis of atom probe data, Ultramicroscopy. 154 (2015) 7–14.

[32] P. V Liddicoat, X.-Z. Liao, Y. Zhao, Y. Zhu, M.Y. Murashkin, E.J. Lavernia, et al., Nanostructural hierarchy increases the strength of aluminium alloys., Nature Communications. 1 (2010) 63.

[33] L. Yao, S.P. Ringer, J.M. Cairney, M.K. Miller, The anatomy of grain boundaries: Their structure and atomic-level solute distribution, Scripta Materialia. 69 (2013) 622–625.

8 Publication C

Grain boundary study of technically pure molybdenum by combining APT and TKD

K. Babinsky[1], W. Knabl[2], A. Lorich[2], R. De Kloe[3], H. Clemens[1], S. Primig[1]

1 Department of Physical Metallurgy and Materials Testing, Montanuniversitaet Leoben, Austria

2 Plansee SE, Metallwerk-Plansee-Straße 71, 6600 Reutte, Austria

3 AMETEK B. V., EDAX business unit, The Netherlands

Abstract:

Molybdenum is an eligible material for high performance applications. However, its applicability is limited because of a brittle-to-ductile transition around room temperature, depending on the grain size and the content of interstitial impurities present at grain boundaries. The total amount of impurities in the current quality of molybdenum has become very small in the last decades. Therefore, the atom probe with its atomic resolution is the only suitable site-specific analysis technique. Nevertheless, a site-specific specimen preparation by focused ion beam (FIB) is required to study the grain boundary chemistry effectively. With a novel method, which combines re-sharpening of pre-electro-polished tips by FIB with transmission Kikuchi diffraction (TKD), a grain boundary can easily be positioned in the first 200 nm of an atom probe sample. Furthermore, the high resolution technique of TKD gives the opportunity to get crystallographic information of the mapped area and, therefore, an analysis of the grain boundary character to support the interpretation of the atom probe data files.

In the present study, APT specimens of technically pure molybdenum which contain grain boundaries were prepared by FIB in support of TKD and subsequently were measured in the atom probe. The difference of segregation content at unequal types of grain boundaries in the as-deformed and recrystallized state is discussed.

8.1 Introduction

Due to its excellent physical and chemical properties molybdenum is used for several high performance applications, as in electronics, coatings, high temperature-engineering, and lighting-technology. However, until today its intergranular embrittlement is not well understood and limits the field of application [1,2]. In general, molybdenum is ductile in its deformed state at room temperature, but recrystallization leads to intergranular fracture behavior which is believed to be caused by impurity segregation at grain boundaries [2,3]. The intergranular embrittlement has been studied intensively [2,4–11]. On the one side, it is believed that segregated elements may weaken or strengthen the grain boundaries and, therefore, influence the mechanical properties. As investigated by Kumar et al. [2], Suzuki et al. [7] and Krajnikov et al. [12], carbon has been reported to increase the grain boundary strength. Oxygen has been identified as weakening impurity element in molybdenum [2]. However, on the other side some authors believe that intergranular fracture is an intrinsic property of molybdenum [13,14]. T. Watanabe et al. [11] investigated the fracture mode of materials related to the grain boundary energy and reported that random grain boundaries are not resistant against crack propagation. Therefore, intergranular fracture occurs more often in microstructures with many random boundaries. Low-angle and special boundaries (for example (111) $\Sigma 3$ coincidence boundary in molybdenum [13]) show higher fracture stress and cause transgranular fracture. Therefore, the grain boundary character plays a significant role for the understanding of the fracture behavior of pure molybdenum.

The amount of impurities in the current quality of powder metallurgical produced molybdenum has become so low during the last decades, that surface sensitive techniques as Auger electron or secondary ion mass spectroscopy are not applicable anymore [15,16]. Only the three-dimensional atom probe with its almost atomic resolution seems to be an adequate analysis technique [16]. With the sensitivity of atom probe tomography (APT) it is possible to detect individual atoms, even in the parts per million range [17–19]. Therefore, it is considered to be the most suitable method to study grain boundary segregation in technically pure molybdenum.

A limitation of APT for the study of grain boundaries is the complex site-specific specimen preparation [20]. The chance to analyze a grain boundary prepared by conventional electro-polishing methods is negligible if the grain size is in the micrometer range. With modern focused ion beam (FIB) systems it is nowadays possible to produce specimens out of site-specific regions of interest, e.g. with the lift-out technique as proposed by Miller et al. [21]. Besides this method, APT specimens with a grain boundary can be prepared by re-sharpening electro-polished tips within the FIB [22–24]. For an improved visibility of the region of interest in the FIB/scanning electron microscope (SEM) the last preparation steps are often supported by transmission electron microscopy (TEM) [25]. For this procedure a time-consuming repeated exchange between TEM and FIB/SEM is necessary [23]. To overcome

this time-consuming process, the recently proposed transmission Kikuchi diffraction (TKD) technique is used in this study to support the site-specific APT specimen preparation of molybdenum grain boundaries. Lately, the authors of reference [26] recommended the application of TKD on APT specimens to simplify the preparation process and to obtain detailed information about the crystallographic grain boundary properties. Keller et al. [27] firstly proposed to position a thin TEM foil above a commercial EBSD camera to acquire Kikuchi patterns by collecting transmitted forward- scattered electrons. Due to the enhanced spatial resolution TKD has been mostly used for the investigation of ultrafine-grained materials so far [28].

In our study, segregation at high-angle grain boundaries in as-deformed and recrystallized technically pure molybdenum is investigated. It is assumed that the recrystallization treatment influences the segregation behavior and, therefore, the fracture mode [29]. A detailed understanding of the location and nature of impurities in technically pure molybdenum could help to develop molybdenum parts with improved mechanical properties in the future.

8.2 Material and methods

For this study two industrially processed hot-rolled sheets of technically pure molybdenum in their as-deformed and recrystallized state were used to investigate segregation at high-angle grain boundaries. The same material has been studied by TEM and APT [23] or TKD and APT [26] in previous studies which can be used as references. The production procedure of these sheets and the microstructures are described in detail in [23]. The recrystallized average grain size of sheet 1 and sheet 2 were ~48 µm and ~55 µm parallel to the rolling direction, as determined by standard linear intercept method from electron channeling contrast imaging micrographs. The as-deformed sheets exhibit a recovered subgrain structure with many low-angle grain boundaries. The chemical compositions as determined by Glow Discharge Mass Spectroscopy (GDMS) are given in Table 1 [23].

Previous to the novel preparation process by FIB and TKD [26], APT specimens were prepared by the standard electro-polishing method. Small rods ($10 \times 0.3 \times 0.3$ mm^3) were cut out of the sheets with their largest dimension parallel to the normal or to the rolling direction. The electrolyte for the polishing procedure was 12.5 vol. % H_2SO_4 in ethanol. A detailed description of the electro-polishing process is given in [18].

The FIB preparation was performed with a FEI Versa 3D DualBeam (FIB/SEM) microscope. The annular milling steps were carried out with an acceleration voltage (Acc. V.) of 30 kV and a tilt angle of 52°. To keep the gallium implantation low, the last annular milling steps were carried out at an Acc. V. of 5 kV. For a successful APT measurement, the region of interest has to be located in the first few hundreds of nanometers below the apex. Nevertheless, the spatial resolution of the SEM is too poor during the last preparation step, therefore, grain boundaries are not visible anymore in the volume. For this reason, TKD analyses were applied

to support the process. In reference [26] the novel preparation technique by combining FIB and TKD is described in detail. The FIB/SEM workstation used in this study is equipped with an EDAX Hikari XP EBSD system, hence, no exchange between different microscopes was necessary. The EDAX OIM Data Collection 7 software was used for the measurements and the EDAX OIM Analysis 7 for the evaluation of the EBSD data files.

Table 1: Chemical compositions of the two sheets determined by GDMS. The absolute accurateness is typically +/- factor of 2 [35].

Sample Element	Sheet 1 [µg/g]	Sheet 2 [µg/g]
C	< 8.5	< 6.5
O	< 12	< 5.9
N	< 1.3	< 0.4
K	4	19
Ba	1.0	2.2
P	2.4	1.2
La	0.02	0.4
Fe	3.7	3.2
Si	1.1	1.3
Mg	0.9	1.1
Al	0.2	0.2
Ca	0.2	0.3
S	0.09	0.08
W	120	140

< below detection limit

As demonstrated in a previous study [26], Fig. 1 shows the schematic set-up at 0° (a) and 52° (b) in the microscope chamber. To obtain correct crystallographic directions the tilt angle of the data collection software was set from 70° (standard EBSD) to -38° (TKD) [26]. All TKD scans were carried out at a 4x4 binning (i.e. a resolution of 160 x 120) and an Acc. V. of 30 kV with a spot size of 2.5 (11nA). The step size was set to 10 nm and for the last scan prior to the APT measurement to 5-7 nm. A classical Hough type and a low Hough resolution were selected as well as a binned pattern size of 120 and a Theta step size of 0.5. Enhanced background corrections were used to optimize the pattern quality. Previous to the FIB/TKD preparation process all specimens were plasma-cleaned for 5 min to reduce the carbon contamination.

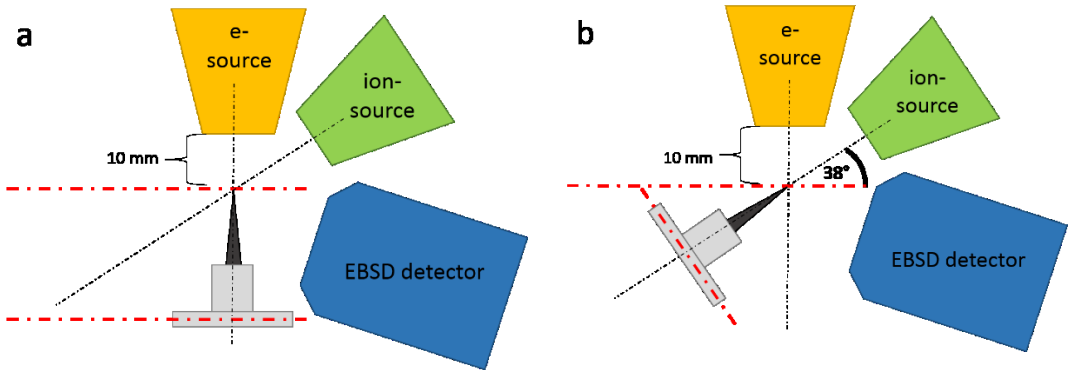

Fig. 1: (a) Schematic set-up in the microscope chamber at a tilt angle of 0°. The ion source (green) is located in an angle of 52° to the electron source. The beams have their intersection point at a working distance of 10 mm; (b) schematic set-up in the microscope chamber at a tilt angle of 52°. The specimen tilt is 52°, therefore, the data collection software was set to a tilt angle of -38° [26].

For a clear identification of the grain boundary, image quality (IQ) maps overlaid with inverse pole figure (IPF) crystal direction maps were constructed after each annular milling step. In the analysis software, the minimum confidence index was set to 0.1 in order to discard false-indexed points [26]. Several repetitions of annular milling and TKD analyses were required to locate the grain boundary close to the apex of the APT tip. During the FIB procedure material was removed from the apex of the specimen to position the boundary in the first 200 nm. Fig. 2 shows the typical preparation steps of a single grain boundary in a tip of technically pure molybdenum in the as-deformed state by FIB and TKD. The right image in Fig. 2 shows the finished APT specimen containing a high-angle boundary. The inset shows the IPF coloring which indicates the crystal direction perpendicular to the normal direction (ND), which is parallel to the z-axis of the tip.

The technique of TKD supports the final tip sharpening but even more gives additional crystallographic information as for example the misorientation of the grain boundary in the prepared APT sample. Therefore, no TEM is necessary and hence no exchange between different microscopes.

Field ion images of some tips were recorded prior to the APT runs in an Oxford Nanoscience 3DAP at 40K with helium as imaging gas. All APT specimens were analyzed with a LEAP 3000X HR from Cameca. Brittle materials, like molybdenum, tend to fail easily in the atom probe [30] especially, if there is a grain boundary present in the sample volume.

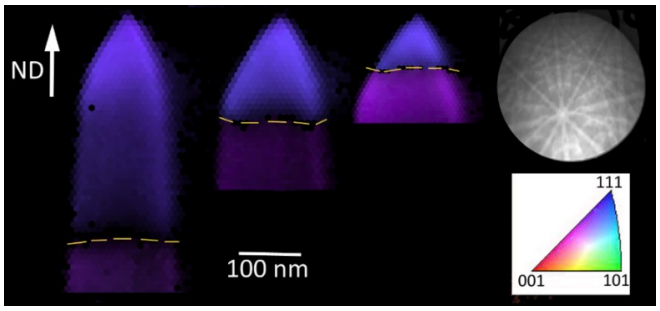

Fig. 2: The typical FIB/TKD APT specimen preparation of a high-angle grain boundary in technically pure molybdenum (as-deformed state, sheet 1). Image quality (IQ) maps overlaid with inverse pole figure (IPF) crystal direction maps were constructed after each annular milling step. Several exchanges between annular milling and TKD analyses were required to locate the grain boundary (marked with yellow lines) in the first 200 nm of the APT tip (left to right). The inset shows the IPF coloring which indicates the crystal direction perpendicular to the normal direction (ND), which is parallel to the z-axis of the tip. In the upper right corner a typical Kikuchi pattern is shown.

Therefore, different temperatures in voltage mode (as shown in Table 2) were applied to optimize the analyses. At higher temperatures the tip should be more mechanically stable, resulting in larger measured volumes without failure at the grain boundary, although the resolution decreases [24]. The target evaporation rate was set to 0.5% for all measurements. The voltage mode with a pulse rate of 200 kHz and a pulse fraction of 15% was used for all analyses. All data files were reconstructed with the IVAS 3.6.6 software from Cameca using the voltage curve. The radius and shank angle were checked with the SEM images and as well with the TKD scans. Furthermore, the trace of the region of interest in the reconstruction was supported by the TKD analyses.

8.3 Results

8.3.1 FIB/TKD combined APT specimen preparation process

TKD is a new promising technique for the site-specific preparation of grain boundaries in APT specimens. With the obtained crystal data it is possible to determine the misorientation (51°) of the grain boundary present in Fig. 2. The crystallographic information supports the evaluation of the APT reconstructions. Due to the fact that diffraction patterns come from the last 20 nm of the sample [31], this technique may under/overestimate the location of the grain boundary in a 3D volume. Therefore, the final APT specimen was imaged from four different sides to estimate the grain boundary trace [26]. In Fig. 3 the TKD scans (every 90 degree) of the ready prepared tip from Fig. 2 are shown.

At the grain boundary no crystallographic information is collected due to the overlap of the Kikuchi patterns from both grains as well as the mismatch of atoms in this area. However, the position of the grain boundary in the volume is clearly visible. In all areas of different thickness transmitted forward-scattered electrons were collected resulting in high-quality Kikuchi patterns. The reconstruction of the measured tip (voltage mode at 103 K) in Fig. 4

shows the same grain boundary with phosphorus segregation. For improved visibility of the grain boundary trace a phosphorus density-isosurface with an isovalue of 0.18 atoms/nm³ was determined.

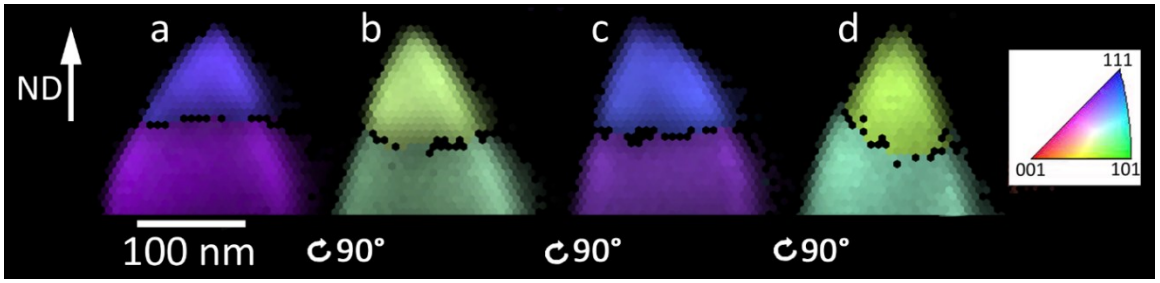

Fig 3: (a)-(d) Image quality (IQ) maps overlaid with inverse pole figure (IPF) crystal direction maps from every 90° of the ready prepared tip of the as-deformed state (sheet 1) as shown in Fig. 2. These scans represent accurately the position of the grain boundary. The inset shows the IPF coloring which indicates the crystal direction perpendicular to the ND.

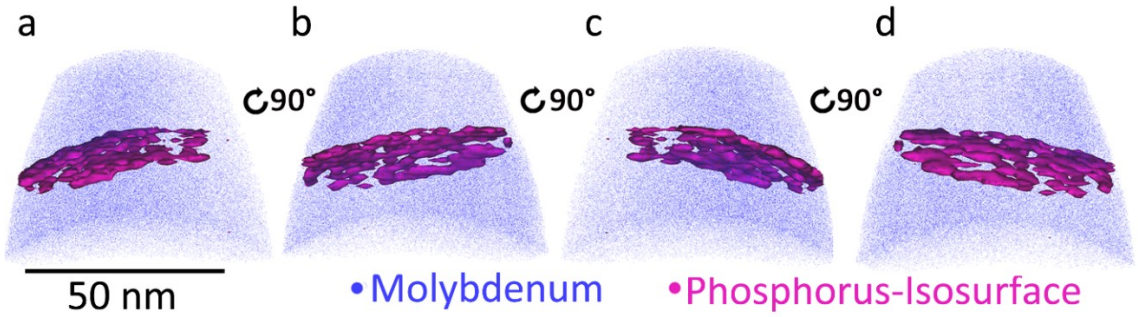

Fig. 4: Reconstruction of the APT specimen shown in Fig. 3. (a)-(d) are side views from every 90° of the reconstructed volume. For improved visibility of the grain boundary trace a density-isosurface (isovalue of 0.18 atom/nm³) of phosphorus was determined. The inset shows the corresponding color code for the molybdenum ions detected.

The reconstruction is imaged from every 90° for a good representation of the measurement and to allow a direct comparison with the TKD data. The received analyses visible in Figs. 3 and 4 are in good agreement. The start of the reconstruction was selected after a constant evaporation field was obtained. Therefore, the grain boundary is closer to the apex in Fig. 4 than in the TKD scans shown in Fig. 3. Further optimizations during the reconstruction such as detector image alignments lead to a smaller size of the analyzed specimen in the reconstructed volume. To compare the results of TKD analyses with crystallographic information obtained by APT, a field ion image was recorded of one of the molybdenum tips in recrystallized state. In Fig. 5 the final TKD scan of this tip and the corresponding field ion image of the upper grain in this tip are shown. The TKD scan is showing a side view of the specimen, whereby the field ion image is indicating a top view of the tip. The lattice orientation for both grains is shown in Fig. 5a. The results of both analyzing techniques match because the poles in the field desorption map visible in Fig. 5b indicate the view close to a (002)-plane. In Fig. 5c the field desorption map of the tip measured in the LEAP 3000X HR is shown. Therein, the same poles as identified by field ion imaging are present.

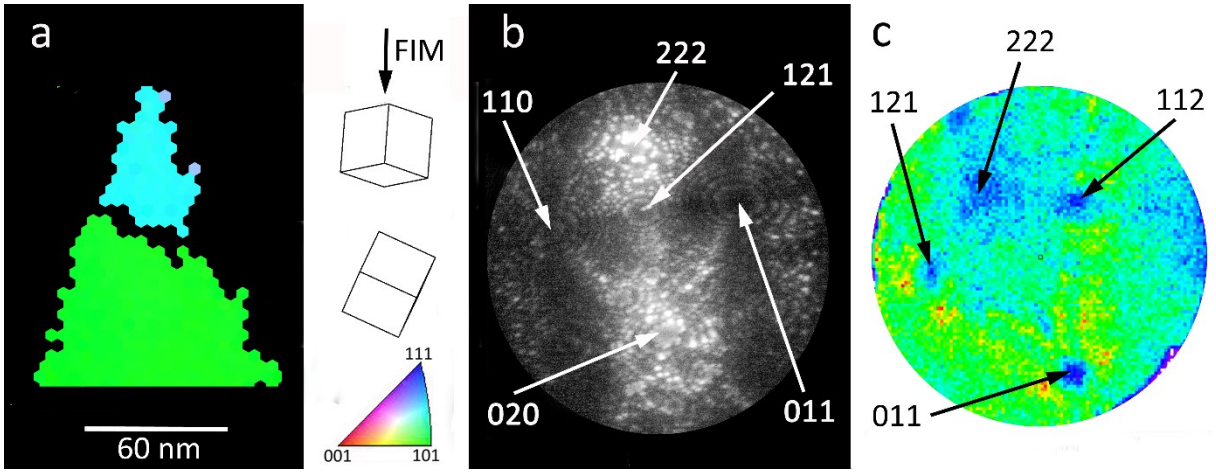

Fig. 5: (a) Final TKD scan of a molybdenum tip in recrystallized state (sheet 2). The TKD scan is showing a side view of the tip. (b) Field ion image of the upper grain indicating the view close to a (002)-plane. (c) Field desorption map of the tip measured in the LEAP 3000X HR. The same poles as detected by field ion imaging are visible.

8.3.2 Application of TKD on technically pure molybdenum

APT measurements of high-angle grain boundaries in the recrystallized and as-deformed state of molybdenum were performed to show a trend of segregation behavior at different types of grain boundaries. In Table 2 an overview of the APT results is illustrated. The misorientation angle, the impurity elements of different types of grain boundaries as well as the APT parameters are summarized. Furthermore, the maximum phosphorus content at the grain boundaries (determined by an one-dimensional concentration profiles in a region of interest over the entire grain boundary) is shown. Note that especially the phosphorus content in the recrystallized state of sheet 2 may be underestimated due to the rather small grain boundary area present in the measured volume.

According to Table 2 all measured high-angle grain boundaries contain segregated phosphorus and nitrogen. Some of the nitrogen is detected as molybdenum-nitrogen molecules. Furthermore, two specimens show a small increase in molybdenum-oxygen molecules at the grain boundary. Fig. 6a shows the reconstruction of the measured tip presented in Fig. 4 (misorientation: 51°). A one-dimensional concentration profile through the entire grain boundary indicates the segregated phosphorus and nitrogen as illustrated in Fig. 6b. The broadening of the grain boundary (thickness of around 6 nm according to the one-dimensional concentration profile) is caused by the bent shape of the interface. The obtained phosphorus content is higher than the nitrogen content in three of the measurements as the other analyses with misorientations of 53° and 33° show the same trend. In case of the analyzed tip with the grain boundary misorientation of 43° the nitrogen content is higher than the phosphorus content, although both amounts are rather low (P is 0.04 at. %, N is 0.26 at. %).

Table 2: Overview of APT analyses of different high-angle boundaries in technical pure molybdenum in recrystallized and as-deformed state. The misorientation angle, the impurity elements as well as the APT parameters are depicted. The maximum phosphorus content at the grain boundary (determined by a one-dimensional concentration profile in a region of interest over the entire grain boundary) is shown.

State	Sheet	Misorientation	Impurity elements	Maximum P content at grain boundary	APT parameters
As-deformed	1	53°	P, N, MoO	0.28 at. %	Voltage, 103 K
state	1	51°	P, N	0.68 at. %	Voltage, 103 K
Recrystallized	1	33°	P, N, C	1.47 at. %	Voltage, 77 K
state	2	43°	P, N, MoO	0.04 at. %	Voltage, 77 K

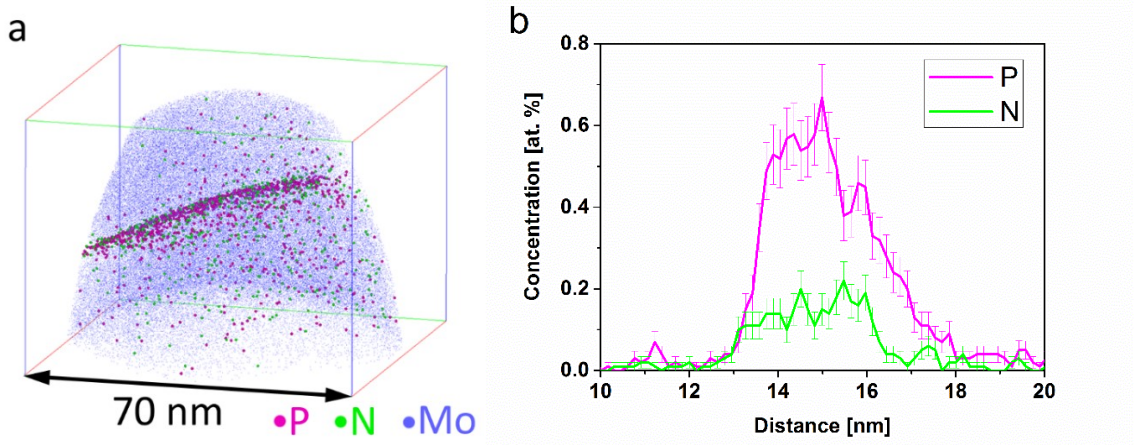

Fig. 6: (a) APT reconstruction of the same specimen as shown in Fig. 4 (sheet 1, as-deformed state). A high-angle grain boundary with phosphorus and nitrogen segregation is visible. The inset shows the corresponding color code for the ions detected. Oxygen and gallium atoms as well as molybdenum-oxide molecules are blanked for better visibility. (b) One-dimensional concentration profile through the entire grain boundary showing an increase of phosphorus and nitrogen at the interface. The phosphor content in this profile is higher than the nitrogen content.

In Table 3 the chemical composition observed by the atom probe of the entire measured volume as shown in Fig. 6 is given. In addition to nitrogen and phosphorous, gallium and oxygen are present as impurity atoms. Oxygen may be present in the material itself or arise from the atom probe chamber and hits the detector often as molybdenum- oxide. Gallium occurs due to the FIB preparation process and is not present in the sample material itself. The GDMS analyses indicate tungsten impurities but no evidence is found in the atom probe results. Tungsten has four isotopes with similar natural abundances. Due to the small analyzed volumes (detection of around 3 million ions) the tungsten peaks are not visible in the spectrum. If a larger number of ions (around 10 million) would have been detected the tungsten peaks could have been identified.

In Fig. 7 the mass spectrum of the measurement shown in Fig. 6 is indicated which represents a characteristic analysis of a molybdenum grain boundary. The seven molybdenum speaks are

clearly visible as well as the molybdenum- oxide peaks. The phosphorus, nitrogen and oxygen peaks can be identified. Gallium occurs due to the FIB preparation process.

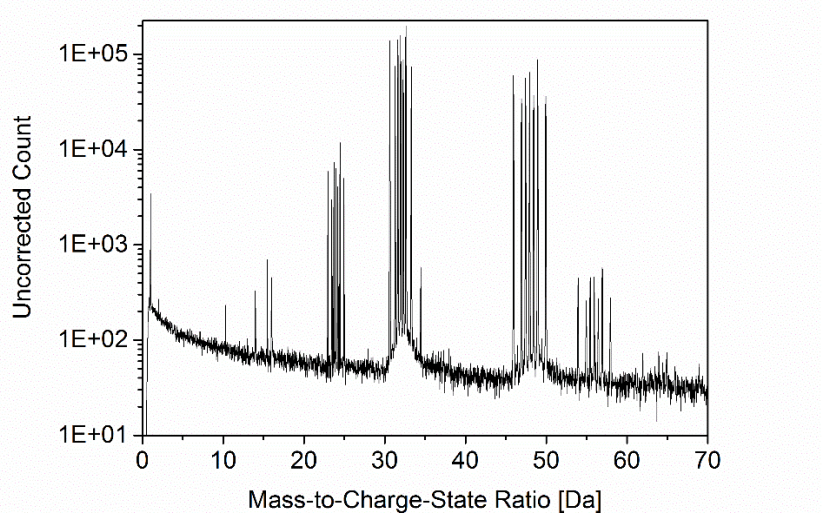

Fig. 7: APT mass spectrum of the measurement shown in Fig. 6 which represents a characteristic analysis of a molybdenum grain boundary. The seven molybdenum speaks are clearly visible as well as the molybdenum- oxide peaks. The phosphorus, nitrogen and oxygen peaks can be identified. Gallium occurs due to the FIB preparation process.

Fig. 8 represents the investigation of the tip from the recrystallized state (sheet 1) exhibiting a grain boundary of 33° misorientation. The TKD scan of the ready tip is shown in Fig. 8a. The reconstruction (Fig. 8b) exhibits phosphorus, nitrogen and carbon segregation at the grain boundary as visible in the one-dimensional concentration profile in Fig. 8c. This grain boundary exhibits segregated carbon with higher amount than phosphorus. However, some carbon could arise from the TKD analyses - even if the tips have been plasma cleaned – and/or from the atom probe chamber. As the preparation time for each APT specimen differs the degree of carbon contamination might change as well. In general, carbon contamination induced by the electron beam is known to behave similar to gallium contamination induced by the ion beam. A typical gradient of contamination content with a maximum at the top of the tip is observed. Even more the orientation of the grains is known to play a significant role for the penetration depth of gallium [25]. A chemical composition determined by APT is depicted in Table 3. Oxygen and gallium show no segregation at grain boundary. Carbon occurs in the entire volume but an increase of up to 2.8 at.% was detected at the interface. Due to the grain boundary brittleness that particular tip fractured before the entire grain boundary was evaporated. Such events happen quite often and complicate the APT study of grain boundary segregation in molybdenum.

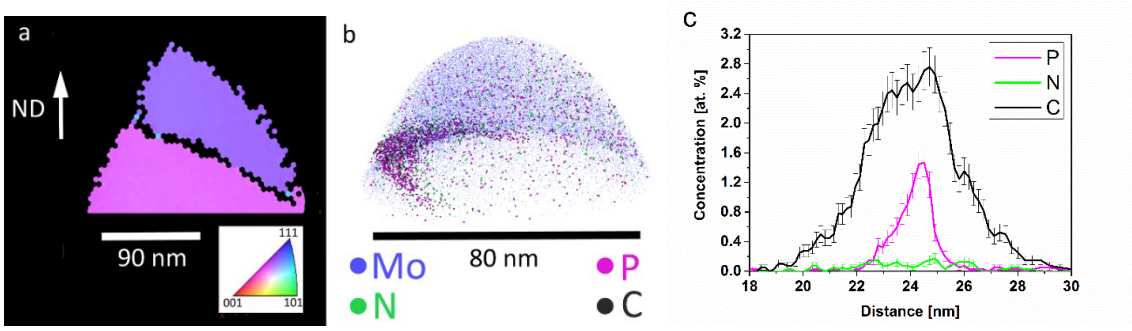

Fig. 8: (a) Final TKD scan of a molybdenum tip prepared from recrystallized state (sheet 1) showing a grain boundary with misorientation of 33°. The inset shows the IPF coloring which indicates the crystal direction perpendicular to the ND. (b) APT reconstruction of the measured specimen shown in a). A high-angle grain boundary with phosphorus, nitrogen and carbon segregation is visible. The inset indicates the corresponding color code for the ions detected. Oxygen and gallium atoms as well as molybdenum-oxide molecules are blanked for better visibility. (c) One-dimensional concentration profile through the grain boundary showing an increase of phosphorus, nitrogen and carbon at the interface. The carbon content is higher than the phosphorus content.

Table 3: Chemical composition obtained by APT of the measured volumes as shown in Fig. 6 (sheet 1, as-deformed state) and Fig. 8b (sheet 1, recrystallized state).

	Sheet 1, as-deformed state		Sheet 1, recrystallized state	
Element	Content [at. %]	σ [at. %]	Content [at. %]	σ [at. %]
Mo	99.601	0.091	99.5854	0.0782
Ga	0.034	0.001	0.0067	0.0005
P	0.040	0.001	0.0185	0.0008
N	0.016	0.001	0.0041	0.0004
O	0.309	0.004	0.2722	0.0029
C			0.1130	0.0019

8.4 Discussion

In this study the preparation process of APT specimens containing high-angle grain boundaries was successfully supported by TKD. Between annular milling steps TKD scans reveal the grain boundary location in the volume. Standard TEM analyses, which are more common in the APT community [25], are time-consuming and contaminate the specimen especially during recording of diffraction patterns for crystallographic investigations. Studies by Baik et al. [32] present the use of standard EBSD for the preparation of grain boundaries with special orientations. Mandal et al. [33] determined all five rotational degrees of freedom of a grain boundary by standard EBSD without using the TEM for a further APT analysis. Nevertheless, also this process is time-consuming and a lift out technique is required to cut out the APT specimen of the analyzed volume. Due to the fact that an APT tip can be easily imaged from different side-views as shown in Fig. 3 it might also be possible to determine all five rotational degrees of freedom of a grain boundary by TKD.

For this study TKD is preferred due to its simplicity and shorter preparation time. As visible in Fig. 2, the observation of crystal orientation data even for diameters of 150 nm is possible although molybdenum exhibits an atomic number of 42. Yao at al. [34] proposed to use the 3D Hough transformation method for crystallographic structural analysis of atom probe data as for example the measurement of crystal geometry around grain boundaries. Sha et al. [35] employed this method to study segregation at grain boundaries in an ultrafine grained Al-Zn-Mg-Cu alloy. However, this technique is complex and crystallographic poles in the field desorption maps, as shown in Fig. 5c, are not always clearly visible. Due to the grain boundary brittleness of molybdenum many APT runs fail during the evaporation of the grain boundary region. As this complicates the identification of poles required for crystallographic analyses, the field desorption maps are not always applicable. However, TKD investigations give quick and clear information about the grain boundary character and, therefore, support the reconstruction of the APT measurements. Also laser mode analyses which usually do not contain crystallographic poles can be interpreted well with the information by TKD.

Different types of high-angle grain boundaries of technically pure molybdenum were prepared easily and analyzed successfully in the atom probe with this technique. According to the chemical GDMS analyses [23] elements as carbon, oxygen, nitrogen, potassium and phosphorus are present in the part per million range in molybdenum sheets. As examined by Auger electron spectroscopy of the same material [15,23] most of the impurity elements remain in former sinter pores which are compressed during deformation. Furthermore, especially potassium and oxygen are present at small pores located at grain boundaries [15]. Additional, the position of these former sinter pores influences the content and type of segregation present at the different types of grain boundaries. In reference [23] an APT measurement of a molybdenum grain boundary and a segregated region is shown. These regions significantly influence the content and type of impurities present at neighboring grain boundaries. APT investigations [26] identified phosphorus and nitrogen at a high-angle boundary in technically pure molybdenum in the recrystallized state. In this study, all analyses indicate phosphorus and nitrogen segregation at high-angle grain boundaries. Although the statistics are still not perfect and the detector efficiency is just 37% no differences in segregation behavior between recrystallized and as-deformed state were observed here. Nevertheless, the as-deformed state is more ductile than the recrystallized state although both conditions indicate segregation at grain boundaries. It is believed that with decreasing grain size the impurities distribute over a larger interface area according to less impurity content at the grain boundaries in the as-deformed state [2,3,23,36]. For quantitative statement about the segregation contents a detailed APT parameter study of different types of grain boundaries is still necessary. Even if it seems that the phosphorus content of the grain boundaries is increased in the recrystallized state of sheet 1 the values must be treated carefully because they depend on the evaporation field and the parameters of the reconstruction. Furthermore, impurity atoms could be forced inside the grains during

deformation [2,3,23,36]. However, bulk analyses do not show any impurities outside the grain boundary regions except of oxygen and tungsten. Miller et al. [8,10] investigated welded molybdenum alloys with zirconium, boron and carbon additions. Their atom probe tomography (APT) results indicate no significant oxygen, but zirconium, carbon and boron segregation at the grain boundaries. Due to the presence of these elements at the interface the fracture mode changed from intergranular to transgranular fracture [8,10].

In this study, carbon was observed at an interface with misorientation angle of 33°. A special crystallographic type of the grain boundary, a former sinter pore in close proximity and the contamination induced by the electron beam might cause this carbon segregation. Kumar et al. [2], Suzuki et al. [7] and Krajnikov et al. [12] investigated pure and alloyed molybdenum and confirmed the increase of grain boundary strength due to the addition of carbon. Recently, Kadokura et al. [37] reported that the intergranular fracture mode changed to the transgranular fracture mode by increasing the carbon content in molybdenum. Ab Initio simulations conducted by Tahir et al. [38] and Janisch et al. [39] confirm the beneficial effects of carbon segregation. Oxygen has been identified as grain boundary weakening impurity element in molybdenum [2]. In two analyses no oxygen but small amounts of molybdenum-oxygen segregation were recognized. The bulk analyses show a small amount of oxygen present in the volume. However, so far only some different types of high-angle boundaries were investigated. Probably, low-angle boundaries in the as-deformed state have an additional strong impact on the fracture mode. An APT study of low-angle boundaries in the as-deformed state which is currently under progress will help to clarify if impurities are also present at this type of boundary.

8.5 Conclusions

The APT specimen preparation of grain boundaries can be easily supported by TKD analyses in-between the FIB process. The location of the grain boundary in the APT tip can be easily adjusted in a short time. Furthermore, crystallographic data obtained by TKD can assist the reconstruction and interpretation of the APT data files. In this study, APT specimens of technically pure molybdenum containing high-angle boundaries were successfully prepared by FIB and TKD and subsequently analyzed in the atom probe. All measurements indicate phosphorus and nitrogen segregation at high-angle grain boundaries. Furthermore, two specimens show a small increase in molybdenum-oxygen molecules at the grain boundary. No differences between the recrystallized and as-deformed state with regard to the segregation behavior at high-angle grain boundaries have been observed yet. A detailed APT study of low-angle boundaries and their segregation behavior is still required in order to answer the question if these boundaries are free from impurities.

References

[1] L. Northcott, Molybdenum, Butterworths, 1956.

[2] A. Kumar, B.L. Eyre, Grain Boundary Segregation and Intergranular Fracture in Molybdenum, Proceedings of the Royal Society A: Mathematical, Physical and Engineering Sciences. 370 (1980) 431–458.

[3] E. Pink, Rekristallisationsdiagramme von Molybdän und Wolfram, Planseeberichte Für Pulvermetallurgie. 13 (1965) 100–104.

[4] A. Krajnikov, A. Drachinskiy, V. Slyunyaev, Grain boundary segregation in recrystallized molybdenum alloys and its effect on brittle intergranular fracture, International Journal of Refractory Metals and Hard Materials. 11 (1992) 175–180.

[5] M. Oku, S. Suzuki, H. Kurishita, H. Yoshinaga, Chemical states of oxygen segregated intergranular fracture surfaces of molybdenum, Applied Surface Science. 26 (1986) 42–50.

[6] H. Kimura, Overview, Intergranular Fracture in BBC metals, Transactions of the Japan Institute of Metals. 29 (1988) 521–539.

[7] S. Suzuki, H. Matsui, H. Kimura, The effect of heat treatment on the grain boundary fracture of recrystallized molybdenum, Materials Science and Engineering. 47 (1981) 209–216.

[8] M. Miller, A. Bryhan, Effect of Zr, B and C additions on the ductility of molybdenum, Materials Science and Engineering: A. 327 (2002) 80–83.

[9] B.V. Cockeram, E.K. Ohriner, T.S. Byun, M.K. Miller, L.L. Snead, Weldable ductile molybdenum alloy development, Journal of Nuclear Materials. 382 (2008) 229–241.

[10] M. Miller, E. Kenik, M. Mousa, K. Russell, A. Bryhan, Improvement in the ductility of molybdenum alloys due to grain boundary segregation, Scripta Materialia. 46 (2002) 299–303.

[11] T. Watanabe, S. Tsurekawa, The control of brittleness and development of desirable mechanical properties in polycrystalline systems by grain boundary engineering, Acta Materialia. 47 (1999) 4171–4185.

[12] A. Krajnikov, F. Morito, V. Slyunyaev, Impurity-induced embrittlement of heat-affected zone in welded Mo-based alloys, International Journal of Refractory & Hard Materials. 15 (1997) 325–339.

[13] S. Tsurekawa, T. Tanaka, H. Yoshinaga, Grain boundary structure, energy and strength in molybdenum, Materials Science and Engineering: A. 176 (1994) 341–348.

[14] J.B. Brosse, R. Fillet, M. Biscondi, Intrinsic intergranular brittleness of molybdenum, Scripta Metallurgica. 15 (1981) 619–623.

[15] K. Babinsky, S. Primig, W. Knabl, A. Lorich, Grain boundary segregations in technically pure molybdenum, in: 18. Planseeseminar, Plansee SE, 2013: pp. RM111/1–15.

[16] V.J. Keast, D.B. Williams, Grain boundary chemistry, Current Opinion in Solid State and Materials Science. 5 (2001) 23–30.

[17] B. Gault, M.P. Moody, J.M. Cairney, S.P. Ringer, Atom probe crystallography, Materials Today. 15 (2012) 378–386.

[18] M.K. Miller, A. Cerezo, M.G. Hetherington, G.D.W. Smith, Atom probe field ion microscopy, Clarendon Press, Oxford, 1996.

[19] M.K. Miller, R.G. Forbes, Atom probe tomography, Materials Characterization. 60 (2009) 461–469.

[20] T.F. Kelly, M.K. Miller, Invited review article: Atom probe tomography, The Review of Scientific Instruments. 78 (2007) 031101–1–20.

[21] M.K. Miller, K.F. Russell, G.B. Thompson, Strategies for fabricating atom probe specimens with a dual beam FIB., Ultramicroscopy. 102 (2005) 287–298.

[22] J. Weidow, H.-O. Andrén, Grain and phase boundary segregation in WC–Co with TiC, ZrC, NbC or TaC additions, International Journal of Refractory Metals and Hard Materials. 29 (2011) 38–43.

[23] K. Babinsky, J. Weidow, W. Knabl, A. Lorich, H. Leitner, S. Primig, Atom probe study of grain boundary segregation in technically pure molybdenum, Materials Characterization. 87 (2014) 95–103.

[24] B. Gault, M. Moody, J. Cairney, S. Ringer, Atom probe microscopy, Springer, 2012.

[25] P.J. Felfer, T. Alam, S.P. Ringer, J.M. Cairney, A reproducible method for damage-free site-specific preparation of atom probe tips from interfaces, Microscopy Research and Technique. 75 (2012) 484–491.

[26] K. Babinsky, R. De Kloe, H. Clemens, S. Primig, A novel approach for site-specific atom probe specimen preparation by focused ion beam and transmission electron backscatter diffraction, Ultramicroscopy. 144 (2014) 9–18.

[27] R.R. Keller, R.H. Geiss, Transmission EBSD from 10 nm domains in a scanning electron microscope, Journal of Microscopy. 245 (2012) 245–251.

[28] P.W. Trimby, Orientation mapping of nanostructured materials using transmission Kikuchi diffraction in the scanning electron microscope., Ultramicroscopy. 120 (2012) 16–24.

[29] S. Primig, H. Leitner, W. Knabl, Static Recrystallization of Molybdenum After Deformation Below 0.5* TM (K), Metallurgical and Materials Transactions A. 43 (2012) 4806–4818.

[30] K.F. Russell, M.K. Miller, R.M. Ulfig, T. Gribb, Performance of local electrodes in the local electrode atom probe., Ultramicroscopy. 107 (2007) 750–5.

[31] A.J. Wilkinson, T.B. Britton, Strains, planes, and EBSD in materials science, Materials Today. 15 (2012) 366–376.

[32] S.-I. Baik, M.J. Olszta, S.M. Bruemmer, D.N. Seidman, Grain-boundary structure and segregation behavior in a nickel-base stainless alloy, Scripta Materialia. 66 (2012) 809–812.

[33] S. Mandal, K.G. Pradeep, S. Zaefferer, D. Raabe, A novel approach to measure grain boundary segregation in bulk polycrystalline materials in dependence of the boundaries' five rotational degrees of freedom, Scripta Materialia. 81 (2014) 16–19.

[34] L. Yao, M.P. Moody, J.M. Cairney, D. Haley, a V Ceguerra, C. Zhu, et al., Crystallographic structural analysis in atom probe microscopy via 3D Hough transformation., Ultramicroscopy. 111 (2011) 458–63.

[35] G. Sha, L. Yao, X. Liao, S.P. Ringer, Z. Chao Duan, T.G. Langdon, Segregation of solute elements at grain boundaries in an ultrafine grained Al-Zn-Mg-Cu alloy., Ultramicroscopy. 111 (2011) 500–5.

[36] E. Pink, R. Eck, Refractory metals and their alloys, in: R.W. Cahn, P. Haasen, E.J. Kramer, K.H. Matucha (Eds.), Materials Science and Technology, VCH, Weinheim, New York, Basel, Cambridge, Tokyo, 2006: pp. 591–638.

[37] T. Kadokura, Y. Hiraoka, Y. Yamamoto, K. Okamoto, Change of Mechanical Property and Fracture Mode of Molybdenum by Carbon Addition, Materials Transactions. 51 (2010) 1296–1301.

[38] A. Tahir, R. Janisch, A. Hartmaier, Ab initio calculation of traction separation laws for a grain boundary in molybdenum with segregated C impurites, Modelling and Simulation in Materials Science and Engineering. 21 (2013) 075005.

[39] R. Janisch, C. Elsässer, Interstitial impurities at grain boundaries in metals: insight from atomistic calculations, International Journal of Materials Research. 100 (2009) 1488–1493.

9 Publication D

Towards grain boundary segregation engineering of technically pure molybdenum

K. Leitner (née Babinsky)[1], P. Felfer [2, 3], D. Holec[1], J. Cairney[2], W. Knabl[4], A. Lorich[4], H. Clemens[1], S. Primig[1, 5]

1 Department of Physical Metallurgy and Materials Testing, Montanuniversität Leoben, Austria
2 Australian Centre for Microscopy and Microanalysis, School of Aerospace, Mechanical and Mechatronic Engineering, The University of Sydney, NSW 2006, Australia
3 Institute for General Materials Properties, Department of Materials Science, Friedrich-Alexander University Erlangen-Nürnberg, 91058 Erlangen, Germany
4 Plansee SE, Metallwerk-Plansee-Straße 71, 6600 Reutte, Austria
5 School of Materials Science & Engineering, UNSW Sydney, NSW 2052, Australia

Abstract:

Grain boundaries (GBs) play an essential role in the structure-property relationship of polycrystalline materials. In particular, the decoration of GBs with solutes influences their properties and may lead to either a strengthening or a weakening of these interfaces.

The room-temperature brittleness and intergranular fracture of Mo-based materials limits their structural application, especially in the recrystallized state. However, it is believed that segregation of certain solutes to GBs has a positive effect on their ductility and strength. Therefore, a more comprehensive study of GBs is essential to improve the mechanical properties of future Mo products required for e.g. structural, electronic and coating applications. With novel characterization techniques such as the atom probe and electron microscopy, it is now possible to study the structure and chemistry of GBs at the atomic scale, enabling this approach.

Here, we show the first comprehensive overview of solute segregation at several different types of GBs in technically pure Mo plates in their as-deformed and recrystallized states. The crystallographic and chemical character of each GB is revealed by combining transmission Kikuchi diffraction (TKD) with atom probe microscopy (APM). The interfacial excess in both material states shows P, N, and O as characteristic GB decorations in technically pure Mo plates. First principle calculations verify the increased C versus nitrogen enrichments observed experimentally at sigma and random GBs in the recrystallized state.

This study opens promising pathways to segregation engineering that will facilitate the design of Mo materials with improved mechanical properties for structural applications.

9.1 Introduction

The characteristics of grain boundaries (GBs) and their influence on mechanical properties are a key area in materials science and engineering. It is well known that the character of individual GBs and their decoration with solutes contribute significantly to the strength and ductility of structural metallic materials [1–4].

By optimizing the grain boundary type and structure, a specific microstructure can be provided to control the brittleness of several metals. The term 'grain boundary engineering' has been introduced to describe any targeted process design in order to achieve predominant formation of certain desirable grain boundary types [5].

Furthermore, solute atoms tend to segregate to certain GBs in polycrystalline materials, especially when they exhibit a low solubility in the bulk [6]. This directly affects the GB energy and strength, and thus, significant changes of the materials properties can be provoked [7]. Dependent on the grain boundary character, the species of solute atoms, and the chemistry of the matrix, either a strengthening or a weakening of the GB effect may occur [8]. The targeted manipulation of GB properties by certain solute decorations has been termed `grain boundary segregation engineering' [2]. GB strengthening by targeted GB decoration is a promising microstructural design method to improve the mechanical properties. This area of research is still in its early years as sufficient high-resolution characterization methods required to image the structure and chemistry of GBs at the atomic scale have only widely become available recently. Today, it is not only possible to measure the five macroscopic degrees of freedom of a GB (rotation axis and angle, GB plane), but even further to determine the accurate chemical composition of the interface at the atomic scale across the entire periodic table, thus, revealing the six degrees of freedom of a GB [1,2,9]. By combining state-of-the-art methods such as atom probe microscopy (APM) and transmission Kikuchi diffraction (TKD), crystallographic information can be linked to the local chemistry at the interface [10–12].

In molybdenum (Mo) based materials in particular grain boundary segregation engineering can provoke a significant modification of the mechanical properties. Mo is a refractory metal applied in numerous structural, electronic and coating applications demanding a low thermal expansion coefficient and a good thermal and electrical conductivity. Apart from typical high-temperature applications, examples of important current Mo products include heat sinks for high performance electronics and sputter targets for coatings in solar cell and flat panel display industries [13].

However, Mo commonly suffers from brittle fracture around room temperature. Furthermore, recrystallization leads to a significant higher ductile-to-brittle transition temperature (DBTT), limiting the application of the material. Additionally, the recrystallized state is prone to intergranular fracture, whereas the as-deformed state shows more ductile fracture [14,15].

This embrittlement has also been linked to the predominance of certain GB types in Mo materials [5,16].

Tsurekawa et al. [17,18] reported that a high fraction of low energy GBs are effective against intergranular fracture, concluding that this brittleness is an intrinsic property of Mo. Other authors investigated the effect of solutes reporting that O has a detrimental influence on the grain boundary strength [19,20]. In these studies, mainly Auger electron spectroscopy (AES) was used to characterize the grain boundary enrichments. However, Waugh and Southon already performed atom probe experiments in the late seventies and confirmed the existence of O segregation at Mo GBs [21,22]. Actual APM findings indicate that GB segregation of N and O promotes intergranular fracture of these intrinsically weak GBs [23–25]. It has also previously been reported that C directly strengthens the GB bonding [20,23,26,27] and these results are supported by first principles calculations [28–30]. At the same time, C segregation is known to reduce the local O level, further leveraging the GB strengthening effect of C. Recent atom probe investigations of technically pure Mo processed by powder metallurgy (PM) revealed the presence of P, N and O segregation at a single GB as reported in [31,32].

In the present study, a variety of high-angle GBs in technically pure Mo was measured in the atom probe to overcome the challenge of the small sample volume probed. Therefore, the as-deformed and recrystallized state, which show a drastic difference in fracture behavior, were thoroughly investigated for two different Mo plates in terms of GB crystallography and chemistry. Furthermore, previous data [31,32] has been re-analyzed to obtain more accurate results by crystallography- supported atom probe reconstruction. Applying focused-ion-beam (FIB) preparation with correlative TKD enables the full crystallographic and chemical characterization of many different GBs.

9.2 Materials and methods

9.2.1 Materials

Two plates of technically pure Mo, denoted as plate 1 (thickness 40 mm) and plate 2 (thickness 48 mm), in their as-deformed and recrystallized state were used for this study. The standard PM production route of pressing, sintering, hot-rolling, and recrystallization annealing are explained elsewhere [32]. The as-deformed material state is less prone to brittle fracture than the recrystallized state and exhibit a lower DBTT as described in [14,33]. An overview of the chemical composition of the main impurities of both plates is listed in Table 1 [32,34,35]. Plate 2 can be distinguished from plate 1 by its higher O and K content. In contrast, Plate 1 exhibits a higher P content.

Table 1: Chemical composition in µg/g of main impurities of plate 1 and 2.

Element	C[b]	O[c]	N[a]	Fe[a]	P[a]	Si[a]	K[a]	Ba[a]	Al[a]	Ca[a]	W[a]
Plate 1	11	19	< 1.3	3.7	2.4	1.1	4	1.0	0.2	0.2	120
Plate 2	11	31	< 0.4	3.2	1.2	1.3	19	2.2	0.2	0.3	140

a...Glow discharge mass spectroscopy, b...Combustion analysis, c...Carrier-gas analysis

Electron backscatter diffraction (EBSD) was used to analyze the microstructure. The metallographic preparation was performed along all three direction of plate 1 by mechanical grinding and polishing followed by an electrolytic polishing with a 12.5 vol.% H_2SO_4 solution in ethanol [36]. The EBSD analyses were conducted in a FEI Versa 3D DualBeam workstation equipped with an EDAX Hikari XP EBSD system using analytical mode with a 0.8 µm step size, a 10 mm working distance, a 20 kV acceleration voltage, a current of 11 nA and a 8x8 binning. The obtained crystallographic information was evaluated using the OIM data Analysis 7 (EDAX Inc.) software.

9.2.2 Sample preparation for atom probe microscopy

Two different preparation techniques of the APM specimens containing GBs were applied:

1) FIB preparation combined with TKD of single pre-electro-polished atom probe samples as described in [37].
2) FIB-assisted site-specific preparation of particular GBs, which were pre-selected by EBSD, supported by either correlative transmission electron microscopy (TEM) or TKD during the last preparation steps of annular milling.

For technique 1, small blanks (10 × 0.3 × 0.3 mm^3) were cut from the as-deformed and recrystallized materials with their axis in normal direction (ND) of the plates. The blanks were sharpened by electro-polishing in a 12.5 vol.% H_2SO_4 solution in ethanol [38]. The annular FIB milling and TKD mapping was done in the above mentioned microscope following the procedure described in [37]. Nevertheless, no straightforward pre-selection of a particular GB type was possible with this method.

In contrast to that, technique 2 allowed for site-specific preparation by FIB using correlative TEM or TKD. The metallographic preparation for EBSD was performed in the rolling–normal direction plane. EBSD analyses were performed using analytical mode with a 1 µm step size, a 10 mm working distance, a 20 kV acceleration voltage, a current of 11nA, and a 6x6 binning. GBs with specific misorientation were selected and lifted-out according to [39]. The entire preparation process of a GB is shown and explained in Fig. 1. The final milling steps with 5 kV were either supported by correlative TEM (Fig. 1, g) or TKD (remaining samples with the parameters in [34,37], Figs. 1, h1-5). The TKD datasets in Figs. 1, h1-5, were rotated 90° to obtain a top view on the sample (rotation around axis A2 in the OIM data Analysis 7). Two samples prepared by a correlative TEM procedure were lifted-out in a Zeiss

Auriga microscope and FIB sharpened in an FEI Quanta 200 3D FIB/SEM after imaging in a 200kV FEG-TEM (JEOL 2200 FS) to check the location of the GB.

The misorientation information of the GBs was either taken from TKD maps or from EBSD (samples prepared by correlative TEM). The rotation angle and the rotation axis are used to describe the GB character. The coincidence-site-lattice (CSL) character of the investigated boundaries was determined using the Brandon criteria [40] in the OIM data Analysis 7 with n = 0.5 and K = 15.

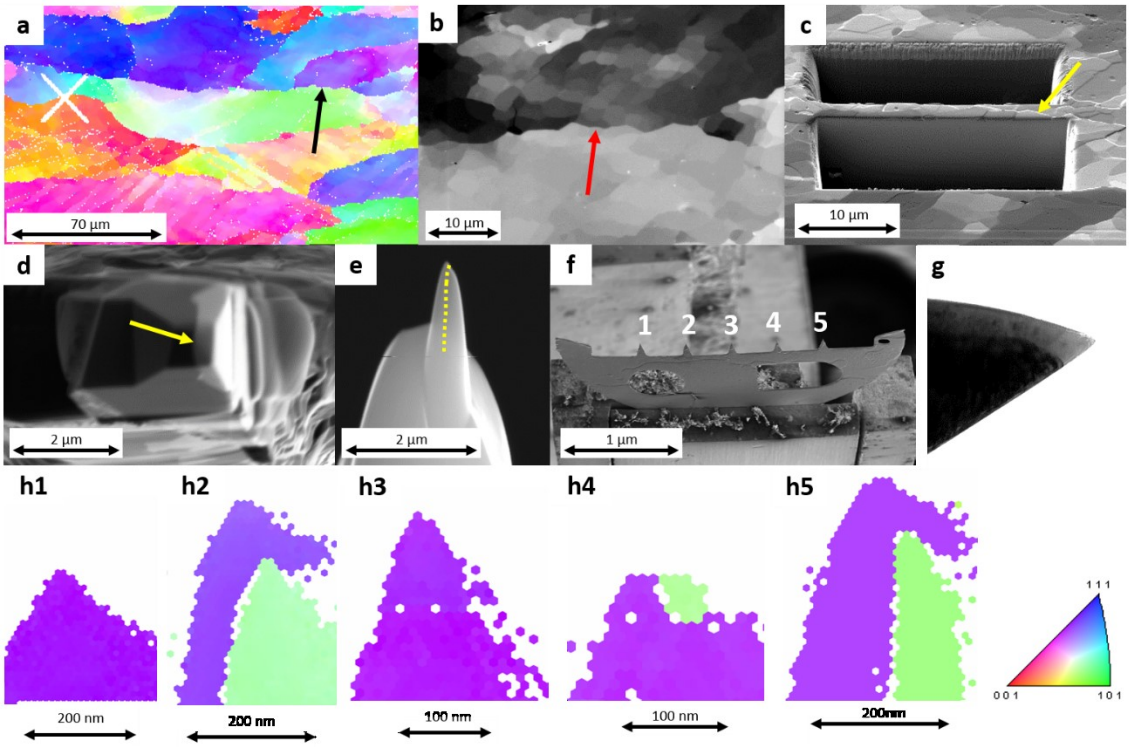

Fig. 1. Site-specific APM sample preparation of a GB with a misorientation of around 20° in the as-deformed state of Mo plate 1. The arrows mark the position of the GB. a) EBSD map for the selection of the GB; b) FIB image of the same position before the ion milling; c) final wedge after milling containing the GB; d) one of the samples after pyramidal milling; e) final shape of the APM sample after 5 kV milling. The GB is marked by yellow dots; f) a Mo grid with five positions was used as a post; g) correlative TEM to locate the GB in the first 100 nm; h1-5) correlative TKD maps of the five APM samples on the Mo grid; h2) and h5) show a GB within the first 100 nm of the sample with a misorientation angle of 22°.

9.2.3 Atom probe microscopy and data evaluation

APM samples were run in a Cameca LEAP 3000 X HR instrument in the laser mode with 0.6 nJ laser energy (525 nm laser with ~10 µm spot size), 250 kHz pulse repetition rate at a set temperature of 60 K, and a detection rate of 0.005-0.01 atoms per pulse. Due to the brittleness of Mo, the laser pulsed APT analysis was used to achieve better specimen survival. To gauge a possible influence of the laser energy on the detected amount of segregation at the GB, one GB was analyzed with varying laser energies of 0.6 and 0.3 nJ. However, no differences in detected segregation were observed. Additionally, two recrystallized specimens were analyzed in a Cameca LEAP 4000 X Si using pulsed laser field evaporation with 0.1 nJ laser energy (355 nm laser with ~2 µm spot size), 500 kHz pulse repetition rate at a temperature of 54 K, and a detection rate of 0.005-0.01 atoms per pulse. The total standing voltage during laser assisted pulsing for both instruments was in the range between 3-12 kV. The IVAS 3.6.8 software was used for the tomographic reconstruction of the obtained data. For an accurate determination of the grain boundary area analyzed, the average image compression factor and field factor were calibrated using crystallographic poles in the atom probe data of both grains as described by Gault et al. [41,42]. This reduces quantification errors to a minimum [43]. If the crystallographic features were too weak in one grain, the information of only one grain was taken for the reconstruction calibration.

For the quantification of the GB segregation content, the Gibbs interfacial excess (IFE) value in atoms/nm^2, which is insensitive to reconstruction artefacts commonly observed at grain boundaries diagrams, was determined from so-called ladder diagrams [44,45]. A cylindrical region of interest (ROI) with the largest possible diameter was positioned perpendicular to the GB so that the GB was in the center of the ROI. By plotting the cumulative number of a specific atomic species against the cumulative number of all atoms (ladder diagram), the number of excess atoms was determined and related to the surface area of the ROI. These IFE values were then compared to the measured misorientation of the GBs obtained by TKD or EBSD.

Additionally, the results previously reported in [34] and [37] were re-analyzed by calibrating the reconstruction as described above, and by calculating the IFE using ladder diagrams. These improved datasets have been added to the new results obtained in the present study.

9.2.4 First principles calculations of thermodynamic force for segregation of C versus N

First principles calculations using the Vienna Ab initio Simulation Package (VASP) [46,47] were done in order to verify thermodynamic driving forces for C versus N segregation at low-Σ CSL boundaries versus random GBs. Low-Σ GBs are specific symmetrical high-angle GBS as described by the coincidence-site-lattice model, whereas random GBs show almost no coincidence of atomic positions in both adjoining grains. The calculations of the low-Σ GBs employed projector-augmented wave method capable pseudopotentials [48] and 400 eV plane

wave cut-off energy. The reciprocal space was sampled with 4 x 2 x 6 k-points for a supercell model of the Σ5(310)[001] GB [49] with 80 atoms (each grain 40 atoms, periodic boundary conditions (PBCs)) having dimensions 2.043 nm, 1.001 nm and 0.628 nm along the <310>, <-130> and [001] directions, respectively. After a full structural relaxation (cell shape, volume and atomic positions), a solute atom (C and N) was inserted into an interstitial position at the GB (resulting total energy is denoted E_{GB}) and in the middle of the grain (E_{bulk}). A negative value of an energy difference $\Delta E = E_{GB} - E_{bulk}$ quantifies a thermodynamic force for segregation of a solute into the GB, a positive value of ΔE suggests the solute to be repelled by the GB.

While Σ GBs can be modeled in a straightforward manner, random GBs represent an obstacle for ab initio codes taking an advantage of PBCs. In order to restore the PBCs of a simulation box, vacuum was added around the whole slab containing two grains and the GB. Two different configurations with two 1 x 1 x 1 nm^3 grains (136 atoms in total) and two 1.5 x 1.5 x 1.5 nm^3 grains (452 atoms in total), respectively, and vacuum in both cases having thickness of at least 1 nm, were considered. Again, C and N solutes were inserted in the middle of the GB plane and in the grain volume, and ΔE was evaluated. To reveal the impact of the slab geometry, i.e. the presence of artificial free surfaces, the Σ5 (310)[001] GB was also modelled using the slab with two 1 x 1 x 1 nm^3 grains.

9.3 Results

9.3.1 Microstructural characterization

The microstructure of Mo plate 1, which is also representative of the microstructure of plate 2, is illustrated in Fig. 2 by EBSD maps. The as-deformed material exhibits a recovered subgrain structure with a weak rolling texture as reported in [35]. In the recrystallized material grains are close to equiaxed with an average grain size of 48 μm (plate 1) and 55 μm (plate 2) parallel to the rolling direction. Here, the total amount of GBs is much lower than in the as-deformed material.

During the atom probe sample preparation, correlative microscopy was used to determine the misorientation of investigated GBs as illustrated in Fig. 1. To get a comprehensive overview of GB segregation in Mo, several different types of GBs in both states were analyzed.

9.3.2 As-deformed material states

An overview of the solute decoration at several high-angle GBs present in the as-deformed state is shown in Fig. 3a. Typical solutes observed at Mo GBs are P, O and N. Their excess values in atoms/nm^2 are plotted for each GB which is defined by its rotation angle and axis. Connecting lines are drawn for better visualization. Fe is only detected in trace amounts at these GBs (around 0.08 atoms/nm^2) and is therefore omitted in Fig. 3.

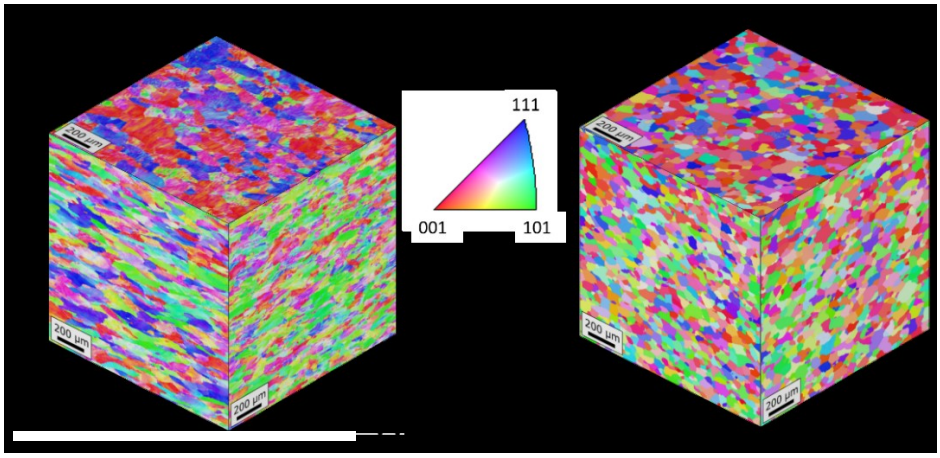

Fig. 2. Representative microstructure of Mo plate 1 in the a) as-deformed and b) recrystallized state as determined by EBSD. The insets in the middle show the inverse-pole-figure (IPF) coloring which indicates the crystal direction perpendicular to the specimen surface and the orientation of the cube with respect to the rolling process (RD rolling direction, ND normal direction, TD transverse direction).

The IFE is below 2.1 atoms/nm² for all segregated elements in all analyzed samples of as-deformed Mo. Very broadly speaking, the segregation of O and N to GBs shows a tendency to increase with an increasing GB rotation angle. However, especially the O segregation exhibits minima at the GBs with 22°, 29° and 48° rotation angle. Also, the overall content of solute atoms detected at the boundaries follows the trend with their overall concentration in each plate (see Table 1). This is reflected e.g. in the P IFE of GBs with similar rotation angle from the two different Mo plates as shown in Fig. 3b.

Similarly, GBs from plate 2 show a greater IFE of O than GBs with similar rotation angles from plate 1, which have a higher IFE for P, again reflecting the overall chemical composition of the two plates (see Fig. 3a, gray highlighted data). Furthermore, the P content at GBs of plate 2 is exceptionally low, which correlates to the total P content of 1.2 µg/g which is half of that of plate 1 (2.4 µg/g). The element N exhibits no clear trend if compared to the overall chemical composition. Except for P, N, O, and Fe, no other GB decorations were found in both plates in the as-deformed state. GBs that are close to a low-sigma GB, defined by the CSL model, are marked by an arrow in Fig. 3. The Σ33a GB with a deviation of 2° indicates no significant segregation except a slight increase of O. No unusual decoration pattern was detected at the other two GBs with a close proximity to a low-sigma GB (Σ29b with 2.3°, Σ11 with 4.2°).

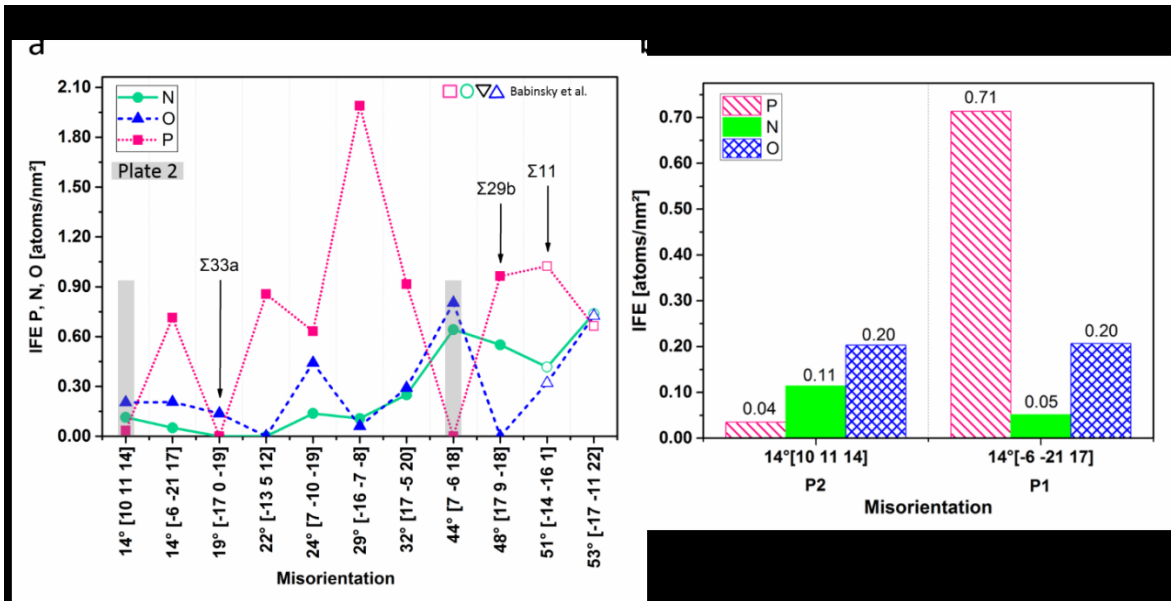

Fig. 3. a) Overview of segregation present at several GBs in the as-deformed Mo plates. The IFE in atoms/nm² of P, N and O is plotted for each GB defined by its rotation angle and axis. Analyses from plate 2 are highlighted in gray. CSL GBs are marked by arrows. Measurements from [36,106] are shown as open symbols. b) Detailed overview of the IFE of two measurements of plates 1 and 2 with the same rotation angle.

9.3.3 Recrystallized material states

The APM reconstruction of one of the recrystallized samples is shown in Figs. 4a and b. A one-dimensional concentration profile (10 nm diameter) through the interface clearly indicates the segregation of P, O and N with concentrations of 1.4 at.% for O (see Fig. 4 c). We note here that concentration values across such a concentration profile provide only a qualitative comparison due to the projection deviation inherent to APT at GBs. Accurate quantification is achieved through IFE calculations [50].

Some O and N ions were detected as complex ions together containing Mo. These complex ions were decomposed to achieve the correct O and N content for in the concentration profiles and the excess values.

Fig. 5 gives a comparison of the IFE of all analyzed high-angle GBs in the recrystallized state of technically pure Mo. Solute decorations of P, N, O, Fe, and C were detected. Their excess values in atoms/nm² are plotted for each GB, denoted by their rotation angle and axis. Analyses from Mo plate 2 are highlighted in gray.

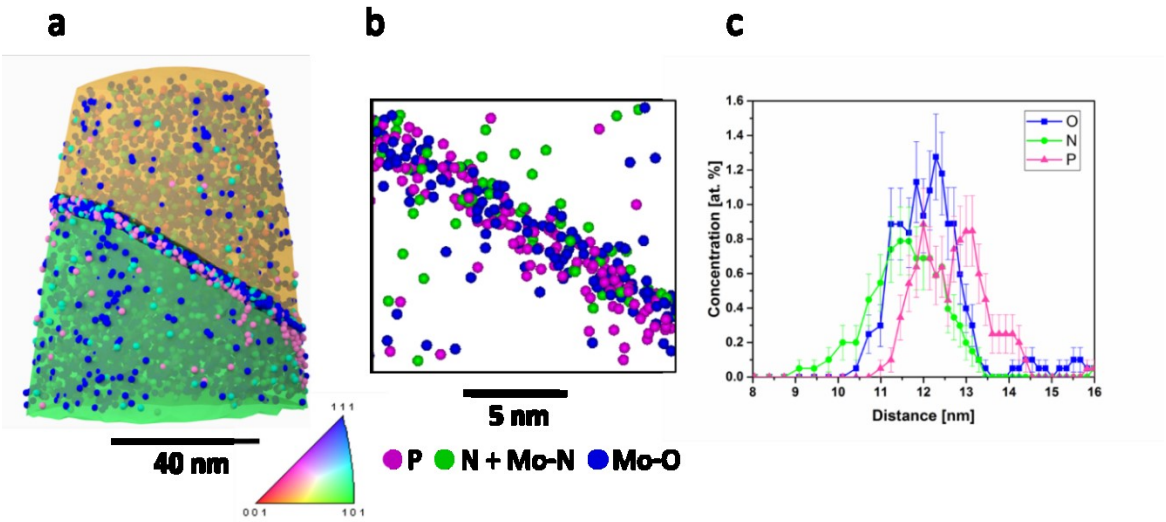

Fig. 4. a) APM-reconstruction of a measured atom probe sample with a GB of 45° rotation angle and [-7 -11 10] rotation axis (recrystallized material from Mo plate 1). The IPF coloring obtained by TKD is overlaid in the reconstruction. The Mo atoms are not shown for clarity. Some O and N ions were detected as molybdenum-molecules (Mo-N and Mo-O); b) detailed view on the grain boundary. All elements except of P, N and O are blanked; c) one-dimensional concentration profile of the interface analyzed with a 10 nm diameter cylindrical ROI through the interface.

No clear effect of the GB rotation angle on the IFE is apparent in the recrystallized state. The IFE for all segregation elements is below 2.8 atoms/nm² which is slightly higher than in the as-deformed Mo. Traces of Fe segregation were determined with an IFE below 0.07 atoms/nm² at the GB (not shown in Fig. 5). The influence of the overall solute content in the recrystallized state on the IFE is similar to the as-deformed state. In general, GBs from Mo plate 2 (32° [-8 -1 19], 43°[-14 25 -5], 55°[-11 -1 -10]) show a tendency to higher IFE for O and lower IFE for P which correlates with high overall O and low overall P concentrations.

Figure 6a illustrates the IFE values of C over the GB rotation angle. It is evident that the low-Σ GBs (Σ3 with 7° deviations and Σ5 with deviation of 5.6°) exhibit an increased segregation of C with 12.2 atoms/nm² for Σ5. Additionally, two random GBs with 15° and 24° rotation angle show IFE values between 1.4-2.7 atoms/nm². In Figs. 6b and c the APM reconstruction of the analyzed Σ3 (57° [-6 7 -8]) is presented. Solutes of P, N and O and traces of Fe were detected at this interface, however, additional C segregation is present here. Two GBs with rotation angles of 15° and 24° exhibit higher solute decorations of C. We note here that the preparation process of these GBs was different. These samples were prepared in a Zeiss Auriga and a FEI Quanta FIB with correlative TEM. It is possible that the electron beam causes carbon contaminations that increases the IFE of C at these random GBs.

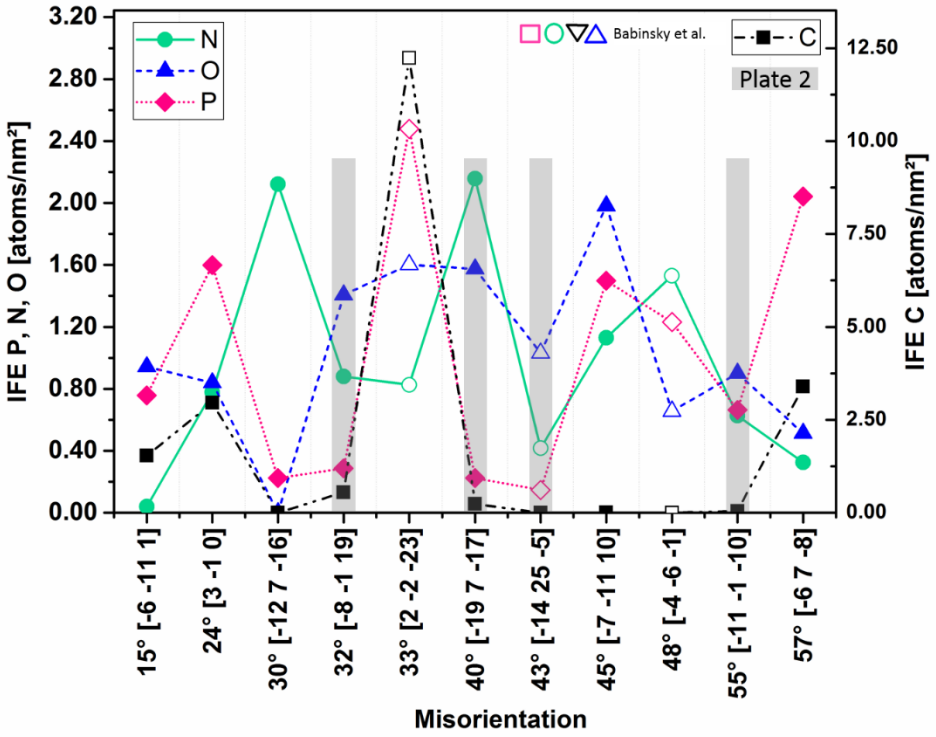

Fig. 5. Overview of GB segregation at several GB types present in the recrystallized Mo plates. The IFE in atoms/nm^2 of P, N, O, and C is plotted for each GB defined by its rotation angle and axis. (P, N and O are plotted on the left axis, C is plotted on the right axis). Analyses from plate 2 are highlighted in gray. Measurements from [36,106] are shown as open symbols.

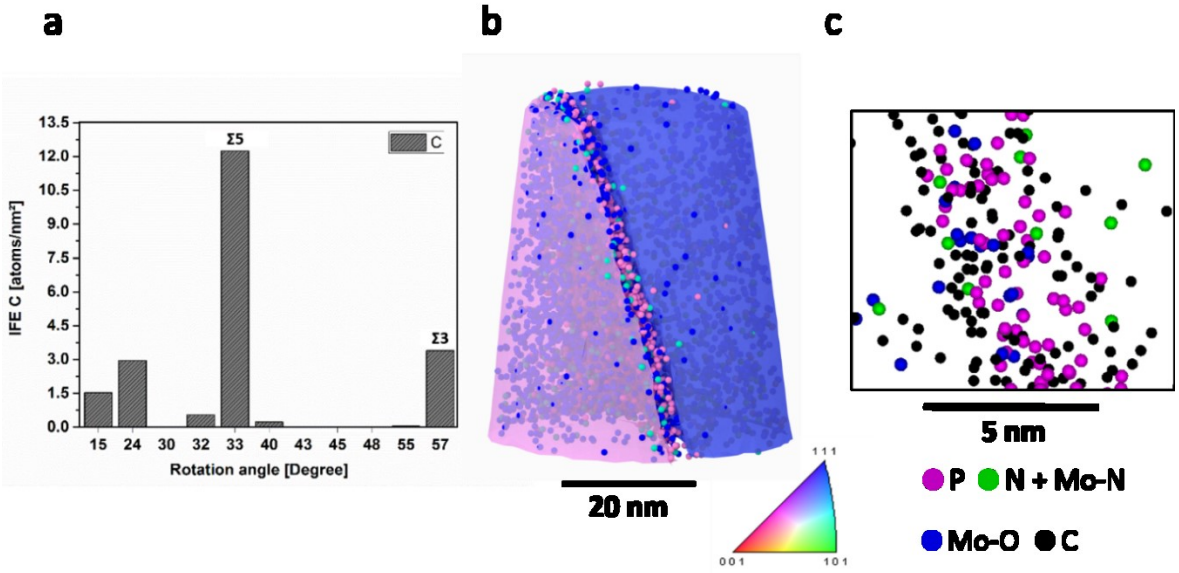

Fig. 6. a) Bar chart of the IFE of C atoms as a function of the GB rotation angle in the recrystallized state already shown in Fig. 5; b) APM-reconstruction of the measured Σ3 GB with 57°[-6 7 -8]. The IPF coloring obtained by TKD is overlaid in the reconstruction. Mo atoms are blanked for a better visibility. Some O and N ions were detected as molybdenum-molecules (Mo-N and Mo-O); c) detailed image of the GB showing P, N, O, and C.

9.3.4 First principles calculations of thermodynamic force for segregation of C versus N

The first principles calculation of enrichments at low-Σ GBs predicted $\Delta E(C, \Sigma)$=-2.15 eV in the case of C and $\Delta E(N, \Sigma)$=-1.51 eV for N (Table 2). Interestingly, when calculated using the slab geometry, C still prefers to segregate to GBs (ΔE<0 eV), while N prefers to remain in the grain interior. In case of random GBs, the obtained values for the smaller slab (136 atoms) were ΔE(N, random)=-0.53 eV and ΔE(C, random)=-1.32 eV for N and C, respectively. The calculations with a larger slab suggest that ΔE(N, random) gets more negative (~-0.9 eV) while ΔE(C) becomes less negative (~-1.15 eV) as compared to the smaller slab of 136 atoms, i.e. converging to similar values with an increasing supercell size. The obtained ΔE values are summarized in Table 2.

Table 2: Calculated $\Delta E(X)=E_{GB}-E_{bulk}$ values for N and C of Σ5(310)[001] and random GBs by first principle calculations. $\Delta E(X)$<0 eV suggests segregation of X into the GB.

	Σ GB	random GB (136 atoms)	random GB (452 atoms)
ΔE (C)	-2.15 eV	-1.32 eV	~-1.15 eV
ΔE (N)	-1.51 eV	-0.53 eV	~-0.9 eV

9.3.5 Comparison of as-deformed and recrystallized materials

In order, to compare the as-deformed and recrystallized material states, the total IFE of all solute elements at each GB is plotted over the GBs rotation angle in Fig. 7a. In general, the amount of segregation in the as-deformed materials slightly increases with the GBs rotation angle. In the recrystallized materials no dependency on the rotation angle is apparent, but an increase of the amount of segregation compared to the as-deformed materials is visible. In general, the recrystallized state exhibits larger variations in the total amount of segregation content than the as-deformed state. A closer view of GBs with the same rotation angle in both material states (see Fig. 7b) reveals, that Mo exhibits a higher IFE at GBs in the recrystallized state than the as-deformed state.

9.4 Discussion

In order to study the segregation phenomena in technically pure Mo a detailed APM analysis of several high-angle GBs in the as-deformed and recrystallized state was conducted. In addition, our previous measurements in [32,37] and [34] were re-analyzed for a comprehensive overview of solute decorations at GBs in an industrially PM processed Mo by characterizing the IFE values in correlation with the GBs rotation angle and axis.

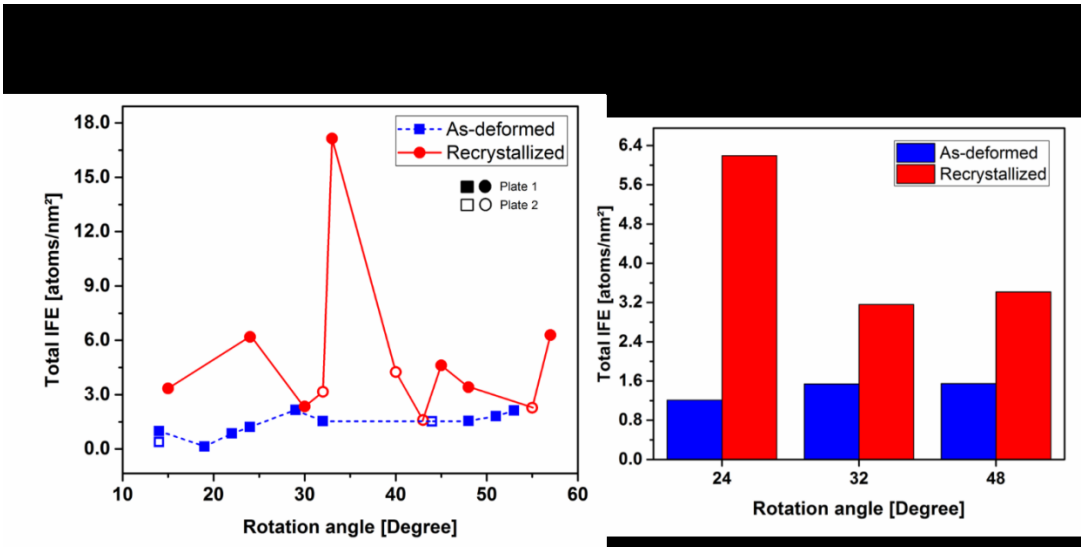

Fig. 7: a) Total IFE in atoms/nm² of as-deformed versus recrystallized materials plotted over the rotation angle of analyzed Mo GBs. Plates 1 and 2 are marked with different symbols. b) IFE of three GBs with different rotation angles which were measured in both states. The IFE is plotted over the GBs rotation angle.

9.4.1 Segregation in as-deformed material states

Several high-angle GBs with rotation angles between 14° and 53° were analyzed in the as-deformed state. Apart from the CLS Σ33a GB, all other GBs exhibit a certain amount of solute decorations of P, N, O, and Fe. Fe has a distinctly low IFE (0.08 atoms/nm²) because of the increased bulk solubility in Mo. The interstitial solute elements N and O show nearly no solubility in Mo (N: 0.001 at.% at RT, O: 0.002 at.% at RT) which leads to higher enrichments at GBs with IFE values of up to 0.9 atoms/nm² [51,52]. P with the highest IFE up to 2.1 atoms/nm² is substitutional in the bulk but is suspected to segregate to interstitial sites at the GB [30]. Very low bulk solubility explains the high segregation tendency of the P atoms which are present in the material [53], although the overall concentration is lower than for Fe. The IFE of O and N increase with increasing rotation angle of the GB. Also the total IFE slightly increases with the rotation angle as presented in Fig. 7a. Higher rotation angles may result in larger GB free volumes which, in turn, offer more space for solutes. However, the precise atomic structure of each GB, which is not known and may vary with solute decoration and history, defines the amount of solutes it may accommodate. Therefore, the same rotation angle shall not unconditionally lead to the same solute decoration behavior at the interface. Furthermore, the overall concentration of solutes in the starting material seems to influence the amount of GB segregation significantly [6]. A high overall concentration of a specific element with low bulk solubility lead to a high IFE value at the GB. The P and O segregation contents show a clear trend with the overall chemical composition of the starting material which is visible in Figs. 3a and b.

9.4.2 Segregation in recrystallized material states

Several high-angle GBs with rotation angles between 15° and 58° of the recrystallized material states were characterized. Most of the GBs of recrystallized Mo exhibit the same solute decorations (P, N, O, and Fe) as in the as-deformed material states. The amount of solute decorations in this material state shows the same dependency with bulk solubility and overall concentration as the as-deformed state. However, the overall amount of segregation is much higher than in the as-deformed state. In the deformed microstructure, a wide distribution of solutes over a large GB area is possible due to the presence of numerous subgrain boundaries and GBs. Recrystallization leads to an increase of the overall grain size, hence, less GB volume is available to accommodate solutes.

By using the following equations

$$n^{GB}_{Foreign\ atom} = A_{Grains} \cdot IFE_{Foreign\ atom} = \frac{6 \cdot V}{d} \cdot IFE_{Foreign\ atom} \quad (1)$$

$$n^{Total\ amount}_{Foreign\ atom} = 2 \cdot \frac{V}{a^3_{Mo}} \cdot c_{Foreign\ atom} \quad (2)$$

the average fraction of segregated solutes ($\frac{n^{GB}_{Foreign\ atom}}{n^{Total\ amount}_{Foreign\ atom}}$) in both material states for P, N and O can be estimated. In this equations V defines the volume of a sphere (approximation to grain shape) with d as grain size diameter to estimate the grain boundary area. Therefore, the average IFE of each segregation is used as well as an average grain size of both plates. Additionally, it is estimated that the segregation behavior at each GB is similar. In Table 3 it can be seen that unquestionably not all foreign atoms segregate to GBs. O atoms are distributed over several micro-pores in the structure [31] which leads to a very low fraction at the GBs. In general, the amount of segregated atoms in both material states seems to be similar except of N. In the recrystallized state N and P atoms strongly segregate to the GB, whereas Fe, which has a solubility in Mo, stay in the grain interior causing a low fraction.

Table 3: Average fraction of segregated solutes of the as-deformed and recrystallized state of technically pure Mo plates.

	Average grain	Average IFE [atoms/nm²]					Fraction of segregated solutes [%]				
State	size [µm]	P	N	O	C	Fe	P	N	O	C	Fe
As-deformed	49.46	0.71	0.27	0.29	-	0.02	24.03	8.88	0.37	0.00	0.73
Recrystallized	51.50	1.01	0.98	1.04	1.91	0.02	33.01	30.72	1.26	3.94	0.54

By comparing the IFE with the rotation angle in the recrystallized state, no specific pattern is obvious. It seems that the segregation behavior is more or less random when the IFE and rotation angle are correlated. This may be explained in terms of the history of GB migration during recrystallization. Recrystallization usually means preferential growth of specific grain orientations which is also known as selected growth mechanism [54]. During recrystallization each front (GB) presumably drags solutes from its local surroundings, hence, each individual front may pick-up specific solute decorations. If the recrystallization front migrates through

many other as-deformed GBs with high IFE, the migrating GB will have a high enrichment of solute decorations.

In conclusion, the IFE of each GB in the recrystallized state is mainly influenced by the GB migration history, the overall chemical composition of the starting material and the available GB volume. Nevertheless, the amount of GB segregation is also defined by the specific atomic structure of each GB. In general, the recrystallized material state shows a higher IFE than the as-deformed state which explains the increased brittleness.

9.4.3 Carbon versus nitrogen segregation to CSL-grain boundaries

In addition to the solute decorations of P, N, O, and Fe, exceptionally high segregation of C was measured at low-Σ GBs in the recrystallized material states. It seems that C preferentially segregates at GBs with a highly ordered structure. A high amount of possible octahedral gaps at such low-Σ GBs can increase the driving force for C segregation. Unexpectedly, C segregation can only be detected in the recrystallized state. The as-deformed structure exhibits many dislocations, subgrain and GBs (see Fig. 1a) where C can easily distribute over a large area. This wide distribution of C causes a low IFE which may not be detectable in the atom probe. After recrystallization, the materials contain a very low number of subgrain boundaries and dislocations, therefore, C segregates to its preferential sites in this structure, namely the low-Σ GBs. Two other GBs also show an increase of C but this enrichment can be linked to contaminations during the preparation process likely from electron beam penetration. It is apparent that the preparation procedure has a significant influence on the segregation behavior but a careful analysis of the observed data values as performed here (see Section 3.3) allows to filter this impact out.

The first principles calculations to verify the trend of more favorable C versus N enrichments at the low-Σ GBs predicted $\Delta E(C, \Sigma)$=-2.15 eV which is smaller than $\Delta E(N, \Sigma)$=-1.51 eV. While in both cases, segregation at the GBs is predicted, the thermodynamic driving force for C segregation is much larger than for N. This is well in accordance with the evaluated IFE of low-Σ CSL GBs in the recrystallized state (see Fig. 5) showing that the amount of C is an order of magnitude larger than that of N.

Also in the case of random GBs, the obtained values confirm the stronger segregation tendency of C when compared to N (cf. Table 2). The calculations also suggest that the difference between ΔE for low-Σ GBs and random GBs is significantly larger for C than for N, suggesting that C should strongly prefer to segregate to low-Σ GBs. These results are in line with the segregation trend as observed by APM (see Fig. 5).

Interestingly, using the slab geometry also for the low-Σ GBs, C still preferably segregates to GBs (ΔE<0 eV), while N prefers to remain in the grain interior. This may be interpreted as N being strongly attracted to the free surface (present due to the slab geometry in our model, see section “2.4.”). Indeed, such situations appear experimentally in PM produced materials

due to the presence of micro-voids in the specimens [31,32]. The free surface of voids present additional segregation places for N, consequently, the amount of N present at GBs is further lowered.

9.4.4 Towards grain boundary segregation engineering of Mo

The comprehensive atom probe study of several high-angle GBs presented shows that P, N, O, Fe, and C are the characteristic solute decorations present in industrial PM produced technically pure Mo. All detected elements except C indicate a detrimental effect on the GB energy and strength. The detection of O at the interfaces is in good agreement with the literature. Waugh and Southon [21,22] reported O as typical segregation element in Mo, however, it is well known that this element weakens the GBs bond [19]. However, most of the O impurities are supposed to be located in micropores of these plates [31] which were former sinter-pores that were compressed during rolling. Additionally, nanometer-sized regions close to GBs exist which contain remaining trace elements of such micro-pores [32]. Also N, which decreases the fracture energy [49,55], was detected in sintered PM produced Mo besides of S, O, and C segregation by means of AES [56]. First principles calculations do not confirm a strong interaction of N segregation with the intense embrittlement of Mo. AES measurements of recrystallized Mo [31] reported no N solutes at GBs, but P segregation is assumed. In this study, solute decorations of P, which exhibits a detrimental effect according to calculations [30], were detected at most of the GBs. Also, in PM produced pure W Joshi and Stein [57] reported P segregation at GBs which was correlated with the occurrence of embrittlement. However, Gludovatz et al. [58] revealed the same results in W by AES, but excluded the direct effect of segregated P on the ductility and strength.

The present study shows that the material´s overall chemical composition is the main factor influencing the IFE. A high content of solutes connected with a low bulk solubility causes high GB enrichment. To reduce the detrimental presence of O at the GBs, a low overall concentration is required. It is also revealed that the IFE can be controlled by reducing the grain size. The smaller the grain size, the larger the GB volume is, thus, decreasing the segregation concentration. Additionally, it is evident that a high amount of GBs with high rotation angles in the as-deformed state are undesirable due to their increased segregation content. Recrystallized microstructures should have a high amount of low-Σ CSL GBs due to the beneficial effect of C on ductility and strength [20,23,26,27]. However, it is unclear if the amount of C at the GBs in the current study is sufficient to achieve these positive effects. Additionally, it seems that the C enrichments are too low to replace O at the GBs.

9.5 Conclusions

Several high-angle GBs in the as-deformed and recrystallized state of two industrial PM produced technically pure Mo plates were characterized by using APM. Crystallographic information of GBs from TKD was correlated with the segregation contents from IFE:

- The GBs of the as-deformed material states exhibit P, N, and O solute decorations with additional traces of Fe. The segregation of N and O show an increase of the IFE with increasing GB rotation angle.
- The GBs of the recrystallized state exhibit the same solute decorations as in the as-deformed state, but there is no direct correlation to the GB rotation angle. This is thought to be the GB migration history during recrystallization.
- Because of the lower amount of available GB volume after recrystallization a higher IFE of solute decorations at individual GBs was observed than in the as-deformed material states. This can explain the pronounced intergranular brittleness of the recrystallized state.
- Additional C segregation at low-Σ GBs of the recrystallized state (excess values up to 12.5 atoms/nm^2) can be explained in terms of its thermodynamic force predicted by first principles calculations.
- All types of segregating elements in the studied PM produced Mo plates indicate a detrimental effect on the GB energy and strength except for C. A high fraction of low-Σ GBs with C decorations may have a positive effect on the materials ductility and strength.

For grain boundary segregation engineering as a potential materials design method, the overall P, N and O contents must be decreased while certain solute contents of C may be favorable.

Additionally, the segregation content can be controlled by decreasing the grain size and the overall chemical composition of detrimental solutes. The intrinsically weak GBs of Mo can be further deteriorated by specific GB segregation. Removing these weakening elements may help to increase the GB strength to achieve improved materials properties, thus enlarging the application of Mo as structural and functional material.

Acknowledgements

The authors want to acknowledge the fruitful discussions about the reconstruction of atom probe data sets with S. P. Ringer, A. J. Breen and A. V. Ceguerra. Special thanks to V. Maier-Kiener, A. Leitner and T. Leitner for their help in all belongings. The computational results presented have been achieved using the Vienna Scientific Cluster (VSC).

References

[1] D. Raabe, S. Sandlöbes, J. Millán, D. Ponge, H. Assadi, M. Herbig, et al., Segregation engineering enables nanoscale martensite to austenite phase transformation at grain boundaries: A pathway to ductile martensite, Acta Materialia. 61 (2013) 6132–6152.

[2] D. Raabe, M. Herbig, S. Sandlöbes, Y. Li, D. Tytko, M. Kuzmina, et al., Grain boundary segregation engineering in metallic alloys: A pathway to the design of interfaces, Current Opinion in Solid State and Materials Science. 18 (2014) 253–261.

[3] P. Lejcek, S. Hofmann, A. Krajnikov, Chemical aspects of brittle fracture: grain boundary segregation, Materials Science and Engineering: A. 234-236 (1997) 283–286.

[4] B.V. Cockeram, E.K. Ohriner, T.S. Byun, M.K. Miller, L.L. Snead, Weldable ductile molybdenum alloy development, Journal of Nuclear Materials. 382 (2008) 229–241.

[5] T. Watanabe, S. Tsurekawa, The control of brittleness and development of desirable mechanical properties in polycrystalline systems by grain boundary engineering, Acta Materialia. 47 (1999) 4171–4185.

[6] M.P. Seah, E.D. Hondros, Grain Boundary Segregation, Proceedings of the Royal Society A: Mathematical, Physical and Engineering Sciences. 335 (1973) 191–212.

[7] P. Lejcek, Grain Boundary Segregation in Metals, Springer Berlin Heidelberg, Berlin, Heidelberg, 2010.

[8] M.P. Seah, Grain boundary segregation, Journal of Physics F: Metal Physics. 10 (1980) 1043–1064.

[9] M. Herbig, D. Raabe, Y.J. Li, P. Choi, S. Zaefferer, S. Goto, Atomic-scale quantification of grain boundary segregation in nanocrystalline material, Physical Review Letters. 112 (2013) 1–5.

[10] S. Mandal, K.G. Pradeep, S. Zaefferer, D. Raabe, A novel approach to measure grain boundary segregation in bulk polycrystalline materials in dependence of the boundaries' five rotational degrees of freedom, Scripta Materialia. 81 (2014) 16–19.

[11] M. Herbig, P. Choi, D. Raabe, Combining structural and chemical information at the nanometer scale by correlative transmission electron microscopy and atom probe tomography, Ultramicroscopy. 153 (2015) 32–39.

[12] A.J. Breen, K. Babinsky, A.C. Day, K. Eder, C.J. Oakman, P.W. Trimby, et al., Correlating Atom Probe Crystallographic Measurements with Transmission Kikuchi Diffraction Data, Microsc. Microanal. 0 (2017) 1–12.

[13] W. Martienssen, H. Warlimont, Springer Handbook of Condensed Matter and Materials Data, Springer, Berlin, Heidelberg, New York, 2005.

[14] K. Babinsky, S. Primig, W. Knabl, A. Lorich, R. Stickler, H. Clemens, Fracture Behavior and Delamination Toughening of Molybdenum in Charpy Impact Tests, JOM. 68 (2016) 2854–2863. [15] A.J. Bryhan, Joining of Molybdenum Base Metals and Factors Which lnfluence Ductility, WRC Bulletin. 312 (1986) 21.

[16] J.B. Brosse, R. Fillet, M. Biscondi, Intrinsic intergranular brittleness of molybdenum, Scripta Metallurgica. 15 (1981) 619–623.

[17] S. Tsurekawa, T. Tanaka, H. Yoshinaga, Grain boundary structure, energy and strength in molybdenum, Materials Science and Engineering: A. 176 (1994) 341–348.

[18] S. Tsurekawa, S. Kokubun, T. Watanabe, Effect of grain boundary microstructures of brittle fracture in polycrystalline molybdenum, Materials Science Forum. 304-306 (1999) 687–692.

[19] M. Oku, S. Suzuki, H. Kurishita, H. Yoshinaga, Chemical states of oxygen segregated intergranular fracture surfaces of molybdenum, Applied Surface Science. 26 (1986) 42–50.

[20] A. Kumar, B.L. Eyre, Grain Boundary Segregation and Intergranular Fracture in Molybdenum, Proceedings of the Royal Society A: Mathematical, Physical and Engineering Sciences. 370 (1980) 431–458.

[21] A.R. Waugh, M.J. Southon, Surface studies with an imaging atom-probe, Surface Science. 68 (1977) 79–85.

[22] A.R. Waugh, M.J. Southon, Surface analysis and grain-boundary segregation measurements using atom-probe techniques, Surface Science. 89 (1979) 718–724.

[23] M.K. Miller, H. Kurishita, APFIM Characterization of Grain Boundary Segregation in Titanium Carbide-Doped Molybdenum, Le Journal de Physique IV. 6 (2008) 1–6.

[24] M.K. Miller, E.A. Kenik, M.S. Mousa, K.F. Russell, A.J. Bryhan, Improvement in the ductility of molybdenum alloys due to grain boundary segregation, Scripta Materialia. 46 (2002) 299–303.

[25] M.K. Miller, A.J. Bryhan, Effect of Zr, B and C additions on the ductility of molybdenum, Materials Science and Engineering A. 327 (2002) 80–83.

[26] S. Suzuki, H. Matsui, H. Kimura, The effect of heat treatment on the grain boundary fracture of recrystallized molybdenum, Materials Science and Engineering. 47 (1981) 209–216.

[27] A. Krajnikov, A. Drachinskiy, V. Slyunyaev, Grain boundary segregation in recrystallized molybdenum alloys and its effect on brittle intergranular fracture, International Journal of Refractory Metals and Hard Materials. 11 (1992) 175–180.

[28] A. Tahir, R. Janisch, A. Hartmaier, Ab initio calculation of traction separation laws for a grain boundary in molybdenum with segregated C impurites, Modelling and Simulation in Materials Science and Engineering. 21 (2013) 075005.

[29] D. Scheiber, R. Pippan, P. Puschnig, A. V. Ruban, L. Romaner, Ab-initio search for cohesion-enhancing solute elements at grain boundaries in molybdenum and tungsten, International Journal of Refractory Metals and Hard Materials. 60 (2016) 75–81.

[30] D. Scheiber, R. Pippan, P. Puschnig, A. Ruban, L. Romaner, Ab-initio search for cohesion-enhancing solute elements at grain boundaries in molybdenum and tungsten, International Journal of Refractory Metals and Hard Materials. 60 (2016) 75–81. doi:10.1016/j.ijrmhm.2016.07.003.

[31] K. Babinsky, S. Primig, W. Knabl, A. Lorich, T. Weingärtner, J. Weidow, et al., Grain boundary segregations in technically pure molybdenum, in: 18. Planseeseminar, Plansee SE, 2013: pp. RM111/1–15.

[32] K. Babinsky, J. Weidow, W. Knabl, A. Lorich, H. Leitner, S. Primig, Atom probe study of grain boundary segregation in technically pure molybdenum, Materials Characterization. 87 (2014) 95–103.

[33] E. Pink, R. Eck, Refractory metals and their alloys, in: R.W. Cahn, P. Haasen, E.J. Kramer, K.H. Matucha (Eds.), Materials Science and Technology, VCH, Weinheim, New York, Basel, Cambridge, Tokyo, 2006: pp. 591–638.

[34] K. Babinsky, W. Knabl, A. Lorich, R. De Kloe, H. Clemens, S. Primig, Grain boundary study of technically pure molybdenum by combining APT and TKD, Ultramicroscopy. 159 (2015) 445–451.

[35] S. Primig, H. Leitner, W. Knabl, Textural Evolution During Dynamic Recovery and Static Recrystallization of Molybdenum, Metallurgical and Materials Transactions A. 43 (2012) 4794–4805.

[36] S. Primig, H. Leitner, A. Lorich, W. Knabl, H. Clemens, R. Stickler, SEM and TEM investigations of recovery and recrystallization in technically pure molybdenum, in: Praktische Metallographie Sonderband 42, 2010: pp. 289–294.

[37] K. Babinsky, R. De Kloe, H. Clemens, S. Primig, A novel approach for site-specific atom probe specimen preparation by focused ion beam and transmission electron backscatter diffraction, Ultramicroscopy. 144 (2014) 9–18.

[38] M.K. Miller, A. Cerezo, M.G. Hetherington, G.D.W. Smith, Atom probe field ion microscopy, Clarendon Press, Oxford, 1996.

[39] P.J. Felfer, T. Alam, S.P. Ringer, J.M. Cairney, A reproducible method for damage-free site-specific preparation of atom probe tips from interfaces, Microscopy Research and Technique. 75 (2012) 484–491.

[40] D.G. Brandon, The structure of high-angle grain boundaries, Acta Metallurgica. 14 (1966) 1479–1484.

[41] B. Gault, M.P. Moody, F. De Geuser, G. Tsafnat, A. La Fontaine, L.T. Stephenson, et al., Advances in the calibration of atom probe tomographic reconstruction, Journal of Applied Physics. 105 (2009).

[42] B. Gault, F. de Geuser, L.T. Stephenson, M.P. Moody, B.C. Muddle, S.P. Ringer, Estimation of the Reconstruction Parameters for Atom Probe Tomography, Microscopy and Microanalysis. 14 (2008) 296–305.

[43] P.J. Felfer, C.R. Killmore, J.G. Williams, K.R. Carpenter, S.P. Ringer, J.M. Cairney, A quantitative atom probe study of the Nb excess at prior austenite grain boundaries in a Nb microalloyed strip-cast steel, Acta Materialia. 60 (2012) 5049–5055.

[44] D.N. Seidman, J.G. Hu, S.-M. Kuo, B.W. Krakauer, Y. Oh, A. Seki, Atomic resolution studies of solute-atom segregation at grain boundaries: Experiments and Monte Carlo simulations, Le Journal de Physique Colloques. 51 (1990) C1–47–C1–57.

[45] M. Thuvander, H.-O. Andrén, APFIM studies of grain and phase boundaries: a review, Materials Characterization. 44 (2000) 87–100.

[46] G. Kresse, J. Furthmüller, Efficient iterative schemes for ab initio total-energy calculations using a plane-wave basis set, Physical Review B. 54 (1996) 11169–11186.

[47] G. Kresse, J. Furthmüller, Efficiency of ab-initio total energy calculations for metals and semiconductors using a plane-wave basis set, Computational Materials Science. 6 (1996) 15–50.

[48] G. Kresse, From ultrasoft pseudopotentials to the projector augmented-wave method, Physical Review B. 59 (1999) 1758–1775.

[49] R. Janisch, C. Elsässer, Segregated light elements at grain boundaries in niobium and molybdenum, Physical Review B. 67 (2003) 224101.

[50] B. Gault, M. Moody, J. Cairney, S. Ringer, Atom probe microscopy, Springer, 2012.

[51] P. Villars, H. Okamoto, eds., Mo-N Binary Phase Diagram 0-0.1 at.% N, (n.d.). http://materials.springer.com/isp/phase-diagram/docs/c_0903138, January 2017

[52] P. Villars, H. Okamoto, eds., Mo-O Binary Phase Diagram 0-0.12 at.% O, (n.d.). http://materials.springer.com/isp/phase-diagram/docs/c_0903137, January 2017

[53] B. Predel, Mo-P (Molybdenum-Phosphorus), in: O. Madelung (Ed.), Li-Mg – Nd-Zr, Springer-Verlag, Berlin/Heidelberg, n.d.: pp. 1–2.

[54] D. Juul Jensen, Growth rates and misorientation relationships between growing nuclei/grains and the surrounding deformed matrix during recrystallization, Acta Metallurgica Et Materialia. 43 (1995) 4117–4129.

[55] Y. Hiraoka, B. Edwards, B. Eyre, Effects of Nitrogen on Grain Boundary Fracture in Molybdenum, Materials Science Forum. 126-128 (1993) 153–156.

[56] S.M. Tuominen, S.P. Clough, Grain boundary segregation of sulfur and nitrogen in sintered molybdenum, Metallurgical Transactions A. 10 (1979) 127–129.

[57] A. Joshi, D.F. Stein, Intergranular brittleness studies in tungsten using Auger spectroscopy, Metallurgical Transactions. 1 (1970) 2543–2546.

[58] B. Gludovatz, S. Wurster, T. Weingärtner, a. Hoffmann, R. Pippan, Influence of impurities on the fracture behaviour of tungsten, Philosophical Magazine. 91 (2011) 3006–3020.

10 Publication E

Materials by design: engineering grain boundary chemistry in molybdenum

K. Leitner[1], D. Scheiber[2], S. Primig[1, 3], H. Clemens[1], E. Povoden-Karadeniz[4], L. Romaner[2]

1 Department of Physical Metallurgy and Materials Testing, Montanuniversität Leoben, Austria
2 Materials Center Leoben Forschung GmbH, Roseggerstraße 12, 8700 Leoben, Austria
3 School of Materials Science & Engineering, UNSW Australia, Sydney NSW 2052, Australia
4 Institute of Materials Science and Technology, TU Wien, Vienna, Austria

Abstract

We present an investigation about the relationship between grain boundary chemistry and fracture behavior in a metallic alloy at an unprecedented level of accuracy. By combining atom probe tomography and ab-initio simulations of grain boundaries (GBs) we unravel the origin for the transition between intergranular and transgranular fracture upon alloying in a specific class of technological Mo-Hf model alloys. We show that the main agents affecting grain boundary strength are not the primary alloying element, Hf, but rather the impurities O, C, and B. With larger Hf additions, an intricate interplay between segregation and precipitation leads to a strong enrichment of C and B at the GBs and to a depletion of O and Hf which eventually results in higher cohesion of GBs and in a change in fracture mode. Our investigation exemplarily demonstrates that smallest additions of solutes can be decisive and can significantly control mechanical materials behavior on the macroscale. Although, local chemical composition of GBs is challenging to predict and detect, it must be taken into account for knowledge-based materials engineering of the future.

10.1 Introduction

Since thousands of years, materials design has been pushed forward by trial and error and the questions why the addition of one element increases material performance or why a specific temperature treatment deteriorates a material remained often unanswered [1–3]. In the last century, with the rise of modern technology for experimental and theoretical investigations, the systematic unraveling of the underlying phenomena becomes possible. In this context, atom resolved methods such as atom probe tomography (APT) and even more recent ab-initio modelling of materials form the forefront of present-day materials design [4,5].

Materials design is necessary to fulfill the pressing need for excellent materials. For high-temperature, high-strength, lighting, electronic and coating applications, Mo is the first choice due to its exceptional material properties. Yet at room temperature and below, Mo exhibits brittle fracture that runs mainly along grain boundaries (GBs) [6–8]. We have recently shown that this preferred intergranular fracture correlates with a particularly low ratio of GB cohesion to bulk cohesion from and ab-initio point of view [9]. The task for materials design is to find strategies to impede crack propagation along the GBs by suitable GB engineering.

Different approaches to increase the GB cohesion in Mo have been discussed, e.g. a controlled distribution of GBs in the material with a focus on GBs with high cohesion [10], increasing the number of GBs in the material (nano-crystalline) [11] or via segregation of GB cohesion enhancing elements to GBs [12,13]. Especially the introduction of GB cohesion enhancing elements has high potential for Mo, but also for many other technologically relevant materials.

In this work, we investigate a series of Mo alloys with increasing Hf content, which primary were used to study the solution-solution hardening [14] and softening [15] effect of Hf in Mo to understand the strengthening behavior of the Mo based alloy MHC . Incidentally, a change in fracture mode from intergranular to transgranular fracture was observed with increasing Hf content. The first and obvious explanation that Hf segregates to GBs and increases GB cohesion is unlikely to be valid as ab-initio calculations [12] show a reduction of GB cohesion with Hf segregation. We reveal the true underlying phenomena of the increasing GB cohesion with increasing bulk Hf content with a combined experimental and theoretical approach. From the experimental side, mechanical fracture tests of the different samples are applied and APT experiments of an unprecedented number of GBs is performed. From theoretical side, a GB with various elements at the GB is modelled using ab-initio density functional theory and a kinetic segregation model is applied.

10.2 Methodology

10.2.1 Alloy production

For this study, six different molybdenum alloys (A0–A5) were produced by a typical powder metallurgical (PM) production route of pressing, sintering, and forging followed by a recrystallization annealing for 1h. Alloys A1-A3 were recrystallized at 1600°C and alloys A4 and A5 at 2000°C. A detailed description of the processing procedure is given elsewhere [14,15]. Alloy A0 represents the references material, a technically pure Mo plate produced by the PM production route specified in Babinsky et al. [16].

10.2.2 Characterization

The chemical composition of the alloying element Hf was analyzed by inductively coupled plasma-optical atom emission spectroscopy (ICP-OES). The amount of C was detected by the combustion analysis (CE) and the amount of O was studied by carrier gas hot extraction (CGHE). The glow discharge mass spectroscopy (GDMS) was used to verify the amount of impurities with very low concentrations as for example B and Fe. However, it must be noted that a deviation of factor of two for the true values of the GDMS-analyses can be possible. The grain size was determined by Pöhl et al. [15] using the linear intercept method (ASTM E112) with optical micrographs. The fracture surfaces were investigated by a Zeiss EVO 50. The electron backscatter diffraction (EBSD) characterizations were performed in a FEI Versa 3D DualBeam workstation equipped with an EDAX Hikari XP EBSD system with the OIM data collection 7 and evaluated in the OIM data Analysis 7 (EDAX Inc.). An acceleration voltage of 20 kV, a spot size of 2.5, a 6x6 and 8x8 binning and a step size of 3 and 5 µm were used. The corresponding specimen preparation was done according to [17].

10.2.3 Atom probe tomography

The grain boundary chemistry was investigated with atomic scale APT experiments. By using the combined technique of focused ion beam (FIB) and transmission Kikuchi diffraction (TKD) a successful preparation of sharp needle-shaped specimens containing a single crystallographic GB in the first 200 nm was ensured [18]. On the one hand pre-electro polished single tips were prepared by a FIB sharpening combined with TKD according to [18]. On the other hand EBSD was used to pick out specific GBs, as for example low-Σ coincidence site lattices (CSL), which further on were prepared by a FIB-assisted site-specific preparation combined with TKD [Leitner et al.]. These low-Σ GBs were defined by the Brandon criteria [19] in the OIM data Analysis 7 with n = 0.5 and K = 15.

The APT samples were analyzed in a LEAP 3000X HR (525 nm laser with ~10 µm spot size) from Cameca in laser mode. To promote a successful measurement of a GB a laser energy of 0.6 nJ and a temperature of 60 K were used. The pulse frequency was set to 250 kHz during a standing voltage between 3 and 12 kV at a detection rate of 0.005-0.01 atoms per pulse.

The visualization of the obtained data points was enabled by the IVAS 3.6.8 software. For an accurate representation of the GB shape a calibrated reconstruction [20,21] was used. Further on the interfacial excess value (IFE) was determined by ladder diagrams [22,23] to receive a more precise value of the grain boundary segregation content than in one-dimensional concentration profiles. Of each alloy at least two GBs and their solute decorations were analyzed and evaluated.

10.2.4 Density functional theory

The density functional theory (DFT) simulations were performed using the Vienna ab-initio simulation package (VASP) [24–31] with projector augmented wave functions (PAW) and the improved PBEsol xc-functional [32]. Further details for the DFT simulations, the computation of segregation energies or the supercell setup are given elsewhere [9,12,13].

10.2.5 Segregation, kinetics

The simulation of GB segregation with DFT yields segregation energies for each solute to different sites at the GB. These segregation energies are an important input parameter for the estimation of the GB concentration. To take different sites at the GB as well as the site competition of the solutes with each other into account, a modification of the classical McLean isotherm [33] was used, where for each site and every solute A, the occupation is given by:

$$\frac{c^A_{GB,i}}{1-\sum_X c^X_{GB,i}} = \frac{c^A_{\text{bulk}}\exp\left(-\beta E^A_{\text{seg},i}\right)}{1-\sum_X c^X_{\text{bulk}}} \quad (1)$$

Here, c^A_{bulk} is the occupation of a bulk concentration of solute A, $E^A_{\text{seg},i}$ is the segregation energy of solute A to site i, $\beta = 1/(k_B T)$ is the inverse of the Boltzmann constant and the temperature. With the occupation of all sites, the average occupation at the GB for a solute A is given by:

$$c^A_{GB} = \frac{1}{N}\sum_i^N c^A_{GB,i} \quad (2)$$

Here, N denotes the number of all occupied sites at the GB. The IFE for solute A is obtained from c^A_{GB} with:

$$IFE = \left(c^A_{GB} - c^A_{\text{bulk}}\right) N_{\text{bulk}}/A, \quad (3)$$

where A is the GB area and N_{bulk} is the number of atoms in the GB volume per area.

With equations 1-3, the equilibrium concentration at a certain temperature T can be computed. However, this equilibrium concentration is not reached instantaneous, but rather depends on the temperature history and the diffusive properties of the respective material. A kinetic segregation model proposed by Svoboda et al. [34] connects the concentration at the grain boundary with the diffusivity of the solute element in a differential equation. The

formulation by Svoboda et al. only takes into account one segregation site and one solute species at a fixed temperature. To suit our needs, this single-solute single site model has been transferred to our multi-solute multi-site system with a time-dependent temperature, which leads to a system of first order differential equations:

$$\dot{c}^{A}_{GB,i}(t) = \frac{10D^{A}\big(T(t)\big)}{R_G\delta}\tilde{c}^{A}_{\text{bulk}}(t)\left(\ln\frac{\tilde{c}^{A}_{\text{bulk}}(t)\big(1-\sum_X c^{X}_{GB,i}(t)\big)}{c^{A}_{GB,i}(t)\big(1-\sum_X \tilde{c}^{X}_{\text{bulk}}(t)\big)}+\beta E^{A}_{\text{seg},i}\right). \quad (4)$$

In here, $\dot{c}^{A}_{GB,i}$ denotes the rate with which the occupation probability at the GB changes, D^{A} is the diffusion coefficient of A, R_G is the grain radius, δ the GB thickness and $\tilde{c}^{A}_{\text{bulk}}$ the renormalized bulk concentration:

$$\tilde{c}^{A}_{\text{bulk}}(t) = \frac{\left(c^{A}_{\text{bulk}} - r\,c^{A}_{GB,i}(t)\right)}{(1-r)} \text{ with } r = \frac{3\delta}{2R_G}. \quad (5)$$

10.3 Results

10.3.1 Characterization

The results of the chemical and microstructural analyses of the six alloys are given in Table 1. The main feature is the intended increase of the Hf content from 0 to 3.3 at.% for the alloys A0 to A5. The other elements investigated in the chemical analysis can be divided into two groups: one, where the content does not show a clear trend with the Hf alloying, and one, where the content increases linearly with the Hf content. In the first group is the element C, whereas a strong increase in alloying content is observed for O and B.

Another feature observable from Table 1 is that the grain size changes considerably for the different alloys. While the average grain size for alloy A0 is 50 µm, the grain size increases for alloys A1 – A2 to 80 µm, for alloy A3 to 120 µm and for alloy A4 an even larger grain size with 200 µm is observed. Previous studies [14,15] already ascertained that deviations in the grain size between the alloys occur (see Table 1 and Figs.1a and c) due to differences in number of forging steps, total degree of deformation and recrystallization temperatures. Both EBSD images (Figs. 1a and c) indicate a typical recrystallized structure with almost globular grains. Alloy A1 exhibits a finer grain size than alloys A4 and a lower content of hafnium dioxides (marked with an arrow in Fig. 1c).

10.3.2 Fracture tests

Fracture tests were performed on all investigated alloys. The fracture tests showed intergranular fracture for alloys A0 to A2 and nearly complete transgranular fracture for alloys A3 and A4. In Fig. 1b, a typical intergranular fracture surface of alloy A1 is shown, while Fig. 1d depicts the typical transgranular fracture surface observed for alloys A3 and A4. This change in fracture mode is depicted also in Fig. 2 with respect to the Hf bulk concentration.

Table 1: Total chemical composition showing the investigated elements in the five alloys in at. %. The APT investigations depict the concentration of Hf, C and O in solid-solution in the bulk.

	ICP-OES	CA	CGHE	GDMS	APT (elements in solid-solution)			Grain size [µm]
Alloys	Hf	C	O	B	Hf	C	O	
A0	0.00000	0.01078	0.01004	0.00000	0.00	0.0012	0.0325	52
A1	0.17758	0.01040	0.02101	0.00001	0.15	0.0003	0.0000	82
A2	1.08685	0.01125	0.33781	0.00001	0.96	0.0002	0.0000	70
A3	2.16719	0.02023	0.55280	0.00005	1.91	0.0021	0.0003	120
A4	3.32426	0.01306	0.60073	0.00007	3.03	0.0031	0.0019	200

ICP-OES...Inductively coupled plasma-optical atom emission spectroscopy
CA...Combustion analysis
CGHE...Carrier gas hot extraction
GDMS... Glow discharge mass spectroscopy

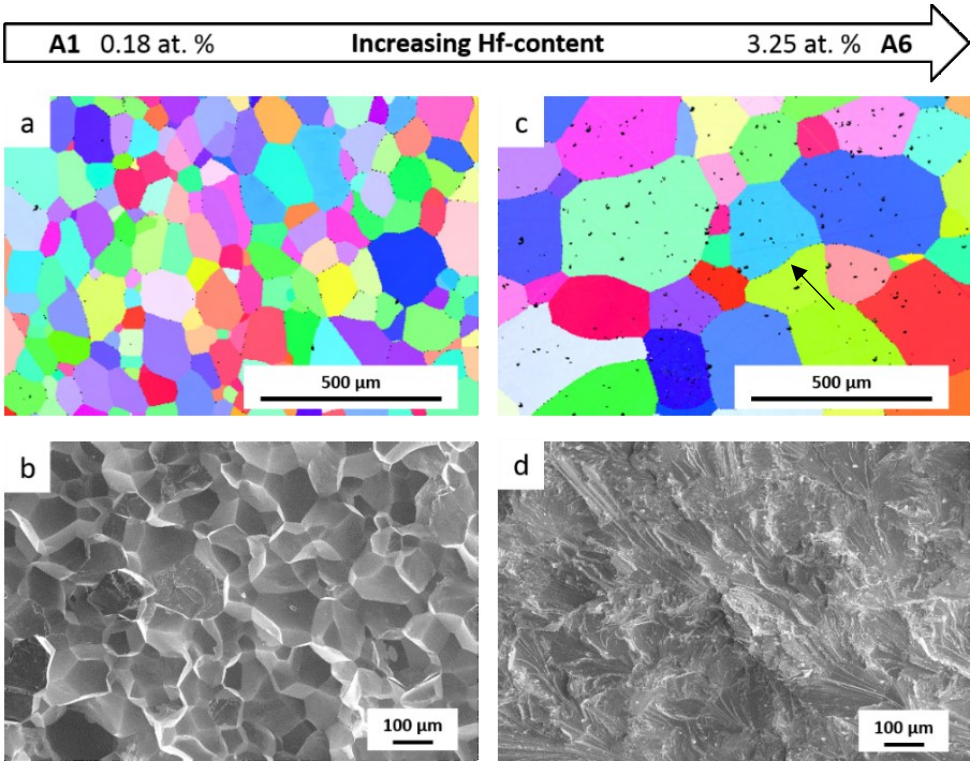

Fig. 1: (a) Microstructure of alloy A1 (0.18 at% Hf) characterized by EBSD. (b) Intergranular fracture surface of alloy A1. (c) Microstructure of alloy A4 (3.3 at% Hf) characterized by EBSD. The arrow marks one of the HfO_2, which show a poor indexing in the EBSD analysis. (d) Transgranular fracture surface of alloy A4.

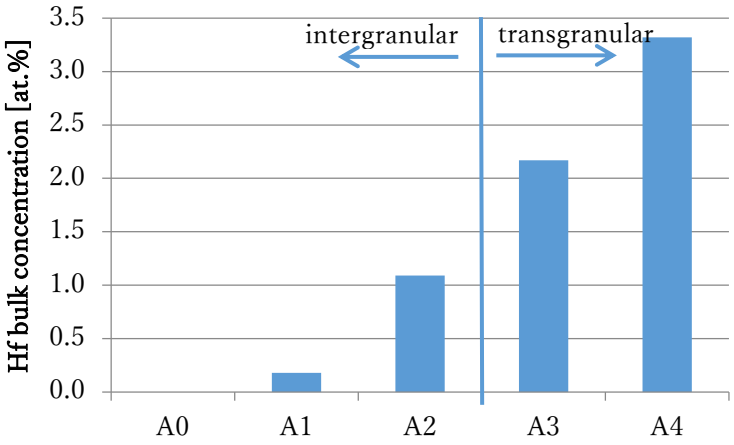

Fig. 2: A picture of Hf content vs intergranular fracture.

10.3.3 Grain boundary and bulk chemistry from APT

APT experiments were conducted to investigate the chemistry at the GB and in solid-solution in the bulk. A detailed description of the elements in solid solution is given by Pöhl et al. [15]. However, in the study by Pöhl et al., the peak of Ti was wrongly assigned to O, which led to the erroneous assumption that Hf in solid-solution increases the O solubility in Mo. The correct analysis depicts that Ti, which was introduced during the production route, increases in solid solution with the rising Hf content. The correct values for O, as well as for the elements important for this study, are given in Table 1. It is important to recognize that the concentration of solute elements in solution can deviate strongly from the total composition. This is in particular the case for C and O which in addition to segregating to GBs, also segregate at dislocations and enrich in Hf precipitates, HfO_2 and micro-pores.

The results of the GB chemistry from APT experiments are summarized in Fig. 3. For each alloy, at least two GBs were measured. In Fig. 3 the main segregated elements, Hf, O, B, and C, are presented by the average IFE in atoms/nm² in dependence of the alloy systems. The error bar indicates the maximum and minimum excess detected.

It is obvious that the O concentration at the GB decreases with increasing Hf content of the alloys. In contrast, the C and B content increases with the Hf content, especially after the fracture mode change between alloy A3 and A4. In Fig. 4, a reconstruction of alloy A1 (a) and A4 (b) is presented. A1 exhibits a high O and N content as visible in Fig. 4a. In A4 (Fig. 4b), O is not observed at the GB, but instead a high concentration of B and C. The main alloying element Hf shows a slight segregation tendency for alloys A1 and A2, however in A3 and A4, a depletion zone was observed close to the GB (see also Fig. 6).

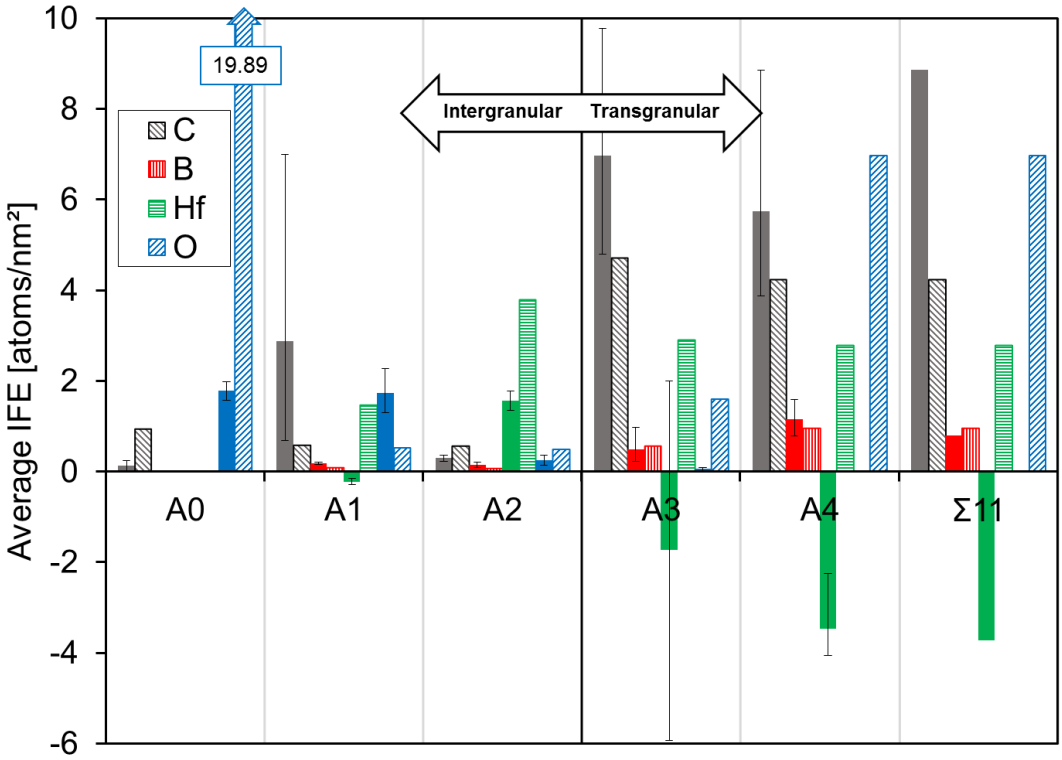

Fig. 3: The average IFE values in atoms/nm² of C, B, Hf and O of the APT and ab-initio calculations are presented in dependence of the alloy systems. The fully colored bars indicate the APT measurements. The error bar shows the maximum and minimum excess detected. The predicted IFE values from DFT are given by the partially colored bars. Between alloy A3 and A4 the fracture mode change was observed.

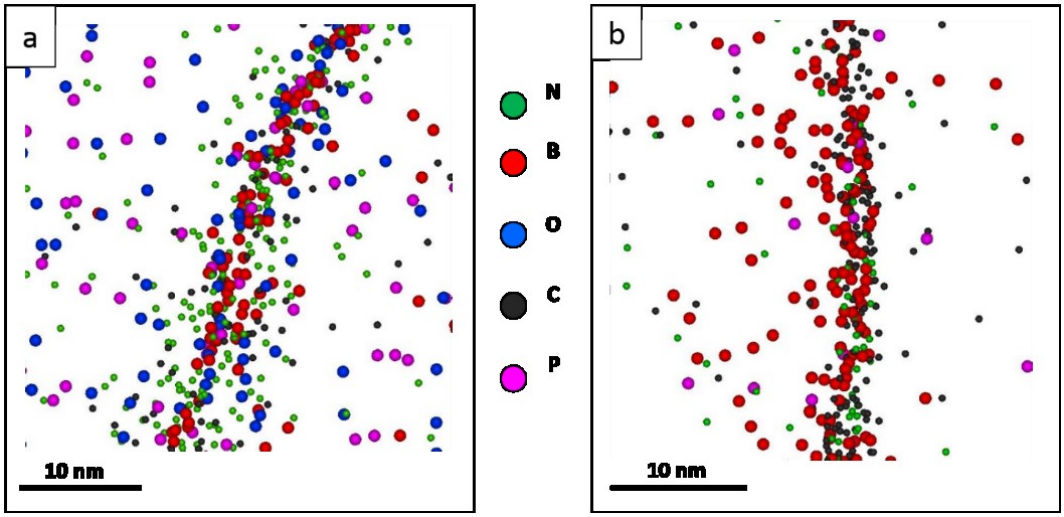

Fig. 4: (a) Small area of the 3D reconstruction of one measurement of alloy A1. (b) Small area of the 3D reconstruction of one measurement of alloy A4. For a better visualization the N, B, O, C and P atoms are shown.

To compare experimental results with calculations, a specific GB of alloy A4 close to a low-Σ value according to the coincidence side lattice model was prepared and the five degrees of freedom of the GB were determined (see Table 2). In Fig. 5a, an EBSD map of A4 is presented and the selected GB is indicated by an arrow. From the APT measurement, the 3D-reconstruction of this GB is shown in Fig. 5b. At the interface, mainly C and B were detected, whereas neither O nor P segregation is observed. The spot with the strong accumulation of C indicates the early stages of a Hf-rich carbide precipitation. Also marked in Fig. 5b is the region of interest (ROI) for a one-dimensional concentration profile through the GB in an area without carbides. This one-dimensional concentration profile is given in Fig. 6a, where it is evident that Hf depletes at the interface, whereas C and B strongly segregate. The C concentration is about six times higher than the B concentration. This can also be inferred from the corresponding IFEs depicted in Fig. 6b. Additionally, a slight segregation tendency for N and Fe is found.

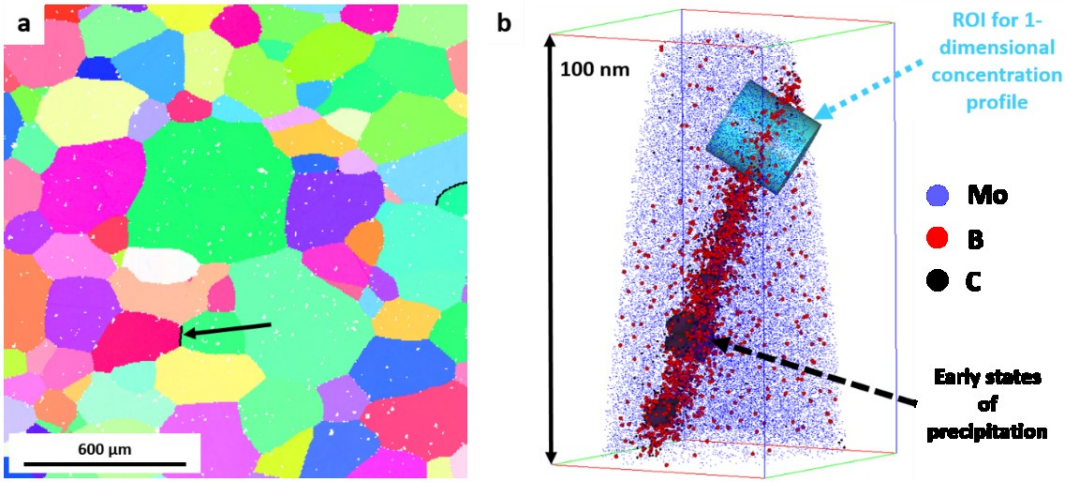

Fig. 5: (a) EBSD map of A4 with markings (black highlighting of GB) for the GBs, which are close to a Σ11 configuration. The prepared GB with 2.5° deviation from Σ11 according the Brandon criterion is indicated by an black arrow. (b) 3D reconstruction of this GB. The main segregation elements, C and B are shown with Mo. Small carbides formed at the GB, which are presented with an isosurface value of 8% Hf and C. The ROI is used for a one-dimensional concentration profile through the GB in an area without carbides.

Table 2: The crystallographic orientation of the GB as observed by EBSD and TKD and as constructed for the DFT simulation.

	Angle	Axis	Plane 1	Plane 2
APT	51.5	[1 20 19]	[24 -15 -7]	[-13 0 -11]
DFT	50.5	[0 1 1]	[13 -8 -3]	[-1 0 -1]

a

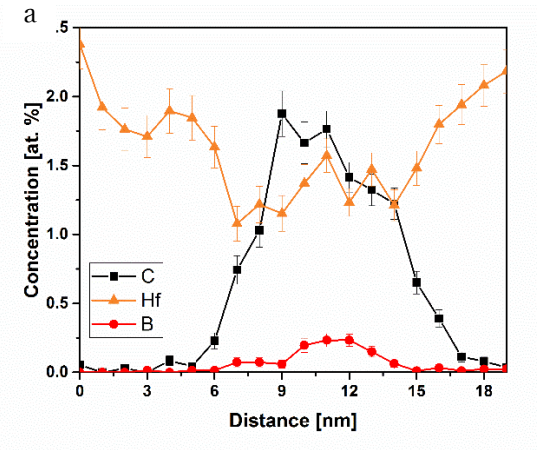

b

Element	IFE-Value [atoms/nm²]
B	0.2932
N	0.0191
C	3.276
Fe	0.0095
Hf	-1.3812

Fig. 6: (a) One-dimensional concentration profile through the GB in the region of interest where no carbide is formed. The main segregation elements are presented. (b) IFEs for the same GB in atoms/nm².

10.4 Theoretical

10.4.1 Segregation energies

With the experimental characterization of the GB misorientation as a starting point, a Σ11 mixed tilt and twist GB was found with only minor deviations to the GB analyzed with APT (see Table 2). The simulation cell chosen for the GB consists of 198 atoms and has the dimensions 7.7 x 9.9 x 40 Å with an additional 8 Å thick vacuum slab on top. The GB plane is in the xy plane. The GB ground-state structure was determined using a γ-surface approach [9] and exhibits a GB energy of 1.81 J/m2. The ground state structure is shown in Fig. 7. A comparison to the GB energies of other Mo GBs [9] shows that this GB has a GB energy comparable to other high-energy GBs.

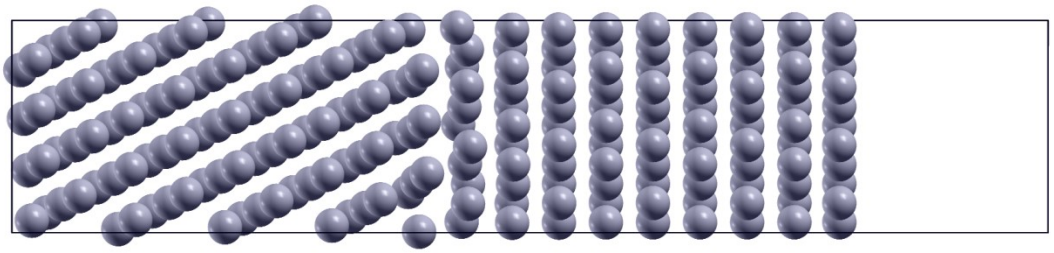

Fig. 7: Ground state structure of the Σ11 mixed tilt and twist GB with a vacuum slab on top.

To determine the possible segregation sites, a Voronoi volume analysis of all sites in the GB structure was performed. The Voronoi volumes as a function of the z coordinate are plotted Fig. 8a. It can be seen that the largest deviation from the bulk volume is found at 20 Å. The bulk values are reached at around ±4 Å, leading to a GB thickness of 8 Angstrom. Within these 8 Å, all possible sites were considered, which lead to 42 substitutional sites. The interstitial segregation sites were identified by using an empty sphere analysis of the GB, resulting in 36 interstitial sites in the GB region. According to [13], the elements C and B prefer the octahedral interstitial position in bulk, while O prefers the tetrahedral position. These were taken as the reference position in the bulk for the segregation energies.

The resulting segregation energies are shown in Figs. 8. Similar as for the Voronoi volumes, largest magnitudes for the segregation energies are found at 20 Å where the GB is located. The strongest segregation energies are observed for B, followed by O, C and Hf. For B, almost all sites exhibit negative segregation energies, which indicate attractive positions for the solute. This tendency for attractive segregation sites ever more decreases when going to Hf, for which only some sites are still attractive, while most sites already exhibit positive segregation energies corresponding to anti-segregation.

When comparing the maximum segregation energies of the solutes to the results found in [12,13], it is found that the magnitudes of the segregation energies in this study are smaller. The most probable reason for this is that the GB used here exhibits a smaller GB energy (1.81 J/m2) than the Σ3 GB (1.93 J/m2) used in [12,13]. Although the magnitudes in segregation energies differ, the trend between the solutes is still the same.

10.4.2 Grain boundary chemistry

Using equations 1-5, the GB chemistry can be computed. For Hf, C and O, the bulk concentrations determined with APT were used for c_{bulk}^{X} , the grain size is given in Table 1 with $R_G = 200$ µm, the GB thickness from DFT is taken as 8 Å (see Fig. **7**), the experimental diffusion coefficients used are given in Table 3 and to simulate the cooling after recrystallization, the temperature as a function of time is given as:

$$T(t) = T_0 + t\,dT, \tag{7}$$

which represents a linear change in temperature with time. In this equation, T_0 is the recrystallization temperature (T_0=1600°C for alloys A0 to A2 and T_0=2000°C for alloys A3 and A4) and dT the cooling rate, i.e. dT=-0.3 K/s in this case. The solutes B, C and O are treated in dependence of each other, for they all occupy interstitial sites at the GB, whereas Hf prefers substitutional sites and therefore is modelled without dependence on the other solutes. With this, the GB concentrations of the solutes are computed and presented in Fig. 3 together with the APT observations.

We can assume that there is a not considered O trapping taking place. The reason for the increased C excess for alloys A3 and A4 is a result of the increased content in solid solution. B has no solubility in Mo and directly segregates to the GBs, therefore, the reason for the increased B excess can be correlated to the increased overall concentration in the alloys with higher Hf content. Another difference between APT and DFT values is found for Hf, as DFT predicts a positive excess at the GB with alloying while APT observed depletion. However, while Hf at the GB in solution decreases, the APT measurements showed a strong increase in Hf-rich carbides at the GB and indeed, a measurement over the GB with carbides yields a positive IFE value also for Hf.

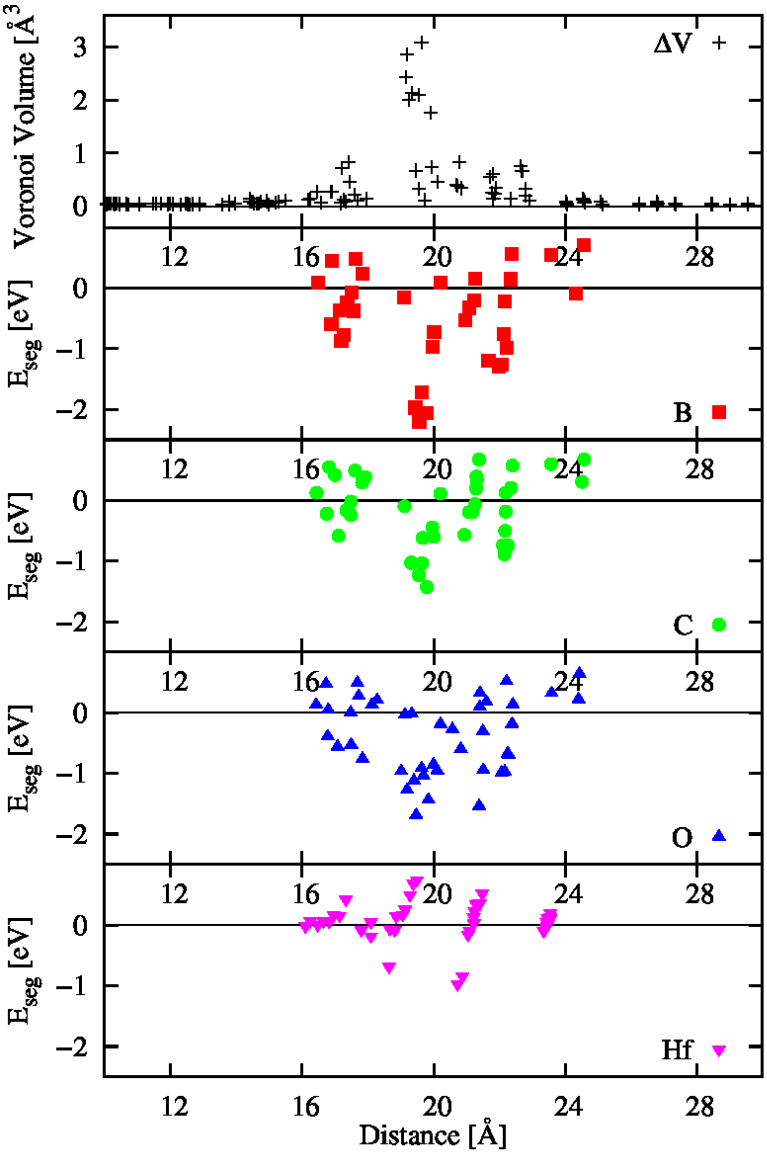

Fig. 8: From top to bottom: Voronoi volume analysis and segregation energies of B, C, O and Hf as a function of the z coordinate in the supercell. The GB is located at 20 Angstrom.

Table 3: Diffusion data used for modelling the kinetics of segregation. The diffusion data for C in Mo [35] is also used for B and O. In lack of diffusion data for Hf in Mo, the data for Hf in W [36] is used.

	Nb	C
D_0 [10^{-6}m²/s]	1.5	3.4
E_a [eV]	4.5584	1.7788

10.4.3 Role of grain boundary chemistry for fracture mode

After comparing the experimentally observed GB chemistries by theoretical simulations, the role of the GB chemistry for cohesion is evaluated. We estimate the impact of GB chemistry on cohesion with an equation similar to equations 14 and 15 in [37]

$$\Delta E_{coh} = -\sum_X c_{GB}^X \, SE_X \, . \qquad (6)$$

The strength of embrittlement SE is taken from our recent studies [12,13] and is given by the difference in segregation energy between the free surface and the GB. The average occupation is taken from the APT measurements. With this equation the combined effect of occupation and the change in bonding due to a solute is taken into account.

The resulting change in GB cohesion is plotted in Fig. 9. It is seen that for alloys A3 and A4, the GB cohesion is increased due to segregation of C and B, while for alloys A0 to A2 only minor changes for the GB cohesion are expected. From our recent study [13] we know that the increase for B and C for the same amount of the solute element at the GB is quite similar. However, the GB concentrations observed in experiment and estimated by simulations show a much higher C content at the GB. Therefore, the main effect of strengthening of the GBs is a result of the increased C content, while the increased amount of B only plays a minor role.

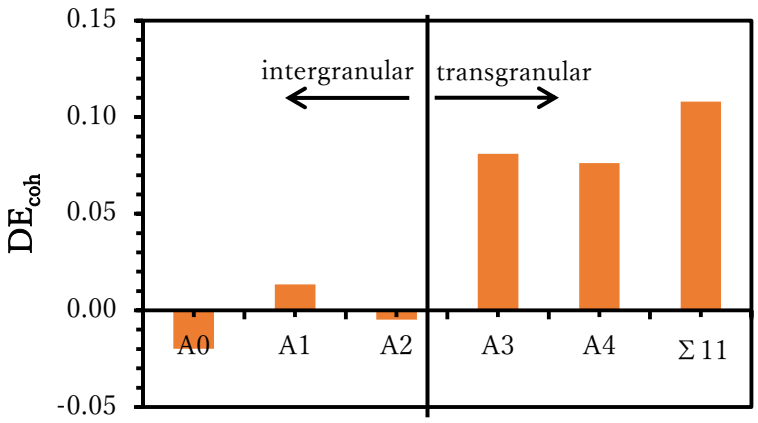

Fig. 9: Change in GB cohesion due to segregation of solute elements as calculated by a combination of DFT and APT results.

10.5 Conclusion

In this study, the surprising observation of a change in fracture mode with increased Hf alloying is resolved by an interconnected framework of experimental and theoretical investigations. By APT analysis of many GBs, the changes in GB chemistry were identified; the subsequent modelling of an observed GB with various elements with DFT resolved the underlying energetics. With the application of a kinetic segregation model, the production process itself was taken into account and the changes in solute excess at the GB with alloying could be understood. By combining the effect on cohesion of the various elements on the GB with their respective observed and predicted concentration at the GB, C and B were identified as the main strengthening elements.

The present work shows that only with both experimental and theoretical investigation, the true underlying processes in technological materials can be understood, e.g. the atomistic simulation alone would not have been able to predict the GB chemistry, for this was just possible with the APT bulk measurements of the concentrations, whereas APT measurements alone do not give indications on the effect of elements on GB cohesion.

Acknowledgements

The authors thank W. Knabl and J. Schatte from the company Plansee SE for the provided material and David Lang for the support of the atom probe experiments.

References

[1] W. Hampe, Beiträge zu der Metallurgie des Kupfers, in: Zeitschrift Für Das Berg-, Hütten- Und Salinenwesen in Dem Preussischen Staate, Hertz, W., 1874: pp. 93–139.

[2] W.C. Roberts-Austen, On certain Mechanical Properties of Metals considered in relation to the Periodic Law, Philosophical Transactions of the Royal Society of London A: Mathematical, Physical and Engineering Sciences. 179 (1888) 339–349.

[3] A.H. Cottrell, A centenniel report, MRS Bulletin. 25 (2000) 43–46.

[4] G.B. Olson, Computational Design of Hierarchically Structured Materials, Science. 277 (1997) 1237–1242.

[5] A. Jain, S.P. Ong, G. Hautier, W. Chen, W.D. Richards, S. Dacek, et al., The Materials Project: A materials genome approach to accelerating materials innovation, APL Materials. 1 (2013) 11002.

[6] A. Kumar, B.L. Eyre, Grain Boundary Segregation and Intergranular Fracture in Molybdenum, Proceedings of the Royal Society A: Mathematical, Physical and Engineering Sciences. 370 (1980) 431–458.

[7] A.S. Drachinskiy, A. V. Kraynikov, V.N. Slyunyaev, Interrelation of Impurity Enrichment of Grain Boundaries and the Cold-Shortness Point During Annealing of Molybdenum, Phys. Met. Metallogr. 66 (1988) 111–119.

[8] S. Tsurekawa, T. Tanaka, H. Yoshinaga, Grain boundary structure, energy and strength in molybdenum, Materials Science and Engineering: A. 176 (1994) 341–348.

[9] D. Scheiber, R. Pippan, P. Puschnig, L. Romaner, Ab initio calculations of grain boundaries in bcc metals, Modelling and Simulation in Materials Science and Engineering. 24 (2016).

[10] T. Watanabe, S. Tsurekawa, The control of brittleness and development of desirable mechanical properties in polycrystalline systems by grain boundary engineering, Acta Materialia. 47 (1999) 4171–4185.

[11] B. Gludovatz, S. Wurster, T. Weingärtner, a. Hoffmann, R. Pippan, Influence of impurities on the fracture behaviour of tungsten, Philosophical Magazine. 91 (2011) 3006–3020.

[12] D. Scheiber, R. Pippan, P. Puschnig, A. V. Ruban, L. Romaner, Ab-initio search for cohesion-enhancing solute elements at grain boundaries in molybdenum and tungsten, International Journal of Refractory Metals and Hard Materials. 60 (2016) 75–81.

[13] D. Scheiber, R. Pippan, P. Puschnig, L. Romaner, Ab initio search for cohesion-enhancing impurity elements at grain boundaries in molybdenum and tungsten, Modelling and Simulation in Materials Science and Engineering. 24 (2016) 085009.

[14] C. Pöhl, J. Schatte, H. Leitner, Solid solution hardening of molybdenum–hafnium alloys: Experiments and Modeling, Materials Science and Engineering: A. 559 (2013) 643–650.

[15] C. Pöhl, J. Schatte, H. Leitner, Solid solution softening of polycrystalline molybdenum–hafnium alloys, Journal of Alloys and Compounds. 576 (2013) 250–256.

[16] K. Babinsky, J. Weidow, W. Knabl, A. Lorich, H. Leitner, S. Primig, Atom probe study of grain boundary segregation in technically pure molybdenum, Materials Characterization. 87 (2014) 95–103.

[17] C. Pöhl, J. Schatte, H. Leitner, Metallographic characterization of the molybdenum based alloy MHC by a color etching technique, Materials Characterization. 77 (2013) 63–69.

[18] K. Babinsky, R. De Kloe, H. Clemens, S. Primig, A novel approach for site-specific atom probe specimen preparation by focused ion beam and transmission electron backscatter diffraction, Ultramicroscopy. 144 (2014) 9–18.

[19] D.G. Brandon, The structure of high-angle grain boundaries, Acta Metallurgica. 14 (1966) 1479–1484.

[20] B. Gault, M.P. Moody, F. De Geuser, G. Tsafnat, A. La Fontaine, L.T. Stephenson, et al., Advances in the calibration of atom probe tomographic reconstruction, Journal of Applied Physics. 105 (2009).

[21] B. Gault, F. de Geuser, L.T. Stephenson, M.P. Moody, B.C. Muddle, S.P. Ringer, Estimation of the Reconstruction Parameters for Atom Probe Tomography, Microscopy and Microanalysis. 14 (2008) 296–305.

[22] B.W. Krakauer, D.N. Seidman, Absolute atomic-scale measurements of the Gibbsian interfacial excess of solute at internal interfaces, Physical Review B. 48 (1993) 6724–6727.

[23] D.N. Seidman, B.W. Krakauer, D. Udler, Atomic scale studies of solute-atom segregation at grain boundaries: Experiments and simulations, Journal of Physics and Chemistry of Solids. 55 (1994) 1035–1057.

[24] G. Kresse, J. Hafner, Ab initio molecule dynamics for liquid metals, Phys. Rev. B. 47 (1993) 558.

[25] G. Kresse, J. Hafner, Ab initio molecular-dynamics simulation of the liq-metal-amorphous-semiconductor transistion in germanium, Phys. Rev. B. 49 (1994) 14251.

[26] G. Kresse, J. Hafner, Norm-conserving and ultrasoft pseudopotentials for first-row and transition-elements, J. Phys.: Condens. Matter. 6 (1994) 8245.

[27] G. Kresse, J. Furthmüller, Efficiency of ab-initio total energy calculations for metals and semiconductors using a plane-wave basis set, Computational Materials Science. 6 (1996) 15–50.

[28] G. Kresse, J. Furthmüller, Efficient iterative schemes for ab initio total-energy calculations using a plane-wave basis set, Physical Review B. 54 (1996) 11169–11186.

[29] D. Vanderbilt, Soft self-consistent pseudopotentials in a generalized eigenvalue formalism, Phys. Rev. B. 41 (1990) 7892.

[30] P.E. Blöchl, Projector augmented-wave method, Physical Review B. 50 (1994) 17953–17979.

[31] G. Kresse, D. Joubert, From ultrasoft pseudopotentials to the projector augmented-wave method, Phys. Rev. B. 59 (1999) 1758.

[32] J.P. Perdew, A. Ruzsinszky, G.I. Csonka, O.A. Vydrov, G.E. Scuseria, L.A. Constantin, et al., Restoring the Density-Gradient Expansion for Exchange in Solids and Surfaces, Phys. Rev. Lett. 100 (2008) 136406.

[33] P. Lejcek, Grain Boundary Segregation in Metals, Springer Berlin Heidelberg, Berlin, Heidelberg, 2010.

[34] J. Svoboda, G. a. Zickler, E. Kozeschnik, F.D. Fischer, Kinetics of interstitial segregation in Cottrell atmospheres and grain boundaries, Philosophical Magazine Letters. 95 (2015) 458–465.

[35] P.S. Rudman, No Title, Trans. Metall. Soc. AIME. (1967) 239.

[36] G.J. Beyer, No Title, ZfK-310 (Zentralinstitut Fuer Kernforschung, Dresden, DDR). (1976).

[37] D. Scheiber, V.I. Razumovskiy, P. Puschnig, R. Pippan, L. Romaner, Ab initio description of segregation and cohesion of grain boundaries in W-25 at.% Re alloys, Acta Materialia. 88 (2015) 180–189.

11 Publication F

Fracture behavior and delamination toughening of molybdenum in Charpy impact tests

K. Babinsky[1], S. Primig[1, 2], W. Knabl[3], A. Lorich[3], R. Stickler[4], H. Clemens[1]

1 Department of Physical Metallurgy and Materials Testing, Montanuniversität Leoben, Austria
2 School of Materials Science & Engineering, UNSW Australia, Sydney NSW 2052, Australia
3 Plansee SE, Metallwerk-Plansee-Straße 71, 6600 Reutte, Austria
4 University of Vienna, Austria

Abstract

This study combines advanced characterization techniques with conventional Charpy impact tests to relate the mechanical properties to the microstructure of technically pure molybdenum, especially regarding its toughness. V-notched samples with different orientations were prepared from a rolled molybdenum plate in the stress-relieved and recrystallized condition. The ductile-to-brittle-transition-temperature was analyzed in terms of the delamination behavior influenced by the microstructure. A pronounced increase of toughness was found specific oriented samples, which can be explained by macroscopic delamination. Elongated grains lead to enhanced delamination in Charpy impact tests with variations for different orientations. In general, delamination occurs as a result of brittle fracture, however, an increase in toughness in the Charpy impact test can be provoked. This mechanism is called thin-sheet toughening or delamination toughening. Electron-backscatter-diffraction measurements were performed to get a deeper knowledge about the crack propagation and the delamination behavior in the rolled plate. Recrystallization shifts the transition region to significantly higher temperatures, which is explained by the globular grain shape as well as grain boundary segregation. The occurrence of delamination is discussed, taking texture, grain shape and segregation effects into account.

11.1 Introduction

Molybdenum belongs to the group of refractory metals and has a high melting point, high temperature strength and good electrical and thermal conductivity. Due to these outstanding properties it is used for several high performance applications, in electronics, coatings, high temperature engineering, and lighting technology. Nevertheless, its fabrication and processing as well as its applicability as a high performance material are limited because of a ductile-to-brittle-transition-temperature (DBTT) around room temperature [1–3]. With its body-centered cubic (bcc) structure, thermal activation is necessary to overcome the Peierls potential for plastic deformation causing a pronounced transition from ductile to brittle. However, controlling grain size, grain shape, grain boundary character, alloying content, and stress state seem to be key approaches to influence the DBTT of molybdenum [4–12]. Nevertheless, recrystallization annealing of the as-deformed and stress-relieved condition of molybdenum leads to a significant increase of the DBTT and even more to intergranular embrittlement, which is believed to be caused by the larger grain size and segregation enrichments at the grain boundaries [3,5,13–18]. Recent atom probe investigations revealed phosphor, nitrogen and oxygen impurities at the grain boundaries of technically pure molybdenum [19,20] of which especially segregated oxygen is assumed to promote intergranular fracture [14,15,17]. By adding small amounts of carbon and boron the ductility of molybdenum can be improved [5,15,21].

However, molybdenum suffers from severe delamination, a typical splitting of grains boundaries, in the transition- and upper shelf region due to the anisotropic grain geometry which makes its processing challenging. In history, different investigation methods have been applied to solve the problem of delamination [22,23]. Quasi-static pull tests lead to the assumption that linear arrangements of former micro-pores, which become flattened during hot-deformation, cause the delamination susceptibility of molybdenum [24]. Cockeram [5–9] tested the fracture toughness and mechanisms of wrought molybdenum and molybdenum alloys. He observed a pronounced dependency of the DBTT on the grain size and grain shape. An elongated, pancake-shaped grain structure leads to an anisotropy in fracture toughness. In the transition- and upper shelf region splitting of grains boundaries occurs and generates a ductile laminate failure mode. This cracking of grain boundaries leaves ligaments which stretch and fail under a plane stress condition in a ductile manner. This thin sheet toughening, which is also known as delamination toughening, occurs to a different extent depending on the specimen orientation in respect to the grain shape [4–12].

In previous studies, tensile tests were used to characterize the DBTT of molybdenum. Fracture toughness tests provide more accurate measurements of the DBTT for potential applications due to the predominant triaxial stress-state during the experiments ahead of the crack tip [7–9]. However, as structural materials are exposed to impact loadings, the Charpy impact test seems to be an adequate technique to gain a better understanding of fracture at

high deformation speeds and low test temperatures at multi-axial stress states [4,10,12]. This testing method is, besides hardness and tensile tests, a common method for technical investigations in industry due to its simplicity. Charpy impact tests are a straightforward method to reveal brittleness caused by an increase of deformation speed or a decrease of test temperature, as it preferentially occurs in bcc metals. In recent studies the mechanical properties of pipeline steels and ultrafine grained bcc steels have been, amongst other methods, characterized by Charpy impact tests [12].

In this work, Charpy impact tests, which are widely used in industry, are combined with advanced characterization techniques to relate mechanical properties to the microstructure of technically pure molybdenum. Tensile tests and Charpy impact tests were conducted on samples of a technically processed molybdenum plate to investigate the role of delamination and crystallography on the DBTT. It will give an overview of the DBTTs in differently oriented specimens of a technically pure molybdenum plate in its stress-relieved and recrystallized state. Scanning electron microscopy (SEM) and electron backscatter diffraction (EBSD) is used to examine fracture surfaces and delamination cracks in more detail. The deviations in the DBTTs for different orientations and states are discussed in terms of delamination related to the apparent texture and grain shape.

11.2 Materials and methods

An industrially processed 14.5mm thick plate of technically pure molybdenum in the stress-relieved and recrystallized state was used for this investigation. The concentration of the main impurities in this plate are shown in Table 1

Table 1: Concentration of the main impurities in the investigated molybdenum plate.

Element	Concentration [µg/g]
C	19
O	11
Fe	6
W	126

The molybdenum plate was produced by a typical powder-metallurgical production route by cold-isostatic pressing followed by a conventional sintering process. Subsequent hot-rolling was performed to reach a final thickness of 14.5 mm.

Tensile tests at room temperature were carried out on round 5 x 25 mm tensile test specimens, based on the DIN 50125, taken longitudinal (L) and transverse (T) to the rolling direction of the processed molybdenum plate in the stress-relieved and recrystallized state. After passing the yield point (Rp0.2 or Re) with 30 MPa s-1, a constant crosshead speed of 5

mm min-1 with a gauge length of 25 mm was used according to DIN EN ISO 6892-1-method B.

The samples used for the Charpy impact toughness tests were 2 mm deep V-notched specimens with the dimensions 10 mm x 10 mm x 55 mm, derived on the DIN EN ISO 148-1 standard. Fig. 1 shows the extraction direction (L-S, L-T, T-S, T-L) of the specimens relative to the plate processing geometry according to ASTM E399. The two letter code was used to specify the samples with the first letter indicating the normal direction to the crack plane and the second letter describing the direction of the global crack propagation.

After manufacturing of the Charpy specimens, a stress-relief annealing treatment was performed. The recrystallization treatment was performed on the final V-notched samples. Ultrasonic tests were performed to exclude pre-damaged samples. The impact tests were conducted between room temperature and 500°C in a Zwick-Roell testing machine (BRA 342038204) with a RKP300 Joule and RKP450 Joule Charpy impact hammer. The specimens were heated in an HKE-GmbH furnace and the temperature was measured by a thermocouple on the surface of the sample. When the set-point temperature was reached, the specimen was moved to the testing machine and analyzed at least after 2s. According to DIN EN ISO 148-1 a Charpy impact test is valid when the absorbed impact energy is lower than 80% of the potential starting energy and the crack propagated in the designated crack growth direction indicated by the V-notch.

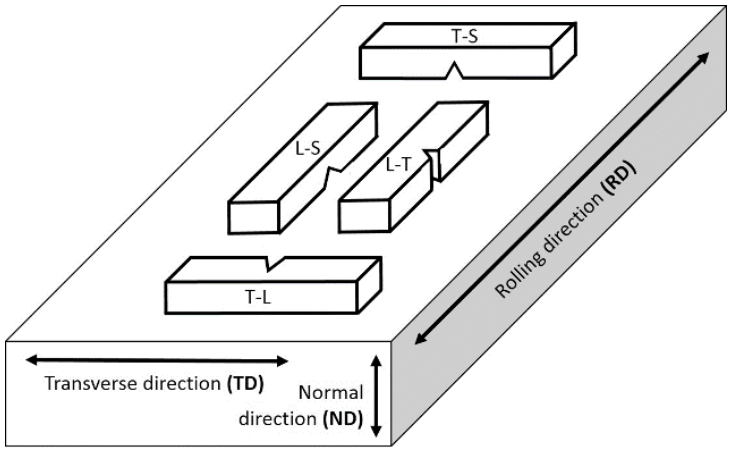

Fig. 1: The extraction direction of the specimens relative to the plate processing geometry (RD = rolling direction, ND = normal direction, TD = transverse direction) is specified by the two letter code according to ASTM E399. L is the direction of principal deformation (maximum grain flow). T represents the direction of least deformation and S the third orthogonal direction. The two letter code was used to specify the samples with the first letter indicating the normal direction to the crack plane and the second letter describing the direction of the global crack propagation.

The stress-relieved specimens were measured in the L-S, L-T, T-S, and T-L orientation. The L-S and T-S samples were tested with the 450J hammer and the L-T and T-L samples with the 300J hammer. Additionally, recrystallized specimens in the L-S and L-T direction were investigated. The DBTT was determined at the half value of the upper shelf energy in the obtained Charpy curves. In all curves the standard deviation is only shown if the value scatters more than 5J.

The samples for EBSD investigations were prepared by mechanically grinding and polishing followed by an electrolytic polishing with a 12.5 vol.% H2SO4 solution. The EBSD scans were taken with 30 kV, 2.5 spot size, 8x8 binning and 10 mm working distance or with 6x6 binning and 15 mm working distance in a FEI Versa 3D DualBeam focused ion beam/scanning electron microscope (FIB/SEM) workstation equipped with an EDAX Hikari XP EBSD system. Inverse pole figure (IPF) maps were used to characterize the microstructural evolution and texture. Fracture surfaces close to the V-notch were analyzed in a stereomicroscope (Zeiss Discovery V20), and SEM. The macro- and microscopic delamination was investigated by EBSD analyses. The Charpy specimens for EBSD analyses were prepared before the impact tests to prevent artifacts due to the grinding and polishing process.

11.3 Results

11.3.1 Microstructure and tensile test

In Fig. 2 the microstructures of molybdenum in the stress-relieved (a) and recrystallized (b) state are shown. A distinct recovered sub-grain structure with a weak rotated cube texture is present in the warm-deformed and stress-relieved state. Recrystallization leads to an almost globular grain shape with a mean grain size of 92 µm and a random texture with a small maximum at the weak γ-fiber showing a <111> direction parallel to the normal direction (ND).

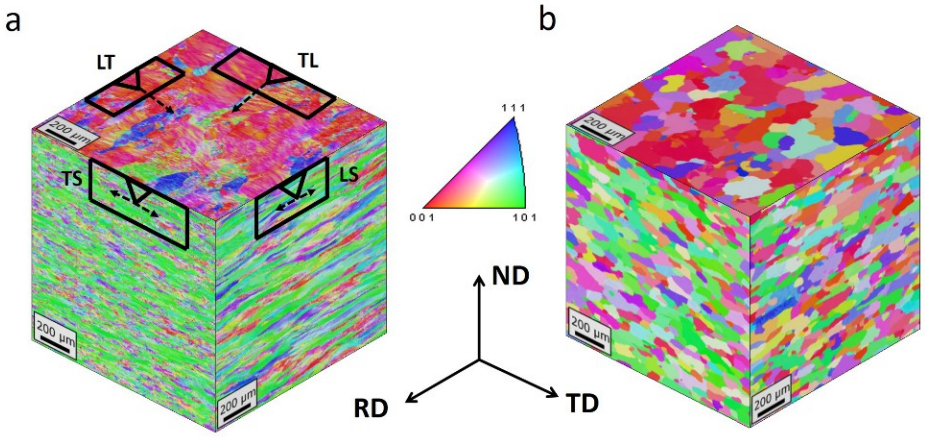

Fig. 2: IPF maps of molybdenum in the (a) stress-relieved and (b) recrystallized state determined by EBSD. The insets in the middle show the IPF coloring, which indicates the crystal direction perpendicular to the specimen surface, and the orientation of the cube in respect to the rolling process. In (a) the orientation of the tested samples are marked.

Tensile tests indicate differences in strength and elongation depending on the specimen orientation in the plate and the applied heat treatment. Stress-relieved molybdenum shows a higher yield (617 and 688MPa) and tensile strength (665 and 685 MPa) as well as a larger fracture strain (32.5 and 22.2 %) and uniform elongation (7.7 and 6 %) compared to recrystallized molybdenum. For all longitudinal samples a slight increase in the uniform elongation was measured. Specimens tested in the transversal direction exhibit a less ductile behavior and an increase of strength. The results of all tensile tests are shown in the *electronic supplementary Table 1*.

11.3.2 Charpy impact tests of stress-relieved molybdenum

In Fig. 3a data of the impact tests on differently oriented stress-relieved molybdenum samples are presented. For L-T and T-L oriented samples, a low upper shelf energy of around 53J was found, whereas the upper shelf energy of L-S and T-S is significantly higher with energy values of around 300 J for the L-S and 150 J for the T-S orientation. The transition from brittle to ductile behavior occurs for L-S and L-T samples in a similar temperature range of around 100-250°C and for T-L and T-S of around 200-350°C. The T-L and L-T oriented specimens exhibit a typical DBTT-curve with no significant scattering. The upper shelf energy is around 53J but a slight shift to higher energy values and a lower DBTT (shown in Fig. 3b) is visible for the L-T orientation. The energy values of L-S and T-S show more scattering in comparison to the L-T and T-L orientations.

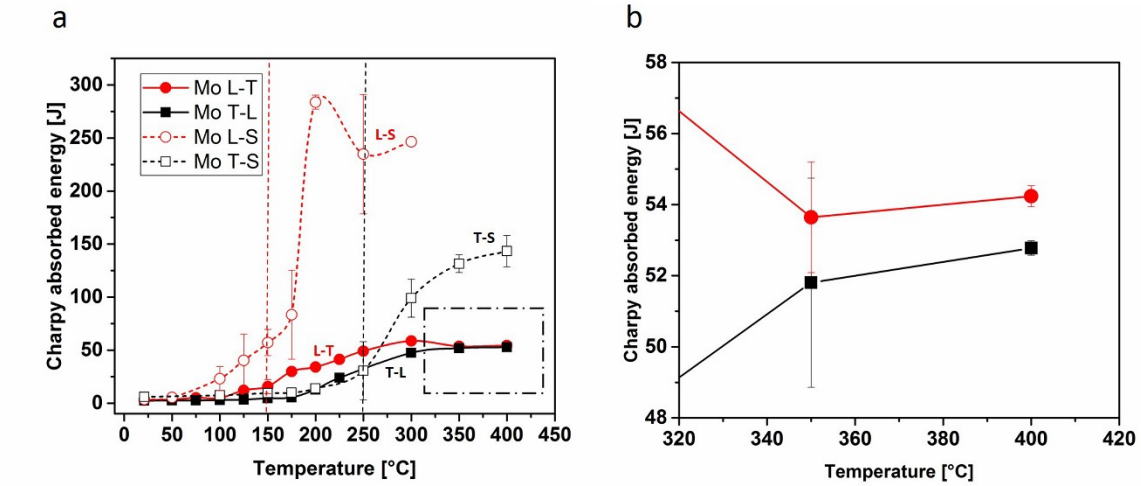

Fig. 3: (a) Charpy impact test curves for molybdenum in the stress-relieved state in all four orientations. The vertical dashed lines indicated the temperatures above which the samples did not break anymore during the impact test (red for L-S orientation, black for T-S orientation). (b) Data of the upper shelf region of T-L and L-T, marked by the inset in (a), between 320 and 420°C. Note: In (a) the standard deviation is only shown if values scatter more than 5J. Only in (b) the scattering for values lower than 5J, is presented.

11.3.2.1 T-L and L-T orientation

The fracture surfaces close to the notch root of the L-T and T-L specimens at 23°C (lower shelf), 150°C (transition), and 300°C (upper shelf) are shown in the electronic supplementary Fig. 1. At room temperature, i.e. in the lower shelf region, both orientations exhibit transgranular cleavage (electronic supplementary Figs. 1a and d). At 150°C the L-T oriented sample indicates the transition to a ductile fracture behavior with dimples visible on the fracture surface. At the same temperature the T-L oriented sample still breaks almost in the brittle fracture mode. The same trend is visible in the DBTT-curves in Fig. 3 with a higher energy value for the L-T direction than for the T-L at 150°C. At 300°C both sample orientations show a ductile fracture behavior, prominent for the upper shelf. In the transition region microscopic delamination cracks normal to the global crack propagation direction start to appear. In Figs. 4a and b stereographic images of the fracture surfaces of samples in the L-T and T-L orientation tested in the transition region (225°C) are presented. At this temperature ductile laminate features (white arrows in Figs. 4a and b) start to occur. In L-T oriented samples more delamination cracks can be seen than in T-L oriented samples.

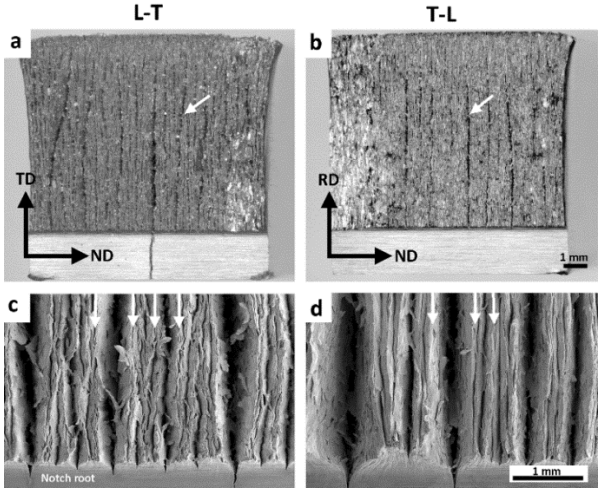

Fig. 4: Analyses of the fracture surfaces in the transition region (225°C) and upper shelf region (400°C). (a) Stereomicroscope image of the L-T orientation tested at 225°C. (b) Stereomicroscope image of the T-L orientation tested at 225°C. (c) SEM image close to the former V-notch of the L-T orientation tested at 400°C. (d) SEM image close to the former V-notch of the T-L orientation tested at 400°C.

This is even more evident by analyzing the SEM images of both orientations tested at 400°C in the upper shelf, which are shown in Figs. 4c and d. The L-T orientation exhibits finer ductile sheet-like laminate features than the T-L orientation.

The microscopic delamination cracks in L-T and T-L orientation occur normal to the global crack growth direction. An EBSD investigation of a longer delamination crack shown in Fig. 5a indicates that cracks propagate between grains with high misorientation (see IPF maps in Figs. 5b and c). It seems obvious that delamination occur along high-angle grain boundaries (HAGB).

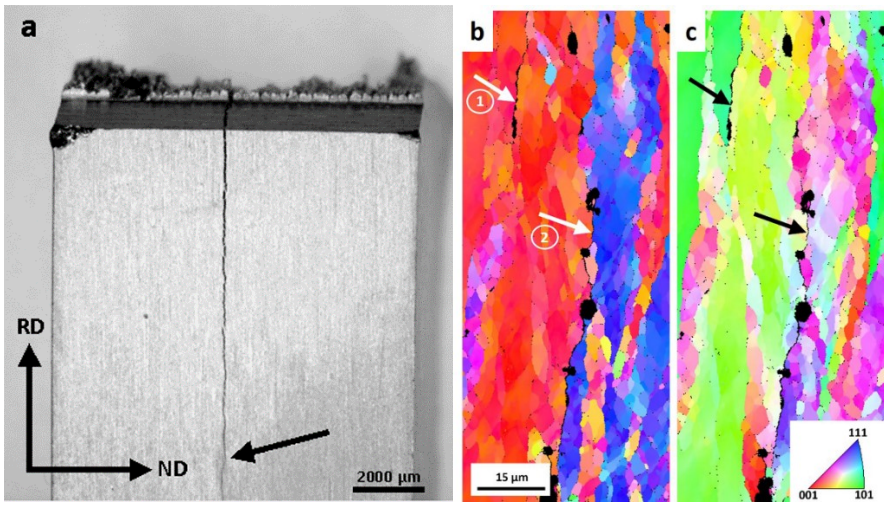

Fig. 5: (a) Stereomicroscope image of the half impact bar (side view) tested in L-T orientation in the transition region (150°C). (b) IPF map of delamination cracks marked in Fig. 6a. Two cracks are visible. (c) 90 degree rotated IPF map. The inset in the lower right corner shows the IPF coloring which indicates the crystal direction perpendicular to the (b) ND and (c) TD direction.

11.3.2.2 T-S and L-S orientation

Figure 6a represents a L-S specimen tested in the lower shelf region (50°C) with macroscopic delamination cracks. These delamination cracks do not propagate in the designated crack growth direction, but branch parallel to the longitudinal direction of the impact test bars. With a closer investigation of the surface of the delamination (marked by the arrow in Fig. 6a) a typical intergranular fracture surface can be observed in Figs. b-d. The L-S oriented samples did not break into two pieces above 150°C and the T-S oriented samples not above 250°C.

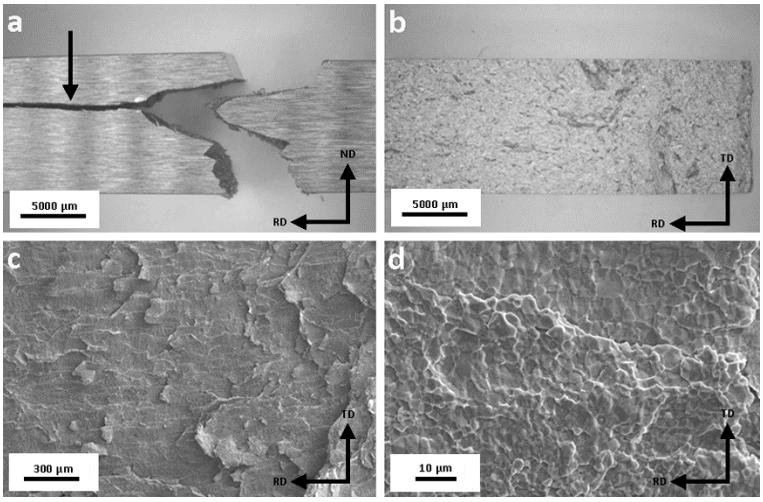

Fig. 6: (a) Stereomicroscope image of a L-S specimen tested in the lower shelf region (50°C) with macroscopic delamination cracks. (b) Stereomicroscope image of the delamination marked by the arrow in a. (c) SEM image of the delamination shown in b. (d) Higher magnification SEM image of the delamination visible in c.

In the transition region the T-S oriented specimens also exhibits delamination cracks and large deviations from the global crack path. The variation in the position and the size of

delamination cracks results in a strong scattering of the energy values in the DBTT-curve, as visible in Fig 3a. In the electronic supplementary Fig. 2a a T-S sample tested at 50°C is presented. The arrows mark large delamination cracks.
To study these cracks in more detail EBSD investigations were performed. In the electronic supplementary Figs. 2b-d delamination cracks are shown in SEM images and IPF maps. Typically, delamination takes place between different grain orientations, as visible in the electronic supplementary Fig. 2b. This behavior is shown in more detail in high magnification EBSD analyses in the electronic supplementary Figs. 2c and d. These cracks propagate between grains of high misorientation, however, cracks also occur perpendicular to the delamination in regions with small grain misorientation (white arrow).

11.3.3 Charpy impact tests of recrystallized molybdenum

After recrystallization, the molybdenum samples exhibit an almost globular grain structure as shown in Fig. 2b. In the DBTT-curves of recrystallized molybdenum in the L-T and L-S orientation, shown in Fig. 7a, a clear increase of the DBTT is apparent in comparison to stress-relieved molybdenum. The L-T oriented samples of the recrystallized state show higher upper shelf energy than in the stress-relieved state. For the L-S orientation an upper shelf energy of around 300 J for both stress-relieved and recrystallized molybdenum can be observed. Both orientations in the recrystallized condition indicate a similar DBTT lying between 400 and 450°C. The image visible in Fig. 7b represents a characteristic specimen tested at 450°C in the upper shelf region. Due to the ductile behavior at elevated temperatures the samples did not break. No large delamination cracks can be observed in both tested orientations. The DBTT of the L-T orientation is slightly shifted to lower values.
In the electronic supplementary Figs. 3a–c the fracture surfaces of the L-T and L-S oriented samples in the recrystallized state in the lower shelf are shown (sample tested at 23°C and 375°C for the L-T orientation and 250°C for the L-S orientation). Intergranular fracture behavior with small transgranular cleavage regions can be observed in both orientations in the lower shelf region. However, in the transition- and upper shelf region the L-T specimens exhibit a small tendency towards delamination. In the electronic supplementary Fig. 3d the SEM image of the fracture surface of a L-T oriented sample tested in the transition region (375°C) is presented, where small delamination cracks can be observed (marked with an arrow). The L-S oriented samples show no delamination in the transition- and upper shelf region.

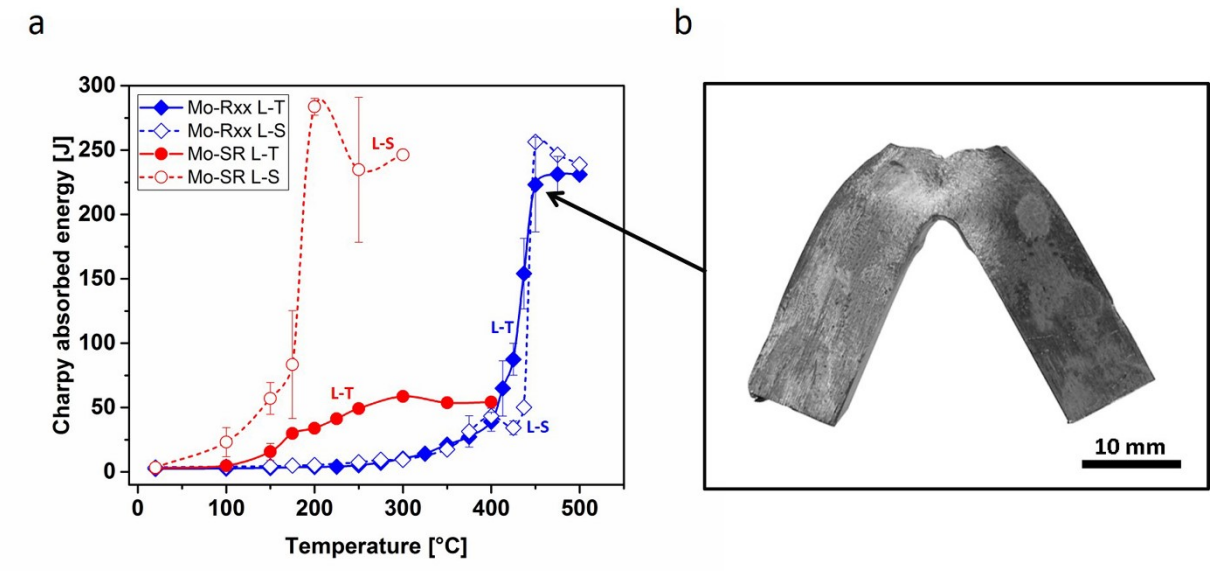

Fig. 7: (a) Charpy impact test curves of recrystallized molybdenum in the L-T and L-S orientation. (b) Photograph of a tested L-T sample at 450°C.

11.3.4 Ductile-to-Brittle-Transition-Temperatures

To compare the obtained results all DBTTs are summarized in Table 2. In the stress-relieved state the lowest DBTT with 169°C was determined for the L-T orientation. The L-S oriented specimens show a slightly higher DBTT (181°C), followed by the T-L oriented samples with 229°C. T-S oriented samples indicate the highest DBTT with 280°C. After recrystallization the DBTT increased significantly. Both orientations, the L-T and L-S, exhibit equal transition values of around 429-442°C. Only a small difference can be observed.

Table 2: Summary of all DBTTs

	DBTT [° C]			
	L-T	T-L	L-S	T-S
Mo stress-relieved	169	229	181	280
Mo recrystallized	429	-	442	-

11.4 Discussion

In the following, the results from tensile tests at room temperatures and Charpy impact experiments between 23°C and 500°C are discussed, with special focus on the orientation dependency and micro-and macroscopic delamination in technically pure molybdenum.

11.4.1 Tensile tests

The tensile tests exhibit the typical decrease in yield and tensile strength due to recrystallization of molybdenum. The embrittlement is deduced by the uniform elongation, which is reduced from 6-8% to 2-3%. By a closer examination of the stress-relieved condition of the transversal sample (T) a slight increase of yield and tensile strength as well as a drop of fracture strain and uniform elongation can be observed. The same tendencies were found for stress-relieved molybdenum [5] and for an API-X80 pipeline steel [12], which was explained by a closer spacing of grain boundaries in the transversal orientation.

11.4.2 Stress-relieved molybdenum in the Charpy impact test

In general, the stress-relieved samples can be classified in two groups: Firstly, there are the L-T and T-L oriented samples, where the global crack propagates in the designated crack growth direction. Secondly, in L-S and T-S oriented samples the crack deviates from the designated direction due to macroscopic delamination. Due to the additional delamination cracks the local driving force for the crack propagation is reduced for L-S and T-S and a larger surface area is created, leading to higher upper shelf energies. However, it seems that the DBTT values are rather influenced by the orientation of the crack plane, than by the crack propagation direction as the L-T and L-S. The T-L and T-S show similar transition regions. In the following the characteristics of the two groups will be discussed in more detail.

11.4.2.1 T-L and L-T orientation

L-T and T-L samples show quite similar DBTT curves, with a slightly higher upper shelf energy and a lower DBTT for L-T. Both orientations have in common that cracks propagate without large deviations in the designated crack growth direction.

The DBTTs are in good accordance to the fracture surface observations indicating the transition from a transgranular cleavage to a ductile laminate failure mode with dimples. In these orientations the designated crack growth direction is parallel to the long axis of the elongated grains. Thus, the crack can easily propagate along the HAGBs. However, microscopic delamination was found on both fracture surfaces perpendicular to the crack growth direction in the transition- and upper shelf region. It is well known that the occurrence of these delamination cracks, which looks like thin sheet ligaments, generate a toughening mechanism, also known as delamination toughening [4–6,12,25]. These thin ligaments deform plastically under a plane stress state introducing a larger plastic zone. The fracture

toughness is increased due to the relaxation of the triaxial stress state at the crack tip. By the formation of microscopic delamination cracks the thickness of the original sample is reduced to a bunch of many small thin sheet ligaments. The triaxial stress component decreases causing a plane stress state. The sample acts like a stack of many thin samples instead of one thick sample. Thinner delamination segments will have a larger tendency for plane stress with the result of a higher toughness [12]. Delamination toughening can be observed for example in the L-T oriented samples in Fig. 4. Comparing the fracture surfaces of the T-L and L-T orientation, the L-T samples exhibit thinner ligaments which lead to an improved toughness in the upper shelf energy apparent in the DBTT-curves, shown in Fig. 3b. Hence, an increase of around 2 J of the upper shelf energy for the L-T orientation can be observed. The same toughening effects were studied by Joo et al. [26,25,27] in an API-X80steel, by Song et al. [12,28] and by Kimura et al. [11] in an ultrafine grained steel and by Cockeram [6,7] in wrought molybdenum and its alloys. EBSD investigations of such delamination cracks (Fig. 5) indicate cracking along HAGB which correlates well with the result of Cockeram [6,7], who describes delamination as the splitting of grain boundaries. In recent atom probe studies oxygen, phosphorus and nitrogen segregations at HAGB were found, which can decrease the grain boundary strength causing these grain boundary cracks [20]. Additionally, it is believed that the HAGBs of molybdenum are intrinsically weak [29–31].

The DBTT of the L-T oriented sample is lower, which can be correlated with the premature occurrence of delamination cracks causing an increase in toughness. This phenomenon seems to be mainly influenced by the orientation of the crack plane independent of the crack propagation direction.

11.4.2.2 T-S and L-S orientation

Both orientations exhibit a higher upper shelf energy than the T-L and L-T orientations which is related to large deviations in the crack path, caused by macroscopic delamination. The cracks branch perpendicular to the designated propagation direction, whereby the local crack driving force is reduced and, even more, a much larger new surface is created. As a consequence, the upper shelf energy is significantly higher than in T-L and L-T orientation and depends on the degree of macroscopic delamination [11]. Each sample showed delamination of a different extent, which explains the intense scattering of the energy values especially in L-S oriented samples. The vertical dashed lines in the DBTT-curves in Fig. 3 indicate the temperature where the specimens did not break into two pieces due to pronounced delamination. In the L-S samples the designated crack plane is perpendicular to the longer axis of the elongated grains, causing the strongest delamination effect (visible in Fig. 6). In the T-S oriented specimens the grain elongation is less pronounced (visible in Fig. 2a), leading to less pronounced delamination (Electronic supplementary Fig. 2a). The occurrence of delamination in the Charpy impact test is related to weak interfaces or planes

normal to the V-notch and the designated crack growth direction of the samples [11]. EBSD investigations of the T-S oriented samples (visible in the electronic supplementary Figs. 2b-d) reveal a splitting of grain boundaries between grains with high misorientation. High magnification SEM images indicate that the crack tips grow along HAGB, especially between the strong partial α-fiber with <110>//RD and the weak γ-fiber with <111>//ND [32,33]. Kimura et al. [11] identified the anisotropic grain shape as main reason for the occurrence of delamination. Strength, toughness and ductility are significantly increased at low temperature due to ultrafine elongated grains along the rolling direction and nanometer particles, which promote splitting between grain boundaries. In this study, the molybdenum plate shows a weak texture, but the crack follows the interfaces between the slight γ- and α-fiber along HAGBs. Between these boundaries also transgranular fracture is observed, where the crack connects elongated grain boundaries as visible in the electronic supplementary Fig. 2b (marked by an arrow). By a closer investigation of the fracture surface of the delamination (visible in Figs. 6b-d) a typical intergranular fracture mode is apparent. It is interesting that delamination, which is a result of brittle fracture, causes an increase in Charpy impact toughness. Therefore, the L-S oriented samples in the stress-relieved state seem to be the toughest orientation due to enhanced macroscopic delamination.

11.4.3 Recrystallized molybdenum in the Charpy impact test

In order to study the effect of texture and grain elongation on the DBTT and the delamination behavior, the recrystallized condition of the molybdenum plate in the L-T (microscopic delamination in the stress-relieved state) and L-S orientation (macroscopic delamination in the stress-relieved state) is studied.

After recrystallization an almost globular grain structure with a weak γ-fiber can be observed. However, the grains are still slightly elongated along the rolling direction as visible in Fig. 2b.

The DBTT-curves of the recrystallized molybdenum reveal a clear increase in the DBTT compared to the stress-relieved condition. In the lower shelf intergranular facture is apparent for both orientations (visible in the electronic supplementary Figs. 3a-c). On the one hand this embrittlement is a results of impurities, which segregate to the grain boundaries. Especially, oxygen segregations weaken the grain boundaries [14,15,17]. On the other hand it is believed that the embrittlement is an intrinsic property of molybdenum [29–31]. Intergranular fracture occurs more often in microstructures with many random high-angle grain boundaries. Low-angle and special boundaries, such as sigma grain boundaries, seem to cause transgranular fracture [29].

In addition, the shape of the grains influences the DBTT. The only slight elongation of the grains causes no branching of the crack and, therefore, no delamination occurs which leads to an increase in the DBTT [10].

In the transition region of the L-T samples, small ductile laminate features can be observed which are similar to the ligaments in the L-T samples in the stress-relieved state. A small decrease in the DBTT for the L-T sample is apparent compared to L-S (L-T at 429°C, L-S 442°C), which can be related to this delamination toughing effect.

11.5 Conclusions

In this study advanced characterization techniques were successfully combined with simple Charpy impact tests to relate the mechanical properties to the microstructure of technically pure molybdenum, especially regarding its toughness and delamination behavior. An anisotropy of fracture toughness in stress-relieved molybdenum was observed due to a pancake-shaped, elongated grain structure. Hence, the grain geometry controls the crack propagations. Elongated grains lead to enhanced delamination in Charpy impact test depending on the specimen orientation. Microscopic delamination in the L-T and T-L samples in the stress-relieved state are found to be beneficial due to the effect of delamination toughening. A pronounced increase of toughness is apparent in the L-S and T-S samples, which is related to macroscopic delamination. These delamination cracks follow grain boundaries between grains of high misorientation, which are weakened by impurities at the interfaces. Although, delamination is a result of brittle fracture, an increase in toughness in the Charpy impact test is provoked. Therefore, the L-S oriented samples reveal the highest toughness, followed by the T-S and L-T sample. The T-L oriented samples are showing the lowest resistance against crack propagation. Recrystallization leads to a significant increase of the DBTT, caused by the globular grain structure and impurities present at the grain boundaries. In conclusion, the elongated grain structure plays a significant role for the toughness of bcc- structured metals, especially in correlation with the weak bonding of random high-angle grain boundaries in molybdenum, which are related to either an extrinsic (grain boundary segregation) or intrinsic (microstructure) property.

Acknowledgments

Thanks to Walter Kopper, the responsible technician of the Charpy impact test machine at our Department, who conducted all impact tests for this study. Furthermore, the authors are grateful to Dipl.-Ing. Thomas Leitner from the Chair of Materials Physics of the Montanuniversität Leoben for his scientific and technical input in terms of fracture mechanics.

References

[1] W. Martienssen, H. Warlimont, Springer Handbook of Condensed Matter and Materials Data, Springer, Berlin, Heidelberg, New York, 2005.

[2] T. Watanabe, S. Tsurekawa, Toughening of brittle materials by grain boundary engineering, Materials Science and Engineering: A. 387-389 (2004) 447–455.

[3] L. Northcott, Molybdenum, Butterworths Scientific Publications, London, 1956.

[4] M.S. Joo, D.-W. Suh, J.H. Bae, H.K.D.H. Bhadeshia, Role of delamination and crystallography on anisotropy of Charpy toughness in API-X80 steel, Materials Science and Engineering: A. 546 (2012) 314–322.

[5] B.V. Cockeram, E.K. Ohriner, T.S. Byun, M.K. Miller, L.L. Snead, Weldable ductile molybdenum alloy development, Journal of Nuclear Materials. 382 (2008) 229–241.

[6] B. V. Cockeram, The role of stress state on the fracture toughness and toughening mechanisms of wrought molybdenum and molybdenum alloys, Materials Science and Engineering A. 528 (2010) 288–308.

[7] B. V. Cockeram, The mechanical properties and fracture mechanisms of wrought low carbon arc cast (LCAC), molybdenum-0.5pct titanium-0.1pct zirconium (TZM), and oxide dispersion strengthened (ODS) molybdenum flat products, Materials Science and Engineering A. 418 (2006) 120–136.

[8] B. V. Cockeram, Measuring the fracture toughness of molybdenum-0.5 pct titanium-0.1 pct zirconium and oxide dispersion-strengthened molybdenum alloys using standard and subsized bend specimens, Metallurgical and Materials Transactions A. 33 (2002) 3685–3707.

[9] B. V. Cockeram, The fracture toughness and toughening mechanisms of wrought low carbon arc cast, oxide dispersion strengthened, and molybdenum-0.5 pct titanium-0.1 pct zirconium molybdenum plate stock, Metallurgical and Materials Transactions A. 36 (2005) 1777–1791. doi:10.1007/s11661-005-0042-2.

[10] Y. Hiraoka, H. Kurishita, M. Narui, H. Kayano, Fracture and Ductile-to-Brittle Transition Characteristics of Molybdenum by Impact and Static Bend Tests, Materials Transactions, JIM. 36 (1995) 504–510.

[11] Y. Kimura, T. Inoue, F. Yin, K. Tsuzaki, Inverse Temperature Dependence of Toughness in an Ultrafine Grain-Structure Steel, Science. 320 (2008) 1057–1060.

[12] R. Song, D. Ponge, D. Raabe, Mechanical properties of an ultrafine grained C-Mn steel processed by warm deformation and annealing, Acta Materialia. 53 (2005) 4881–4892.

[13] E. Pink, R. Eck, Refractory metals and their alloys, in: R.W. Cahn, P. Haasen, E.J. Kramer, K.H. Matucha (Eds.), Materials Science and Technology, VCH, Weinheim, New York, Basel, Cambridge, Tokyo, 2006: pp. 591–638.

[14] A. Kumar, B.L. Eyre, Grain Boundary Segregation and Intergranular Fracture in Molybdenum, Proceedings of the Royal Society A: Mathematical, Physical and Engineering Sciences. 370 (1980) 431–458.

[15] M.K. Miller, A.J. Bryhan, Effect of Zr, B and C additions on the ductility of molybdenum, Materials Science and Engineering A. 327 (2002) 80–83.

[16] H. Kimura, Overview, Intergranular Fracture in BCC metals, Transactions of the Japan Institute of Metals. 29 (1988) 521–539.

[17] A.S. Drachinskiy, A. V. Kraynikov, V.N. Slyunyaev, Interrelation of Impurity Enrichment of Grain Boundaries and the Cold-Shortness Point During Annealing of Molybdenum, Phys. Met. Metallogr. 66 (1988) 111–119.

[18] A. Krajnikov, A. Drachinskiy, V. Slyunyaev, Grain boundary segregation in recrystallized molybdenum alloys and its effect on brittle intergranular fracture, International Journal of Refractory Metals and Hard Materials. 11 (1992) 175–180.

[19] K. Babinsky, J. Weidow, W. Knabl, A. Lorich, H. Leitner, S. Primig, Atom probe study of grain boundary segregation in technically pure molybdenum, Materials Characterization. 87 (2014) 95–103.

[20] K. Babinsky, W. Knabl, A. Lorich, R. De Kloe, H. Clemens, S. Primig, Grain boundary study of technically pure molybdenum by combining APT and TKD, Ultramicroscopy. 159 (2015) 445–451.

[21] T. Kadokura, Y. Hiraoka, Y. Yamamoto, K. Okamoto, Change of Mechanical Property and Fracture Mode of Molybdenum by Carbon Addition, Materials Transactions. 51 (2010) 1296–1301.

[22] C. Stickler, Charakterisierung des Delaminationsverhalten von Mo-Ronden mittels Biegeversuch, Plansee Report 97DEL2a. (1997) 6.

[23] R. Stickler, H. Hödl, Charaketrisierung des Delaminationsverhalten von Mo-Blechen. Vorversuche zur Entwicklung einer Prüfmethode., Plansee Report 96DEL2a. (1996) 12.

[24] R. Stickler, H. Hödl, Charakterisierung des Delaminationsverhalten von Mo-Blechen. Messungen an 5mm und 2mm Blechen im Anlieferungszustand., Plansee Report 96DEL3a. (1996) 4.

[25] M.S. Joo, D.W. Suh, J.H. Bae, N. Sanchez Mouriño, R. Petrov, L. a I. Kestens, et al., Experiments to separate the effect of texture on anisotropy of pipeline steel, Materials Science and Engineering A. 556 (2012) 601–606.

[26] M.S. Joo, D. Suh, J. Bae, H.K.D.H. Bhadeshia, Toughness Anisotropy in X70 and X80 Linepipe steels, Materials Science and Technology. 30 (2014) 439–446.

[27] R. Song, D. Ponge, D. Raabe, J.G. Speer, D.K. Matlock, Overview of processing, microstructure and mechanical properties of ultrafine grained bcc steels, Materials Science and Engineering A. 441 (2006) 1–17.

[28] S. Tsurekawa, T. Tanaka, H. Yoshinaga, Grain boundary structure, energy and strength in molybdenum, Materials Science and Engineering: A. 176 (1994) 341–348.

[29] J.B. Brosse, R. Fillet, M. Biscondi, Intrinsic intergranular brittleness of molybdenum, Scripta Metallurgica. 15 (1981) 619–623.

[30] T. Watanabe, S. Tsurekawa, The control of brittleness and development of desirable mechanical properties in polycrystalline systems by grain boundary engineering, Acta Materialia. 47 (1999) 4171–4185.

[31] S. Primig, H. Leitner, W. Knabl, Textural Evolution During Dynamic Recovery and Static Recrystallization of Molybdenum, Metallurgical and Materials Transactions A. 43 (2012) 4794–4805.

[32] S. Primig, H. Leitner, W. Knabl, a. Lorich, H. Clemens, R. Stickler, Influence of the heating rate on the recrystallization behavior of molybdenum, Materials Science and Engineering: A. 535 (2012) 316–324.

Electronic supplementary Tables and Figures:

Supplementary Table 1: Results of the tensile tests in longitudinal (L) and transverse (T) direction of molybdenum in the stress-relieved and recrystallized state (mean values of 5 samples)

	Direction	Yield strength [MPa]	σ	Tensile strength [MPa]	σ	Fracture strain [%]	σ	Uniform elongation [%]	σ
Mo stress-relieved	L	617	11	665	7	32.5	3.0	7.7	0.1
	T	688	4	685	4	22.2	2.3	6.0	0.3
Mo recrystallized	L	361	2	467	33	3.2	1.4	3.2	1.4
	T	351	2	431	40	1.9	0.8	1.9	0.8

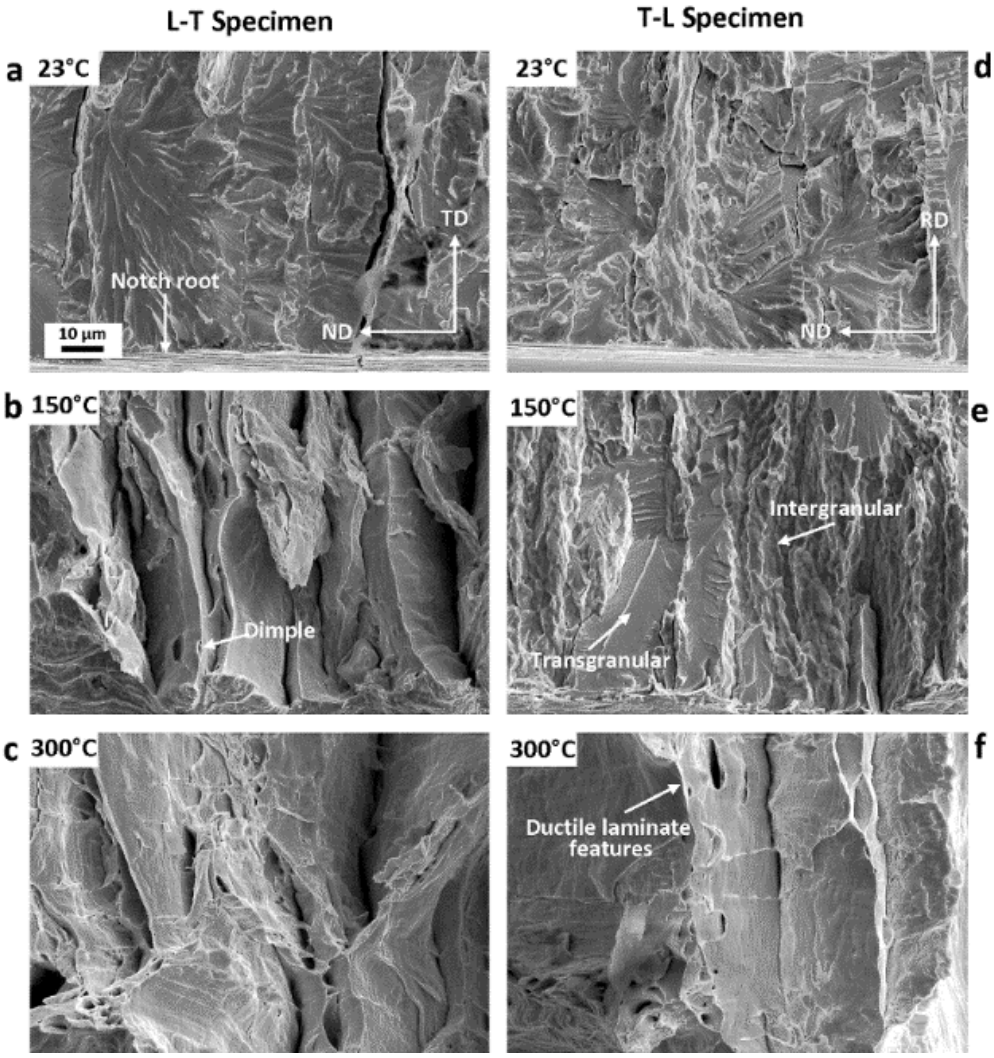

Supplementary Fig. 1: SEM-images of the fracture surfaces of the L-T and T-L specimens tested at 23°C (a, d), 150°C (b, e) and 300°C (c, f) representing the lower shelf-, transition– and upper shelf-region. The images were taken close to the former V-notch.

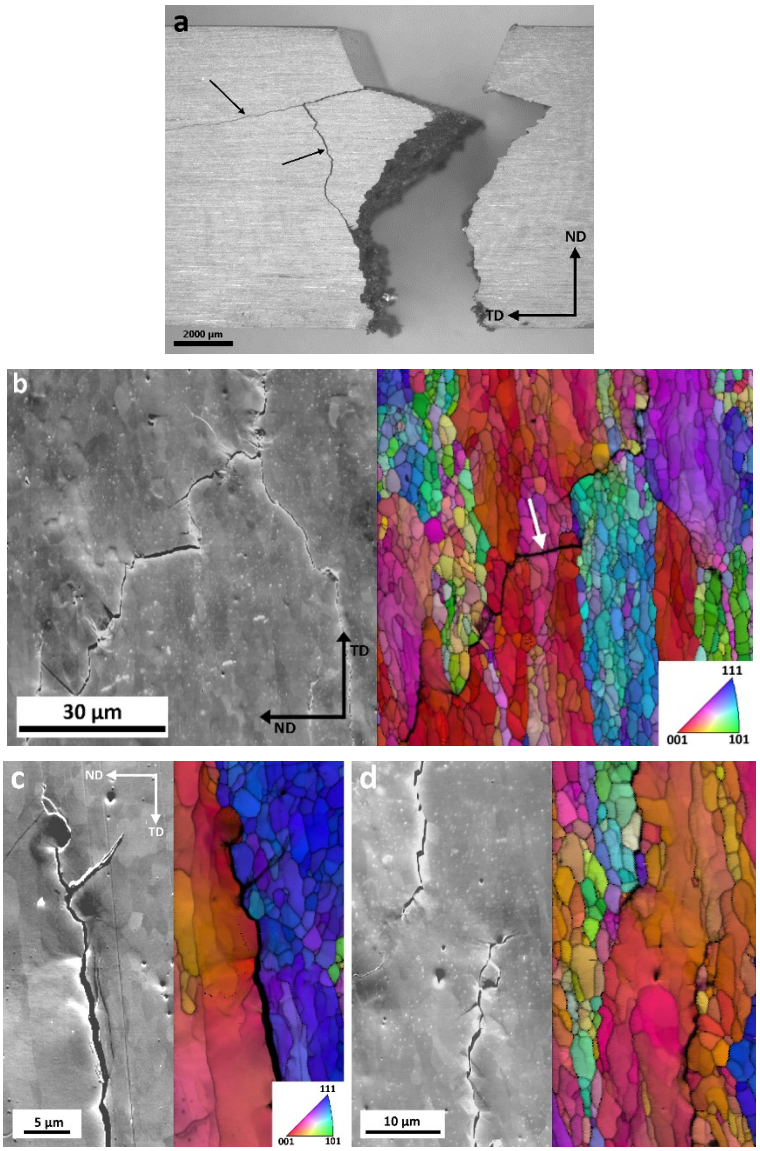

Supplementary Fig. 2: a) Stereomicroscope image of a T-S oriented specimen tested in the lower shelf (50°C). The arrows mark large delamination cracks. b) SEM image (left) and IPF map (right) of delamination cracks in a T-S oriented a sample in the lower shelf (75°C). c-d) Higher magnification SEM images and IPF maps of two different delamination crack tips in the sample shown in b. The inset in the lower right corner of b and c shows the IPF coloring which indicates the crystal direction perpendicular to the ND direction.

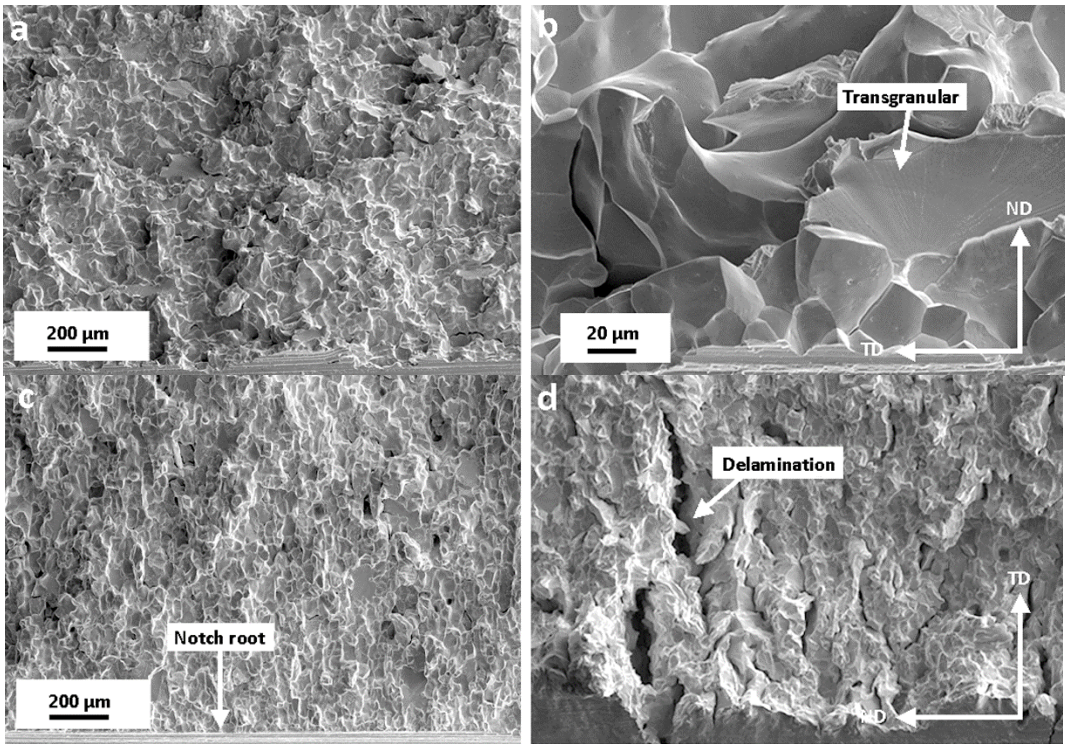

Supplementary Fig. 3: (a) SEM image of the fracture surface close to the former V-notch of a L-S oriented sample tested in the lower shelf region (250°C). (b) Higher magnification image of the sample shown in a). Some transgranular islands are visible in the intergranular fractured surface. (c) SEM images of the fracture surface close to the former V-notch of a L-T oriented sample tested in the lower shelf region (23°C). (d) SEM image of the fracture surface close to the former V-notch of a L-T oriented sample tested in the transition region (375°C). Small delamination cracks occur.

Appendix A

MATERIALS CHARACTERIZATION 87 (2014) 95–103

Available online at www.sciencedirect.com

ScienceDirect

www.elsevier.com/locate/matchar

Atom probe study of grain boundary segregation in technically pure molybdenum

K. Babinsky[a], J. Weidow[b], W. Knabl[c], A. Lorich[f], H. Leitner[a,1], S. Primig[a,*]

[a]Montanuniversität Leoben, Department of Physical Metallurgy and Materials Testing, Franz-Josef Straße 18, 8700 Leoben, Austria
[b]Chalmers University of Technology, Department of Applied Physics, 412 96 Gothenburg, Sweden
[c]PLANSEE SE, Metallwerk-Plansee-Straße 71, 6600 Reutte, Austria

ARTICLE DATA

Article history:
Received 9 September 2013
Received in revised form 31 October 2013
Accepted 2 November 2013

Keywords:
Molybdenum
Grain boundary segregation
Atom probe tomography (APT)
Focused ion beam (FIB) microscopy
Transmission electron microscopy (TEM)

ABSTRACT

Molybdenum, a metal with excellent physical, chemical and high-temperature properties, is an interesting material for applications in lighting-technology, high performance electronics, high temperature furnace construction and coating technology. However, its applicability as a structural material is limited because of the poor oxidation resistance at high temperatures and a brittle-to-ductile transition around room temperature, which is influenced by the grain size and the content of interstitial impurities at the grain boundaries. Due to the progress of the powder metallurgical production during the last decades, the amount of impurities in the current quality of molybdenum has become so small that surface sensitive techniques are not applicable anymore. Therefore, the atom probe, which allows the detection of small amounts of impurities as well as their location, seems to be a more suitable technique. However, a site-specific specimen preparation procedure for grain boundaries in refractory metals with a dual focused ion beam/scanning electron microscope is still required.

The present investigation describes the development and successful application of such a site-specific preparation technique for grain boundaries in molybdenum, which is significantly improved by a combination with transmission electron microscopy. This complimentary technique helps to improve the visibility of grain boundaries during the last preparation steps and to evidence the presence of grain and subgrain boundaries without segregants in atom probe specimens. Furthermore, in industrially processed and recrystallized molybdenum sheets grain boundary segregation of oxygen, nitrogen and potassium is successfully detected close to segregated regions which are believed to be former sinter pores.

© 2013 Elsevier Inc. All rights reserved.

1. Introduction

Molybdenum is a metal with excellent physical and chemical properties used for applications in lighting-technology, high performance electronics, high temperature furnace construction and sputtering targets. However, its fabrication and applicability as a structural material are still limited because of the typical change of fracture behavior due to the brittle-to-ductile transition temperature around room-temperature [1]. In its deformed state molybdenum is ductile at room temperature, but recrystalliza-

* *Corresponding author*. Tel.: +43 3842 402 4217; fax: +43 3842 402 4202.
E-mail addresses: katharina.babinsky@stud.unileoben.ac.at (K. Babinsky), jonathan.weidow@chalmers.se (J. Weidow), wolfram.knabl@plansee.com (W. Knabl), alexander.lorich@plansee.com (A. Lorich), harald.leitner@bohler-edelstahl.at (H. Leitner), sophie.primig@unileoben.ac.at (S. Primig).
[1] Now at: Böhler Edelstahl GmbH & Co KG, 8605 Kapfenberg, Austria.

1044-5803/$ – see front matter © 2013 Elsevier Inc. All rights reserved.
http://dx.doi.org/10.1016/j.matchar.2013.11.001

tion leads to intergranular brittle fracture which is believed to be caused by impurity segregation at the grain boundaries [2]. Furthermore, it has been observed that an increase in degree of deformation leads to an increase in ductility. It is assumed that either individual grain boundaries need to accommodate less impurities per unit area with decreasing grain size or that the impurity atoms are forced inside the grains during deformation.

The intergranular fracture of body-centered-cubic (bcc) metals like iron and molybdenum is well known, but the influence of interstitial atoms on the mechanical properties is still not understood in detail [2–4]. In the past, Kumar et al. [2] was one of the first who investigated binary molybdenum–oxygen and ternary molybdenum–oxygen–carbon alloys with Auger electron spectroscopy. These alloys showed intergranular fracture due to oxygen segregation at the grain boundaries. Additionally, their measurements revealed that carbon has a beneficial effect on the grain boundary strength. Suzuki et al. [5] investigated the effect of recrystallization on the ductility of high purity molybdenum. These authors also confirmed the increase of grain boundary strength due to the addition of carbon. Krajnikov et al. [6] studied welded molybdenum based alloys and suggested that in annealed molybdenum carbon strengthens the grain boundaries and reduces the oxygen segregation. Kimura [7] found that recrystallized molybdenum showed intergranular fracture even if the grain boundaries were free of impurities. Other authors assumed that the brittleness is an intrinsic property of molybdenum, because high purity materials also exhibited brittle intergranular fracture [8–10]. However, additional segregation of impurities might also weaken the poor intrinsic grain boundary strength. Miller et al. [4,11] investigated welded molybdenum alloys in order to understand the influence of the elements zirconium, carbon and boron. Atom probe tomography (APT) results showed no significant oxygen but zirconium, carbon and boron segregation at the grain boundaries. This replacement of segregation elements causes also a change in fracture mode from intergranular to transgranular failure [4]. Tahir et al. [12] recently investigated the influence of carbon on the mechanical properties of the symmetrical tilt grain boundary in molybdenum by means of ab initio. Their calculations indicated that carbon decreases the grain boundary energy and, therefore, improves the driving force for carbon segregation. Furthermore, a strengthening effect of carbon was determined.

Due to the progress of the powder metallurgical production during the last decades, the amount of impurities in the current quality of molybdenum has become exceptionally low. Thus, surface sensitive techniques as Auger electron or secondary ion mass spectroscopy are not applicable anymore as the impurity contents are below their detection limits [13]. Nowadays, the three-dimensional atom probe with its almost atomic resolution is the most sensitive tool to detect individual atoms, even in the parts per million range, using a needle shaped specimen [14–16]. Therefore, it is considered to be the most suitable analysis method to study grain boundary segregation in technically pure molybdenum. However, the chance to coincidentally detect grain boundaries in the small volumes examined by APT is negligible if conventional APT specimen preparation techniques by electro-polishing are used. Today's new techniques for the preparation of APT specimens by focused ion beam (FIB) systems expand the areas of applications of APT [17–19]. The lift-out technique proposed by Miller [20], was the first site-specific method applied to study grain boundaries in the atom probe. A small wedge or lamella is lifted out of the bulk material with a micromanipulator and attached to a post material by welding with e.g. platinum. Felfer et al. [21], Pérez-Willard et al. [22] and Cairney et al. [23] applied and improved these techniques. Besides the lift-out technique, electro-polished APT specimens can be prepared and re-sharpened with a FIB [24]. For an improved visibility of the region of interest in such APT specimens transmission electron microscope (TEM) studies can support the specimen preparation.

Although Miller et al. [4,11] studied the influence of impurities in welded molybdenum alloys, technically pure molybdenum with no additional elements has not been examined so far which justifies this study. A detailed understanding of the location and content of impurities in molybdenum could help to develop molybdenum parts with improved mechanical properties in the future.

Therefore, in the present investigation two molybdenum sheets in the as-deformed and recrystallized state were studied by APT. The main focus was laid on the finding of the ideal preparation technique to analyze grain boundary segregation in technically pure molybdenum by means of APT.

2. Materials and Methods

The specimens for the APT analyses were taken out of two industrially processed hot-rolled sheets of technically pure molybdenum, designated as sheet 1 and sheet 2. The sheets were produced by cold-isostatic pressing of molybdenum powder followed by a conventional sintering process above 1800 °C. During the subsequent hot-rolling process above 1000 °C, the final passes were carried out to assure a sufficient degree of deformation (>60%) for complete recrystallization in case of a subsequent recrystallization annealing [25]. This recrystallization annealing was performed for 2 h at 1300 °C in hydrogen atmosphere. Specimens for the study of grain boundary segregation were extracted from both sheets in the as-deformed and recrystallized conditions. These specimens were then analyzed. The global chemical compositions of the two sheets in the as-deformed condition were determined by Glow Discharge Mass Spectrometry (GDMS) and are reported in Table 1.

In Fig. 1 the microstructure of sheet 2 in the as-deformed and recrystallized state studied by electron channeling contrast imaging (ECCI) [26] in a Zeiss Evo 50 scanning electron microscope (SEM) is shown. The recrystallized state of sheet 2 (Fig. 1a) exhibits a grain size of ~55 μm parallel to the rolling direction and ~42 μm vertical to the rolling direction which was determined by the standard linear intercept method from ECCI micrographs. The microstructure in Fig. 1b shows small areas of uniform contrast which are recovered subgrains with well-defined subgrain boundaries. The subgrain diameters are in the range between 1 and 5 μm. Sheet 1 has a similar microstructure, and, therefore, it is not shown here. The recrystallized grain size of sheet 1 is ~48 μm parallel to the rolling direction and ~35 μm vertical to the rolling direction.

Appendix A

Table 1 – Chemical compositions of the two sheets in the as-deformed condition determined by Glow Discharge Mass Spectrometry (GDMS). Sheet 2 has an increased potassium content. Deviations up to factor 2 of the true value are possible. ("<" indicates a value below the detection limit and "≤" a value which is not stable).

Element	Sheet 1		Sheet 2	
	[μg/g]	[wt.%]	[μg/g]	[wt.%]
C	<8.5	<0.00085	<6.5	<0.00065
O	≤12	≤0.00120	<5.9	<0.00059
N	<1.3	<0.00013	<0.4	<0.00004
K	4	0.00040	19	0.00190
Ba	1.0	0.00010	2.2	0.00022
P	2.4	0.00024	1.2	0.00012
La	0.02	0.00000	0.4	0.00004
Fe	3.7	0.00037	3.2	0.00032
Si	1.1	0.00011	1.3	0.00013
Mg	0.9	0.00009	1.1	0.00011
Al	0.2	0.00002	0.2	0.00002
Ca	0.2	0.00002	0.3	0.00003
S	0.09	0.00001	0.08	0.00001
W	120	0.01200	140	0.01400

For the APT specimen preparation three different techniques were used. First, the lift-out technique [20] was used for specimens from the recrystallized states due to the good visibility of the high angle grain boundaries as shown in Fig. 1. Second, the electro-polishing method with subsequent FIB preparation was applied for specimens from the recrystallized and as-deformed states. The third method was a combination of electro-polishing with subsequent FIB preparation and TEM investigations [27].

The FIB preparation of wedges from several grain boundaries was performed on a FEI Versa 3D DualBeam (FIB/SEM) workstation with a platinum gas injection system and an Omniprobe 100 micromanipulator. All preparation steps were carried out with an acceleration voltage of 30 kV and a suitable current for a balance between re-deposition and cutting time. To protect the region of interest from gallium implantation, a platinum layer was deposited on the surface. After the clearance cutting, wedges were lifted out with the micromanipulator and transferred to a post which was a silicon needle pad or a pre-electro-polished APT specimen. The specimens were attached to the post with a platinum deposition weld. Subsequently, annular milling was performed to give the APT specimens the right radius and shank length. In Fig. 2 a SEM image of an APT specimen of sheet 1 in the recrystallized condition is shown after the first annular milling steps. The platinum layer, the grain boundary, the platinum weld and the post are marked with arrows. The visibility of the grain boundary at this stage is still sufficient but for APT studies further annular milling has to be carried out. After this, the last preparation steps (cleaning) were carried out using the acceleration voltages 5 and 2 kV in order to reduce the gallium implantation. Applying this preparation method, the grain boundaries were initially visible on the surface of the specimens but their progression under the surface was not known. Furthermore, there were experimental problems during the APT measurements of such lift-out APT specimens. Several specimens melted due to poor heat discharge because of large differences in heat conductivity of the molybdenum APT specimens and the post materials (silicon needle pads). The use of molybdenum or steel tips did not significantly improve these experimental problems because in this case the platinum welds frequently fractured.

Therefore, pre-electro-polished specimens were produced out of the as-deformed and recrystallized states of each sheet and sharpened with the FIB. Small rods ($10 \times 0.3 \times 0.3$ mm^3) were cut from with their largest dimension parallel to the normal direction of the sheets. The electrolyte for the polishing of the APT specimen was 12.5 vol.% H_2SO_4 in ethanol in a gold ring (microloop) as counter electrode. A general description of the specimen preparation for APT by electro-polishing can be found in [28]. With subsequent annular milling in the FIB, the grain boundary could be positioned in the first 100 nm below the apex. However, it was always difficult to deduce if the grain boundary was in the volume which was later examined by APT or not for radii lower than ~500 nm due to the poor visibility in the FIB/SEM.

For this reason, a third method was applied which was expected to overcome the limitations of the other two methods. Electro-polished APT specimens were produced, sharpened with a FIB and analyzed by TEM to give additional information about the exact location of the grain boundary in the APT specimen at small radii. This part of the work was carried out with a FEI Strata DB 235 DualBeam FIB at an acceleration voltage of 30 kV. The TEM analyses were performed using a FEI Tecnai G2 TEM equipped with a LaB_6 filament at 200 kV. The specimens were characterized with the TEM between the milling steps to examine the remaining distance of the grain boundaries to the apex of the APT specimens by bright field and dark field imaging. To keep the electron-beam-contamination of the specimen low, only quick TEM analyses were made and, therefore, no orientation measurements by diffraction were carried out. After re-sharpening in the FIB, the specimens were analyzed in the TEM and inserted into the FIB again to bring the grain boundary into the first 100 nm. Repeated exchanges between the FIB and TEM were necessary for this technique.

All APT specimens were analyzed with a LEAP 3000X HR from Cameca operated in laser mode. A laser energy of 0.6 nJ, a base temperature of 60 K and a pulse rate of 200 kHz were used. The target evaporation rate was set to 0.5%. For the reconstruction of the analyses the IVAS 3.6.0 data software from Cameca was used.

3. Results

Prior to the site-specific analyses of the location and the contents of the impurities the chemical compositions of both sheets in the as-deformed state were determined globally by GDMS. This was primarily done to find out which impurity elements are in the sheets in order to facilitate the search for small peaks in the APT spectra. In Table 1, the GDMS results are shown. Sheet 1 may have an increased oxygen content (12 μg/g versus 5.9 μg/g in sheet 2) even if the value determined by GDMS was not stable. Oxygen has a low solubility in molybdenum and, therefore, is supposed to accumulate at the grain boundaries [29]. The main difference between the two

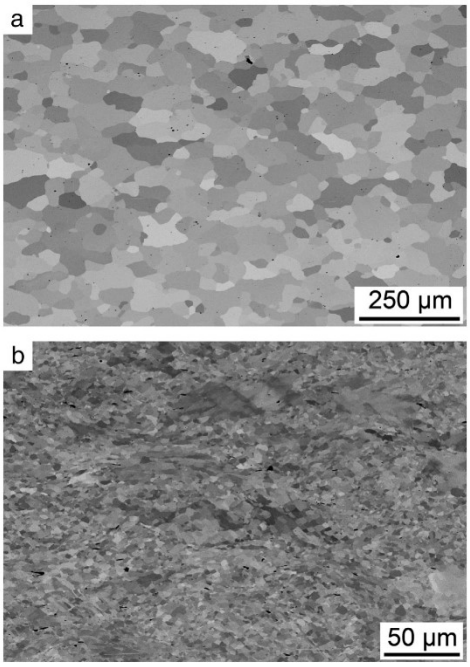

Fig. 1 – SEM ECCI images of the microstructure of sheet 2 in the (a) recrystallized and (b) as-deformed states. The horizontal direction is the rolling direction and the vertical direction is the normal direction.

sheets is the potassium content. Potassium is also believed to segregate at the grain boundaries [13]. Sheet 2 has an increased potassium content of 19 µg/g while only 4 µg/g were detected in sheet 1. In the case of potassium deviations up to a factor of two are possible. Therefore, the obtained values should be treated carefully. A deviation up to a factor of two means that even if 4 µg/g were detected in sheet 1 the true value might be between 2 and 8 µg/g. The same is true for sheet 2 (true value between 10 and 38 µg/g). Even if the true values cannot be determined, the difference in potassium content between the two sheets is significant. A high amount (>100 µg/g) of tungsten was found in both sheets which is typical for the current quality of technically pure molybdenum [30,31]. However, tungsten is not supposed to segregate at the grain boundaries. Further impurity contents of elements as for example magnesium, nitrogen, calcium, aluminum, barium, iron or silicon are also in the µg/g range.

Three results of the APT analyses are presented in this section. Fig. 3 shows the reconstruction of an analyzed APT specimen from the as-deformed state of sheet 2 which was prepared by sharpening of pre-electro-polished APT specimens by FIB without TEM investigations. No impurities were found in the analyzed volume except of small amounts of oxygen (0.024 at.%) and magnesium (0.003 at.%). Therefore, no

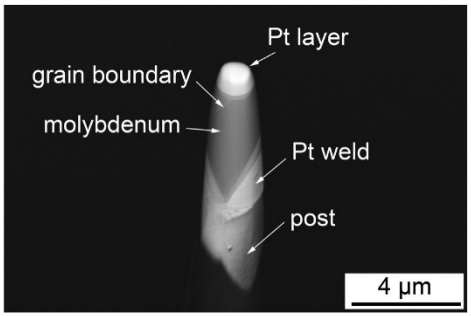

Fig. 2 – SEM image of a FIB prepared APT specimen of molybdenum out of sheet 1 in recrystallized condition with a single grain boundary after the first annular milling steps.

grain boundary is visible in Fig. 3. It cannot be deduced without doubt if a grain boundary without segregants was present in the measured volume by APT because no additional TEM studies were carried out. Although tungsten was observed in the GDMS chemical analyses (Table 1), it was not detected in the APT analyses.

In Fig. 4, a TEM bright (a) and two dark field (b,c) images of another APT specimen are shown. Fig. 5 is the corresponding reconstruction of the APT analysis. This specimen was also prepared from sheet 2 in the as-deformed state. A grain

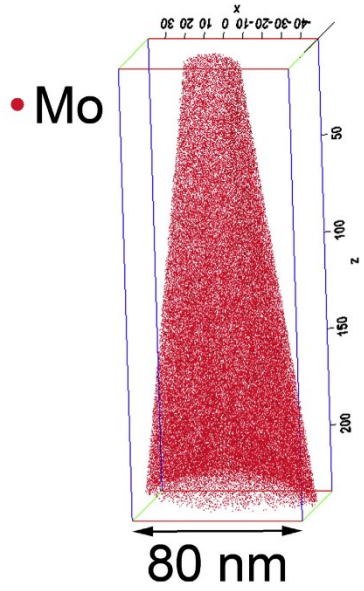

Fig. 3 – APT reconstruction of an APT specimen from the as-deformed state of sheet 2 after the atom probe measurement. The inset shows the corresponding color code for the ions/molecules detected.

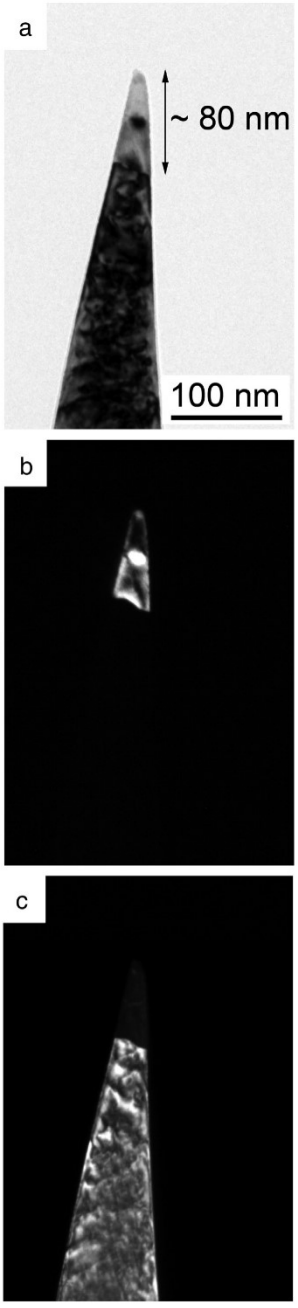

Fig. 4 – TEM image of FIB prepared APT specimen out of sheet 2 in the as-deformed state (a) bright field image (b) dark field image (c) dark field image.

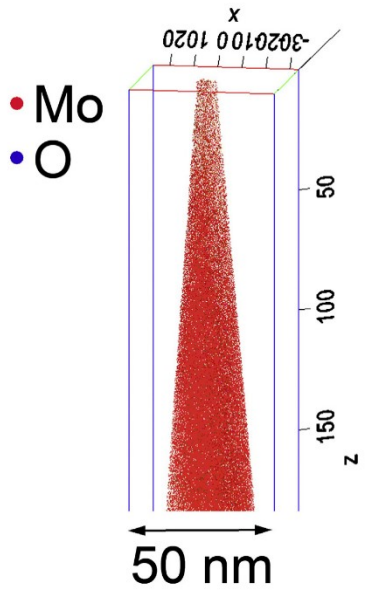

Fig. 5 – APT reconstruction of the APT specimen from sheet 2 in the as-deformed state after the atom probe measurement. The inset shows the corresponding color code for the ions/molecules detected. Gallium is blanked for improved visibility.

boundary is visible within the first ~80 nm of the TEM bright field image which is additionally pointed out by the two dark field images of the apex grain and the grain below. The reconstruction of the APT measurement shows no grain boundary segregation at ~80 nm below the apex even if in this case the grain boundary must have been contained in the volume examined. Molybdenum, oxygen and gallium atoms were found in the bulk chemical analysis of this APT specimen. Gallium was implanted during FIB preparation without cleaning at low acceleration voltage but is not shown in Fig. 5. Molybdenum, molybdenum–oxygen and oxygen ions and molecules were preferentially detected on one side of the APT specimen because of the direction of the laser beam.

Nevertheless, grain boundary segregation was found in some other specimens. The specimen presented in Fig. 6 is from sheet 1 in the recrystallized state. Fig. 6 shows a TEM bright field image (a) and the corresponding APT reconstruction (b) of this specimen with a "segregated region" and a grain boundary with segregants which are marked by the green and the blue arrow, correspondingly. In this APT reconstruction only molybdenum–oxygen, gallium and oxygen molecules and ions are shown. Phosphorus, nitrogen and oxygen were detected at the grain boundary with the atom probe as shown in the reconstruction of the same specimen in Fig. 7 where all other elements except molybdenum and gallium are shown. The elements magnesium, oxygen, nitrogen, calcium, potassium, aluminum, barium, iron and silicon are concentrated in the "segregated region".

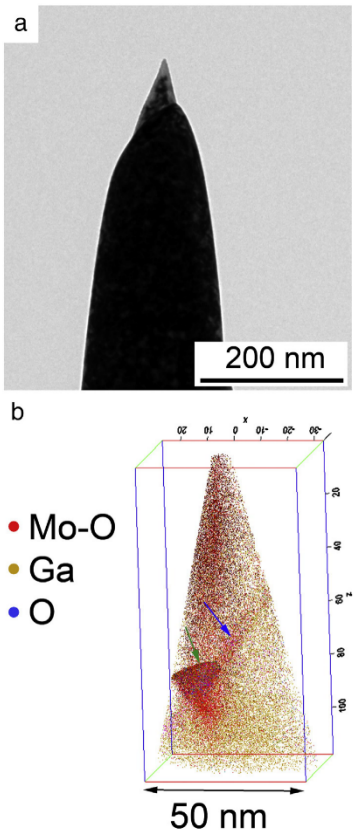

Fig. 6 – TEM image of a FIB prepared APT specimen of the recrystallized state of sheet 1 (a) bright field image (b) APT reconstruction of APT specimen. The green arrow in (b) marks a "segregated region", the blue arrow the grain boundary with segregants and the inset shows the color code for the ions/molecules detected. In the reconstruction only molybdenum–oxygen, gallium and oxygen are shown. (For interpretation of the references to color in this figure legend, the reader is referred to the web version of this article.)

Molybdenum–oxygen molecules are concentrated in the grain boundary, in the "segregated region" and on one side of the APT specimen due to the direction of the laser beam. The concentration of gallium is also increased in the segregated region and at the grain boundary. The bulk composition as determined by APT is summarized in Table 2. Most of the elements which have been detected by GDMS (Table 1) were also found in this APT specimen. The only elements which were not found in the APT specimen are sulfur, lanthanum and tungsten. Furthermore, no carbon was detected in the APT analyses. For the APT bulk composition a volume of around 0.0003 μm^3 was analyzed. This volume contains the contaminated grain boundary as well as the "segregated region" as shown in the reconstruction in Fig. 6b. Therefore, the content of impurity elements in the bulk composition determined by APT is higher than in case of the GDMS analyses. Gallium in Table 2 originates from the FIB preparation, and hydrogen is possibly an impurity from the chamber of the atom probe.

To study the impurity elements in this APT specimen in more detail, one-dimensional concentration profiles were calculated over special regions of interest. These regions and arrows which indicate the directions of the x-axes of the corresponding concentration profiles are shown in Fig. 7. One area was selected to create a one-dimensional concentration profile over the "segregated region" and another one over the grain boundary. Only phosphorus, nitrogen and oxygen are detected at the grain boundary, the other elements are accumulated only in the "segregated region". The one-dimensional concentration profile through the grain boundary in Fig. 8 shows that the contents of oxygen, nitrogen and phosphorus increase at around 10 nm distance from the origin. Oxygen has a maximum content of ~0.35, nitrogen of ~0.2 and potassium ~0.08 at.%. The other elements which are listed in the bulk composition (Table 2) are not present close to the grain boundary. The one-dimensional concentration profile for the "segregated region" (Fig. 9) shows that the contents of several further elements are also increased in this area. The majority of the potassium (up to 1.5 at.%) is in the upper part of this region and all other elements accumulate beneath. The most heavily segregated elements are magnesium (~2.5 at.%), nitrogen (~1.7 at.%) and calcium (~1.2 at.%).

4. Discussion

Due to state-of-the-art fabrication processes, it is possible to produce pure metals with impurity contents in the parts per million range. However, impurities still cannot be completely avoided during the production and subsequent processing of pure metals. As shown in Table 1, technically pure molybdenum produced by state-of-the art powder metallurgical processes contains e.g. impurity elements such as oxygen, potassium, barium, iron, aluminum, phosphorus, magnesium and silicon. In case of chemical analyses such as GDMS, the content of impurity elements can be measured, but not their location in the microstructure to study grain boundary segregation [32,33]. Furthermore, the impurity contents in the current quality of technically pure molybdenum are so small that they are below the detection limits of surface sensitive methods such as Auger electron spectroscopy which are, for this reason, not applicable anymore [13]. Therefore, atom probe tomography seems to be the only suitable experimental technique with its almost atomic resolution and the possibility to study "virgin" grain boundaries due to a layer by layer removal of atoms. However, a site-specific FIB specimen preparation procedure for molybdenum or refractory metals in general still has to be established which is attempted in the present study. Initially, during the FIB preparation several problems occurred.

In case of the lift-out technique, the grain boundaries were visible on the surface of the specimens (as shown in Fig. 1), but their progression under the surface was not known. It could be possible that the grain boundary exited the wedge after some nanometers below the surface. A three dimensional view of the boundary was not possible prior to the lift-out of the wedge.

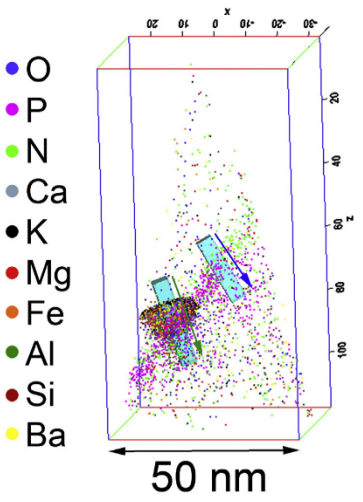

Fig. 7 – APT reconstruction of the grain boundary and the "segregated region". The regions of interest for the one-dimensional concentration profiles for the grain boundary (direction of analysis indicated by the blue arrow) and for the one-dimensional concentration profile for the "segregated region" (direction of analysis is indicated by the green arrow) are shown as turquoise boxes. The inset shows the color code for the ions/molecules detected. Molybdenum and gallium atoms are omitted to point out the other elements. (For interpretation of the references to color in this figure legend, the reader is referred to the web version of this article.)

Furthermore, the visibility of the grain boundary during the annular milling process at radii lower than ~500 nm was very poor and lead to "blind preparation". In case of the lift-out prepared APT specimens there was no evidence if a boundary was in the volume examined by APT especially if there were no segregants detected.

Additionally, electro-polished APT specimens were produced and sharpened in the FIB. However, for these APT specimens similar visibility problems occurred as for the lift-out prepared APT specimens even if the APT measurements were in general more successful. During the first annular milling steps the boundary was visible, but when the radii were below ~500 nm the grain boundary became indiscernible.

Table 2 – Bulk composition of a specimen from sheet 1, recrystallized state, as determined by APT.

Element	Content [at.%]	Content [wt.%]
Mo	98.271	99.165%
Ga	0.882	0.647%
H	0.039	0.000%
O	0.591	0.099%
N	0.046	0.007%
K	0.025	0.010%
Ba	0.018	0.026%
P	0.031	0.010%
Fe	0.015	0.009%
Si	0.006	0.002%
Mg	0.039	0.010%
Al	0.009	0.003%
Ca	0.029	0.012%

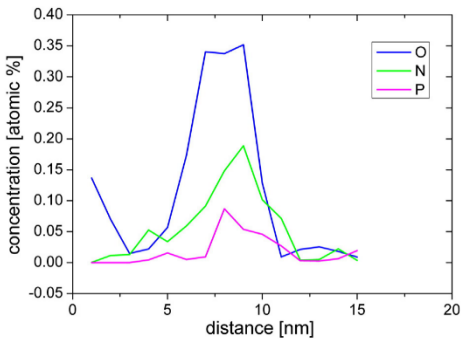

Fig. 8 – One-dimensional concentration profile of the region of interest marked in Fig. 7. This profile runs through the grain boundary.

The reconstruction of an electro-polished APT specimen out of the as-deformed state of sheet 2 (Fig. 3) without TEM characterization exhibits no segregation. Due to the low visibility of the grain boundary in the APT specimen after the milling process in the FIB/SEM it is not sure if a boundary without segregants was in the analyzed part of the APT specimen.

Therefore, the third method of preparation which was expected to overcome the limitations of the other two methods was applied. TEM analyses in-between the FIB preparation steps of pre-electro-polished APT specimens were performed to give information about the exact position of the grain boundaries. In the past, this method has already been used to study grain and phase boundary segregants of e.g. hard metals [24]. The FIB/TEM combination improved the preparation process due to the clear identification of the grain boundary in the APT

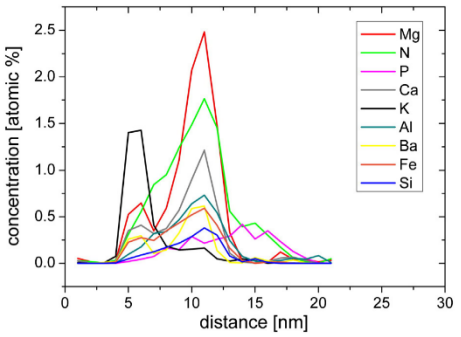

Fig. 9 – One-dimensional concentration profile of the region of interest marked in Fig. 7. This profile runs through the "segregated region". Molybdenum, oxygen and gallium are not shown to enhance the illustration of the other impurity elements.

specimens as shown in Figs. 4 and 6. Furthermore, the shank and the radius of each APT specimen could be measured in the TEM exactly which was useful to define a correct reconstruction of the APT specimen.

The TEM images in Fig. 4 (as-deformed state of sheet 2) show a boundary in the first 80 nm of the APT specimen of the as-deformed state. Therefore, this grain boundary must be in the detected volume of the APT measurement of this specimen. As visible in Fig. 5, the reconstruction shows no segregation at this grain boundary. This could be caused by two facts. Either the grain boundary did not contain any impurities or a subgrain boundary in the as-deformed state was measured. However, the second option seems more plausible in case of the recovered subgrain structure as shown in Fig. 1b where the majority of boundaries are of low angle character. The same might be the case for the reconstruction of the APT specimen without TEM characterization shown in Fig. 3. The third preparation method is the only one which can be applied to evidence the presence of grain boundaries without segregants by APT. Therefore, this method is superior for the study of grain boundary segregation in molybdenum.

The recrystallized state contains mostly high angle grain boundaries, but still some low-angle and low-sigma boundaries may exist, even after recrystallization. A representative measurement (Fig. 6) of the recrystallized state of sheet 1 shows a boundary with a "segregated region" and segregants at the grain boundary. Phosphorus, oxygen and nitrogen are detected at the grain boundary which might affect the local fracture behavior. Gludovatz et al. [34] investigated the influence of impurities on the fracture behavior of tungsten and discovered phosphorus at the grain boundaries as well. Furthermore, his results showed that intergranular fracture does not have a direct relation to differences in grain boundary impurities. Effects as the shape of grains, grain size distribution, texture, dislocation density and temperature influence the fracture behavior in a greater manner than grain boundary segregation themselves. However, Gludovatz et al. assumed that even if the impurities have no direct correlation to the fracture behavior in tungsten, they do have an impact on the ductility in the form of initiators for cracks or pores. The "segregated region", in the present study which is possibly a former pore, contains the same impurity elements as detected by the GDMS analysis except sulfur, tungsten and carbon. These elements are, therefore, supposed to occur only locally in the molybdenum sheets. Furthermore, the content of impurity elements of the APT bulk composition analysis is quite higher than for the GDMS characterization. With the APT just a volume of 0.0003 μm^3 was investigated which included the restricted "segregated region" and the grain boundary with segregants. Therefore, the difference in impurity element contents occurred. The micropores originate from the sinter process and are closed during the hot-rolling of the sheets. It is assumed that impurities are still located in the regions of such former pores after a degree of deformation of ~60% and might act as crack initiators in molybdenum sheets as well. Upon subsequent recrystallization annealing as carried out in the present study, these impurities might diffuse along the grain boundary such as the one which runs through the segregated region as shown in Fig. 7. Therefore, for a more homogenous distribution of the impurities further deformation and annealing steps are suggested.

Due to the apparently inhomogeneous distribution of impurities in the sheets of the present investigation and the limited number of successful APT measurements it was not possible to reveal differences in between the two sheets in terms of potassium or oxygen contents. Therefore, based on the results of the present investigation, more detailed studies will be carried out in the future using sheets with higher degrees of deformation. These studies should also reveal the influence of different impurity contents on the type and location of impurities and the grain boundary character in more detail which could help to develop molybdenum parts with improved grain boundary strength and, thus, resulting mechanical properties.

5. Conclusions

In this work, a site-specific specimen preparation technique for the investigation of grain boundary segregation in technically pure molybdenum by APT is developed and successfully applied.

The main results of the present investigation can be summarized as follows:

- The most applicable preparation technique is the sharpening of pre-electro-polished APT specimens by FIB in combination with TEM studies. The TEM studies give exact information about the position of the grain boundary in the APT specimen which is not possible by FIB/SEM due to the low visibility during the last preparation steps.
- Due to the almost atomic resolution of the APT low concentrations of grain boundary segregation as present in the current quality of high purity molybdenum can be studied.
- Some boundaries without segregation were found in as-rolled microstructures which are possibly subgrain boundaries. However, in this case complementary TEM investigations are necessary in order to evidence that the boundary was contained in the volume examined.
- Segregation of oxygen, nitrogen and potassium was detected at grain boundaries in recrystallized sheets close to "segregated regions" which are believed to be former sinter pores. In such "segregated regions" several further impurities which have also been detected by GDMS analyses of the bulk material were found.

This preparation technique could be used in the future to study the content and location of grain boundary segregation in molybdenum in more detail in order to analyze the influence of impurities on the grain boundary strength and the resulting mechanical properties.

REFERENCES

[1] Schneibel JH, Brady MP, Kruzic JJ, Ritchie RO. On the improvement of the ductility of molybdenum by spinel (MgAI204) particles. Z Metallkd 2005;96:632–7.
[2] Kumar A, Eyre B. Grain boundary segregation and intergranular fracture in molybdenum. Proc R Soc Lond A Math Phys Sci 1980;370:431–58.
[3] Pink E. Rekristallisationsdiagramme von Molybdän und Wolfram. Planseeberichte für Pulvermetallurgie 1965;13:100–4.

Appendix A

[4] Miller M, Bryhan A. Effect of Zr, B and C additions on the ductility of molybdenum. Mater Sci Eng A 2002;327:80–3.
[5] Suzuki S, Matsui H, Kimura H. The effect of heat treatment on the grain boundary fracture of recrystallized molybdenum. Mater Sci Eng 1981;47:209–16.
[6] Krajnikov A, Morito F, Slyunyaev V. Impurity-induced embrittlement of heat-affected zone in welded Mo-based alloys. Int J Refract Met Hard Mater 1997;15:325–39.
[7] Kimura H. Overview, intergranular fracture in BBC metals. Trans Jpn Inst Met 1988;29:521–39.
[8] Geller CB, Smith RW, Hack JE, Saxe P, Wimmer E. A computational search for ductilizing additives to Mo. Scr Mater 2005;52:205–10.
[9] Tsurekawa S, Tanaka T, Yoshinaga H. Grain boundary structure, energy and strength in molybdenum. Mater Sci Eng A 1994;176:341–8.
[10] Brosse JB, Fillet R, Biscondi M. Intrinsic intergranular brittleness of molybdenum. Scr Metall 1981;15:619–23.
[11] Miller M, Kenik E, Mousa M, Russell K, Bryhan A. Improvement in the ductility of molybdenum alloys due to grain boundary segregation. Scr Mater 2002;46:299–303.
[12] Tahir A, Janisch R, Hartmaier A. Ab initio calculation of traction separation laws for a grain boundary in molybdenum with segregated C impurities. Model Simul Mater Sci Eng 2013;21:075005.
[13] Babinsky K, Primig S, Knabl W, Lorich A, Weingärtner T, Weidow J, et al. Grain boundary segregations in technically pure molybdenum. Proc. 18th Plansee seminar, Plansee SE; 2013. p. RM111/1-15.
[14] Miller MK, Forbes RG. Atom probe tomography. Mater Charact 2009;60:461–9.
[15] Miller MK. The development of atom probe field-ion microscopy. Mater Charact 2000;44:11–27.
[16] Miller MK, Kelly TF, Rajan K, Ringer SP. The future of atom probe tomography. Mater Today 2012;15:158–65.
[17] Kelly TF, Miller MK. Invited review article: atom probe tomography. Rev Sci Instrum 2007(78) [031101-1-20].
[18] Cerezo A, Clifton PH, Galtrey MJ, Humphreys CJ, Kelly TF, Larson DJ, et al. Atom probe tomography today. Mater Today 2007;10:36–42.
[19] Munroe PR. The application of focused ion beam microscopy in the material sciences. Mater Charact 2009;60:2–13.
[20] Miller MK, Russell KF. Atom probe specimen preparation with a dual beam SEM/FIB miller. Ultramicroscopy 2007;107:761–6.
[21] Felfer P, Ringer SP, Cairney JM. Shaping the lens of the atom probe: fabrication of site specific, oriented specimens and application to grain boundary analysis. Ultramicroscopy 2011;111:435–9.
[22] Pérez-Willard F, Wolde-Giorgis D, Al-Kassab T, López GA, Mittemeijer EJ, Kirchheim R, et al. Focused ion beam preparation of atom probe specimens containing a single crystallographically well-defined grain boundary. Micron 2008;39:45–52.
[23] Cairney JM, Saxey DW, McGrouther D, Ringer SP. Site-specific specimen preparation for atom probe tomography of grain boundaries. Phys B 2007;394:267–9.
[24] Weidow J, Andrén H-O. Grain and phase boundary segregation in WC–Co with small V, Cr or Mn additions. Acta Mater 2010;58:3888–94.
[25] Primig S, Leitner H, Clemens H, Lorich A, Knabl W, Stickler R. On the recrystallization behavior of technically pure molybdenum. Int J Refract Met Hard Mater 2010;28:703–8.
[26] Simkin B, Crimp M. An experimentally convenient configuration for electron channeling contrast imaging. Ultramicroscopy 1999;77:65–75.
[27] Weidow J, Andrén H-O. Grain and phase boundary segregation in WC–Co with TiC, ZrC, NbC or TaC additions. Int J Refract Met Hard Mater 2011;29:38–43.
[28] Miller MK, Cerezo A, Hetherington MG, Smith GDW. Atom probe field ion microscopy. Oxford: Claredon Press; 1996.
[29] Srivastava S, Seigle L. Solubility and thermodynamic properties of oxygen in solid molybdenum. Metall Trans 1974;5:49.
[30] Primig S, Leitner H, Knabl W, Lorich A, Clemens H, Stickler R. Textural evolution during dynamic recovery and static recrystallization of molybdenum. Metall Mater Trans A 2012;43:4794–805.
[31] Primig S, Leitner H, Knabl W, Lorich A, Stickler R. Static recrystallization of molybdenum after deformation below 0.5*T M (K). Metall Mater Trans A 2012;43:4806–18.
[32] Bogaerts A, Gijbels R. Fundamental aspects and applications of glow discharge spectrometric techniques. Spectrochim Acta B 1998;53:1–42.
[33] King FL, Teng J, Steiner RE. Glow discharge mass spectrometry: trace element determinations in solid samples. J Mass Spectrom 1995;30:1061–75.
[34] Gludovatz B, Wurster S, Weingärtner T, Hoffmann A, Pippan R. Influence of impurities on the fracture behaviour of tungsten. Phil Mag 2011;91:3006–20.

Appendix B

Author's personal copy

Originalarbeit

BHM (2015) Vol. 160 (5): 204–208
DOI 10.1007/s00501-015-0358-1
© Springer-Verlag Wien 2015

BHM Berg- und Hüttenmännische Monatshefte

Boron Grain Boundary Segregation in a Heat Treatable Steel

Phillip Haslberger[1], Christoph Turk[1], Katharina Babinsky[1], Devrim Caliskanoglu[2], Helmut Clemens[1] and Sophie Primig[1]

[1]Department of Physical Metallurgy and Materials Testing, Montanuniversitaet Leoben, Leoben, Austria
[2]Buderus Edelstahl GmbH, Wetzlar, Germany

Received January 30, 2015; accepted February 23, 2015; published online March 20, 2015

Abstract: By applying a heat treatment, such as hardening and tempering, the properties of a heat treatable steel, like 42CrMo4, can be adjusted over a wide range. In addition to the heat treatment, an appropriate alloying concept is crucial to be able to guarantee an outstanding performance over a large variety of applications. In the present study, the effects of boron as a microalloying element on a heat treatable steel were examined. It is well known that boron, if added in a proper amount, can significantly retard the transformation of austenite to bainite or ferrite/pearlite in low alloyed steels. During the heat treatment, it diffuses to the austenite grain boundaries, where it reduces the driving force for the nucleation of new phases. In order to prove this theory in a heat treatable steel, a prior austenite grain boundary was prepared for atom probe tomography (APT). The specimen preparation was carried out by electro-polishing, etching, and sharpening by focused ion beam (FIB) in combination with transmission Kikuchi diffraction (TKD). In the reconstruction of the corresponding APT measurement, boron could be found at the same prior austenite grain boundary.

Keywords: Heat treatable steel, Boron, Austenite grain boundary, Transmission Kikuchi diffraction, Atom probe tomography

Die Korngrenzensegregation von Bor in einem Vergütungsstahl

Zusammenfassung: Durch gezielte Wärmebehandlungen wie Härten und Anlassen können die Eigenschaften eines Vergütungsstahls wie 42CrMo4 in einem großen Bereich eingestellt werden. Zusätzlich zu einer optimierten Wärmebehandlung ist auch das Legierungskonzept entscheidend, wenn man eine herausragende Leistungsfähigkeit in einer Vielzahl von Anwendungen garantieren will. Die Wirkung von Bor als Mikrolegierungselement in einem Vergütungsstahl wurde in dieser Arbeit untersucht. Laut Literatur verzögert Bor in der richtigen Konzentration die Umwandlung von Austenit zu Bainit oder Ferrit/Perlit, indem es während der Wärmebehandlung an die Austenitkorngrenzen diffundiert und dort die Triebkraft für eine Keimbildung neuer Phasen verringert. Um diese Theorie in einem Vergütungsstahl zu verifizieren, wurde eine ehemalige Austenitkorngrenze für eine Untersuchung mit der Atomsonde präpariert. Die Probenpräparation erfolgte durch elektrolytisches Polieren, Ätzen und Spitzen mittels Focused Ion Beam (FIB) in Kombination mit Transmission Kikuchi Diffraktion (TKD). In der Rückkonstruktion der anschließenden Messung mit der Atomsonde konnte Bor an der ehemaligen Austenitkorngrenze gefunden werden.

Schlüsselwörter: Vergütungsstahl, Bor, Austenitkorngrenze, Transmission Kikuchi Diffraktion, Atomsonde

1. Introduction

Heat treatable steels, such as 42CrMo4, can be used for a variety of applications, such as shafts, bolts, and screws. A high strength as well as a reasonable toughness can be achieved by a proper heat treatment consisting of hardening and tempering and an elaborate alloying concept. The cooling time during quenching after austenitization as well as the temperature and time of the tempering step define the microstructure and consequently the mechanical properties of the steel. The microstructure of a heat treatable steel is usually constituted of martensite and/or bainite. The alloying concept plays a vital role in inhibiting the nucleation of soft high-temperature phases like ferrite

Dipl.-Ing. P. Haslberger (✉)
Department of Physical Metallurgy and Materials Testing, Montanuniversitaet Leoben,
Roseggerstraße 12/2,
8700 Leoben, Austria
e-mail: phillip.haslberger@unileoben.ac.at

Author's personal copy

TABLE 1:
Chemical composition of the steel used for the experiments in m %

C	Si	Mn	Cr	Ni	Mo	V	Cu	Ti	N	B	Fe
0.41	0.23	0.85	1.11	0.48	0.28	0.10	0.08	0.019	0.007	0.0037	Rest

and pearlite. Alloying elements such as chromium and manganese reduce the ability of iron atoms to diffuse in the lattice, which impedes the formation of new phases. The effect of boron on the hardenability of steels has been extensively studied in low alloyed manganese steels. By segregating to austenite grain boundaries and hence lowering the grain boundary energy, boron is known to retard the formation of ferrite and pearlite [1–4]. However, well-established techniques such as energy dispersive X-ray spectroscopy (EDX) are not suitable for the qualitative and quantitative detection of boron in a material. As a consequence, little information can be found on experiments evidencing the position of boron in the iron lattice. Therefore, in this study a typical heat treatable steel, 42CrMo4, was studied by means of atom probe tomography. This method based on the field evaporation of individual atoms allows atomic resolution for every element of the periodic table. Thus, it is suitable for the detection of boron in steels. In order to be able to measure a prior austenite grain boundary, a special site-specific specimen preparation procedure was carried out. After electro-polishing, the prior austenite grain boundaries of the tip of the specimen were localized by etching. The grain boundary most closely located to the apex of the tip was selected for a target preparation in a FIB/SEM dual beam microscope in combination with TKD.

2. Boron as a Microalloying Element

Empirical investigations showed that the solubility of boron is between 0.0055 and 0.026 m % at 1150 °C in γ-iron and between 0.002 and 0.008 m % at 910 °C in α-iron [1]. This low solubility leads to a strong tendency of boron to segregate to austenite grain boundaries. During cooling from austenitization, the boron atoms form complexes with voids which diffuse to the grain boundaries by a non-equilibrium mechanism. The energy of the austenite grain boundaries is reduced when boron is introduced into the lattice there [2–4].

Nucleation of new phases occurs due to concentration gradients and energy fluctuations. Apart from an appropriate concentration and lattice configuration, energy is required in order to be able to grow a nucleus [4]. Grain boundaries show a high defect concentration and are accordingly sites of high energy at which nucleation occurs preferentially. Boron reduces the driving force for nucleation by reducing the grain boundary energy. As a result, fewer ferrite particles can be found in a boron-alloyed steel compared to a boron-free steel at a specific temperature [4]. Nevertheless, if the boron concentration exceeds an optimum amount, an oversaturation of the grain boundary leads to an increase of the grain boundary energy, which is detrimental to the described retardation effect [5].

Several experiments led to the conclusion that an amount of ca. 30 ppm boron yields a maximum increase in hardenability. Additionally, a minimum of the brittle to ductile transition temperature appears in the same alloying range [5]. Special attention has to be paid to the amount of free nitrogen in the steel as boron tends to form nitrides which are highly stable. Therefore, strong nitride formers like titanium or zirconium can be added to the steel melt prior to a boron addition, hence allowing boron to stay in solution.

3. Experimental Procedure

3.1 Material

The aim of the experiments was to provide information on the position of boron in a 42CrMo4 heat treatable steel after cooling from the austenite region. The chemical composition is shown in Table 1. The heat treatment was carried out in a TA instruments quenching dilatometer (DIL 805A). The specimen geometry was cylindrical with a diameter of 5 mm and a length of 10 mm. The temperature was controlled by type S thermocouples.

3.2 Site-specific Preparation of a Prior Austenite Grain Boundary for APT

Prior to the APT specimen preparation, the material was austenitized at 870 °C in vacuum for 3 h and subsequently quenched at a rate of 30 K/s using nitrogen gas. The resulting microstructure was fully martensitic. A rod with dimensions of 0.3 × 0.3 × 10 mm³ was cut from the heat treated material and electro-polished in several steps to form a sharp tip using the standard two step procedure [6]. This tip was etched for 5 min using picrinic acid [7] to reveal the prior austenite grain boundaries. Because the volume of material which can be measured in the atom probe is limited, the prior austenite grain boundary had to be positioned in the first 200 nm of the tip. Therefore, an advanced site-specific preparation was carried out in a FEI Versa 3D DualBeam FIB/SEM. The experimental setup in the FIB/SEM is shown in Fig. 1.

Figure 2 shows an SEM (scanning electron microscope) image in secondary electron mode at 30 kV of the tip in the etched condition. Two prior austenite grain boundaries are visible. The grain boundary closer to the apex of the tip was chosen for the site-specific preparation.

When material is removed by annular milling with the ion beam, the grooves produced by former etching disappear deleting the information about the location of the grain boundary. To overcome this difficulty, the preparation process was supported by TKD measurements and

 © Springer-Verlag Wien

Author's personal copy

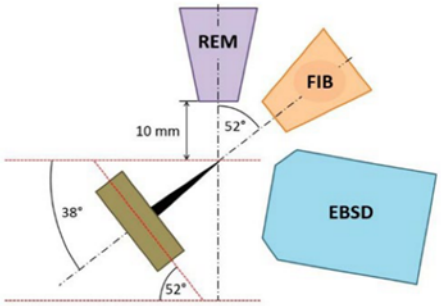

Fig. 1: Experimental setup in the FIB/SEM. The electron column (*SEM*) is used for imaging during the whole preparation procedure and as electron source for the TKD measurements. The transmitted electrons of a TKD measurement are detected by the EBSD detector. The FIB column is used for the annular milling

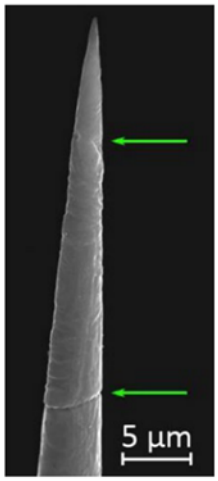

Fig. 2: SEM image of the etched atom probe specimen. The arrows indicate prior austenite grain boundaries which have been revealed by etching

determined the crystallographic disorientation between martensitic laths, similar to a procedure described in [8]. An EDAX Hikari XP EBSD system was used for the TKD measurements. The parameters for the TKD scans were used as shown in Table 2. The data was collected by the EDAX OIM Data Collection 7 software and evaluated with the EDAX OIM Analysis 7 software.

3.3 Atom Probe Tomography

The atom probe tomography measurement of the ready-prepared specimen was carried out in a Cameca LEAP 3000X HR. The tip was measured in laser mode with a green laser (wavelength 532 nm) and a laser energy of 0.3 nJ, a pulse rate of 250 kHz, and a target evaporation rate of 1 % at a temperature of 60 K. The operating principle of the atom probe is explained in detail in [9]. IVAS 3.6.6 was used as software for the reconstruction of the measurement.

TABLE 2:
Parameters for the TKD scans during the atom probe specimen preparation in a FIB/SEM

Parameter	Value
Voltage	30 kV
Current	11 nA
Binning	4×4
Specimen tilt angle	−38°
Step size	8 nm
Background	Enhanced
Hough P. type	Classic+
Hough resolution	Low
Convolution mask	9×9
Binned pattern size	120
Theta step size	0.5

4. Results

4.1 APT Specimen Preparation

The final TKD scans of the prepared tip are displayed in Fig. 3. Different colors indicate different crystal orientations. A grain boundary with a misorientation of 53° was found. According to the Kurdjumov-Sachs orientation relationship, martensitic laths of the same packet exhibit specific angles of misorientation [10]. Therefore, the interface highlighted by a dotted line is a prior austenite grain boundary because of the absence of such an orientation relationship in this case.

4.2 Atom Probe Tomography

The reconstruction of the data received in the atom probe is depicted in Fig. 4a. For a clearer picture of possibly measured grain boundaries, all atoms were hidden, and subsequently only carbon and boron atoms were displayed (see Fig. 4b). Several local enrichments in carbon as well as a large area enriched in carbon and boron (highlighted by an arrow) could be found. By rotating the reconstruction clockwise by 30° (Fig. 4c), a martensitic lath boundary (indicated by arrows) could be revealed clearly.

A cylindrical region of interest with a diameter of 25 nm was used to create a 1D concentration profile through the boron enriched area. The concentration profile (Fig. 5) showed a peak in the boron concentration with about 1.5 at %. Also carbon, molybdenum, and vanadium were enriched at the grain boundary.

 © Springer-Verlag Wien

Author's personal copy

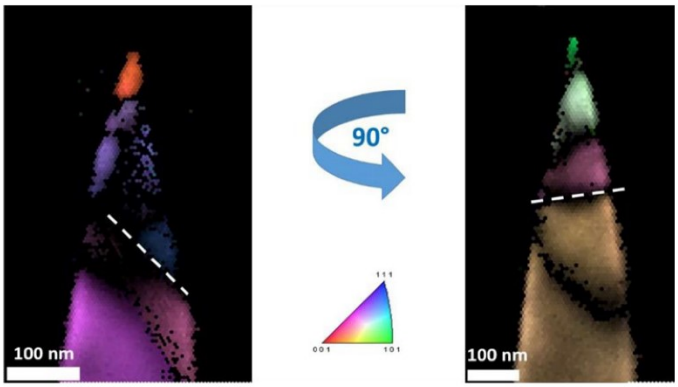

Fig. 3: Final TKD scans of the prepared tip (inverse pole figure + image quality map). Different colors indicate different crystal orientations. The prior austenite grain boundary is highlighted by a dotted line

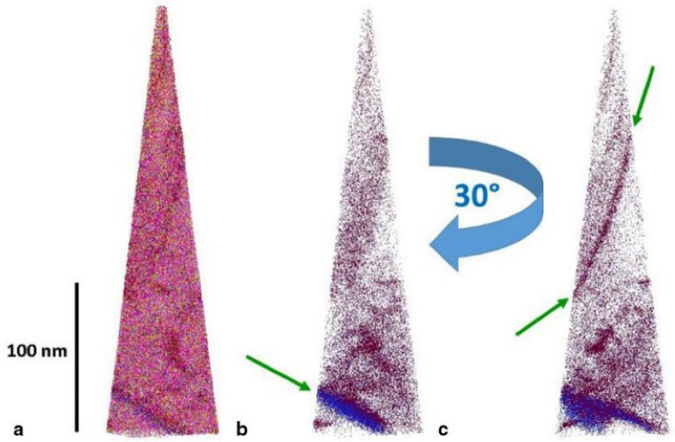

Fig. 4: Reconstruction of the APT measurement. **a** All atoms are displayed. **b** Carbon (*brown*) and boron (*blue*) atoms are displayed. The prior austenite grain boundary is indicated by an arrow. **c** Rotated view of the reconstruction. A martensite lath boundary is indicated by arrows

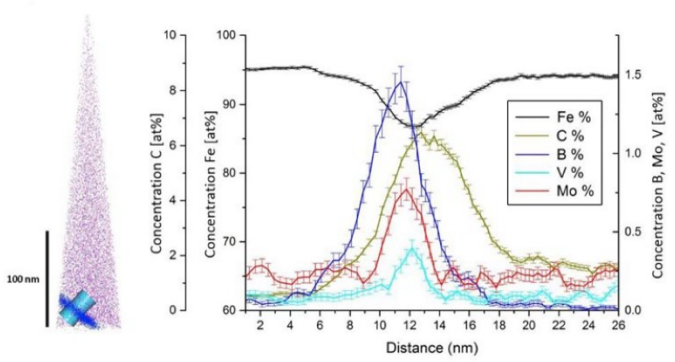

Fig. 5: 1D concentration profile of the prior austenite grain boundary along the longitudinal axis of the cylindrical region of interest in the left-hand picture

 © Springer-Verlag Wien

Author's personal copy

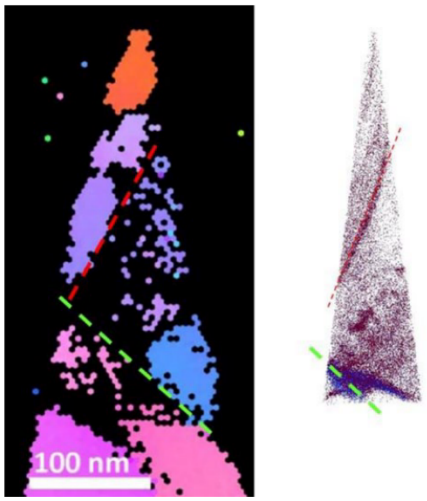

Fig. 6: Comparison between the final TKD scan and the APT reconstruction. The location and size of the interfaces of the TKD scan (*dotted lines*) coincide with the interfaces in the reconstruction

5. Discussion

According to literature a strong effect regarding the hardenability of steels can arise by adding a very small amount of boron, which makes boron an alternative for other transformation retarding elements, such as chromium or manganese.

The atom probe was selected for the detection of boron at a prior austenite grain boundary because of its atomic resolution and its ability to detect light elements. Nevertheless, the volume which can be measured in the APT is very limited. The grain boundary needed to be located close to the apex of the tip, which required a site-specific preparation. Because of the existence of various martensitic lath boundaries, random TKD scans provided little information on the location of a prior austenite grain boundary. Hence, a combination of etching and TKD scans in the FIB/SEM was used to ensure the right grain boundary is being prepared for an APT measurement.

The APT measurement revealed a large amount of boron segregated to a grain boundary. The shape of the tip and the distance of the grain boundary to the apex of the tip in the reconstruction coincide with the shapes and distances in the TKD scans (Fig. 6). Thus it can be stated that the boron actually segregated to an austenite grain boundary during the heat treatment applied in the present study.

6. Conclusions

1. In the 42CrMo4 heat treatable steel, boron segregates to austenite grain boundaries during quenching and retards the formation of high temperature phases by reducing the driving force for nucleation.
2. A preparation process combining etching and transmission Kikuchi diffraction (TKD) scans can be used to prepare a prior austenite grain boundary of a heat treatable steel for atom probe tomography.
3. The atom probe tomography measurement revealed boron segregated to the prior austenite grain boundary with a maximum local concentration of 1.5 at%.

References

1. Keown, S. R.; Pickering, F. B.: Some aspects of the occurrence of boron in alloy steels, Materials science and technology, 11 (1977), no. 7, pp 225–234
2. He, X. L.; Chu, Y. Y.; Jonas, J. J.: The grain boundary segregation of boron during isothermal holding, Acta metallurgica, 37 (1989), no. 11, pp 2905–2916
3. Mun, D. J.; Shin, E. J.; Cho, K. C.; Lee, J. S.; Koo, Y. M.: Cooling rate dependence of boron distribution in low carbon steel, Metallurgical and materials transactions A, 43 (2012), no. 5, pp 1639–1648
4. Simcoe, C. R.; Elsea, A. R.; Manning, G. K.: Study of the effect of boron on the decomposition of austenite, Journal of metals, 7 (1955), pp 193–200
5. Melloy, G. F.; Slimmon, P. R.; Podgursky, P. P.: Optimizing the boron effect, Metallurgical transactions, 4 (1973), no. 10, pp 2279–2289
6. Miller, M. K.; Cerezo, A.; Hetherington, M. G.; Smith, G. D. W.: Atom probe field ion microscopy, Oxford: Clarendon Press, 1996
7. Schacht, E.; Richter, J.: Experiences with etching reagents to show former austenite grain boundaries in steels, Praktische Metallographie, 35 (1998), no. 7, pp 384–395
8. Babinsky, K.; De Kloe, R.; Clemens, H.; Primig, S.: A novel approach for site-specific atom probe specimen preparation by focused ion beam and transmission electron backscatter diffraction, Ultramicroscopy, 144 (2014), pp 9–18
9. Miller, M. K.; Forbes, R. G.: Atom probe tomography, Materials characterization, 60 (2009), no. 6, pp 461–469
10. Morito, S.; Tanaka, H.; Konishi, R.; Furuhara, T.; Maki, T.: The morphology and crystallography of lath martensite in Fe-C alloys, Acta materialia, 51 (2003), no. 6, pp 1789–1799

Appendix C

NEUE ANSÄTZE ZUR ZIELPRÄPARATION VON ATOMSONDENSPITZEN MITTTELS FOCUSED ION BEAM UND DURCHSTRAHLUNGS-EBSD

K. Babinsky, P. Haslberger, Ch. Turk, H. Clemens, S. Primig

Department Metallkunde und Werkstoffprüfung, Montanuniversität Leoben, Österreich

ABSTRACT

Die Atomsondentomographie mit ihrem atomaren Auflösungsvermögen eignet sich hervorragend für chemische Analysen. Da die Zielpräparation von Korngrenzen für Atomsondenmessungen mit Hilfe von Transmissionselektronenmikroskopie sehr zeitintensiv ist, wird in dieser Studie die neuartige Methode „Durchstrahlungs-EBSD“ (t-EBSD) zur Unterstützung der Probenpräparation vorgestellt. Diese erfolgt in einem Standardverfahren mittels Nachspitzen einer elektrolytisch vorbereiteten Spitze mit einem fokussierten Ionenstrahl. Zwischen den einzelnen Präparationsschritten unterstützt die t-EBSD Technik den Prozess. Hierbei wird mittels t-EBSD die kristallographische Information der Spitze detektiert, um die Korngrenze zu identifizieren. Dadurch ist es möglich, eine Korngrenze in den ersten 200 nm der Probe zu positionieren ohne komplementäre Transmissionselektronenmikroskopieanalysen durchführen zu müssen.
Es werden zwei unterschiedliche Anwendungen für diesen neuen Präparationsprozess gezeigt. Eine Parameterstudie an walzhartem, technisch reinem Molybdän in Bezug auf Beschleunigungsspannung und Kippwinkel sowie die Untersuchung von ehemaligen Austenitkorngrenzen in einem mit Bor legierten 42CrMo4 Stahl werden vorgestellt.

1. EINLEITUNG

Mittels der Atomsonde ist es heutzutage möglich alle Elemente des Periodensystems zu detektieren. Multi-Phasen-Werkstoffe, Grenzflächen in Schichten, Versetzungsnetzwerke sowie Korngrenzen können mit dieser Methodik auf atomarer Ebene untersucht werden [1,2]. Durch die Atomsonde ist besonders das Interesse an der Analyse von Korngrenzen, in Bezug auf das Segregationsverhalten von Fremdatomen, gestiegen. Bereits sehr geringe Fremdatomkonzentrationen in technisch reinen Metallen beeinflussen die mechanischen Eigenschaften signifikant [3]. Auch Umwandlungsprozesse, die in Stählen auftreten, können durch Segregationen an Grenzflächen stark verzögert werden [4]. Die Atomsonde bietet eine nahezu atomare Auflösung sowie eine genaue Identifikation des Aufenthaltsortes jedes gemessenen Elementes, wodurch Korngrenzen im Detail analysiert werden können. Dennoch ist die einzigartige Messtechnik durch ihre aufwendige Probenpräparation limitiert. Eine nadelförmige Spitze mit einem Radius von 50 – 100 nm ist notwendig, um eine erfolgreiche Messung zu erzielen. Das analysierte Volumen beträgt rund 200x50x50 nm³, weshalb die zu untersuchende Stelle in den ersten 200 nm der Spitze positioniert werden muss. Konventionelle elektrolytische Präparationstechniken eignen sich für Bulkanalysen, jedoch nicht für orts-spezifische Messungen, wie jene von Korngrenzen. Mit Hilfe eines Focused Ion Beam (FIB) Systems, kombiniert mit einem Rasterelektronenmikroskop (REM), ist es jedoch heutzutage möglich, spezielle Bereiche in den ersten 200 nm einer Spitze zu positionieren [5]. Da jedoch die Auflösung des REMs für die letzten Präparationsschritte zu schlecht ist, sind beispielweise Korngrenzen in den ersten 500 nm der Spitze nicht mehr identifizierbar. Daher sind zeitintensive Transmissionselektronenmikroskopie (TEM) Analysen unumgänglich [3]. Aus diesem Grund wird in dieser Studie die neuartige Methode „Durchstrahlungs-EBSD“ (t-EBSD) zur Unterstützung der Probenpräparation vorgestellt. Diese Methodik vereinfacht die Spitzenpräparation, spart Zeit und gibt Informationen über kristallographische Eigenschaften wie etwa die Missorientierung der Korngrenze. Grundsätzlich wurde die Durchstrahlungsmethodik für eine bessere räumliche Auflösung für die Untersuchung von hochverformtem Material mit geringen Korngrößen entwickelt [6]. Keller et al. [6] schlugen als erste vor, eine dünne TEM-Folie über eine konventionelle EBSD Kamera zu positionieren, um die transmittierten vorwärtsgestreuten Elektronen aufzunehmen. Durch das Durchstrahlen wird eine weitaus höhere räumliche Auflösung erreicht, wodurch nun feinkörnige Gefüge oder auch feine Ausscheidungen mittels EBSD analysierbar sind.

Diese Studie zeigt die Anwendung von t-EBSD an Atomsondenspitzen für die Unterstützung des Präparationsprozesses. Anhand von walzhartem, technisch reinem Molybdän wird eine Parameterstudie in Bezug auf Beschleunigungsspannung und Kippwinkel durchgeführt. Des Weiteren wird auf die t-EBSD unterstützte Präparation einer ehemaligen Austenitkorngrenze in einem mit Bor legierten Vergütungsstahl näher eingegangen.

2. EXPERIMENTELLES

Bevor die Studie und der eigentliche Präparationsprozess mittels FIB/REM und t-EBSD beginnen kann, müssen Spitzen durch elektrolytisches Polieren hergestellt werden. Anfangs werden kleine Stäbchen (10x0.3x0.3 mm³) aus dem Material mit einem Präzisionsschleifgerät herausgeschnitten, welche anschließend in einem Elektrolyten mit einem Goldring als Gegenelektrode gedünnt werden. Die Präparation ist in drei Schritte aufgeteilt. In Schritt 1 wird in der Mitte des Stäbchens ein Hals geformt, der in Schritt 2 durchtrennt wird. Schritt 3 erfolgt zum Nachspitzen, sodass eine messfertige Spitze vorliegt. Eine genauere Beschreibung des gesamten Prozesses liefern Miller et al. [7]. Für die Präparation der Molybdänspitzen wird ein Elektrolyt mit 12.5 vol% H_2SO_4 in Ethanol verwendet. Für das Dünnen des Vergütungstahls dient 25 % Perchlorsäure in reiner Essigsäure für Schritt 1 und 2 % Perchlorsäure in 2-Butoxyethanol für Schritt 2 und Schritt 3. Die anschließende Präparation wird an einem FEI Versa 3D DualBeam Mikroskop ausgestattet mit einem EDAX Hikari XP EBSD System durchgeführt. Für den gesamten Präparationsprozess ist kein Wechsel zwischen unterschiedlichen Mikroskopen erforderlich. Die t-EBSD-Messungen erfolgen mit der EDAX OIM Data Collection 7 Software und die Auswertung mit der EDAX OIM Analysis 7 Software.
Die zu untersuchende Stelle, wie etwa eine Korngrenze, muss sich für eine erfolgreiche Atomsondenmessung in den ersten 200 nm der Spitze befinden. Aus diesem Grund wird durch Abtragen/Annular Milling mittels des Ionenstrahls die Grenzfläche nach vorne positioniert. Die gesamte FIB-Präparation wird bei einer Beschleunigungsspannung von 30 kV, 10 mm Arbeitsabstand und einem Kippwinkel von 52° durchgeführt. Um den Gallium-Eintrag gering zu halten wird im letzten Schritt eine Beschleunigungsspannung von 5 kV gewählt. Da das REM die Korngrenze in Dickenbereichen von 500 nm der Spitze nicht mehr auflösen kann, unterstützt t-EBSD die finale Präparation. Durch abwechselndes Abtragen mittels Ionenstrahl und t-EBSD Analysen wird die Korngrenze in den ersten 200 nm positioniert. Herkömmliche EBSD-Programme sind auf einen Kippwinkel von 70° von der Horizontalen kalibriert. Wie in Abb. 1a und 1b ersichtlich, weisen Atomsondenspitzen einen anderen Winkel bei der t-EBSD Analyse auf. Für eine korrekte Datenauswertung muss das Programm auf den Winkel von -38° eingestellt werden. Die weiteren t-EBSD Einstellungen sind in Tabelle 1 ersichtlich.

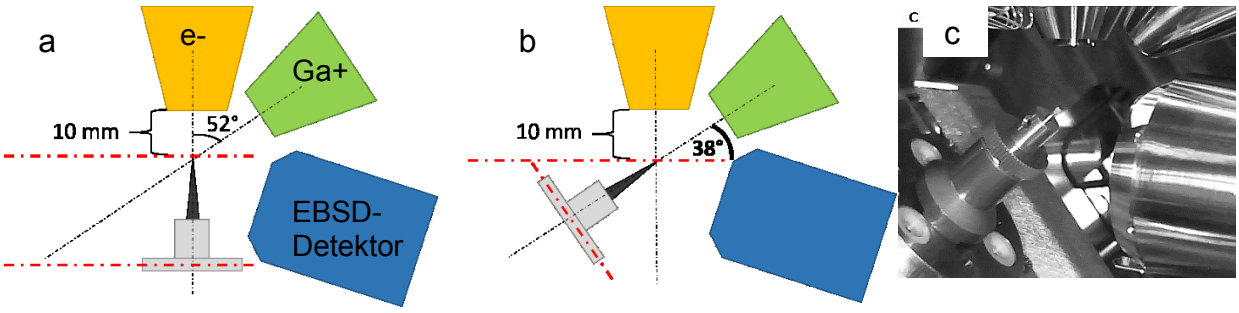

Abb. 1: (a) Schematischer Aufbau der Probenkammer bei einem Kippwinkel von 0°. Elektronen- und Galliumsäule stehen in einem Winkel von 52° zueinander. Die euzentrische Höhe befindet sich bei 10 mm. (b) Schematischer Aufbau der Probenkammer bei einem Kippwinkel von -38° von der Horizontalen (oder 52°). In dieser Position wird die Präparation durchgeführt. (c) Abbildung der Probenkammer beim Kippwinkel von -38° [8].

Tabelle 1: Übersicht der t-EBSD Einstellungen für die Probenpräparation.

Parameter	Wert	Parameter	Wert
Binning	4x4	Convolution Mask	9x9
Hintergrund	Enhanced	Binned Pattern Size	120
Hough P. Type	Classic+	Theta Step Size	0.5
Hough Resolution	Low	Scan step size	20-5 nm

Um die besten Einstellungen zu finden, werden im ersten Teil dieser Arbeit die Parameter wie Beschleunigungsspannung und Kippwinkel variiert. Der Arbeitsabstand von 10 mm und die in Tabelle 1 ersichtlichen Parameter werden konstant gehalten. Als Probenmaterial dient walzhartes, technisch reines Molybdän mit erholter Substruktur.
Anhand dieser Parameterstudie können für den zweiten Teil der Arbeit (Präparation einer ehemaligen Austenitkorngrenze) die optimierten Einstellungen (Beschleunigungsspannung von 30 kV, Kippwinkel von -38° aus der Horizontalen) verwendet werden. Als Probenmaterial dient ein mit Bor legierter 42CrMo4 Vergütungsstahl im gehärteten Zustand. Aufgrund der martensitischen Mikrostruktur enthält dieses Material sehr viele Grenzflächen. Aus diesem Grund müssen Austenitkorngrenzen gezielt gesucht werden. Dies erfolgt mittels einer Tauchätzung (100 ml kaltgesättigte Pikrinsäure, 5 ml Agepon, 10 ml Xylol, 0.5 ml HCl [9]) für 5 Minuten. Nach der Ätzung sind die ehemaligen Austenitkorngrenzen als Gräben auf der Spitze sichtbar (siehe Abb. 2). Durch den Ionenstrahl erfolgt nun das Abtragen der Spitze. Durch dieses Nachspitzen verschwinden jedoch die Gräben und dadurch die offensichtliche Information über die Position der Korngrenze in der Spitze. Der weitere Präparationsprozess wird daher mit t-EBSD-Messungen, die kristallographische Informationen liefern, unterstützt, um die Austenitkorngrenze identifizieren zu können. Ein ehemaliges Austenitkorn ist im martensitischen Zustand in mehrere „Packets“ (Pakete) aufgeteilt. Martensitlatten desselben Packets weisen gemäß der Kurdjumov-Sachs Beziehung nur bestimmte Winkelbeziehungen zueinander auf [10]. Folgende Winkel kommen in Frage: 10.53°; 14.88°; 20.61°; 21.06°; 47.11°; 49.47°; 50.51°; 51.73°; 57.21°; 60°. Zur Identifizierung einer ehemaligen Austenitkrongernze wird nach einem Winkel zwischen Körnern gesucht, der keinen der Kurdjumov-Sachs Winkel aufweist und somit einer Austenitkorngrenze entspricht. Durch abwechselnde Ausführung von Annular Milling und t-EBSD wird nun die Austenitkorngrenze in den ersten 200 nm der Spitze positioniert.

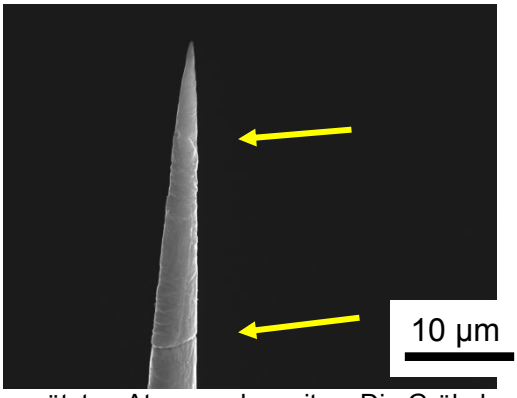

Abb. 2: REM-Aufnahme der angeätzten Atomsondenspitze. Die Grübchen weisen auf eine ehemalige Austenitkorngrenze hin (gelbe Pfeile) [11].

Die Atomsondenmessung der fertigen Spitze erfolgt am Gerät LEAP 3000X HR im Laser Modus mit einer Laserenergie von 0,3 nJ und einer Pulsrate von 250 kHz bei einer Temperatur von 60 K. Die Target Evaporation Rate ist auf 1 % gesetzt. Die Auswertung
erfolgt mittels der Software IVAS 3.6.6 von Cameca.

3. ERGEBNISSE UND DISKUSSION

3.1 PARAMETERSTUDIE

Die Parameterstudie soll zeigen, welche Beschleunigungsspannung und welcher Kippwinkel die Kikuchi-Beugungsbilder und dadurch die t-EBSD Analysen optimiert. Die Qualität der t-EBSD Messung wird anhand von Image Quality Maps, überlagert mit inversen Polfiguren, aufgezeigt. Wie in Abb. 3 ersichtlich, führt eine Beschleunigungsspannung von 30 kV zu einer besseren Durchstrahlung, wodurch auch noch dickere Bereiche analysiert werden können.

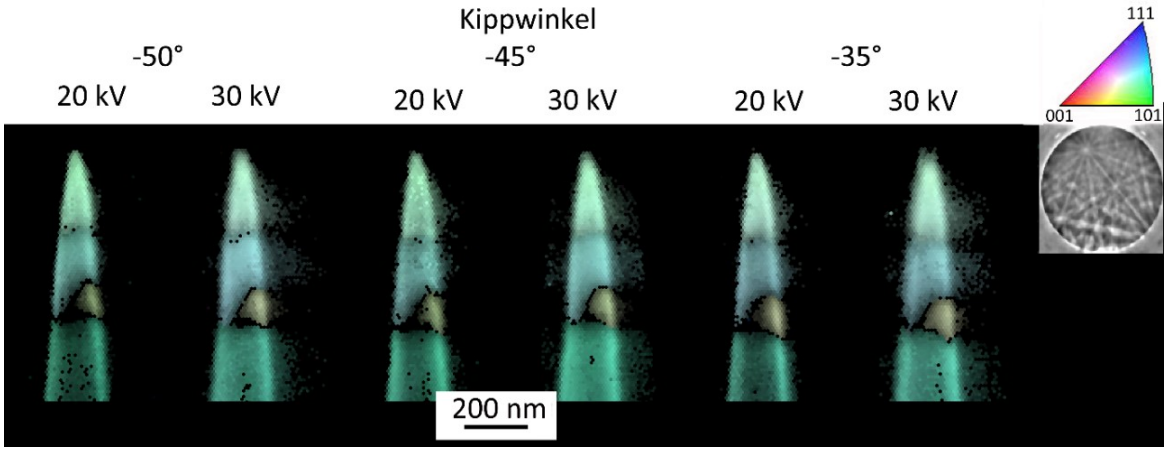

Abb. 3: Image Quality Maps, überlagert mit inversen Polfiguren, für verschiedene Beschleunigungsspannungen und Kippwinkel. Die Kristallrichtung in Bezug auf die inverse Polfigur-Kodierung ist parallel zu der Probenoberfläche. Ein typisches Kikuchi-Beugungsbild für Molybdän ist im rechten oberen Eck ersichtlich [8].

Des Weiteren führt ein Kippwinkel zwischen -45° und -35° zu einer guten Auflösung. In allen Bildern sind die Kleinwinkelkorngrenzen des walzharten Molybdäns erkennbar. Das Annular Milling wird standardgemäß bei einem Kippwinkel von -38° von der Horizontalen (oder 52° aus der Senkrechten) durchgeführt. Da dieser Winkel auch eine optimale Auflösung für t-EBSD Analysen bietet (siehe Abb. 3) muss zwischen Abtragen und t-EBSD Analysen keine Winkeländerung vorgenommen werden.

3.2 PRÄPARATION EINER EHEMALIGEN AUSTENITKORNGRENZE IN EINEM VERGÜTUNGSSTAHL

In Abb. 4a ist der finale t-EBSD Scan ersichtlich, der die ehemalige Austenitkorngrenze in den ersten 200 nm zeigt. Für eine genaue Darstellung der Grenzfläche liegt für 90° eine weitere Analyse vor (siehe Abb. 4b). Laut EBSD hat diese Korngrenze, welche in Abb. 4 entlang der gelb strichlierten Linie verläuft, eine Missorientierung von 53° (Winkelmessung in Abb. 4c und d ersichtlich). Dieser Winkel gehört nicht zu dem von Kurdjumov-Sachs bestimmten Martensitlatten-Winkelbeziehungen. Es wird vermutet, dass hier eine ehemalige Austenitkorngrenze mit eventuellen Bor-Segregationen vorliegt. In Abb. 5a ist die dazugehörige Rückkonstruktion der in der Atomsonde gemessenen Spitze zu sehen.

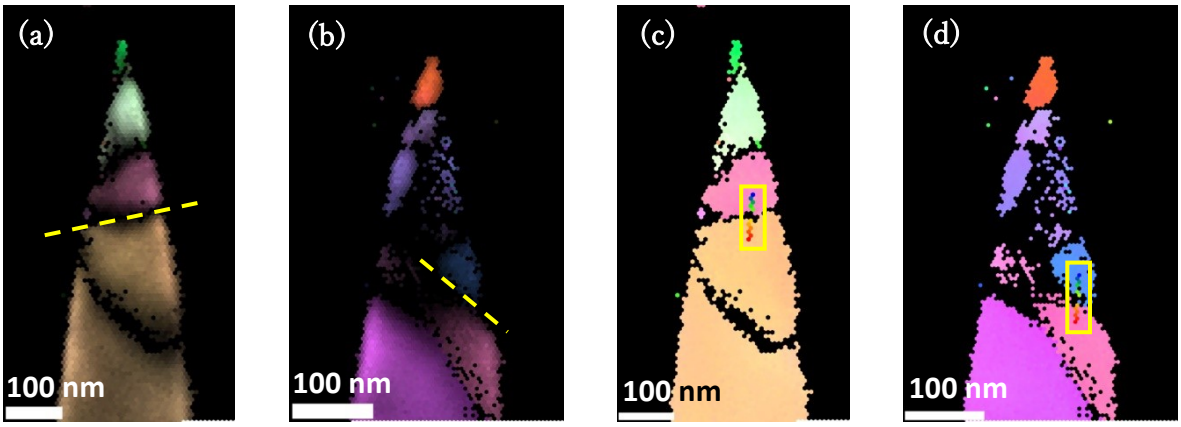

Abb. 4: t-EBSD Messungen des Endzustands der Spitze: (a) Endzustand, (b) Endzustand um 90° gedreht, (c) Winkelmessung 1, (d) Winkelmessung 2. Laut t-EBSD hat die durch eine gelb strichlierte Linie markierte Korngrenze eine Missorientierung von 53° [11].

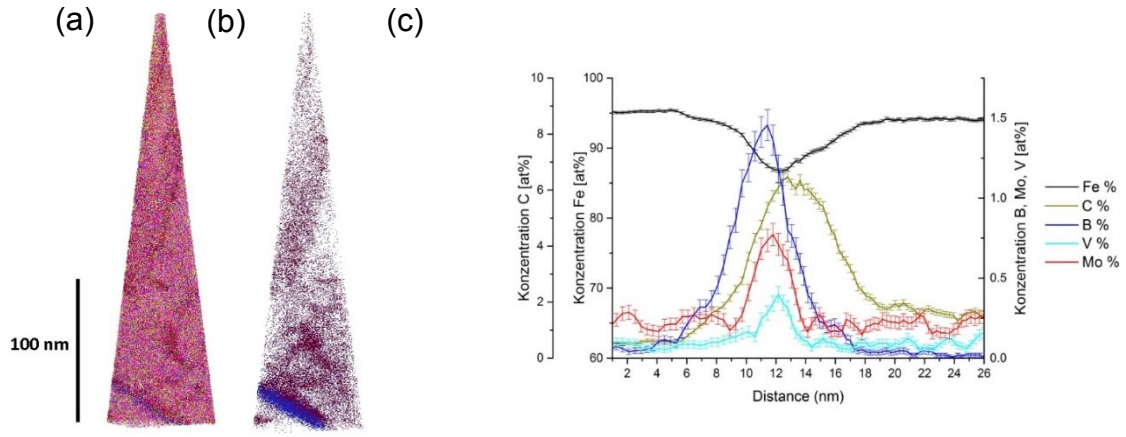

Abb. 5: Rückkonstruktion der Spitze mit ehemaliger Austenitkorngrenze: (a) alle Atome angezeigt. (b) nur C (braun) und B (blau) angezeigt, (c) 1D-Konzentrationsprofil der ehemaligen Austenitkorngrenze [11].

Zur besseren Verwertbarkeit der Rückkonstruktion sind in Abb. 5b alle Atome bis auf Kohlenstoff und Bor ausgeblendet. Man erkennt mehrere kleine Anhäufungen von Kohlenstoff. Am unteren Ende des gemessenen Volumens ist eine starke Anreicherung von Kohlenstoff und Bor zu sehen. Für eine bessere Quantifizierung dieser Grenzfläche dient ein 1D-Konzentrationsprofil (siehe Abb. 5c). Im Bereich der flächigen Anreicherung steigt die Borkonzentration rapide auf einen Maximalwert von ca. 1.5 at% an. Molybdän und Vanadium zeigen ebenfalls einen Anstieg im Konzentrationsprofil, während der Gehalt an Eisenatomen im betrachteten Bereich abfällt. Da Bor in dieser Probe nur an ehemaligen Austenitkorngrenzen sitzen sollte, ist dies der Beweis für den Erfolg dieser Präparationsmethode.

4. ZUSAMMENFASSUNG

Die neue t-EBSD Technik erweitert die Möglichkeiten der Atomsondenprobenpräparation maßgeblich. Zwischen den einzelnen FIB-Präparationsschritten unterstützt t-EBSD die Lokalisierung von Korngrenzen. Zusätzlich sind kristallographische Informationen der Spitze in der Analyse enthalten, die zur Unterstützung der Auswertung der Atomsondendaten dienen. Speziell ehemalige Austentikorngrenzen können mittels t-EBSD identifiziert und durch den gekoppelten Herstellungsprozess in den ersten 200 nm positioniert werden. Die Atomsondenmessung hat gezeigt, dass in einem Vergütungsstahl (42CrMo4) elementares Bor an einer ehemaligen Austenitkorngrenze vorliegt.

5. REFERENZEN

[1] M.K. Miller, R.G. Forbes: “Atom probe tomography”, Mater. Charact. 60, 2009, p.461–469

[2] T.F. Kelly, M.K. Miller: “Invited review article: atom probe tomography”, Rev. Sci. Instrum. 78, 2007, p.031101-1–031101-20

[3] K. Babinsky, J. Weidow, W. Knabl, A. Lorich, H. Leitner, S. Primig: “Atom probe study of grain boundary segregation in technically pure molybdenum”, Mater. Charact. 87, 2014, p.95–103

[4] C.R. Simcoe, A. R. Elsea, G. K. Manning: “Study of the effect of boron on the decomposition of austenite” Trans. AIME 203, 1955, p.193-200

[5] P.R. Munroe: “The application of focused ion beam microscopy in the material sciences” Mater. Charact. 60, 2009, p.2–13

[6] R.R. Keller, R.H. Geiss: “Transmission EBSD from 10 nm domains in a scanning electron microscope” J. Microsc. 245, 2012, p.245–251

[7] M.K. Miller, A. Cerezo, M.G. Hetherington, G.D.W. Smith: “Atom probe field ion microscopy”, Clarendon Press, Oxford, 1996

[8] K. Babinsky, R. De Kloe, H. Clemens, S. Primig: “A novel approach for site-specific atom probe specimen preparation by focused ion beam and transmission electron backscatter diffraction”, Ultramicroscopy 144, 2014, p.9-18

[9] E. Schacht, J. Richter: “Experiences with etching reagents to show former austenite grain boundaries in steels”, Praktische Metallographie 35/7, 1998, p.384-395

[10] S. Morito, H. Tanaka, R. Konishi, T. Furuhara, T. Maki: “The morphology and crystallography of lath martensite in Fe-C alloys”, Acta Materiala 51, 2003, p.1789-1799

[11] P. Haslberger: “Die Wirkung von Bor im Vergütungsstahl 42CrMo4”, Diplomarbeit, Department Metallkunde und Werkstoffprüfung, 2014